Discrete Element Modelling of Permanent Pavement Deformation in Granular Materials

by

Wei Cai, BEng.

Thesis submitted to The University of Nottingham

for the degree of Doctor of Philosophy

June 2015

Abstract

The permanent deformation of a pavement due to vehicle load is one of the important factors affecting the design life as well as the maintenance cost of a pavement. For the purpose of obtaining a cost-effective design, it is advisable to predict the traffic-load-induced permanent pavement deformation. The permanent deformation in pavements (i.e. rutting) can be classified into three categories, including the wearing of the asphalt layers, compaction, and shear deformations. In the present study, discrete element analyses have been performed to predict the permanent deformation of a pavement when subjected to moving wheel loads. Note that the wearing of the asphalt layers has been disregarded.

DEM biaxial test simulations have been carried out in terms of both unbonded and bonded granular materials. The typical stress-strain response, as well as the volumetric strain development, have been reproduced, in qualitative agreement with the experimental results. The factors affecting the mechanical behaviour of granular materials have been investigated, e.g. particle stiffness, sample compaction and parallel bond strength. In addition, the elastic properties, initial yield stress, strength parameters and so on have been analysed. These compression tests provided guidance for the selection of the particle parameters for the subsequent pavement simulation.

The permanent deformation in unbonded pavements was represented under moving wheel loads, and proved to be qualitatively consistent with the laboratory tests. The initial self-weight stress had a significant effect on rutting. When the initial gravity stress was relatively high, both shakedown and surface ratchetting phenomena were observed for different loading levels. However, the accumulation of permanent deformation was continual for pavements with low gravity stress, even if the wheel pressure was small. Other factors affecting the rutting have been taken into consideration, e.g. specimen preparation, interparticle friction, etc. In the case of the single-layered pavement, permanent deformation ceased after the first wheel pass. Plastic deformation increased with the decrease in the self-weight stress. For the double-layered pavement, the permanent deformation continually increased with wheel passes, probably owing

to compaction of the bottom unbound layer. The pavement shakedown phenomenon was not observed prior to wheel pass 300. The permanent deformation increased augmentation of wheel pressure as well as decrease in the sample density and upper layer thickness.

The residual stresses in both vertical and horizontal directions can be obtained using the measurement circle. For all the pavements in the current simulations, the vertical residual stress is nearly always zero, consistent with the equilibrium condition. In the case of the unbonded pavement, the large horizontal residual stress depends on the high initial gravity stress, instead of high wheel pressure or wheel pass number. For the single-layered pavement, the peak of the horizontal residual stress was observed near the pavement surface. The residual stress rises with the augmentation of the wheel pass number and the wheel pressure. In the double-layered pavement, the residual stresses are discontinuous at the interface between different pavement layers. The peak appears near the pavement surface and increases with the reduction in the upper layer thickness as well as the rise in wheel passes and wheel pressure. Nevertheless, residual stress is not apparent in the granular base.

The probability density distribution was investigated in terms of the contact and bond forces. For the normal contact force, a peak generally appeared at small contact forces, followed by a drastic decrease and, after that, the probability density progressively approached zero. For the tangential contact force as well as the bond forces, in general, a peak of the probability distribution was observed at small contact forces, and then a sharp drop followed from the two flanks of the peak point. Finally, there was a gradual decrease until the probability density decayed to zero. The factors, e.g. pavement layer, wheel pass number and wheel pressure, mainly affect the probability distribution of the small contact or bond forces. For both single- and double-layered pavements, the absolute extrema of the bond forces in the top layer increased with the augmentation of the wheel pass number and the wheel pressure.

For the unbonded pavement, the sliding contact ratio was studied and it was significantly affected by the pavement layer, initial gravity stress and sample compaction.

The distribution of the pavement particle displacements were demonstrated. In the unbonded pavement, factors, such as wheel pressure and initial gravity, not only affect the distribution of the relatively large particle displacements but also increase the magnitude of the particle displacements. The directions of the large displacement vectors are diverse as the large gravity acceleration is assigned to the particles but are almost downward when the self-weight stress is small. In the single- or double-layered pavement, factors, such as wheel pass number and wheel pressure, merely increase the values of the particle displacements. The distribution of the displacements is hardly affected. For the single-layered pavement, the large displacements were observed near the pavement surface and their directions are almost contrary to the movement direction of the wheel. In the double-layered pavement, relatively large particle displacements are widely distributed in the pavement. Their directions are in an almost vertical direction.

Acknowledgements

I would like to express my most sincere gratitude to my supervisors, Prof. Hai-Sui Yu and Dr. Dariusz Wanatowski, who have provided me with the excellent opportunity to conduct this project with valuable guidance, interest and encouragement over the years. Also, sincere thanks go to Dr. Xia Li for her rigid guidance and technical support. In addition, I am deeply indebeted to Prof. Hai-Sui Yu for his interest in the current research and the provision of financial assistance.

I would also like to express my gratitude to the following people for their support and suggestions:

My previous office mate, Dr. Juan Wang, for her assistance in the theory of pavement shakedown and daily life;

My friend, Dr. Jipeng Wang, for his support in the DEM numerical simulation and useful discussions on our common interests;

Dr. Jun Ai and Nian Hu for their help and invaluable advice throughout the PhD study;

Dr. Yan Geng, Dr. Jean-Francois Ferellec and Dr. Dunshun Yang for technical support in PFC study;

My colleagues and friends: Yang Lv, Bo Zhou, Dr. Feiran Wang, Shu Liu, Yawen Liu, Hui Wang, Peizhi Zhuang, Ran Yuan, Qiong Xiao, etc.

All the staff in the Nottingham Centre for Geomechanics (NCG) and the Civil Engineering Department in the University of Nottingham.

Finally, my greatest gratitude goes to my parents, my wife, brothers, and sisters for their constant love, support and encouragement. I would especially like to give my deepest thanks to my wife, Shifeng Zhong, for accompanying me through the hard time in my life.

Contents

List of Figures

List of Tables

Nomenclature

Symbols

α	Damping constant in Section 3.2
α	Dip angle of the strength line in Chapter 4
α	Local damping coefficient in Chapter 5
α	Relaxation factor in Section 3.3
α_{ij}	Displacement gradient tensor
$\bar{\lambda}$	Multiplier of parallel-bond radius
$\bar{\sigma}_c$	Normal strength of the parallel bond
$\bar{\sigma}_{ij}$	Average stress tensor
$\bar{\sigma}_{ij}^{(p)}$	Average stress tensor of particle (p)
$\bar{\tau}_c$	Shear strength of the parallel bond
$\bar{A}$	Cross-sectional area of parallel bond
$\bar{F}$	Mean normal force
$\bar{F}_i$	Resultant force within the parallel bond
$\bar{F}_i^n$	Normal force within the parallel bond
$\bar{F}_i^s$	Shear force within the parallel bond
$\bar{I}$	Inertia moment for the parallel bond
$\bar{k}^n$	Normal stiffness of the parallel bond
$\bar{k}^s$	Shear stiffness of the parallel bond
$\bar{M}_3$	Resultant moment within the parallel bond

$\bar{p}$ Mean contact pressures between wheel and pavement surface

$\bar{R}$ Radius of the parallel bond

$\bar{V}_i$ Mean velocity of the N_p particles

$\bar{x}_i$ Mean location of the N_p particles

$\ddot{x}_i$ Translational acceleration of the mass centre of the clump

$\Delta\sigma^{(w)}$ Increment of the wall stress

$\Delta F^{(w)}$ Maximum increment for wall force

ΔF_i^s Shear contact force increment

Δt Time step

ΔU_i^s Shear displacement increment

$\dot{\alpha}_{ij}$ Velocity gradient tensor

$\dot{\omega}_{ij}$ Spin tensor

$\dot{\varepsilon}_{ij}^k$ Kinematically admissible plastic strain rate cycle

$\dot{e}_{ij}$ Rate-of-deformation tensor

$\dot{H}_i$ Time rate-of-change of the angular momentum of the clump

$\dot{u}^{(w)}$ Wall velocity

$\dot{u}_i^k$ Displacement velocity

Γ Gamma function

κ Standard deviation of the normal distribution

λ Dimensionless load parameter in Chapter 2

λ Scale parameter of the Weibull distribution in Chapter 4

λ_d Dimensionless disc radius parameter

λ_s Analytical shakedown limit parameter

μ Particle friction coefficient

ν Poisson's ratio for a plane strain state

ν' Poisson's ratio for a plane stress state

ω_0	Angular velocity of wheel in Chapter 5
ω_{ij}	Rotation tensor
ϕ	Internal friction angle
σ	Stress
σ_0	Required confining stress
σ_1	Major principal stress
σ_3	Minor principal stress
σ_{ic}	Low isotropically compressive stress
σ_{ij}	Stress tensor
σ_{ij}^r	Residual stress tensor
$\sigma_{ij}^{(p)}$	Stress tensor acting on particle (p)
σ_{max}	Maximum tensile stress existing on the bond periphery
σ_{vc}	Low vertical consolidation stress
σ_{ij}^e	Elastic stress tensor
σ_{ij}^k	Stress tensor on the yield surface
τ_{max}	Maximum shear stress existing on the bond periphery
Int[*]	Integer of disc number
θ_p	Direction of anisotropy
$\tilde{F}_i^{[p]}$	Externally-applied force acting on particle (p)
$\tilde{M}_i^{[p]}$	Externally-applied moment acting on particle (p)
ε	Strain
ε_1	Major principal strain
ε_3	Minor principal strain
ε_a	Axial strain
ε_v	Volumetric strain
$\widetilde{\sigma}$	An alternate incorrect expression for the average stress
$\widetilde{k}^n$	Applied normal stiffness of the parallel bond
$\widetilde{k}^s$	Applied shear stiffness of the parallel bond

$\widetilde{R}$	Radius of the elastic beam designated from the contact between particles
$\widetilde{V}_i^{(p)}$	Measured relative velocity of particle (p)
$\widetilde{v}_i^{(p)}$	Predicted relative velocity of particle (p)
ζ	Mean of the normal distribution
A	Area
a	Intercept of the strength line in Chapter 4
a	Semicontact width between wheel and pavement surface in two dimensions
a_p	Magnitude of anisotropy in particle orientation
$A_{(i)}$	Generalised acceleration
c	Cohesion
C_n	Coordination number
c_n	Cohesion of nth layer
C_{rr}	Rolling resistance coefficient
d	Positive constant
E	Young's modulus for a plane strain state
e	Void ratio
E'	Young's modulus for a plane stress state
E_c	Contact Young's modulus
E_n	Young's modulus of nth layer
$E_p(\theta)$	Probability density function of the particle orientation with a directional distribution
e_{ij}	Infinitesimal strain tensor
$F(x, \lambda, k)$	Cumulative distribution function of a Weibull distribution
$f(x, \lambda, k)$	Probability density function of a Weibull distribution
$F(x, \zeta, \kappa)$	Cumulative distribution function of a normal distribution
$f(x, \zeta, \kappa)$	Probability density function of a normal distribution
F	Normal force

f Internal friction coefficient

$f(\sigma_{ij})$ Yield condition

$F^{(c,w)}$ Contact force between particle and wall

F_i Sum of all externally-applied forces acting upon the clump

$F_i^{[p,c]}$ Contact force acting upon particle (p) at contact (c)

$F_j^{(c)}$ Contact force vector

$F_k^{[p,c]}$ Force acting on particle (p) at contact (c)

$F_k^{[p]}$ Resultant force acting on particle (p) at its centroid

F_n Normal force between wheel particle and pavement particle

$F_p(\theta)$ Cumulative distribution function for $\theta_p = 0$

F_s Friction force between wheel particle and pavement particle

$F_{(i)}$ Generalised force

$F_{(i)}^d$ Damping force

F_{nx} Horizontal normal force between wheel particle and pavement particle

F_{ny} Vertical normal force between wheel particle and pavement particle

F_i^n Normal contact force

F_i^s Shear contact force

F_{max}^s Maximum allowable shear contact force

G Shear modulus for a plane strain state in Chapter 4

G "Gain" parameter in Chapter 3

g Gravitational acceleration

g_i Body force acceleration vector arising from gravity loading

H Random variable of a general normal distribution

h Height of the sample vessel in Chapter 5

h Layer thickness for micro-analysis in Chapter 7

I_{ii}	Moments of inertia of a clump
I_{ij}	Products of inertia of a clump
K	Bulk modulus for a plane strain state
k	Shape parameter of the Weibull distribution
k^n	Normal stiffness at contact
k^s	Shear stiffness at contact
k_n	Normal stiffness of ball or wall
$k_n^{(w)}$	Average stiffness of contacts between the particles and the vertical or horizontal walls
k_s	Shear stiffness of ball or wall
L	Current sample length
L	Length of the elastic beam designated from the contact between particles
L_0	Original sample length
M	Constraint modulus for a plane strain state
m	Total mass of the clump
$m^{[p]}$	Mass of the particle (p)
M_i	Resultant moment related to the mass centre
$M_{(i)}$	Generalised mass
n	Porosity
N_b	Number of particles with centroids in the measurement circle
N_c	Number of contacts between the particles and one vertical or horizontal wall
$n_c^{(b)}$	Contact number of the particle (b)
n_i	Unit normal vector
$n_i^{(c,p)}$	Unit-normal vector directed from the particle centroid to the contact location
N_p	Number of particles that intersect the measurement circle
$N_{(c,w)}$	Number of contacts between particle and wall

p	Mean of the major and minor principle stresses in Chapter 4
p	Normal contact pressure
$P(F)$	Probability density distribution of normal forces
p_0	Maximum normal contact pressure
p_{0n}	Unit normal contact pressure
q	Deviatioric stress
q_0	Shear stress
$r^{(p)}$	Radius of the disc (p)
$R^{[p]}$	Radius of the particle (p)
r_m	Mean value of maximum and minimum disc radii
S	Random variable of the Weibull distribution
$S^{(p)}$	Particle surface
S_T	Structure surface where traction are specified
t	Deposition time in Chapter 5
t	Thickness of the cylindrical particle in Chapter 4
T_{0i}	External load
U^n	Normal displacement
u_i	Displacement vector
V	Translational velocity of wheel in Chapter 5
V	Volume
V_0	Linear velocity of wheel corresponding to the angular velocity in Chapter 5
v_i	Velocity vector
$V_i^{(p)}$	Translational velocity of particle (p)
$V_{(i)}$	Generalised velocity
X	A random number for the uniform distribution
$x_i^{(c)}$	Contact location vector
$x_i^{(p)}$	Particle centroid location vector
$x_i^{[G]}$	Location of the mass centre

x_n Interval of normal contact force for micro-analysis

x_t Interval of the tangential force for micro-analysis

Z A random number for the standard normal distribution

z Sum of the squares of the deviations between predicted and measured velocities

erf Gaussian error function

Abbreviations

PFC^{2D} Particle flow code in two dimensions

AASHTO American Association of State Highway and Transportation Officials

DEM Discrete element method

LVDT Linear variable differential transducer

PBS$_{mean}$ Mean parallel-bond strength for both in normal and shear direction

ROSD Ratio of the standard deviation κ to the mean parallel bond strength PBS$_{mean}$

SAMDM South African Mechanistic Design Method

Chapter 1

Introduction

1.1 Background to research

Empiricism is still the important principle behind the design of pavements up to the present time. The thickness of a pavement is determined entirely through experience. A part of road pavements has the same thickness, although different soil subgrades occur in geotechnical engineering. A series of methods has been proposed by various agencies, based on experience, to determine the ideal thickness of road pavements. Flexible pavements usually comprise asphaltic and granular materials. Rutting and cracking of pavement surfaces are the main causes of flexible pavement failures. The design methods of flexible pavements can be divided into five groups, namely the empirical method, the mechanistic-empirical method, the limiting deflection method, the limiting shear failure method, and the regression method (Huang, 1993).

Empirical methods are most widely used to design flexible pavements, e.g. in the Transportation Officials Guide and that of the American Association of State Highways. The current empirical approach is generally based on experimental data from in-service pavement performance and full scale road tests. Some empirical equations, such as the power equation, have been proposed to obtain the permanent deforma-

tion of road pavements under repeated wheel loads (Monismith et al., 1975; Li and Selig, 1996). However, the relationship between the elastic strain and the permanent deformation behaviour of road pavements tends not to be directly established (Shiau, 2001). In general, plastic strain is assumed not to be induced and the importance of plastic behaviour to the pavement life cycle is disregarded. Another weakness of the empirical method is related to the limitation of the environmental, material and loading conditions (Huang, 1993). If these conditions are altered, this method is no longer applicable to the pavement design.

The mechanistic-empirical method of pavement design depends on the mechanical behaviour of materials, e.g. the stress or strain response of road pavements to a wheel pressure. According to laboratory tests and field performance data, prediction of pavement distress is performed using the response values. As first recommended by Kerkhoven and Dormon (1953), the vertical compressive strain on the surface of the subgrade can be applied as a failure criterion for pavement design. In addition, the horizontal tensile strain at the bottom of the asphalt layer is employed to reduce fatigue cracking (Saal and Pell, 1960). Moreover, a mechanistic-empirical design approach, i.e. the South African Mechanistic Design Method, has been used in South Africa (Theyse et al., 1996). Transfer functions are proposed to predict the permanent pavement deformation in terms of the unbound pavement layer, the individual pavement layers and the roadbed. In the mechanistic-empirical framework, there exist the linear elastic model, the linear elastic model with the viscoelastic response and the nonlinear finite element model (e.g. Monismith et al., 1977; Kenis, 1977; Lytton et al., 1993). The strengths of the mechanistic-empirical method are improvement in the reliability of pavement design, and the ability to predict types of pavement distress (Huang, 1993).

The thickness of pavements can be obtained using the limiting shear failure method so that shear failures will not take place (e.g. Barber, 1946; Yoder, 1959). The cohesion and internal friction angle are the main parameters to be determined in terms of pavement materials and subgrade soils. The limiting deflection method is applied to the design of road pavements so that the maximum limit of the vertical deflection

is not exceeded (Huang, 1993). The evident strength of this method is that it can be easily measured in the field. However, pavement failures will be induced by excessive stresses and strains rather than deflections. For the regression method, the regression equations are proposed on the basis of the performance of existing pavements (e.g. Darter et al., 1985; Hall et al., 1989). The advantage of these equations is that the effect of various factors on pavement performance is considered, whereas there is a significant limitation on pavement design due to the many uncertainties concerned (Huang, 1993).

Destruction of road pavements subjected to repeated vehicle loads is generally brought about by progressive deterioration, instead of sudden failure. Therefore, the long-term plastic behaviour needs to be taken into consideration. Over the last three decades, a growing attention has been paid to the application of shakedown theorems so as to study the mechanical behaviour of road pavement structures under repeated traffic loads (e.g. Sharp and Booker, 1984; Collins et al., 1993; Yu and Hossain, 1998; Yu, 2005). Theoretically, there exists a critical load limit below which the accumulation of plastic strain ceases because of the protective residual stress and above which the road pavements will be destroyed as a result of the continuous accumulation of plastic strain. This load limit is called the shakedown limit. Melan (1938) developed a fundamental theorem for static shakedown, which provides a lower bound to the shakedown limit. Later, Koiter (1960) proposed a kinematic shakedown theorem to give an upper bound to the shakedown limit. The shakedown limit load seems first to have been proposed as providing proper parameters for road pavement design by Sharp and Booker (1984). Determination of the shakedown limit for pavement design has been performed (e.g. Yu and Hossain, 1998; Shiau, 2001; Yu, 2005; Wang, 2011). The pavement shakedown phenomenon has also been validated by laboratory wheel tracking tests (e.g. Juspi, 2007) and by the AASHO road test records (see Sharp and Booker, 1984).

A few discrete element modelling (DEM) simulations for road pavements have been proposed. A 2D flexible pavement structure was constructed by Vallejo et al. (2006), composed of a modelled asphalt concrete layer and a granular base. The particle degra-

dation in the granular base was studied and particle crushing was not allowed in the modelled asphalt layer. It was found that particle breakage started at the top of the granular base course and went on to spread towards the bottom of the base layer during repeated wheel loads. In addition, a flexible pavement in three dimensions was established by Dondi et al. (2007), containing an asphalt layer, as well as granular subbase and subgrade courses. The asphalt layer was simulated using Burger's model. The visco-elastic behaviour of the simulated pavement subjected to two circular contact patches was studied. The contact stress distributions within the simulated pavement section were measured in terms of vertical, horizontal and shear stresses. Moreover, some DEM simulations have been performed on the mechanical behaviour of the elementary specimens, comprised of unbound granular materials subjected to quasi-static cyclic loading (e.g. Garca-Rojo and Herrmann, 2005; Luding et al., 2007). The development of permanent deformation with the repetition number of the external loads was recorded. For different load levels, shakedown (i.e. no further accumulation of permanent deformation) and ratchetting (i.e. the continuous accumulation of plastic strain in individual loading cycles) were observed. Therefore, as discussed above, DEM simulation of permanent deformation of road pavements under repeated traffic loads can be carried out. It is potentially useful in pavement structure design.

1.2 Aims and objectives

The overall objective of the research is to study permanent deformation in road pavements at a grain scale. The residual stress will also be measured. In addition, related micro-analysis will be performed to provide an insight into the mechanism of permanent pavement deformation.

The following objectives are included:

1. To gain better understanding of the mechanical behaviour of both unbonded and bonded granular materials.

2. To develop a DEM approach to study the response of road pavements subjected to repeated wheel loads.

3. To examine the permanent deformation in road pavements in terms of the unbound pavement, as well as single-layered and double-layered pavements; to validate the phenomena of pavement shakedown and ratchetting.

4. To obtain the residual stress field in road pavements induced by repeated moving surface loads.

5. To study the influence of selected factors on permanent pavement deformation and the residual stress field.

6. To learn about the probability density distribution of the contact and bond forces as well as the sliding contact ratio.

7. To demonstrate the distribution of the pavement particle displacement vectors for different kinds of road pavements.

1.3 Research overview

This thesis consists of eight chapters. A brief outline is given below:

Chapter 1 introduces the relevant background and crucial objectives of the present study on the road pavement design.

Chapter 2 presents broad literature reviews on pavement definition, pavement response to repeated wheel loads, pavement failure mode and design, and pavement shakedown analysis in pavement engineering.

Chapter 3 reports on DEM biaxial test simulation of unbound granular materials. The mechanical behaviour, including the stress-strain response and volumetric strain de-

velopment, is examined. Some factors affecting the mechanical response, e.g. particle shape, particle friction coefficient and sample compaction are taken into consideration.

Chapter 4 covers the mechanical behaviour of bonded granular materials. The elastic parameters, initial yield stress, strength properties, bond breakage and shear-dilatancy response are considered. The influence of certain factors, e.g. bond size, bond strength distribution and bond strength, on the mechanical response is studied.

Chapter 5 develops a DEM approach to learn about permanent deformation in the unbound pavement. The procedure is validated by comparison with the laboratory tests. The phenomena of both pavement shakedown and ratchetting are examined. The residual stress field in the pavement is obtained by means of measurement circles. A series of factors affecting the permanent deformation and residual stress field are studied, e.g. wheel pressure, and initial self-weight stress.

Chapter 6 studies the permanent deformation in both single- and double-layered pavements. The residual stress distribution in the pavement is analysed. A comparison of permanent deformation and residual stress between different factors is made.

Chapter 7 proposes a micro-analysis for the unbound pavement as well as single- and double-layered pavements. The probability density distribution of both contact and bond forces, the sliding contact ratio and the distribution of pavement particle displacements are studied.

Chapter 8 summarises the major findings of the current research and gives some suggestions for future research.

Chapter 2

Literature Review

2.1 Introduction

This chapter starts with an introduction to pavement analysis and design. The pavement structure and materials are described, and the contact area between wheel tyre and pavement surface as well as the wheel pressure distribution are presented. Afterwards, a literature review associated with pavement response to repeated traffic loads, pavement distress and failure modes and pavement design approaches is introduced. In addition, the shakedown concept is explained and the protective residual stress involved is reviewed. Finally, there is a description of the shakedown analysis in pavement engineering.

2.2 Pavement analysis and design

2.2.1 Introduction

Generally speaking, it is unrealistic for the natural soil to bear the repeated traffic loads without deterioration. Consequently, a protective structure is frequently placed on the natural soil to prevent the failure of the soil foundation. This structure is usually multi-layered and termed as a pavement. Normal pavements have been classified into three categories, namely flexible, rigid and composite pavements (Thom, 2008). The former consists of a bituminous surface course over granular materials, the second positions a concrete slab either straight on the soil or on a thin granular base course, and the latter has an asphalt surface overlying a concrete base.

A major function of the pavement is to make the distribution of the traffic load over the top surface of the soil foundation much larger than the contact area between the wheel tyre and pavement surface, as shown in Figure 2.1. In this way, the maximum stress in the soil foundation can be decreased to a level that the soil can support with acceptable permanent deformation during the design life. The pavement should have sufficient stiffness and thickness to protect the soil foundation, while no significant fracture or large permanent deformation occurs during the life of the pavement. Pavements are normally designed for twenty years or longer.

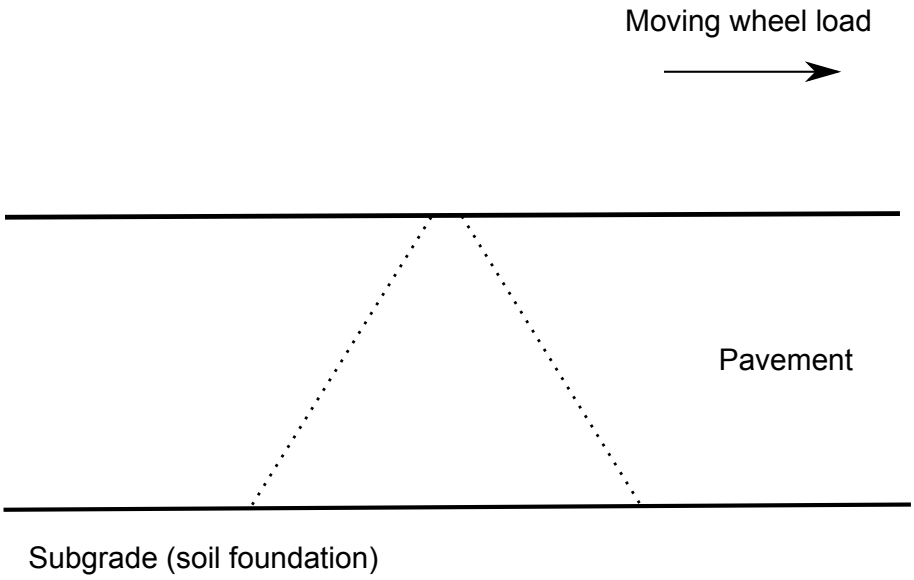

Figure 2.1: Wheel load distribution through pavement structure

2.2.2 Pavement structures

Modern flexible pavements contain three major layers, i.e. bituminous surface course, roadbase and subbase. The soil foundation for flexible pavements is called as a subgrade. The components of flexible pavement structures are demonstrated in Figure 2.2.

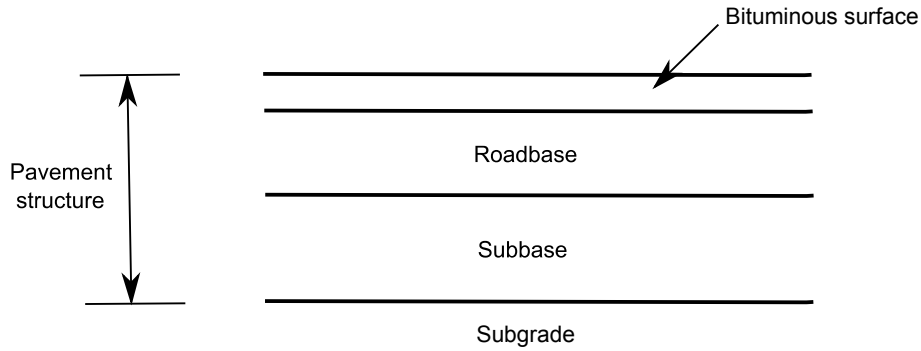

Figure 2.2: Components of flexible pavement structures

2.2.2.1 Bitumen-bound surfaces

Typically, 90% of paved highways contain a bituminous surface layer (Thom, 2008). The function of the surface is to provide a safe and smooth riding surface. Bitumen is a

binder, like Portland cement and some other hydraulic binding agents. However, they have quite different properties. Although a rigid pavement layer is constructed using hydraulic binding agents and has no appreciable deformation under repeated traffic loads, bitumen has the ability to 'flow' since it remains a viscous liquid at in-service temperatures. The main mechanical characteristics of a bitumen-bound layer are shear strength development induced by particle interlock and cohesion, as well as significant tensile strength. The properties are temperature sensitive. The normal distress modes are fracture induced by fatigue and overloading, as well as permanent deformation. The critical properties required for pavement design are stiffness, resistance to deformation under repeated loads and fatigue.

2.2.2.2 Bases and Subbases

A roadbase is the pavement layer lying immediately below the bitumen-bound surface of a pavement, while the subbase is the pavement layer between the base and subgrade. The base course is a major pavement layer to distribute wheel loads (Shiau, 2001). The base layer may be created by stone fragments, soil-aggregate mixtures, cemented-treated granular materials, or slag, etc. The subbase course, consisting of selected materials, such as crushed rock, may also work as a weak load-distributing layer. The subbase can be of lower quality than roadbases, provided that the thickness design criteria are satisfied. The major behaviour characteristics of bases or subbases are shear strength development through particle interlock and a lack of significant tensile strength. The general distress modes are deformation induced by shear and densification, as well as disintegration through breakdown. The key parameters of base or subbase materials are stiffness under transient load, and resistance to accumulation of deformation under repeated loads.

2.2.2.3 Subgrade

There are two roles for the soil foundation. Firstly, it works as a short-term pavement to support the construction wheel load and works as a platform for the construction. Subsequently, the subgrade provides a long-term support system for the finished pavement during its design life (Brown and Selig, 1991). Soils generally vary from clays, through silts and sands to high-strength rocky materials; soils are normally diverse along the road length; soils are very sensitive to water content (Thom, 2008). Like the bases and subbases, the key design properties for subgrade materials are stiffness under transient load and resistance to accumulation of deformation under repeated loads.

2.2.3 Contact area and pressure distribution

The wheel load is transmitted to the pavement surface by means of the wheel tyre. The intensity of the load stresses is reduced by the pavement structure with pavement depth. The contact form between the tyre and the road pavement surface is an important factor to affect the behaviour of pavement structures. The shape of the contact area depends on the ratio of the applied load to the recommended maximum tyre pressure (Croney, 1977). If the ratio is small, an approximately circular contact is observed. Nevertheless, when the ratio is increased, the contact area becomes increasingly elongated.

The contact stress between the wheel tyre and the pavement surface can be classified into three categories, namely vertical/normal, longitudinal, and transverse. As shown in Figure 2.3, the vertical stress is perpendicular to the contact surface; the longitudinal stress is parallel to the central plane of the tyre; the transverse component is perpendicular to the central plane. In practice, the tyre pressure is usually assumed to be the normal contact pressure, around 250kPa for a car and 600kPa for a large truck (Thom, 2008). The typical axle load for highway traffic design is 80 or 100kN, 80kN currently being used in the UK (Thom, 2008).

According to De Beer et al. (1997), the maximum vertical contact stress is under the two sides of the tyre rather than centre; the transverse stress is zero at the tyre centre; the longitudinal stress distribution is sensitive to load and inflation pressure (see Figure 2.4). In theory and simulation studies, the traffic contact pressure could be considered as a Hertz or trapezoidal distribution under plane strain conditions (e.g. Yu, 2005; Yu and Hossain, 1998), while in three dimensions, a Hertz distribution acting on an elliptical or circular area could be used to describe the contact pressure (e.g. Ponter et al., 1985; Yu, 2005). In practice, a uniform pressure distribution is normally assumed (Thom, 2008).

Road pavements usually experience at least dual wheels and certain other axle configurations. However, the effect of axle configuration on the pavement behaviour is not noticeable (Fernando et al., 1987). In service, a road is always subjected to stationary, acceleration and deceleration effects for varied wheel loads. Bonse and Kuhn (1959) found that acceleration and deceleration had a significant effect on the longitudinal pressure distribution. The normal contact pressure is approximately independent of speed (Marwick and Starks, 1941; Bonse and Kuhn, 1959; Himeno et al., 1997).

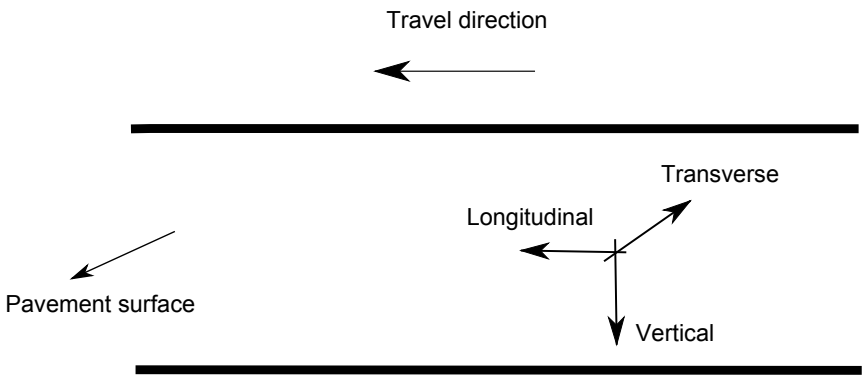

Figure 2.3: Definition of vertical, longitudinal and transverse directions

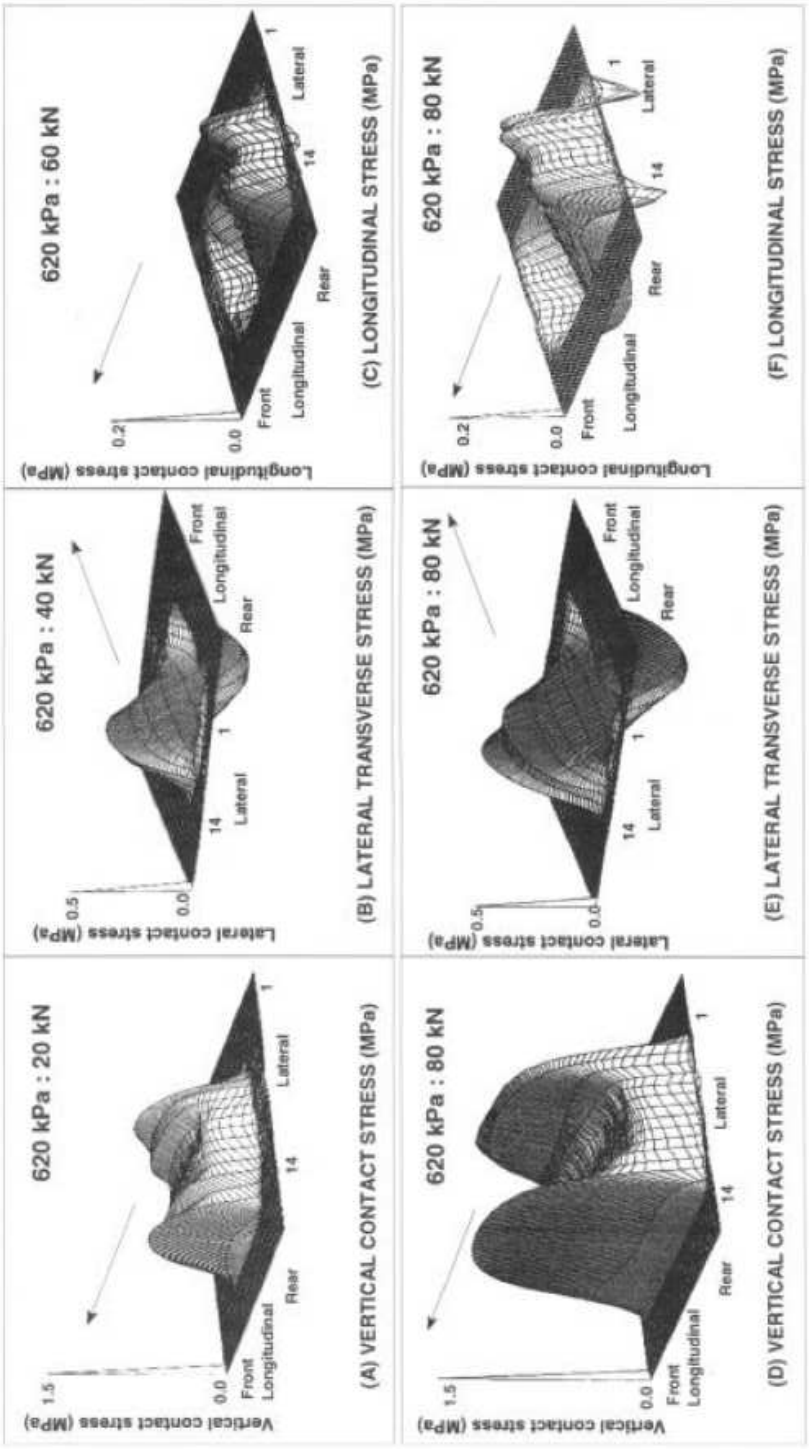

Figure 2.4: Typical contact stress distributions measured in experimental tests (De Beer et al., 1997)

2.2.4 Pavement response to repeated loads

When a wheel moves on a pavement surface, an element in the pavement structure experiences the loading and unloading processes. Its stress pattern is described in Figure 2.5a, where the vertical, horizontal and shear components are included. In unbonded layers, the vertical and horizontal stresses are compressive as the wheel load passes. Nevertheless, there is a reversal of the shear stress. Therefore, a rotation of the principle stress axes is induced. The deformation behaviour of pavement layers subjected to a moving wheel load consists of a resilient (recoverable) deformation and a permanent (residual) deformation (see Figure 2.5b).

An elastic response of road pavements generally takes place when the repeated stress level is either lower or higher than the applied stress during the period of preloading but below the maximum compressive strengths of the pavement materials (Juspi, 2007). The maximum stress level for the elastic response of road pavements is termed as the shakedown limit. Below this limit, a pavement may behave plastically during the initial loading but gives an elastic response for further repeated loading. The elastic behaviour of the pavement has been validated through wheel tracking tests in the laboratory (Juspi, 2007). There is hardly any further accumulation of plastic deformation after a certain number of repeated loads when the pavement is subjected to an applied stress below the shakedown limit.

The accumulation of permanent deformation is the typical plastic response of road pavements. Rutting (i.e. permanent deformation in pavements) may be caused by the compaction (i.e. decrease in volume) and/or the shear distortion at the pavement surface (Monismith and Brown, 1999). When the pavement experiences a repeated stress level above the shakedown limit, the permanent deformation constantly accumulates with the repetition of wheel loads (Juspi, 2007).

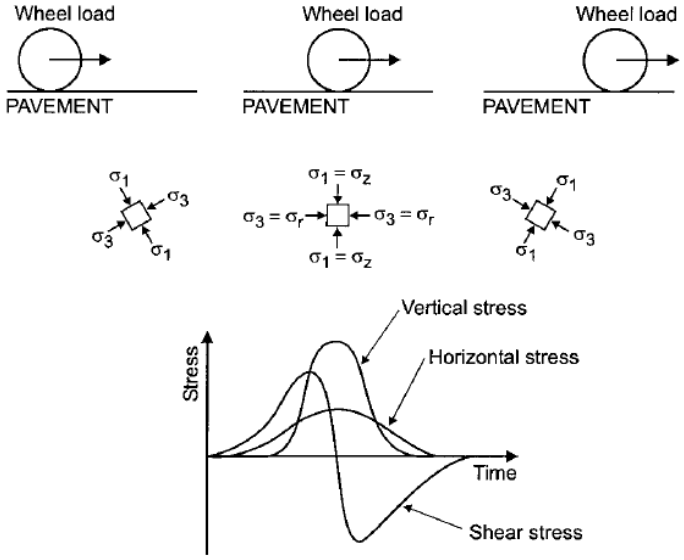

(a) Stress response

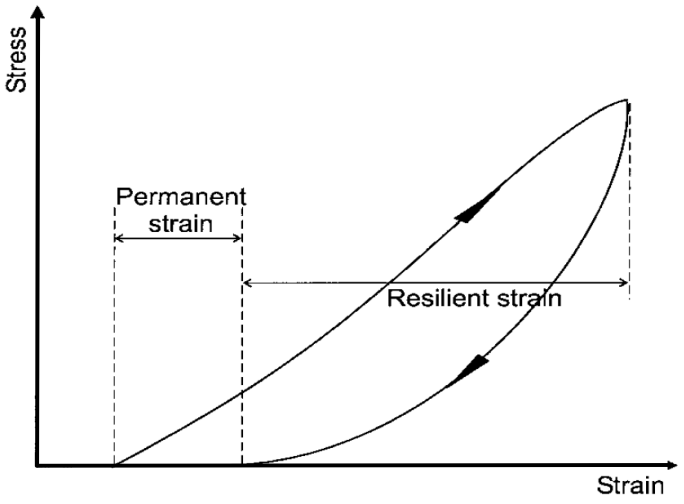

(b) Strain response

Figure 2.5: The stress and strain responses during each pass of the moving wheel load (Lekarp et al., 2000)

2.2.5 Pavement distress modes

There are two different types of pavement failure (Yoder and Witczak, 1975). The first is categorised as the structural failure. The pavement structure may collapse or one or more pavement components break down. As a result, the pavement is incapable of sustaining the traffic loads applied on its surface. The second is regarded as functional failure. This pavement failure tends to take place due to discomfort to passengers induced by the pavement roughness. According to Miller and Bellinger (2003), there are several types of pavement distress. The pavement distress modes generally observed in flexible pavements can be classified into five categories, namely fatigue cracking, permanent pavement deformation or ratchetting, surface defects such as bleeding and ravelling, patching and potholes, and miscellaneous distress such as lane to shoulder drop off. The latter three problems could be solved by an appropriate resurfacing or removal of the excess bituminous binder. The fatigue cracking and permanent deformation induced by repeated traffic loads are the main characteristics of pavement distress.

The most common mode of distress in flexible pavements in the USA has been considered to be fatigue cracking (Monismith, 1973). As shown in Figure (2.6), fatigue cracking may be observed at the surface outside the loaded area or at the bottom of the bituminous layer directly under the load, where the tensile stress is largest (Wang, 2011). With reference to Hveem and Sherman (1962), for a thin asphalt layer, the fatigue cracking evidently occurs at the pavement surface, which is induced by horizontal tensile stresses or strains resulting from flexure of the pavement. As thicker bituminous layers were introduced, in situ measurements of tensile strains were carried out by Klomp and Niesman (1967) and the maximum value was apparently observed at the bottom of the layer rather than at the surface. In practical engineering, the cracks develop and connect to one another with the repetition of traffic loads, as shown in Figure 2.7.

Deterioration in flexible pavements is mainly indicated by permanent deformation, which is attributed to an accumulation of vertical plastic deformation in the pavement

structure and the soil foundation subjected to repeated traffic loads (see Figure 2.8). The pavement structure includes the asphalt layer as well as the granular layer. These deformations may arise from shear deformation, viscous flow, compaction or consolidation. An initial sharp increase in the permanent deformation tends to occur for all flexible pavements, owing to the densification of the pavement layers. For a well-designed road pavement, only a small increase in the permanent deformation appears with time. Figure 2.9 shows the permanent deformation of flexible pavements in practical engineering. Generally, when a value of 15mm for permanent deformation is measured from the original level, the pavement is considered to have reached a critical condition. Pavement maintenance is required to satisfy the future performance (Norman et al., 1973). Once the rut depth exceeds 20mm, the pavement condition is often classified as failed (Croney, 1977).

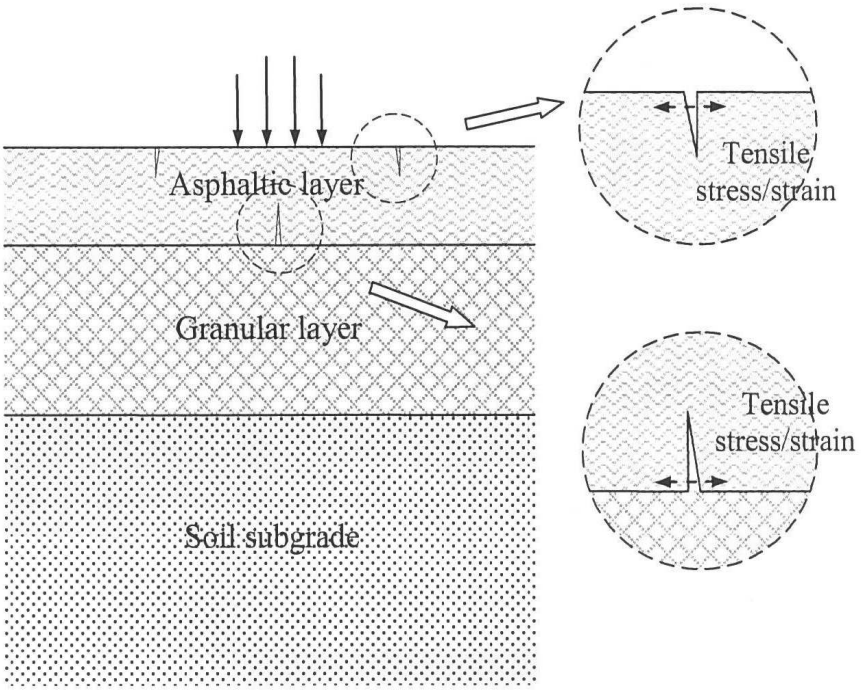

Figure 2.6: Illustration of fatigue cracking in road pavements (Wang, 2011)

Figure 2.7: Fatigue cracking in practical engineering (Fatigue cracking, 2015)

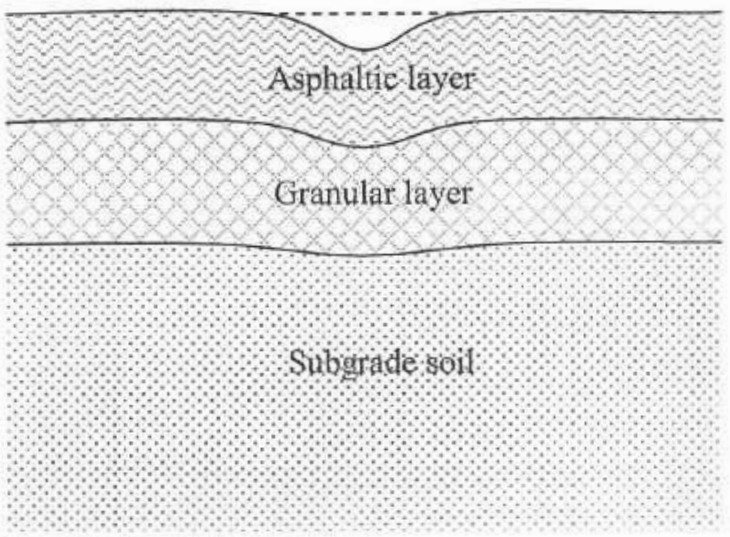

Figure 2.8: Illustration of rutting in road pavements (Wang, 2011)

Figure 2.9: Rutting in practical engineering (Quang, 2014)

2.2.6 Pavement design (Thom, 2008)

There are several engineering principles for a pavement to perform in-service. The fundamental function of a pavement is to protect the soil foundation. Generally, the natural soils will not be strong enough to support the vehicle load directly. There would be a large permanent deformation. The pavement must have adequate stiffness and thickness to distribute the traffic load from the pavement surface over a wide enough area. Thus, no excessive permanent deformation of the subgrade is induced. In addition, the permanent deformation in the pavement layers would be guarded against. The materials used in the pavement must be stable enough to avoid deformation. Moreover, the break-up of the pavement layers should be guarded against. The strength of the pavement materials must be strong enough not to suffer development of excessive cracking under repeated traffic loads. Furthermore, the pavement should be protected from environmental attack. The materials used in the pavement should not lose their properties under any local climate attack. Excessive water build-up at any level in the pavement must be avoided through adequate drainage. Additionally, an appropriate pavement surface should be provided on the basis of the requirements of evenness, skid resistance, noise and so on. Finally, the pavement design must ensure that necessary maintenance can be fulfilled within acceptable performance and cost limits.

In the pavement design, the whole-life cost should be taken into account, including both initial and ongoing costs, namely construction cost, maintenance cost, cost due to the presence of the pavement and accident cost, particularly injury and death. Moreover, the sustainability for a road pavement should be considered since the pavement uses vast resources in terms of tonnages of bulk products and has a complicated relationship with vehicle fuel consumption, noise harmful emissions and so on. In general, an engineer will not be directly concerned with the whole-life cost and sustainability. An economist or an environmental expert will usually be concerned with them.

The traffic loading is the primary design input in pavement design and an important factor for pavement design against the two principal structural distress modes, i.e. rutting and fatigue cracking. The traffic load magnitude, contact pressure, load groups,

dynamic effects, loading speed and lateral wander may also be included in pavement design. Because of very different loads supported by different pavement types, such as highways, airfields, footways etc., it is impossible to give an absolute general regulation for the expression of traffic. Nevertheless, a design load and a number of load repetitions must be determined in the pavement design. The typical axle design load for highway traffic is 80 or 100kN. In the UK, it is 80kN.

In pavement design against rutting, the deformation behaviour for soil foundation, granular materials and asphalt layer should be studied. The design principle is that the stress level, particularly the shear stress level, is never sufficient to cause excessively rapid plastic strain. Consequently, the pavement structure must completely protect the soil foundation. The bonded materials must protect the granular materials positioned above the subgrade. The asphalt mixture must be sufficiently deformation-resistant to avoid excessive rutting.

Design against fatigue cracking depends on the limitation of the stress or the strain in a bound layer to a reasonable value. For the thermally-induced cracking, the limit is possibly close to the tensile strength of the bound material. The low-temperature strength is needed for the asphalt layer. In the case of traffic-induced cracking, a noticeably reduced stress or strain limit is implied by the large number of load applications. For the asphalt layer, a tensile strain must be calculated and applied in combination with a fatigue characteristic. Improvement of the crack-resisting properties of the materials involved, such as reinforcement, could improve the pavement life. Improved pavement life could also be achieved through reducing the magnitude of the critical stress/strain in the pavement. Although sub-base stiffness has a much larger effect on strain at the base of the asphalt compared to subgrade stiffness, we can not deny the fact that foundation stiffness greatly affects the traffic-induced cracking for all pavement designs.

As discussed above, the pavement structural strength has been focused on, guaranteeing that neither permanent deformation nor fatigue cracking is excessive and that there is no deterioration in the material quality with time. Nevertheless, the pavement surface quality is evidently the most important concern in a pavement design from the

perspective of a user. In surface design, the requirements of noise, skid-resistance, spray and ride quality all give the different performances of road pavements. For example, airfield runways demand good skid resistance; spray is possibly a serious issue on high speed roads.

Durability design is commonly concerned with problems induced by water or ice. If water contents can be kept at a low level, there are hardly any pavement durability issues. The importance of drainage should never be underrated. Because of the diversifications of material properties and layer thickness as well as uncertain design traffic loading, there is always a high uncertainty level, even for the best-controlled pavement projects. Pavements demand to be treated statistically and it is senseless to assert that the pavement life is a fixed time or number of passes of a certain design wheel load.

2.3 Pavement shakedown analysis

2.3.1 Introduction

Soils and some other bearing constructions tend to experience cyclic or repeated loading, due to an earthquake, ocean wave or traffic loading. The shakedown phenomenon could be observed in practical engineering. Shakedown theory is both a direct and effective way to obtain the bearing strength and stability capability of elastic-plastic structures under repeated loads. Over the past three decades, shakedown analysis has been playing an important role in the safety load assessment of road pavements. There exist a series of shakedown studies such as Johnson (1962); Sharp and Booker (1984); Collins and Cliffe (1987); Shiau and Yu (2000); Boulbibane and Collins (2000); Yu (2005); Wang (2011).

2.3.2 Shakedown concept and theorems

2.3.2.1 Shakedown concept

When a cyclic load is applied to elastoplastic structures, there may be four situations owing to different load levels, as shown in Figure 2.10. First, if the load amplitude is inside the yield surface of the structure, the material behaviour is always a purely elastic process and no plastic strain arises. Second, when the load amplitude exceeds the elastic limit but is still lower than a critical limit, the structure undergoes a plastic deformation at the beginning of loading cycles. However, after a number of cycles, the plastic deformation will stop developing and only purely elastic response is associated with the remaining load cycles. Elastic shakedown happens and the critical limit is termed as the shakedown limit. Third, plastic shakedown can be found if the loading magnitude is slightly larger than the shakedown limit, where a closed plastic strain cycle substitutes the purely elastic response. This phenomenon is termed as plastic shakedown. In this situation, alternating plasticity collapse may occur due to repeated closed loops developed between two plastic states. Finally, when the loading amplitude is so large that there is an increasing plastic deformation with increasing number of loading cycles, the structure will collapse, which is known as ratchetting.

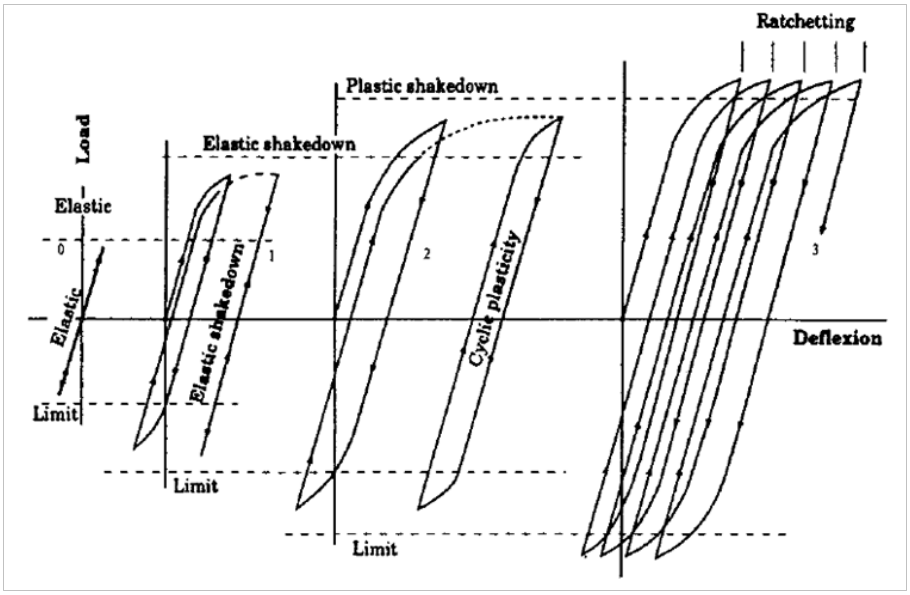

Figure 2.10: Elastic/plastic behaviour of structure subjected to cyclic loads (Johnson, 1986)

2.3.2.2 Shakedown theorems

There exist two kinds of basic shakedown theorems from the macromechanical point of view, which are Melan's static or lower bound theorem (Melan, 1938) and Koiter's kinematic or upper bound theorem (Koiter, 1960). Melan's lower bound theorem can be stated as follows: an elastic-perfectly plastic structure subjected to repeated loading will shakedown, if there exists any self-equilibrated residual stress field, and then the combination of this residual stress field and the elastic stress field due to the applied loads, does not violate the yield condition at any position of the structure. We can indicate the applied load by λp_{0n} where p_{0n} may be normally assigned as the unit pressure in the practical calculation and λ is a dimensionless scale property. Therefore, all the elastic stress components induced by the applied load are proportional to λ. Melan's static shakedown theorem can be expressed as

$$f(\lambda\sigma_{ij}^{e} + \sigma_{ij}^{r}) \leq 0 \tag{2.1}$$

where σ_{ij}^{e} stands for the elastic stress tensor produced by the applied pressure p_{0n},
σ_{ij}^{r} denotes the self-equilibrated residual stress tensor,
$f(\sigma_{ij})$ indicates the yield condition of the material.
The practical shakedown limit $p_s = \lambda_s p_0$ can be obtained by searching all possible self-equilibrated residual stress fields to find the largest value of λ.

Koiter's kinematic shakedown theorem states that an elastic-perfectly plastic structure will not shakedown under repeated loads but will fail finally due to gradual accumulation of plastic strain if any kinematically admissible plastic strain rate cycle and any external loads within the prescribed limits satisfy the conditions as follows:

$$\int_0^t dt \int\int_{S_T} T_{0i}\dot{u}_i^k dS > \int_0^t dt \int\int\int_V \sigma_{ij}^k \dot{\varepsilon}_{ij}^k dV \tag{2.2}$$

where $\dot{\varepsilon}_{ij}^k$ indicates the kinematically admissible plastic strain rate cycle,
T_{0i} is external load,
σ_{ij}^k is the stress tensor on the yield surface,
$\dot{u}_i^k$ denotes displacement velocity,

S_T stands for the structure surface where traction is specified,
V_s is the volume of the structure.

Alternatively, the structure will shakedown if the following condition can be satisfied for all kinematically admissible plastic strain rate cycles

$$\lambda \int_0^t dt \int \int_{S_T} p_{0i} \dot{u}_i^k dS \leq \int_0^t dt \int \int \int_V \sigma_{ij}^k \dot{\varepsilon}_{ij}^k dV \tag{2.3}$$

which provides an upper bound to the shakedown load multiplier λ.

2.3.3 Residual stress

The components of pavement deformations caused by a moving traffic load can be divided into two parts, namely elastic and plastic deformations. After the removal of the applied surface load, the elastic strain will recover and the related elastic stress disappears. However, the plastic deformation remains in the pavement and some stresses have arisen, called residual stress. The equilibrium equations and stress boundary conditions must accord with whatever residual stress fields there are. Generally, a point in a structure may have all six components of residual stress, although some constraints are exerted by conditions such as symmetry and self-equilibrium. Therefore, some of the stress components can be eliminated. In the current study, the pavement material is regarded as isotropic and homogenous, and individual pavement sections in the transverse x-direction undergo the same stress path, owing to the periodic lateral boundary. Therefore, the induced permanent deformation and the residual stress field will be irrespective of the x-direction. In addition, the condition of plane deformation in the longitudinal y-direction removes σ_{xy}^r and σ_{yz}^r, and causes the other stress components to be independent of y. Moreover, based on a traction free surface, residual stresses σ_{zz}^r and σ_{xz}^r must be zero to satisfy the equilibrium condition. After these conditions are all taken into account, $\sigma_{zz}^r = \sigma_{xy}^r = \sigma_{yz}^r = \sigma_{zx}^r = 0$, and the remaining residual stresses are expressed as

$$\sigma_{xx}^r = f(z);\ \sigma_{yy}^r = g(z) \tag{2.4}$$

Radovsky and Murashina (1996) set up a laboratory test to determine the development of residual stress with the repetition number of external loads. The diameter of the cylindrical sandy specimen was 100mm and the height was 130mm. The specimen was positioned in a rigid mold. The horizontal residual stress could be measured using a pressure cell of the diaphragm type of 26mm in diameter and 2.5mm in thickness with a wire strain gauge transducer. The pressure cells were placed 45, 60, and 110mm below the surface. The specimen experienced the repeated loads through a rigid circular plate of 98mm in diameter. One group of test results for horizontal residual stresses are plotted in Figure 2.11. Under repeated loading, the horizontal residual stress was compressive and gradually increased until a nearly constant value (i.e. 220kPa) was reached. The increase in residual stress results from the accumulation of vertical plastic strain, which is consistent with the development of residual stresses, deduced from the computations by Merwin and Johnson (1963), for a semi-infinite solid under repeated normal loads (see Figure 2.12).

A full-scale experiment was performed to assess the general form of the horizontal residual stress distribution within soils by Radovsky and Murashina (1996). The experimental section was located on the road between Kiev and Kharkov in Ukraine during reconstruction of the road. The liquid and plastic limits for the soil were 30% and 21% respectively. There were 10% sand, 77% silt and 13% clay in the soil. The water content of the soil was 15%. The initial and final dry weight were 1.52 and 1.73 mg/m^3. The horizontal residual compressive stresses were measured by pressure cells of the diaphragm type with a soil strain gauge transducer. After soil precompaction, pressure cells were placed in various lateral and vertical positions, as shown in Figure 2.13a, along the central line of a rolling strip. The readings were taken after each pass of the roller. The residual stresses ceased to rise after 12 passes of the roller when the soil compaction terminated. The measured residual stress distribution for the steady state in the elastoplastic half-space with depth is shown in Figure 2.13b, where a comparison with computed residual stresses was made. The friction coefficient in the contact was 0.1 and contact pressure was 310kPa. The semicontact width was 13.5cm.

Pavement shakedown was simulated using the finite element method in 2D by Wang

(2011). The size of the simulated pavement model was $84a$ long by $30a$ high (a is semicontact width). A Hertzian contact was used to model the wheel pressure. Tresca and Mohr Coulomb materials were used for the half-space simulation. Pure rolling contact was considered. The various residual stress distributions with pavement depth for a Tresca half-space are presented in Figure 2.14, where the wheel pass number was three. It was noted that the vertical and shear residual stresses could be disregarded, consistent with the equilibrium condition. For the horizontal and transverse residual stresses, the maximum value was close to the pavement surface. In the case of Mohr Coulomb material, the fully-developed horizontal residual stress fields for various internal friction angles and wheel pressures are demonstrated in Figure 2.15. Their peak points were all located beneath the pavement surface, approximately at $z/a = 0.5$. With the increase in friction angle, the residual stress distributed more and more widely with the increased magnitudes of compressive residual stresses.

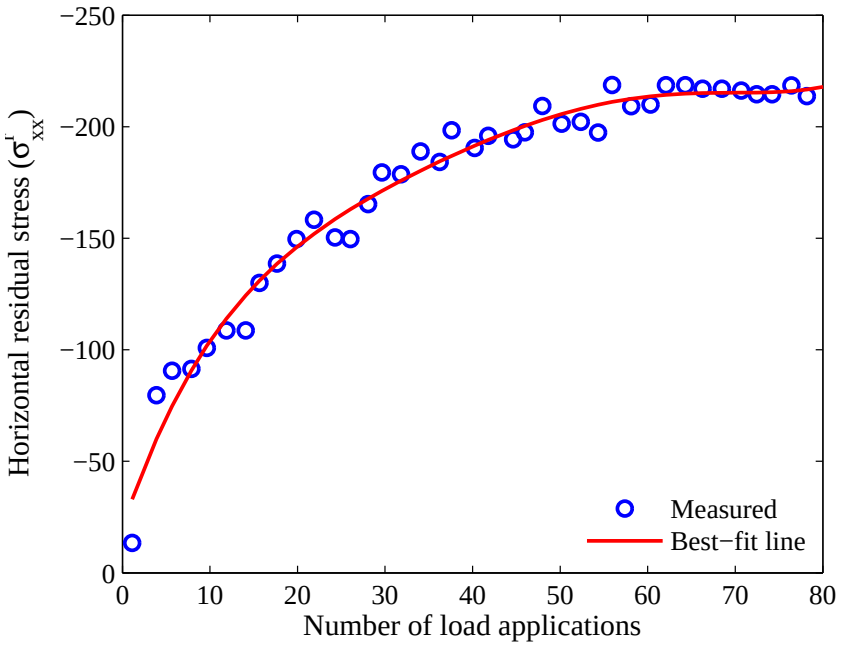

Figure 2.11: Variation of horizontal residual stress (σ^r_{xx}) with number of load applications (Radovsky and Murashina, 1996)

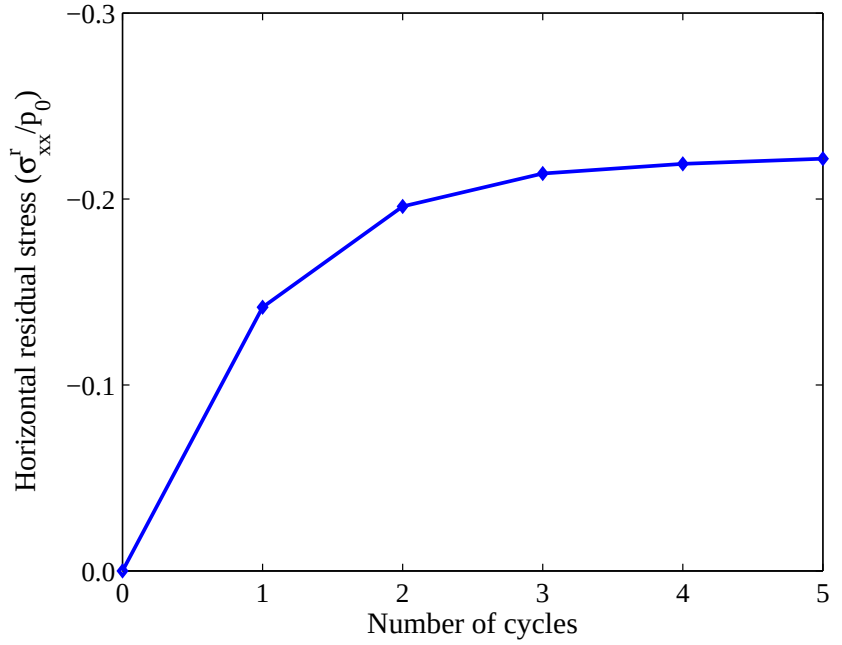

Figure 2.12: Variation of normalised horizontal residual stress (σ^r_{xx}/p_0) with number of load applications, where $p_0/k = 4.76$, $k = 16 \times 10^3 lb/in^2$ (Johnson and Jefferis, 1963)

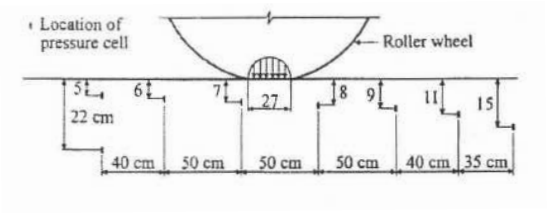

(a) Measurement of horizontal residual stresses

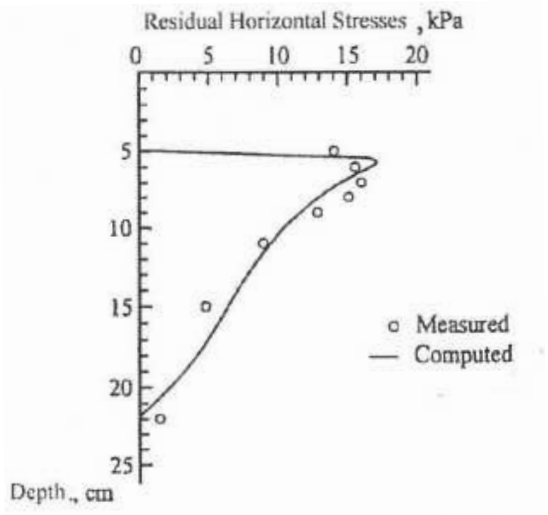

(b) Comparison between measured and computed residual stresses

Figure 2.13: Measurement and distribution of horizontal residual stresses in a full-scale experiment (Radovsky and Murashina, 1996)

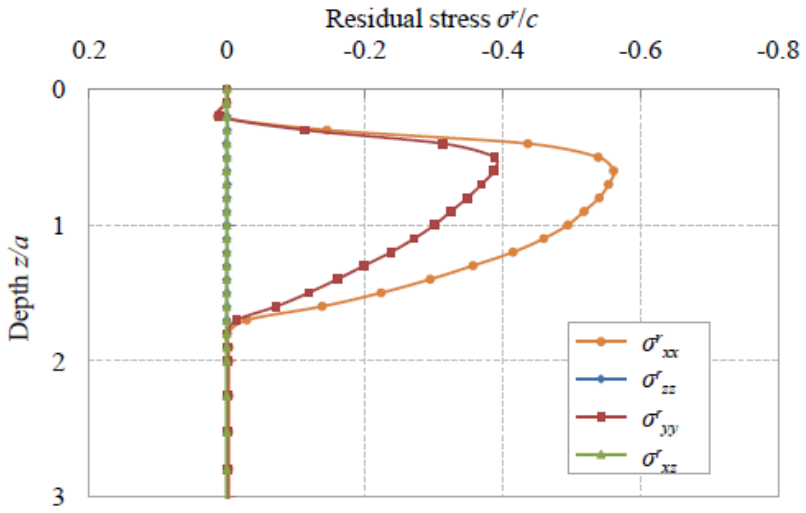

Figure 2.14: Distribution of normalised residual stress (σ^r/c) with pavement depth after three load passes in Tresca half-space, where σ^r_{xx}, σ^r_{zz}, σ^r_{yy} and σ^r_{xz} are horizontal, vertical, transverse and shear residual stress respectively and c is cohesion of the material (Wang, 2011)

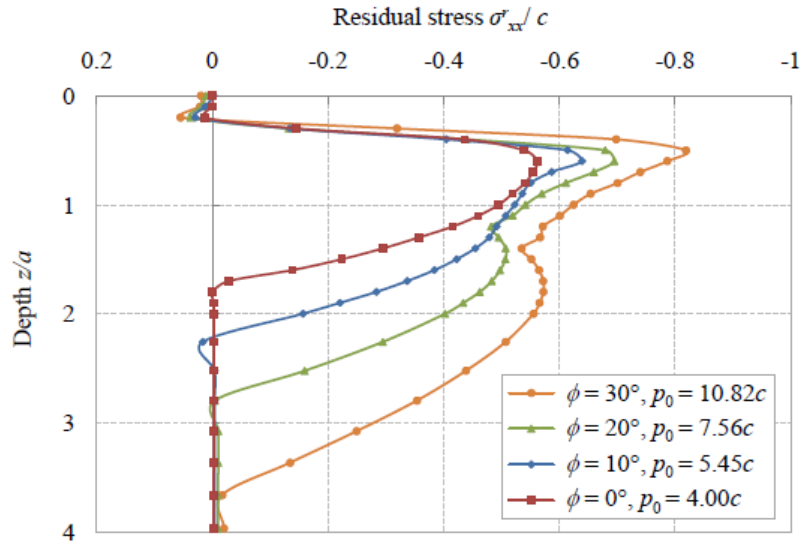

Figure 2.15: Distributions of normalised fully-developed horizontal residual stress(σ^r_{xx}/c) with pavement depth in Mohr Coulomb half-space for various internal friction angles, where ϕ is internal friction angle of the material, p_0 is maximum normal Hertz contact pressure and c is cohesion of the material (Wang, 2011)

2.3.4 Shakedown analysis in pavement engineering

Johnson (1962) conducted a shakedown analysis based on line rolling contact over the surface of an isotropic, elastic-perfectly plastic, half space. Shakedown occurred under repeated rolling loads when the maximum Hertz pressure was less than 4.0 k, where k was the yield stress in simple shear. The shakedown limit did not depend on the yield criterion and was nearly 70 percent in excess of the load to produce initial yield. Continuous permanent deformation was caused with the repetition of rolling loads as the magnitude of applied loads exceeded the shakedown limit. Johnson and Jefferis (1963) also considered sliding contact in shakedown analysis.

Sharp and Booker (1984) proposed some procedures to analyse pavement shakedown under moving surface loads. For a homogeneous isotropic semi-infinite solid, the shakedown limits increased with the friction angle of the material. The friction coefficient between the moving load and pavement surface reduced the shakedown limit. In the case of a two-layer half-space, for a given value of strength, an optimal value of relative stiffness (i.e. E_1/E_2) could be found to maximise the shakedown limit. E_1 and E_2 were the Young's moduli for the first and second layers. At given values of stiffness, the shakedown limit increased with augmentation of the relative strength (i.e. c_1/c_2). c_1 and c_2 were the cohesions of the top and bottom layers. In addition, for given c_1/c_2 and first layer thickness, an optimal value of relative stiffness could be obtained to maximise the pavement resistance to rachetting.

Ponter et al. (1985) used the kinematic shakedown theorem to study the deformation response of an elastic-perfectly plastic half-space under rolling and sliding point contacts. A Hertz pressure distribution and frictional traction acted on an elliptical area. Various traction coefficients and loaded ellipse shapes were used to obtain the optimal upper bound elastic and plastic shakedown limits. Radovsky and Murashina (1996) developed a model through a Mohr-Coulomb failure criterion to predict the shakedown occurrence of subgrade soils. The boundary shakedown loads and pressures increased with an augmentation of the shear strength of subgrade soils. The internal friction angle of the material had an effect on the ratio of the maximum to the smallest boundary

shakedown load.

A lower bound shakedown formulation was proposed using a linear approximation of the Mohr-Coulomb yield criterion by Yu and Hossain (1998). 3-noded triangular elements were used to simulate the residual stress field through a conventional finite element technique. Stress discontinuities could occur at the edges of each triangle. A homogeneous isotropic half space was applied to validate the shakedown formulation. For the two-layer pavement, material properties and layer thickness were considered in the study of shakedown limits. Boulbibane et al. (2000) developed a model to predict the effect of inherent anisotropic cohesion on the shakedown of multi-layered pavements. The lower bound shakedown theorem and diversification of soil strength with direction were considered. The shakedown limit of pavements under repeated loads was obtained. The effect of temperature and asphalt layer thickness on the shakedown phenomenon was studied in terms of various hardnesses of subgrades.

The mechanical behaviour of an unbound pavement under repeated traffic loads was studied by Collins and Boulbibane (2000). A procedure was proposed on the basis of the Mohr-Coulomb criterion and kinematic shakedown theorem. A shakedown limit was obtained above which pavements will eventually fail due to continuous accumulation of permanent deformation and below which pavements initially exhibit some plastic deformation but will eventually shakedown to a steady state. Some factors such as self weight, moisture content, dual loads, relative strengths of the different pavement layers and non-associated plastic flow were considered. Non-linear programming techniques and the displacement-based finite element method were used to perform shakedown analysis of structures by Li and Yu (2006). A general yield criterion and an associated flow rule were applied to the upper bound shakedown theorem. The efficiency and effectiveness of this numerical method were validated by shakedown analysis of pavements and tunnels.

Analytical solutions for shakedown limits of a three-dimensional cohesive-frictional half-space under moving surface loads were proposed by Yu (2005). Melan's static shakedown theorem and Mohr-Coulomb yield criterion were adopted to obtain the

shakedown limits. Decreased contact friction coefficient between traffic load surface and pavement surface and increased internal friction angle of the material both increased the shakedown limits. According to Krabbenhøft et al. (2007), the self-equilibrium condition and yield condition for residual stress were added to the elastic shakedown analysis while the yield condition of residual stress was introduced into the plastic shakedown analysis. Compared to previously published analytical solutions, there was a general decrease in the shakedown limit, especially for large internal friction angle. Wang (2011) proposed a lower-bound shakedown solution deduced by considering the equilibrium condition of residual stresses. These shakedown solutions were applied to one-layered and multi-layered pavements. In the case of single-layered pavements, the rigorous static solutions based on the self-equilibrium residual stress field were smaller than the previous analytical shakedown solutions.

2.4 Summary

In general, a flexible pavement is composed of a bitumen-bound layer, a base course and a subbase course. Rutting and fatigue cracking are the most common distress modes. In pavement design, the basic design principles should be fulfilled by engineers. The traffic load is the primary input for road pavement design. The design axle load needs to be determined. The pavement design includes designs against rutting and fatigue cracking, pavement surface design, durability design, and design reliability. Pavement shakedown is an effective approach to design road pavements. A series of shakedown analyses have been carried out in pavement engineering on the basis of Melan's static or Koiter's kinematic shakedown theorems. The knowledge gap to be filled in the present study, was proposed in Section 1.1 and further emphasised in Subsection 5.2.1.

Chapter 3

DEM Biaxial Test Simulation for Unbonded Materials

3.1 Introduction

In this chapter, the discrete element method (DEM) is used to simulate the stress-strain behaviour of unbonded granular materials in biaxial tests. Particle flow code in 2 dimensions (PFC^{2D}), a powerful DEM software developed by ITASCA in 1994, can solve problems ranging from mechanical element analysis (Li et al., 2013; Ai et al., 2014) to practical engineering problems (Maynar and Rodrguez, 2005). The background and basic assumptions for PFC^{2D} are introduced. In addition, there is a detailed description of its calculation principles and contact constitutive model. Finally, a presentation related to the functional modules of the PFC^{2D}-measurement cycle and clump logic is made.

The procedure of biaxial test simulation is presented, including particle parameter selection, sample generation, the consolidation process and loading mode. The behaviour of granular materials linked to deviatoric stress and volumetric strain versus axial strain can be obtained. After that, a comparison between modelling and the

experimental results is carried out in order to make a validation. Finally, some factors influencing biaxial test simulation are considered. The effects of particle stiffness and friction coefficient on mechanical behaviour are investigated. In order to study the interlocking effect between particles, a clump comprising two particles which are bonded together is introduced in the biaxial test simulation. Moreover, besides the confining pressures, the initial void ratio of the sample has a significant effect on the mechanical responses.

3.2 The PFC^{2D} software

3.2.1 Background and assumptions

In studying the mechanical behaviour of a granular medium, knowledge of stress and strain plays an important role. Since a granular assembly consists of discrete particles, the contact points between these particles bear the force transmission. This kind of discreteness adds complexities to the study of constitutive relationships of granular materials. In addition, the stress existing inside a sample is difficult to measure in a traditional laboratory test. However, an alternative way to make an estimation from the boundary conditions has been set out by Cundall and Strack (1979a).

As discussed above, development in the research of granular media has been promoted in terms of theoretical analysis, physical (typically photoelastic) tests and numerical simulation. Deresiewicz (1958) and Thornton (1979) have put forward some analytical models based on uniform size assemblies. Furthermore, the micromechanical behaviour of a granular medium with random packing has been studied by Chang (1988). However, there exist some restrictions in theoretical analysis, such as the loading paths and the particle shape. Physical techniques are mainly based on photoelastic tests, as carried out by Dantu (1957), Wakabayashi (1950), Drescher (1976) and Oda et al. (1982). But it is time-consuming to determine the contact forces and disc displacements and rotations. Numerical simulation is possibly the most powerful way of

modelling the behaviour of granular assemblies, due to its flexibility in the application of loading paths, granular shape, particle parameters and boundary conditions, as well as data acquisition at any stage of the tests (Cundall and Strack, 1979a).

DEM was first proposed by Cundall (1971, 1974) in order to analyse rock-related problems. After that, the computer programs-BALL (Cundall and Strack, 1979a) and TRUBALL (Cundall and Strack, 1979b) were developed on the basis of this kind of method. Later, the cubic periodic boundaries (Cundall, 1988), and nonlinear contact laws, which are Hertz normal contact and a simplified tangential contact (Mindlin, 1949) respectively, were introduced to DEM. In 1980 Cundall introduced a DEM program, called $UDEC$ to model the behaviour of jointed rock and it became a commercial DEM code in 1984. $3DEC$ and PFC^{2D}/PFC^{3D} were first developed by Itasca in 1988 and 1994 respectively. Additionally, at present there are many other open source DEM programs available such as $LAMMPS$, $SDEC$ and $YADE$. To date, DEM has already proved to be a better means of behaviour modelling for discontinuous media than other simulation tools (e.g. finite element method and boundary element method) with the assumption that the material is continuous, contrary to the nature of granular materials, referred to by Cundall and Hart (1992). As a valid tool for geotechnical research, DEM has been used by Strack and Cundall (1984), Rothenburg and Bathurst (1989), Ng and Dobry (1994), Sitharam (2003), Harireche and McDowell (2003) and many others.

In the current research, the commercial software PFC^{2D} is used to model biaxial tests. Information related to particle displacement and velocity, as well as interacting force between particles, can be traced in the computational process of PFC^{2D}. In this way, macro mechanical parameters such as deviatoric stress and volumetric strain, can be calculated. A description of PFC^{2D} will be given in this subsection and more detailed information can be obtained from the PFC^{2D} manual (Itasca, 2004). PFC^{2D} can be considered as a simplified version of DEM because of the restriction to rigid spherical particles. The following assumptions are provided by Itasca (2004).

1. The particles are treated as rigid bodies.

2. The contact area becomes so small that the contact is considered to occur at a point.

3. The rigid particles are allowed to overlap one another at contact points.

4. The magnitude of the overlap is related to the contact force via the force-displacement law, and all overlaps are small compared to particle sizes.

5. Bonds can exist at contacts between particles.

6. All particles are spherical; however, clump logic supports the creation of super-particles of arbitrary shape. Each clump is comprised of a number of overlapping particles acting as a rigid body with a deformable boundary.

3.2.2 Calculation cycle

A packed particle assembly such as a sand sample, deforms when subjected to external loadings, primarily as a result of the sliding and rotation of particles. Particle rearrangement is caused and then the deformation of the granular assembly is brought about. Generally, the individual particle deformation could be ignored. Therefore, the assumption of particle rigidity in PFC^{2D} could be used effectively to describe the deformation of granular materials. It is not necessary for a precise simulation of particle deformation to obtain the mechanical behaviour of such materials effectively.

To obtain the realistic evolution of stress and strain in a granular assembly, complete information for particles and walls, such as contact force and particle position, can be traced using an explicit time-dependent finite difference technique. This tracking process is executed by a PFC^{2D} calculation cycle in a dynamic mode, as illustrated in Figure 3.1. There are two basic laws included in PFC^{2D} calculation algorithms, which are Newton's second law of motion and a force-displacement law, respectively.

The inter-particle and particle-wall contact information is of great importance to the calculation cycle and will be identified first. After all the contact points have been checked and reported, via the force-displacement relationship, the contact force can be monitored from relative motion at the contact area. The contact forces are then updated and applied to obtain the resultant forces and moment acting on the particle. Next, one can calculate the new linear and angular accelerations of each particle by means of Newton's second law of motion. After that, it is easy to establish the new velocity and displacement increments over a timestep, from which the position information of an individual particle can be updated. In addition, the wall position information can be obtained from the specified wall velocities. The calculation process is repeated to renew the contact forces as well as particle and wall locations.

As discussed above, the overall information for each particle and wall in the granular assembly is recorded, and then the macro stress and strain can be calculated in an averaging process. Finally, one can obtain the macroscopic constitutive relationship between the stress and strain for a granular medium.

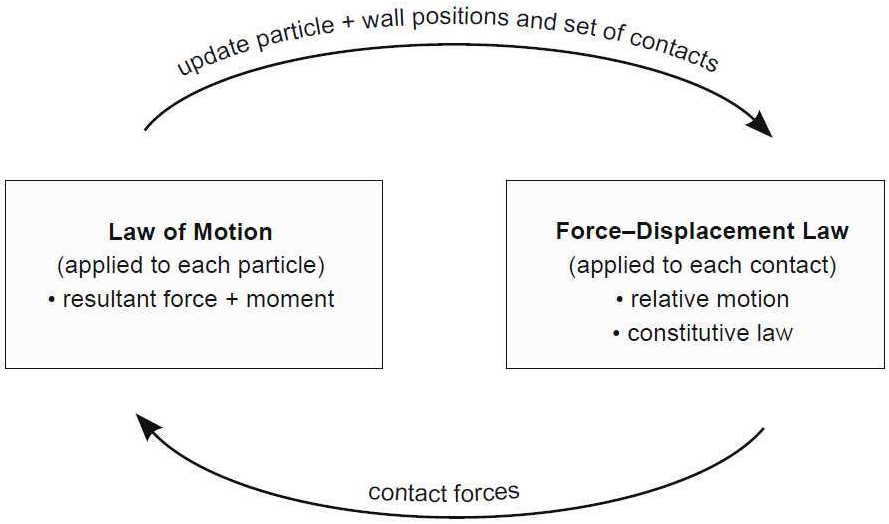

Figure 3.1: Calculation cycle in PFC^{2D} (Itasca, 2004)

3.2.3 Contact constitutive model

The contact constitutive model is applied to describe the law of force-displacement, based on the relative motion between particles. Generally, a contact comprises two parts: a stiffness model and a slip model. The stiffness model describes an elastic relation between the contact force and relative displacement. The slip model indicates a relation between shear and normal contact forces and the slip may occur at the contact area. However, alternative contact models are also available for modelling more complex contact behaviour.

3.2.3.1 Contact-stiffness model

The contact stiffnesses relate the contact forces and relative displacements in normal and shear directions. The normal stiffness k^n is the secant stiffness, which relates total normal force F_i^n to total normal displacement U^n.

$$F_i^n = k^n U^n n_i \tag{3.1}$$

where n_i is the unit normal vector. The shear stiffness is the tangent stiffness k^s, relating the shear force increment ΔF_i^s to the shear displacement increment ΔU_i^s.

$$\Delta F_i^s = -k^s \Delta U_i^s \tag{3.2}$$

The values of contact stiffnesses k^n and k^s can be assigned on the basis of the applied contact-stiffness model. In PFC^{2D}, there are two kinds of contact-stiffness model, which are the linear model and the simplified Hertz-Mindlin model. However, there is no definition for a contact that takes place between a ball with the linear model and a ball with the Hertz model. Moreover, since the tensile force is undefined in the Hertz model, it is incompatible with any type of bonding model. Because a bonding model will be employed for the DEM simulation in Chapters 4 and 6, the linear contact model is selected in the following research.

The linear contact model is based on the normal and shear stiffnesses k_n and k_s of two contacting entities (ball-ball or ball-wall). The stiffnesses of two entities in contact are assumed to act in series. The contact normal secant stiffness is computed by

$$k^n = \frac{k_n^{[A]} k_n^{[B]}}{k_n^{[A]} + k_n^{[B]}} \tag{3.3}$$

while the contact shear tangent stiffness is described by

$$k^s = \frac{k_s^{[A]} k_s^{[B]}}{k_s^{[A]} + k_s^{[B]}} \tag{3.4}$$

where the superscripts [A] and [B] stand for the two contacting entities.

3.2.3.2 The slip model

The slip model is an intrinsic property of the two contacting entities; it provides no normal strength in tension and allows slip to occur by restriction of the shear force. The constitutive behaviour of two entities in contact could be described by the slip model and it is suitable for modelling the behaviour of a disseminate material like sand (Zhou et al., 2006). The model is associated with the friction coefficient μ at the contact, where μ is dimensionless and assigned to the smaller friction coefficient between two contacting entities. The overlap of the two entities is checked to see whether it is less than or equal to zero. If it is, both normal and shear contact forces are set to zero. The slip conditions are checked at the contact area by the calculation of maximum allowable shear contact force F^s_{max} via friction coefficient μ and normal contact force F^n_i

$$F^s_{max} = \mu \left| F^n_i \right| \tag{3.5}$$

If $|F^s_i| > F^s_{max}$, during the next calculation cycle, the magnitude of F^s_i is set equal to F^s_{max} as follows and the slip at the contact is allowed to take place.

$$F^s_i \leftarrow F^s_i (F^s_{max} / \left| F^s_i \right|) \tag{3.6}$$

3.2.4 Measurement circle

In PFC^{2D}, information about a granular medium, including the coordination number, porosity, stress and strain rate, can be obtained by using a specified measurement tool, called the measurement circle. It is a circular area including the particle and contact information, where the measurement quantities can be calculated by means of algorithms. As users do not need to do extra programming themselves to get this information, it is convenient to use. In this subsection, the computation methods with the assumptions and approximations will be described in detail.

3.2.4.1 Coordination number

The coordination number C_n is the definition of the average contact number per particle. The calculation merely considers the particles with centroids that are contained within the measurement circle:

$$C_n = \frac{\sum_{N_b} n_c^{(b)}}{N_b} \tag{3.7}$$

where N_b is the number of particles whose centroids are contained in the measurement circle. Also, $n_c^{(b)}$ denotes the contact number of the particle (b). Generally, the contacts are counted twice. If one ball of a contact pair lies outside of the measurement circle, the contact is considered once.

3.2.4.2 Porosity

The porosity n is defined as the ratio of the void area within the measurement circle to the total measurement circle area:

$$n = \frac{A^{void}}{A^{circle}} = \frac{A^{circle} - A^{ball}}{A^{circle}} = 1 - \frac{A^{ball}}{A^{circle}} \tag{3.8}$$

where A^{circle} and A^{void} are the measurement circle area and void area within the measurement circle. A^{ball} is the area occupied by the balls that belongs to the measurement

circle. A^{ball} is calculated by

$$A^{ball} = \sum_{N_p}(A^{(p)}) - A^{overlap} \tag{3.9}$$

where N_p indicates the number of particles that intersect the measurement circle. $A^{(p)}$ is the area of particle (p) included within the measurement circle; $A^{overlap}$ denotes the particle overlap area belonging to the measurement circle. It is noted that the calculation of A^{ball} takes into consideration both the partial area of particles that intersect the measurement circle and the area of particle overlaps caused by the compressive contact forces.

3.2.4.3 Stress

In the PFC^{2D} model, the forces at the contact pair between two entities (ball-ball or ball-wall) and the displacements of particles can be calculated. These quantities are of great importance to the study of the microscopic behaviour of granular material. However, the stress, as a continuum quantity, does not occur at each contact point in a discrete granular medium. Therefore, stress can not be obtained directly in DEM calculation cycles. An averaging process can be introduced to relate the micro-scale to a continuum.

The average stress tensor $\bar{\sigma}_{ij}$ in a material with a volume V, is described by

$$\bar{\sigma}_{ij} = \frac{1}{V}\int_V \sigma_{ij} dV \tag{3.10}$$

where σ_{ij} is the stress tensor acting within the volume V. Since, in a granular assembly, stresses only exist in the particles, the integral can be displaced by a sum depending on N_p particles that belongs to the volume V:

$$\bar{\sigma}_{ij} = \frac{1}{V}\sum_{N_p} \bar{\sigma}_{ij}^{(p)} V^{(p)} \tag{3.11}$$

where $V^{(p)}$ is the volume of particle (p) and $\bar{\sigma}_{ij}^{(p)}$ denotes the average stress tensor of particle (p), which could be rewritten using Equation (3.10) as

$$\bar{\sigma}_{ij}^{(p)} = \frac{1}{V^{(p)}}\int_{V^{(p)}} \sigma_{ij}^{(p)} dV^{(p)} \tag{3.12}$$

where $\sigma_{ij}^{(p)}$ is the stress tensor acting on particle (p).

Note that Equation (3.12) can be defined as

$$\bar{\sigma}_{ij}^{(p)} = \frac{1}{V^{(p)}} \int_{V^{(p)}} \left[(x_i \sigma_{kj}^{(p)})_{,k} - x_i \sigma_{kj,k}^{(p)} \right] dV^{(p)} \tag{3.13}$$

by means of the identity

$$S_{ij} = \delta_{ik} S_{kj} = x_{i,k} S_{kj} = (x_i S_{kj})_{,k} - x_i S_{kj,k} \tag{3.14}$$

which is suitable for any tensor S_{ij}, where the notation $[_{,i}]$ indicates differentiation concerning the coordinate x_i.

The assumption of continuity and equilibrium is made on the stresses in each particle. If there is no body force, the balance condition can be written as $\sigma_{ij,i} = 0$. Hence, the second term of Equation (3.13) will disappear. The volume integral in Equation (3.13) can be transformed into a surface integral using the Gauss divergence theorem on the first term:

$$\bar{\sigma}_{ij}^{(p)} = \frac{1}{V^{(p)}} \int_{S^{(p)}} (x_i \sigma_{kj}^{(p)}) n_k dS^{(p)} = \frac{1}{V^{(p)}} \int_{S^{(p)}} x_i t_j^{(p)} dS^{(p)} \tag{3.15}$$

where $S^{(p)}$ denotes the surface of particle; n_k is the unit outward normal to the surface; and $t_j^{(p)}$ is the traction vector. Since particles are subjected to point forces acting at discrete contact locations, a sum over the N_c contacts can displace the integral in Equation (3.15) as follows:

$$\bar{\sigma}_{ij}^{(p)} = -\frac{1}{V^{(p)}} \sum_{N_c} x_i^{(c)} F_j^{(c)} \tag{3.16}$$

where $x_i^{(c)}$ and $F_j^{(c)}$ are the location and force of contact (c). Note that the minus sign employed in Equation (3.16) indicates that compressive forces give rise to negative average stresses. Besides, the contact location can be rewritten as

$$x_i^{(c)} = x_i^{(p)} + \left| x_i^{(c)} - x_i^{(p)} \right| n_i^{(c,p)} \tag{3.17}$$

where $x_i^{(p)}$ denotes the particle centroid location; and $n_i^{(c,p)}$ is the unit-normal vector directed from the particle centroid to the contact location. By substituting Equation (3.17) into Equation (3.16), the stress tensor of each particle can be rewritten as:

$$\bar{\sigma}_{ij}^{(p)} = -\frac{1}{V^{(p)}} \sum_{N_c} \left| x_i^{(c)} - x_i^{(p)} \right| n_i^{(c,p)} F_j^{(c)} \tag{3.18}$$

where the equilibrium condition of a particle $\sum_{N_c} F_j^{(c)} \equiv 0$ is introduced.

The averaging process in conjunction with Equations (3.11) and (3.18) can be used to calculate the average stress tensor of all the particles contained in a volume V of a granular medium. The particles within the volume defined by a measurement circle, can be divided into three parts: the particles contained entirely within the volume; the particles with centroids contained within the measurement circle; the particles intersecting the measurement circle in which particle centroids are not contained. In PFC^{2D}, the first two categories of particles are considered to compute the average stress tensor. At the same time, a correction factor, linked with the porosity, is introduced into the computation of the stress tensor. Therefore, the volume of the neglected particles is taken into account.

In order to determine the correction factor, a uniform stress field σ_0 is assumed to exist within the measurement circle. The correct expression of the average stress $\bar{\sigma}$, within a volume V_m defined by a measurement circle, is written as

$$\bar{\sigma} = \frac{1}{V_m} \sum \bar{\sigma}^{(p)} V^{(p)} = \frac{1}{V_m} \bar{\sigma}^{(p)} \sum V^{(p)} = \sigma_0 \left(\frac{\sum V^{(p)}}{V_m} \right) = \sigma_0 (1 - n) \tag{3.19}$$

where all particles and portions of particles contained within the measurement circle are considered; n indicates the porosity within V_m. An alternative incorrect expression for the average stress $\widetilde{\sigma}$ is expressed as

$$\widetilde{\sigma} = \frac{1}{V_m} \sum_{N_p} \bar{\sigma}^{(p)} V^{(p)} = \sigma_0 \left(\frac{\sum\limits_{N_p} V^{(p)}}{V_m} \right) \tag{3.20}$$

where only the particles with centroids contained within V_m are considered. The relationship between the above two stress equations is expressed as

$$\frac{\bar{\sigma}}{\widetilde{\sigma}} = \left(\frac{1 - n}{\sum\limits_{N_p} V^{(p)}} \right) V_m \tag{3.21}$$

By substituting Equation (3.20) into Equation (3.21), the final corrected equation of

the average stress within the measurement circle is expressed as

$$\bar{\sigma} = \left(\frac{1-n}{\sum_{N_p} V^{(p)}} \right) \sum_{N_p} \bar{\sigma}^{(p)} V^{(p)} \tag{3.22}$$

In PFC^{2D}, the final equation to calculate the average stress tensor within a measurement circle is obtained by eliminating $\bar{\sigma}^{(p)}$, using Equation (3.18) to obtain

$$\bar{\sigma}_{ij} = -\left(\frac{1-n}{\sum_{N_p} V^{(p)}} \right) \sum_{N_p} \sum_{N_c} \left| x_i^{(c)} - x_i^{(p)} \right| n_i^{(c,p)} F_j^{(c)} \tag{3.23}$$

where the expression includes two summations executed over the N_p particles with centroids contained within the measurement circle and N_c contacts of these particles;
n denotes the porosity within the measurement circle;
$V^{(p)}$ indicates the volume of particle (p);
$x_i^{(p)}$ and $x_i^{(c)}$ are the particle centroid location and its contact, respectively;
$n_i^{(c,p)}$ is a unit normal vector with a direction from a particle centroid to its contact location; and
$F_j^{(c)}$ represents the force acting over the contact (c).

3.2.4.4 Strain rate

There is much difference between the method to calculate the local strain rate within a volume defined by the measurement circle and that applied to compute the local stress. When determining the local stress, the discrete contact forces are employed to determine the average stress, since the forces in the void are zero. However, it is not reasonable to calculate the average strain rate in terms of the velocities in a similar way, considering the fact that the velocities in the voids are nonzero. Instead of assuming a velocity field in the voids, a best-fit procedure, minimizing the error between the predicted and measured velocities of all particles with centroids contained within the measurement circle, is employed to determine the strain-rate tensor. The links between the strain and strain rate will be explained first in the following.

The displacement gradient α_{ij} is applied to elaborate the relation between the displacements u_i at two neighbouring points. Assume the particles P and P' to be located instantaneously at x_i and $x_i + dx_i$, respectively. The difference in displacement between these two points is

$$du_i = u_{i,j}dx_j = \alpha_{ij}dx_j \tag{3.24}$$

A symmetric and an anti-symmetric tensor can be employed to describe the displacement gradient tensor as

$$\alpha_{ij} = e_{ij} - \omega_{ij} \tag{3.25}$$

where

$$\begin{aligned} e_{ij} &= \frac{1}{2}(u_{i,j} + u_{j,i}) \qquad \text{infinitesimal strain tensor} \\ \omega_{ij} &= \frac{1}{2}(u_{j,i} - u_{i,j}) \qquad \text{rotation tensor} \end{aligned} \tag{3.26}$$

The velocity gradient tensor, $\dot{\alpha}_{ij}$, in a similar way, can be employed to describe the relation between the velocities, v_i , at two neighbouring points. Note that the velocity field is linked to the displacement field via $u_i = v_i dt$, where v_i is the velocity and dt is an infinitesimal interval of time. The particles P and P' are assumed to be located instantaneously at x_i and $x_i + dx_i$, respectively. The difference in velocity between these two points is

$$dv_i = v_{i,j}dx_j = \dot{\alpha}_{ij}dx_j \tag{3.27}$$

Also, a symmetric and an anti-symmetric tensor can be employed to describe the velocity gradient tensor as

$$\dot{\alpha}_{ij} = \dot{e}_{ij} - \dot{\omega}_{ij} \tag{3.28}$$

where

$$\begin{aligned} \dot{e}_{ij} &= \frac{1}{2}(v_{i,j} + v_{j,i}) \qquad \text{rate-of-deformation tensor} \\ \dot{\omega}_{ij} &= \frac{1}{2}(v_{j,i} - v_{i,j}) \qquad \text{spin tensor} \end{aligned} \tag{3.29}$$

In PFC^{2D}, the strain-rate tensor is referred to the velocity-gradient tensor $\dot{\alpha}_{ij}$, which can be determined using the least-squares procedure in the following.

The strain-rate tensor within a specified measurement circle indicates the best fit to the N_p measured relative velocity values, $\widetilde{V}_i^{(p)}$, of the particles whose centroids are included within the measurement circle. The average velocity and position of the N_p particles can be expressed as

$$\bar{V}_i = \frac{\sum_{N_p} V_i^{(p)}}{N_p} \qquad \text{and} \qquad \bar{x}_i = \frac{\sum_{N_p} x_i^{(p)}}{N_p} \tag{3.30}$$

where $V_i^{(p)}$ and $x_i^{(p)}$ are the translational velocity and centroid location, respectively, related to particle (p). The measured relative velocity values are expressed as

$$\widetilde{V}_i^{(p)} = V_i^{(p)} - \bar{V}_i \tag{3.31}$$

When $\dot{\alpha}_{ij}$ is determined, the predicted relative velocity values, $\widetilde{v}_i^{(p)}$, can be described, based on Equation (3.27), as

$$\widetilde{v}_i^{(p)} = \dot{\alpha}_{ij}\widetilde{x}_j^{(p)} \tag{3.32}$$

where $\widetilde{x}_i^{(p)} = x_i^{(p)} - \bar{x}_i$.

These predicted values can induce an error, which is measured by

$$z = \sum_{N_p} \left| \widetilde{v}_i^{(p)} - \widetilde{V}_i^{(p)} \right|^2 = \sum_{N_p} \left(\widetilde{v}_i^{(p)} - \widetilde{V}_i^{(p)} \right) \left(\widetilde{v}_i^{(p)} - \widetilde{V}_i^{(p)} \right) \tag{3.33}$$

where z denotes the sum of the squares related to the deviations between the predicted and measured velocities.

Eliminating $\widetilde{v}_i^{(p)}$ of Equation (3.33) using the Equation (3.32) and differentiating on the basis of the condition of minimum z: $\frac{\partial z}{\partial \dot{\alpha}_{ij}} = 0$, the following set of four equations is obtained as

$$\begin{pmatrix} \sum_{N_p} \widetilde{x}_1^{(p)}\widetilde{x}_1^{(p)} & \sum_{N_p} \widetilde{x}_2^{(p)}\widetilde{x}_1^{(p)} \\ \sum_{N_p} \widetilde{x}_1^{(p)}\widetilde{x}_2^{(p)} & \sum_{N_p} \widetilde{x}_2^{(p)}\widetilde{x}_2^{(p)} \end{pmatrix} \begin{pmatrix} \dot{\alpha}_{i1} \\ \dot{\alpha}_{i2} \end{pmatrix} = \begin{pmatrix} \sum_{N_p} \widetilde{V}_i^{(p)}\widetilde{x}_1^{(p)} \\ \sum_{N_p} \widetilde{V}_i^{(p)}\widetilde{x}_2^{(p)} \end{pmatrix} \tag{3.34}$$

where setting $i = 1,$ and then 2, all four components of the velocity-gradient tensor, i.e. strain-rate tensor can be computed.

3.2.5 Clump logic

Clump logic is employed to create and modify groups of slaved particles or clumps. In PFC^{2D}, a clump is considered as a rigid entity, i.e. the particles comprising the clump keep at a fixed distance from each other. Instead of a non-clump calculation, where all contacts are active, the computation skips the internal contacts within a clump,without affecting the external contacts of the clumps, and therefore computation time is saved. There is some extent of overlap for the internal contacts where contact forces are not generated. However, any contact forces will be preserved unchanged during computation cycling, provided that they exist when the clump is created or when a particle is added to the clump. Since a clump acts as a rigid body with a deformable boundary and will not break apart, regardless of the forces acting upon it, it differs from a group of particles that are bonded to each other, like a particle cluster.

For a general clump, the basic mass properties can be defined in the following:

$$m = \sum_{p=1}^{N_p} m^{[p]} \tag{3.35}$$

$$x_i^{[G]} = \frac{1}{m} \sum_{p=1}^{N_p} m^{[p]} x_i^{[p]} \tag{3.36}$$

$$\begin{aligned} I_{ii} &= \sum_{p=1}^{N_p} \left\{ m^{[p]} \left(x_j^{[p]} - x_j^{[G]} \right) \left(x_j^{[p]} - x_j^{[G]} \right) + \frac{2}{5} m^{[p]} R^{[p]} R^{[p]} \right\} \\ I_{ij} &= \sum_{p=1}^{N_p} \left\{ m^{[p]} \left(x_i^{[p]} - x_i^{[G]} \right) \left(x_j^{[p]} - x_j^{[G]} \right) \right\}; \qquad (j \neq i) \end{aligned} \tag{3.37}$$

where the summations are taken over the N_p particles comprising the clump;
m denotes the total mass of the clump;
$x_i^{[G]}$ indicates the location of the mass centre;
I_{ii} and I_{ij} represent the moments and products of inertia of a clump;
$m^{[p]}$, $R^{[p]}$ and $x_i^{[p]}$ are the mass, radius and centroid location, respectively, of the particle (p).

The resultant force and moment vectors acting over the clump are employed to calculate its motion, which can be divided into the translational motion of a point in the clump and the rotational motion of the entire clump, since the clump is treated as a rigid entity. The translational motion equation can be described in the vector form as

$$F_i = m\left(\ddot{x}_i - g_i\right) \tag{3.38}$$

where F_i is the resultant force, the sum of all externally-applied forces acting upon the clump, m denotes the total mass of the clump, $\ddot{x}_i$ is the translational acceleration of the mass centre of the clump and g_i is the body force acceleration vector arising from gravity loading. The resultant force is calculated via

$$F_i = \sum_{p=1}^{N_p}\left(\tilde{F}_i^{[p]} + \sum_{c=1}^{N_c} F_i^{[p,c]}\right) \tag{3.39}$$

where $\tilde{F}_i^{[p]}$ is the externally-applied force acting on particle (p), but excluding the contact force acting upon particle (p) at contact (c), which is indicated by $F_i^{[p,c]}$.

With reference to Ginsberg and Genin (1984), the expression of rotational motion can be described in a vector form as

$$M_i = \dot{H}_i \tag{3.40}$$

where M_i denotes the resultant moment related to the mass centre, and $\dot{H}_i$ indicates the time rate-of-change of the angular momentum of the clump. The resultant moment M_i is computed by

$$M_i = \sum_{p=1}^{N_p}\left(\tilde{M}_i^{[p]} + \epsilon_{ijk}\left(x_j^{[p]} - x_j^{[G]}\right)F_k^{[p]} + \sum_{c=1}^{N_c}\epsilon_{ijk}\left(x_j^{[c]} - x_j^{[p]}\right)F_k^{[p,c]}\right) \tag{3.41}$$

where $\tilde{M}_i^{[p]}$ is the externally-applied moment acting on particle (p), $F_k^{[p]}$ denotes the resultant force acting on particle (p) at its centroid, and $F_k^{[p,c]}$ represents the force acting on particle (p) at contact (c). The time rate-of-change of the angular momentum can be expressed as

$$\dot{H}_i = \alpha_i I_{ii} - \alpha_j I_{ij} + \epsilon_{ijk}\omega_j\left(\omega_k I_{kk} - \omega_l I_{kl}\right); \qquad (j \neq i, l \neq k) \tag{3.42}$$

where $\alpha_i = \dot{\omega}_i$, and a local coordinate system attached to the clump at its centre of mass is involved, consistent with Equation 3.40.

3.2.6 Local damping

Energy generated in the particle assembly is dissipated by means of frictional sliding. Nevertheless, frictional sliding may not be sufficient to arrive at a steady-state solution in a reasonable number of computation cycles. Local damping in PFC^{2D} can be applied to dissipate energy by efficiently damping the motion equations. The damping constant α can be set for individual particles to control the local damping. For local damping, a damp-force term is added to the motion equations and therefore, the damped motion equation can be expressed as:

$$\begin{aligned} F_{(i)} + F^d_{(i)} &= M_{(i)} A_{(i)}; \quad i = 1...3 \\ M_{(i)} A_{(i)} &= \begin{cases} m\ddot{x}_{(i)}, & \text{for } i = 1...2; \\ I\dot{\omega}_{(i-3)}, & \text{for } i = 3 \end{cases} \end{aligned} \tag{3.43}$$

where $F_{(i)}$, $M_{(i)}$, and $A_{(i)}$ are the generalised force, mass, and acceleration components, respectively; $F_{(i)}$ includes the contribution from gravity force; and $F^d_{(i)}$ is the damping force

$$\begin{aligned} F^d_{(i)} &= -\alpha \left| F_{(i)} \right| sign\left(V_{(i)} \right); \qquad i = 1...3 \\ Sign(y) &= \begin{cases} +1, & \text{if } y > 0; \\ -1, & \text{if } y < 0; \\ 0, & \text{if } y = 0 \end{cases} \end{aligned} \tag{3.44}$$

expressed in terms of the generalised velocity

$$V_{(i)} = \begin{cases} \dot{x}_{(i)}, & \text{for } i = 1...2; \\ \omega_{(i-3)}, & \text{for } i = 3 \end{cases} \tag{3.45}$$

As discussed above, the damping constant α controls the damping force and its default value is 0.7. There are several advantages for this kind of damping. Local damping is only applied to the acceleration motion. Consequently, no damping forces are produced from steady-state motion. In addition, the damping constant α is dimensionless. Damping is frequency-independent, and therefore, the assembly regions are damped equally for the same damping constant. In the current research, local damping is used with the default value of 0.7.

3.2.7 Periodic boundary

The introduction of a periodic boundary is presented here. There exists a square periodic boundary, shown in Figure 3.2. A particle, (marked by red colour) labelled as number 2 is generated in the left boundary and treated as a controller by PFC^{2D}. Another particle (i.e. a yellow one with number 2) will appear at the same horizontal position on the right boundary as a slave. The slave particle has the same properties such as velocity, particle radius and stiffness, as the controller. The information would be exchanged by the controller with its slaves during DEM calculation cycles and they behave as one particle. Similarly, when the red controller particle, number 1, is generated at the corner of the periodic boundary, three slave particles (with yellow colour) are created at the other corners of the periodic boundary. Therefore, for the square periodic boundary, the left boundary is identical to the right. Likewise, the top side is the same as the bottom.

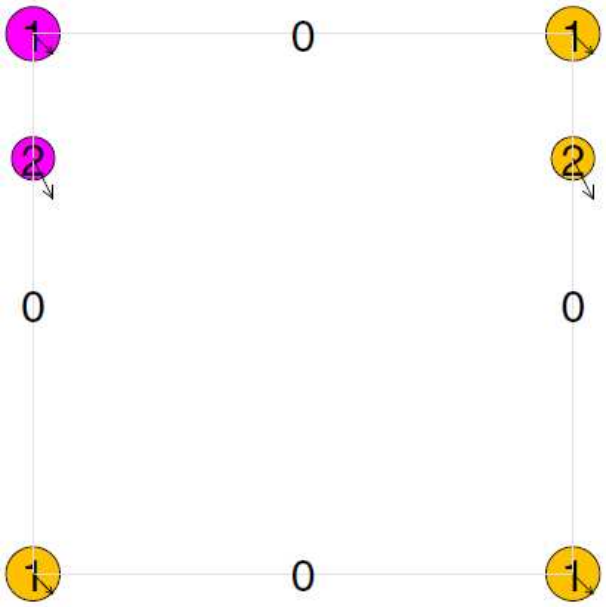

Figure 3.2: Two particles crossing the square periodic boundaries (Itasca, 2004)

3.3 Procedure validation

3.3.1 Introduction

DEM was pioneered by Cundall (1971, 1974), employed as a numerical model capable of modelling the mechanical behaviour of assemblies comprised of discs or spheres. An explicit numerical scheme is introduced in this method in terms of modelling the particle motion particle by particle as well as monitoring the particle interaction contact by contact. A computer model, BALL, was developed by Cundall and Strack (1979a) and validated on the basis of a comparison of contact vector plots between the simulation and a photoelastic analysis (De Josselin de Jong and Verruijt, 1969). The force vector field, described numerically, was in close agreement with that described photoelastically. The extension of the program, BALL, in 2D to TRUBAL, in 3D, was proposed by Cundall and Strack (1979b) with a validation consisting of simulating a physical triaxial test involving hexagonally packed steel spheres (Rowe, 1962). Bathurst (1985) proposed a modified version of the program BALL, which was further updated by Sitharam (1991) and named DISC.

DEM biaxial shear tests were investigated by Sitharam (1999) based on the program DISC in a monotonic loading path. The influence of confining pressure on the behaviour of the granular assembly was studied, indicating that shear strength increases accompanied by a decrease in dilation as the confining pressure rises. This agrees well with the experimental behaviour of actual granular materials (Yamamuro and Lade, 1996). Also, biaxial tests with cyclic loading paths were modelled with DISC by Sitharam (2003). Liquefaction of a loose assembly was observed, induced by a continuous and accumulated reduction of the coordination number under each cycle. Moreover, a continued reorientation of fabric arises with the reversal of the loading orientation. In comparison, there is no accumulated decrease in the contact number in dense granular assemblies, since the fabric reaches a limiting direction because of the higher stress ratios. A virtual experiment technique on DEM simulation of the biaxial test was proposed by Li et al. (2013). The general loading paths like principal stress

rotation, can be applied to the granular element by three control modes: strain control with the motion of the boundary massless walls; stress mode with a servo-control mechanism and a combination of the first two methods as a mixed boundary condition. In conclusion, like the laboratory test, various loading paths can be achieved in DEM simulation of a biaxial test.

The selection of boundary conditions plays an important role in biaxial test modelling with DEM. Generally speaking, the boundary conditions commonly employed in DEM modelling can be concluded to be the rigid wall boundary, periodic boundary and simulated flexible membrane boundary, respectively. The rigid wall, without inertia, is the most widely applied boundary condition. In 2D DEM modelling, a rectangular or square granular specimen can be generated with vertical and horizontal rigid line-walls (Itasca, 2004), as shown in Figure 3.3a, which is similar to laboratory compression tests. However, in this case, the loading paths will be extremely limited, since the introduction of friction to the wall boundaries was not suggested with the intention of minimizing the arching effects of the end boundaries. Hence, a representative element with a convex polygonal boundary is employed by Li et al. (2013), as illustrated in Figure 3.3b. Furthermore, Ai et al. (2014) described a discretised-wall confined granular element to obtain a homogeneous shear field with DEM simulation (see Figure 3.3c). The periodic boundary is another boundary type used in DEM modelling so as to avoid the end effect in real physical tests. The granular assembly can be assumed to be a representative of repeated and identical typical elements. The contacts take place not only between the particles contained internally in the element but also between the particles along the boundaries. Similarly, strain control and stress control modes can be used in the periodic boundary system. For example, a triaxial stress field was realized by Thornton (2000) under periodic boundary conditions. In order to replicate the laboratory tests and study the development of the localization or shear band in the specimen with DEM, a simulated flexible membrane is applied as the element boundary of the biaxial test (e.g. Figure 3.3d). According to Iwashita and Oda (1998), Wang and Leung (2008a,b) and Jiang et al. (2011), a number of particles were bonded together to model the flexible membrane of the physical tests. A desired

confining pressure can be obtained by applying external forces to the membrane particles. As highlighted by Cheung and O'Sullivan (2008), the primary limitation of this approach is the difficulty in relating the properties of the membrane particles and the bonds between particles to a real continuous membrane. Besides, the particle-bonded membrane can not be updated when new particles move to the outside of the assembly, due to the large deformation levels (Tsunekawa and Iwashita, 2001). In contrast, some other authors (e.g. Cui, 2006; Cheung and O'Sullivan, 2008) prefer to apply the equivalent forces directly to the outermost particles of the specimen, which are allowed to deform freely. In this case, a required stress level is realized within the specimen. As pointed out by De Bono (2013), in this approach, the specimen membrane is still considered to be cylindrical, contrary to the changes in membrane shape in actual triaxial tests. Moreover, the external forces were applied to the outermost particles of the specimen with the direction always to the centre of the assembly (Cheung and O'Sullivan, 2008). However, the real confining pressure is normal to the sample surface.

In practice, the shape of granular particles, such as sand, is usually irregular and diversified, and it is impossible to replicate the real shape of each particle in DEM simulation. The particles commonly used in modelling granular materials are discs (Li et al., 2013), clumps (Li and Yu, 2011), 2D elliptical particles (Ng, 1994), polygonal particles (Pena et al., 2008), disc-clusters (Thomas and Bray, 1999), discs with rolling resistance (Mohamed and Gutierrez, 2010), 3D spheres or clumps (Geng, 2010) and 3D ellipsoids (Lin and Ng, 1997). The particle shape has a significant influence on shear strength, deformation behaviour, shear band and fabric statistics of the granular assembly in DEM simulation. Even slight out-of-roundness of particles could greatly increase the shear strength, since the interlocking effect among particles rises and then particle rotations are restrained (Ting et al., 1995). It is also concluded that an irregular shape causes an increase in volumetric dilation at the ultimate state during DEM biaxial test shearing (Geng, 2010). Moreover, particle rolling resistance affects the orientation, thickness and the formation timing of shear bands (Mohamed and Gutierrez, 2010). Besides the application of various particle shapes in DEM simulation, particle breakage is taken into consideration by some researchers. For example, a cluster

comprised of small particles bonded together is treated as a granular particle like sand grain. Internal breakage of the bonding within clusters is used to model the particle crushing. The failure criterion can be structured on the basis of the strength of the bonding. This approach has been applied by Cheng et al. (2003) to model isotropic compression tests and McDowell and Harireche (2002) in replicating the normal compression tests of granular materials. Other authors prefer to use a fracture criterion to model the breakage of a particle, which is replaced by a number of small particles after the breakage. For example, Tsoungui et al. (1999) investigated the particle crushing behaviour of a granular assembly by means of a fracture criterion based on shear stresses in the particles during 2D oedometric compression tests. This particle fracture model is extended from 2D to 3D by De Bono (2013) in order to model high pressure triaxial tests. Moreover, Lobo-Guerrero et al. (2006) used a relatively simplified failure criterion, with regard to the values of the applied load concerning the particle, particle size and the particle coordination number in order to investigate the particle breakage in 2D uniaxial compression.

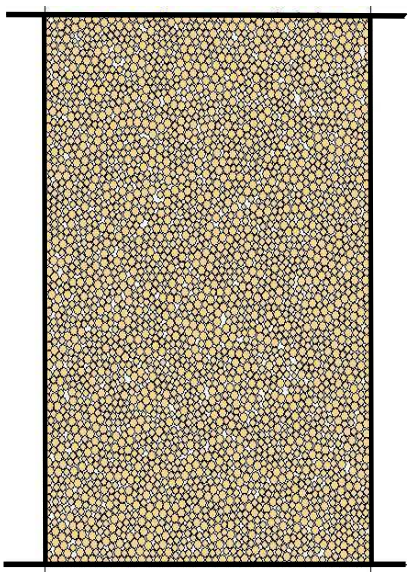

(a) Line-wall boundary

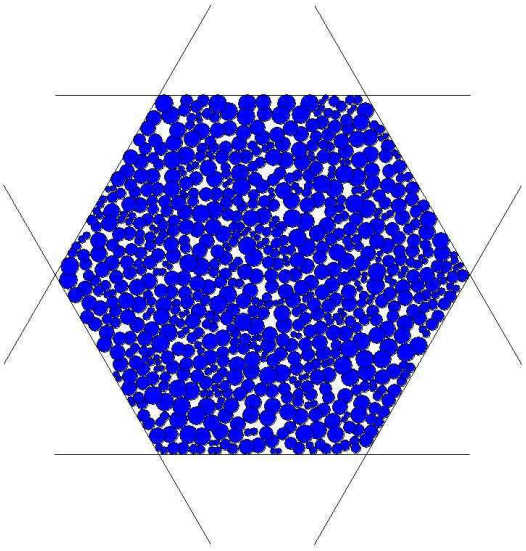

(b) Convex polygonal boundary

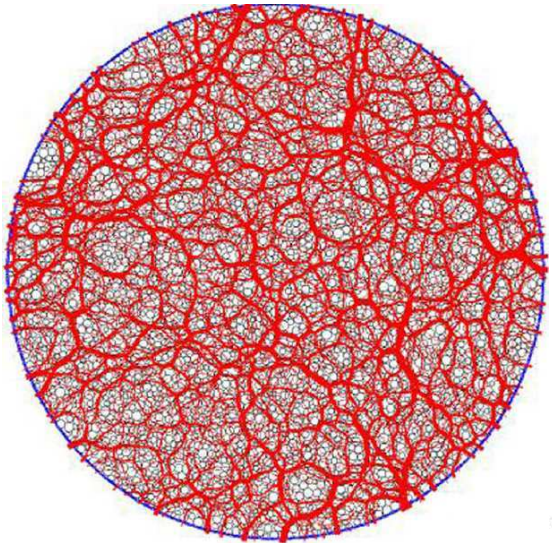

(c) Discretised-wall boundary (Ai et al., 2014)

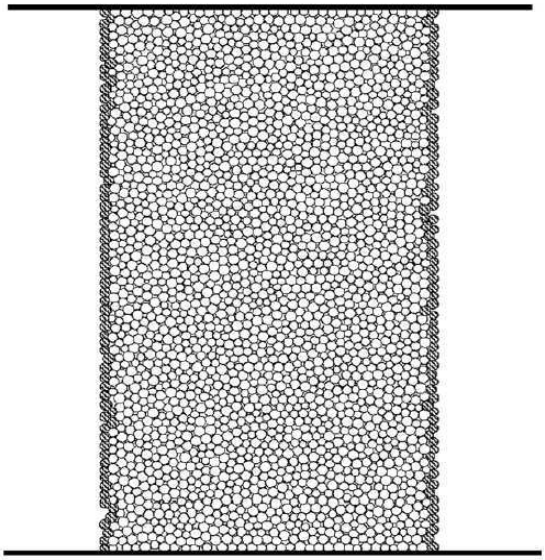

(d) Simulated flexible boudnary (Cheung and O'Sullivan, 2008)

Figure 3.3: The various boundary conditions in DEM biaxial test simulation

3.3.2 Experimental data

Biaxial experiments were carried out to investigate the stress ratio-strain behaviour of sand specimens under drained conditions by Alshibli and Sture (2000). The sand used in the tests was an industrial sub-angular quartz sand with a uniform white colour and specific gravity of 2.65. The minimum and maximum grain sizes were 0.25 and 1.0mm, respectively. The specimens were prepared by filling a split Lexan mold with sand in an air pluviation approach. The internal length and height of the mold were 80.8 and 152.4mm respectively. The experiment apparatus of the biaxial test is shown in Figure 3.4. The lateral deformation was restricted with two Lexan walls bolted to the bottom end platen and braced by two stiff, aluminum plates. In this way, the plane strain conditions could be met. Furthermore, the bottom end platen was fixed and the top end platen fitted together with the loading ram. The axial loading was imposed with a constant axial displacement rate while a cell pressure reservoir was used to realize a constant confining pressure for the specimens, which was 100kPa in these tests. Moreover, the axial load, axial displacement and volume change were measured by a load meter connected to the loading ram, a linear variable differential transducer (i.e. LVDT in Figure 3.4) and a differential pressure transducer (see DPT in Figure 3.4), respectively. The typical relation of stress ratio σ_1/σ_3 (i.e. the ratio of the major principle stress σ_1 to the minor σ_3) to axial strain ε_a was obtained, as shown in Figure 3.5. The DEM simulation results will be used to compare with this laboratory data.

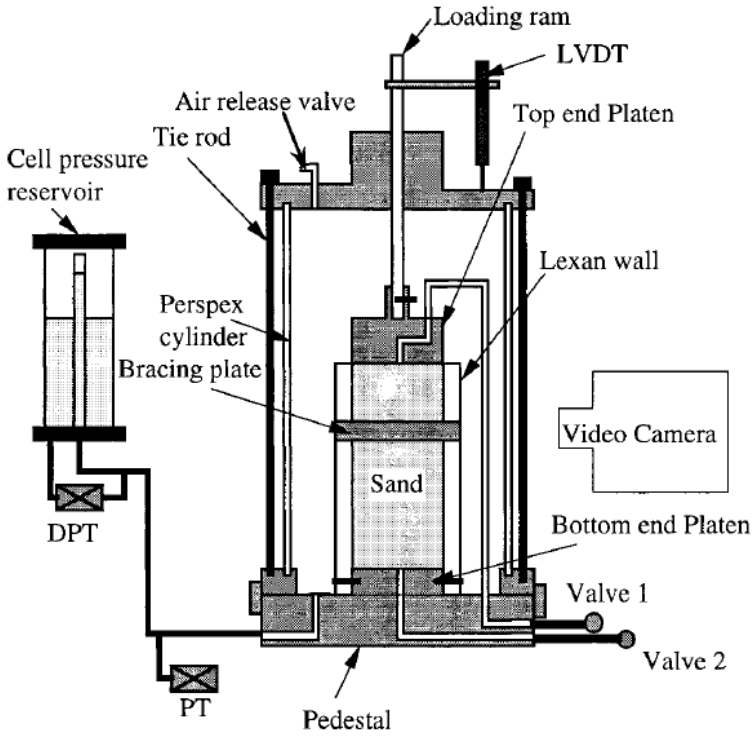

Figure 3.4: The apparatus for biaxial compression experiments (Alshibli and Sture, 2000)

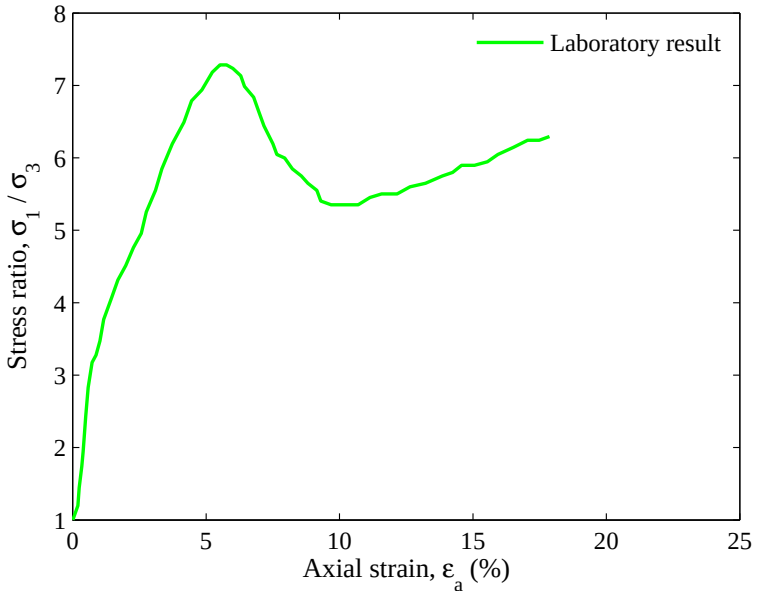

Figure 3.5: The typical relationship between stress ratio and axial strain for biaxial compression tests under a confining pressure of 100kPa (Alshibli and Sture, 2000)

3.3.3 Biaxial test simulation

As discussed in Subsection 3.3.1, several boundary conditions can be used in DEM biaxial test simulations such as the vertical rigid line-walls, convex polygonal boundary, and the simulated flexible membrane boundary, etc. The loading path is quite simple in this biaxial test simulation so it is not necessary to use a complicated convex polygonal boundary to prevent the arching effect. In addition, it is noted that there is not much difference in the stress-strain relationship between the vertical rigid wall boundary and the stress-controlled membrane boundary in biaxial test simulation (Cheung and O'Sullivan, 2008). Since the studies in this chapter mainly focus on the development of stress and volumetric strain versus axial strain, vertical walls will be used as the lateral boundaries in the following simulations. In order to consider the effect of particle shape, the circular grain (i.e. disc) and two-disc clump are introduced in the biaxial test simulations. Finally, particle breakage is not taken into account, since it would make the DEM simulations excessively complicated.

3.3.3.1 Sample preparation

The specimen of the DEM biaxial test is structured as a rectangular cell with four rigid and massless walls where the particles (e.g. discs or clumps) are generated (see Figure 3.3a). The top and bottom walls are used to simulate the loading platens of the experimental tests, while the lateral walls are used as the confinement and to apply the constant confining pressure to the granular assembly. When generating a number of particles in PFC^{2D}, any overlap between the particles is not allowed. If one particle is created having an overlap with another one, the generator will try another position. A specific number of tries can be executed. Hence, it is difficult to produce a relatively dense sample. In order to overcome this problem, the radius expansion method (Itasca, 2004) is applied to the creation of the specimens. Firstly, a vessel is formed by four walls. Then the target number of discs N_p is calculated on the basis of the required porosity n, the mean value of maximum and minimum disc radii r_m and the vessel

area A

$$N_p = \text{Int}\left[\frac{(1-n)A}{\pi r_m^2}\right] \tag{3.46}$$

where Int[*] means that the integer of disc number is to be taken. After that, the discs are generated and filled in the vessel with radii divided by a divisor. Later, all the disc radii are expanded to obtain the desired disc sizes by a multiplier λ_d, which is defined as

$$\lambda_d = \sqrt{\frac{1-n}{1-\left(1-\frac{A_s}{A}\right)}} = \sqrt{\frac{(1-n)A}{A_s}} \tag{3.47}$$

where the total disc area A_s, is the summation of individual disc areas, taken over the N_p discs contained within the vessel A, and defined as

$$A_s = \sum_{N_p} \pi r^{(p)} r^{(p)}. \tag{3.48}$$

where $r^{(p)}$ is the radius of the disc (p). At this time, if the assembly is to be comprised of clumps, each disc can be replaced by the clump with the same area so that the porosity of the specimen remains unchanged. Large overlaps between discs are probably caused by the radius expansion method. To eliminate this effect, a number of calculation cycles are operated until the granular system reaches a steady state, which can be detected by checking whether either the maximum or the average unbalanced force ratio achieves the default value 0.01 in PFC^{2D}. The average unbalanced force ratio indicates the ratio of the average unbalanced force, related to all discs, which is averaged on the basis of the sum of all the unbalanced force components in absolute terms to the average contact force, related to all contacts with nonzero normal force, averaged with regard to the sum of the absolute values of the normal forces. Besides, the maximum out-of-balance ratio denotes the ratio of the maximum out-of-balance force, which is the maximum value of any unbalanced force component over all discs, to the maximum contact force. This is the maximum value of the normal forces in absolute terms over all contacts with nonzero normal force. The granular assembly is finally created with the required porosity n and disc radii. Note that during the entire process of the sample preparation, the wall boundaries remain fixed without any movement.

The length and height of the DEM granular sample are set at 80.8 and 152.4mm respectively, identical to the dimensions of the experimental specimen (Alshibli and Sture, 2000), described in Subsection 3.3.2. The porosity of the initial sample is set at 0.30, although this has little effect on the porosity after consolidation (Zhou, 2011). The minimum and maximum grain sizes were 0.25 and 1.0mm in the laboratory tests. If the same particle sizes were applied in the DEM modelling tests, there would be too many particles generated, which would increase the computation time significantly. For the purpose of reducing the number of discs, in the current research, all the disc sizes are multiplied by a factor of 3.2, with a range of 0.8 to 3.2mm. This approach, designed to save calculation time, is widely adopted by DEM users (e.g. Wang and Leung, 2008a,b; Geng, 2010). In this way, approximately 2700 particles are generated within the granular assembly using the radius expansion method. It is reasonable, based on the conclusion presented by Li (2006), that when the particle number is more than 2000, there is no significant effect on the stress and strain relationships in the DEM biaxial tests. Moreover, the specific gravity of the simulated discs is set at 2.65, the same as the sand grains in the laboratory tests. The elastic parameters of the granular assembly, like Young's modulus and Poisson's ratio, are closely related to the particle normal and shear stiffnesses in the DEM biaxial test simulation. The Young's modulus can be determined by setting the value of the particle normal stiffness, while Poisson's ratio depends on the ratio of particle normal to shear stiffness (Itasca, 2004). In the present study, the particle normal stiffness is assigned as 5×10^7N/m, which proves to be suitable by comparison with the experimental results (see Figure 3.11 in Subsection 3.3.4). To simplify the parameter setting, the particle shear stiffness is assigned to be identical to the normal one. Three friction coefficients for the particles are used in the biaxial shearing simulation, i.e. 0.5, 0.7 and 0.9. The stiffness of the top and bottom walls is assigned as 5×10^7N/m, while the stiffness of the lateral walls is set as one-tenth of the particle stiffness (i.e. 5×10^6N/m) to consider the effect of a "soft" confinement in laboratory tests (Itasca, 2004). The friction coefficient of the walls is 0 to avoid the arching effect of the end boundaries during the biaxial shearing tests. Note that all the particles are set to be of unit thickness, i.e. 1.0m in this study.

Two kinds of granular assembly are created, composed of discs or clumps. The disc as a particle is plotted in Figure 3.6a. The clump specimen is structured by replacing the discs with a corresponding clump of equal area, comprised of two discs with the same radius. The distance between the centres of these two discs is 1.5 times the individual disc radius (see Figure 3.6b). There is an additional parameter to be defined for the clump sample, namely, particle orientation. The probability density function of the particle orientation with a directional distribution can be defined as

$$E_p(\theta) = \frac{1}{2\pi}\left[1 + a_p \cos 2(\theta - \theta_p)\right] \qquad 0 \leq \theta < 2\pi \tag{3.49}$$

where a_p defines the magnitude of anisotropy in particle orientation; and θ_p indicates the direction of anisotropy. If $\theta_p = 0$, the cumulative distribution function can be described as

$$F_p(\theta) = \int_0^{\theta} \frac{1}{2\pi}(1 + a_p \cos 2\theta)\, d\theta = \frac{1}{2\pi}\left(\theta + \frac{a_p}{2}\sin 2\theta\right) \tag{3.50}$$

In order to obtain the particle orientation for each particle, a random number u is generated on the basis of a uniform distribution in the range of 0.0 to 1.0 in PFC^{2D}. Then, letting $F_p(\theta) = u$, the value θ' is calculated using Equation 3.50. Finally, the particle orientation is determined by $\theta = \theta' + \theta_p$. During the process of sample preparation, the particle orientation is set in an isotropic distribution through $a_p = 0$.

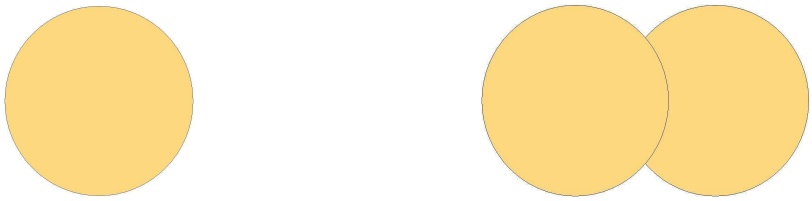

(a) Single disc as a particle *(b) Two-disc clump as a particle*

Figure 3.6: Two kinds of particles used in DEM simulations

3.3.3.2 Sample consolidation and shearing

The stress and strain states of the granular assembly provide the important information for sample consolidation and loading, which is obtained on the basis of the boundary conditions in the simulation of the biaxial test. The stresses in both vertical and

horizontal directions are calculated as

$$\sigma = \frac{\sum_{N_{(c,w)}} F^{(c,w)}}{2L} \tag{3.51}$$

where the summation of the contact forces $F^{(c,w)}$, has been taken over the $N_{(c,w)}$ contacts between the particles and two vertical or horizontal walls; L is the current sample length in the corresponding direction. The strains in both directions are described as

$$\varepsilon = \frac{L - L_0}{\frac{1}{2}(L_0 + L)} \tag{3.52}$$

where L_0 is the original sample length in the corresponding direction. A servomechanism is applied to adjust the wall velocities to conduct the sample consolidation and keep the confining pressure constant during the shearing process (Itasca, 2004). For sample consolidation, the servo control operates on all the walls, while only the lateral walls are controlled by this servo-mechanism to achieve a constant confining pressure. The equation for wall velocity $\dot{u}^{(w)}$ to reduce the difference between the measured and required stress (i.e. σ^{measured} and σ^{required}) is

$$\dot{u}^{(w)} = G\left(\sigma^{\text{measured}} - \sigma^{\text{required}}\right) = G\Delta\sigma \tag{3.53}$$

where G is the "gain" parameter. The maximum increment for wall force $\Delta F^{(w)}$ caused by wall movement in one time step Δt is

$$\Delta F^{(w)} = k_n^{(w)} N_c \dot{u}^{(w)} \Delta t \tag{3.54}$$

where N_c is the number of contacts between the particles and one vertical or horizontal wall, and $k_n^{(w)}$ is the average stiffness of these contacts. The increment of the wall stress is calculated as

$$\Delta\sigma^{(w)} = \frac{k_n^{(w)} N_c \dot{u}^{(w)} \Delta t}{A} \tag{3.55}$$

where A is the wall area in the corresponding direction. For the purpose of stability, the increment of wall stress in absolute terms $\left|\Delta\sigma^{(w)}\right|$ must be smaller than the difference in absolute terms between the measured and required stresses $|\Delta\sigma|$. A relaxation factor, α , is introduced for the stability requirement

$$\left|\Delta\sigma^{(w)}\right| < \alpha\,|\Delta\sigma| \tag{3.56}$$

The Equation 3.56 is re-written, based on Equations 3.53 and 3.55

$$\frac{k_n^{(w)} N_c G \left|\Delta\sigma\right| \Delta t}{A} < \alpha \left|\Delta\sigma\right| \tag{3.57}$$

and the "gain" parameter is obtained

$$G = \frac{\alpha A}{k_n^{(w)} N_c \Delta t} \tag{3.58}$$

During the isotropic consolidation, various particle friction coefficients are used to control the void ratio of the sample (Geng, 2010). To obtain a dense sample, no friction coefficient is assigned for the discs during the consolidation process. The sample was isotropically consolidated to a target confining pressure state, namely, 100kPa, identical to the conditions in the laboratory tests (Alshibli and Sture, 2000). The sample void ratio e is calculated as

$$e = \frac{(A' - A_s)}{A_s} \tag{3.59}$$

where A' is the current sample area and A_s is total particle area, described in Equation 3.48. Note that A_s, calculated before the discs are replaced by clumps with identical area, is applicable to the clump assembly. When the confining pressure is 100kPa, the calculated void ratio, regarded as the initial one, is 0.17 for the disc assembly. For the clump sample, it is noted that when the particle friction coefficient is set as 0.1 during the consolidation, it has the same initial compaction as that of the discs. After the consolidation, the friction coefficient 0.5, 0.7 or 0.9 is assigned to the particles for the shearing process. The particle properties and sample void ratios after consolidation are shown in Table 3.1 for the disc samples and in Table 3.2 for the clump samples.

The loading was carried out by moving the top and bottom walls at a constant rate. A suitable loading velocity needs to be determined, since the velocity has a significant effect on the macroscopic behaviour of the granular materials in DEM simulations (Geng, 2010). Generally, if the loading rate is sufficiently slow, a further reduction in it will not change the sample responses much, but it will increase the computation time. In this research, loading velocities of 0.05, 0.01, 0.005 and 0.001m/s have been studied on the disc assemblies. The particle friction coefficient 0.5 is assigned to the particles

during the shearing. As shown in Figure 3.7, a large loading velocity, i.e. 0.05m/s could increase the stress ratio σ_1/σ_3 significantly. When the velocity is equal to or less than 0.01m/s, the modelling results remain almost unchanged. In the following simulations, a loading velocity of 0.005m/s is selected.

Particle type	Initial void ratio	Particle friction coefficient	Particle stiffness
Disc	0.17	0.5	5×10^7N/m
Disc	0.17	0.7	5×10^7N/m
Disc	0.17	0.9	5×10^7N/m

Table 3.1: The disc properties (after consolidation) and initial void ratios of the specimens for DEM biaxial test simulation

Particle type	Initial void ratio	Particle friction coefficient	Particle stiffness
Clump	0.17	0.5	5×10^7N/m
Clump	0.17	0.7	5×10^7N/m
Clump	0.17	0.9	5×10^7N/m

Table 3.2: The clump properties (after consolidation) and initial void ratios of the specimens for DEM biaxial test simulation

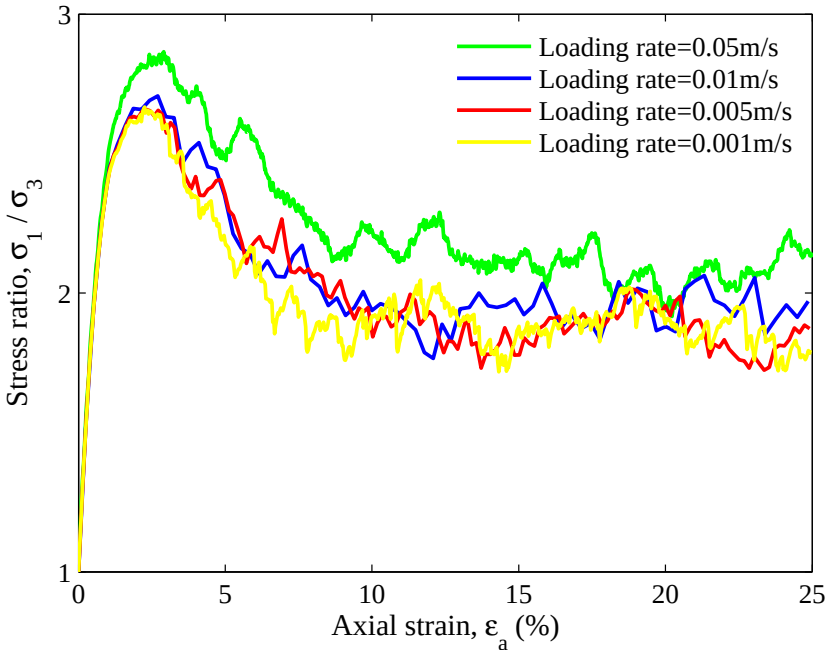

Figure 3.7: The effect of loading velocity on the stress ratio-strain relationship for DEM biaxial test simulations

3.3.4 Modelling results

The modelling results obtained using DEM are used to make a comparison with the experimental biaxial tests in a qualitative way as a validation. The shearing simulations using discs with particle friction coefficients of 0.5, 0.7 and 0.9, were first performed under a confining pressure of 100kPa. The details of the disc properties and sample information are shown in Table 3.1. The relationships between stress ratio σ_1/σ_3 and axial strain ε_a, are plotted in Figure 3.8. There is a rapid and approximately linear increase in the stress ratio at the beginning of the shearing process (i.e. Stage 1). A peak is reached (i.e. Stage 2), followed by a reduction in the ratio (i.e. Stage 3) until a relatively steady state with some fluctuation (i.e. Stage 4) takes place. There is only a slight difference for Stage 1 and Stage 4 between the different particle friction coefficients. However, the peak stress ratio increases greatly when raising the friction coefficient of the discs. Moreover, at Stage 3, the reduction in the ratio is smoother for the friction coefficient of 0.5 than those of 0.7 and 0.9. The comparison between the experimental and simulated results is plotted in Figure 3.9. The initial stiffnesses of the simulated curves related to stress ratio and axial strain have little difference, indicating that the magnitude of the Young's modulus is nearly identical. Nevertheless, there is an obvious contrast for the initial stiffness between the experimental and simulated results. In the experimental tests, a peak is also formed during the shearing, followed by a reduction in the stress ratio. The peak strength of the experimental tests is much larger than that of the simulation. The occurrence of the peak stress ratio for the laboratory tests occurs later than that of the simulation tests.

In the idealisation, the real sand grain is regarded as a disc. The real sand particles are irregular and their mutual contacts are complex, compared to the contacts between discs. It is easy for the phenomenon of interlocking to take place for an actual sand specimen. In order to simulate the interlocking effects, clumps are used in the simulation. The details related to clump generation were described in Subsection 3.3.3. Moreover, Table 3.2 illustrates the clump properties (after consolidation) and the initial compaction of the clump sample. The comparison between the experimental and sim-

ulated results is plotted in Figure 3.10. Like the disc samples, three kinds of friction coefficient (i.e. 0.5, 0.7 and 0.9) are applied to the clump particles during the shearing. There are also four stages for the simulated curves of stress ratio and axial strain, which are stress raising, peak stage, stress reduction and steady stage respectively. The initial stiffness of the curve for a friction coefficient of 0.7 is well simulated in comparison with the experimental results. There is a large increase in the peak strength, but not the ultimate strength, when increasing the particle friction coefficient from 0.5 to 0.9. The peak and ultimate stress ratios with regard to the clump samples are smaller than the experimental results but, compared to the disc specimens, there is a significant increase for the samples comprised of clumps, especially for the peak strength, as shown in Figure 3.11. Note that the comparison between disc and clump specimens is made on the basis of the particle friction coefficient 0.7, as illustrated in Table 3.3.

In conclusion, the mechanical behaviour of the biaxial test can be simulated using DEM, showing qualitative agreement with the laboratory tests (Alshibli and Sture, 2000). The initial stiffness of the stress ratio-axial strain curves is well modelled when the sample is composed of clumps with a friction coefficient of 0.7. The peak and ultimate strengths for both disc and clump samples are considerably lower than the real sand sample. This is probably due to the particle shape. The real sand grain is abnormal and the interlocking effect between particles becomes evident in the sand assembly during the shearing. This means that they are much stronger. In a similar way, compared to the disc sample, the clump sample provides higher peak and ultimate strength. Another parameter to influence the behaviour of granular materials is the particle friction coefficient. There is an increase in the peak stress ratio with a rise in this coefficient, but it has little influence on the ultimate strength.

Particle type	Initial void ratio	Particle friction coefficient	Particle stiffness
Disc	0.17	0.7	5×10^7 N/m
Clump	0.17	0.7	5×10^7 N/m

Table 3.3: The particle properties (after consolidation) and initial void ratios of the specimens for DEM biaxial test simulation

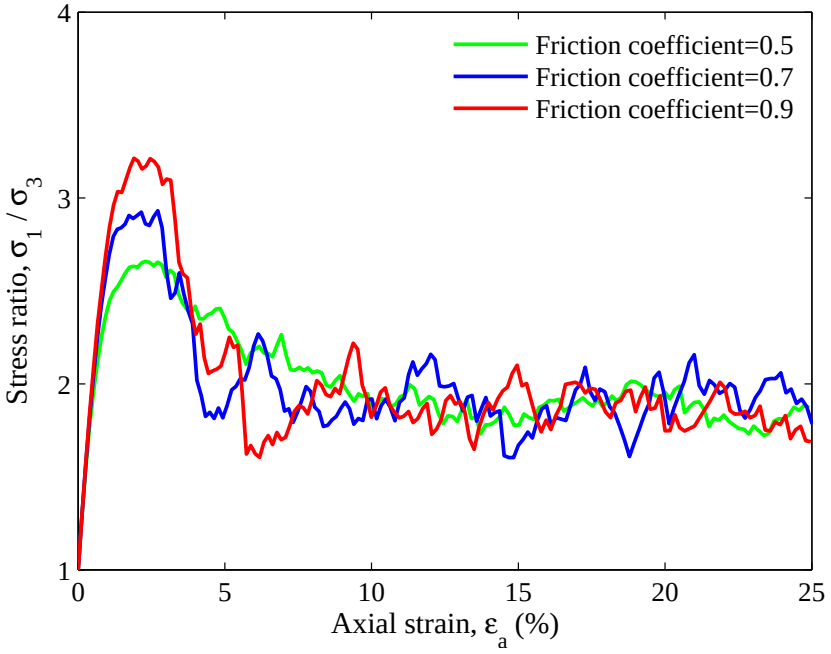

Figure 3.8: The stress ratio-strain relationship for disc samples in DEM simulations

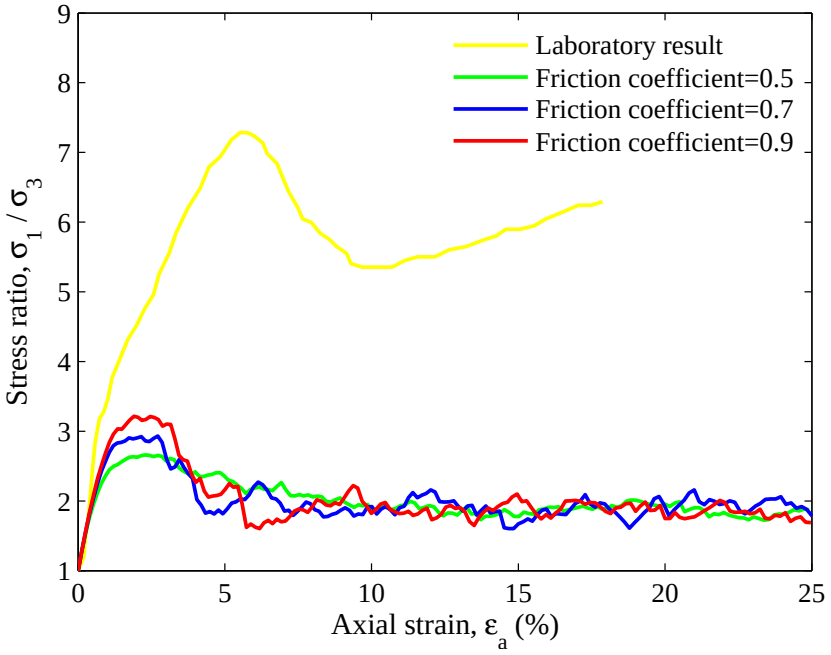

Figure 3.9: Comparison between the experimental data and simulation results (for disc samples)

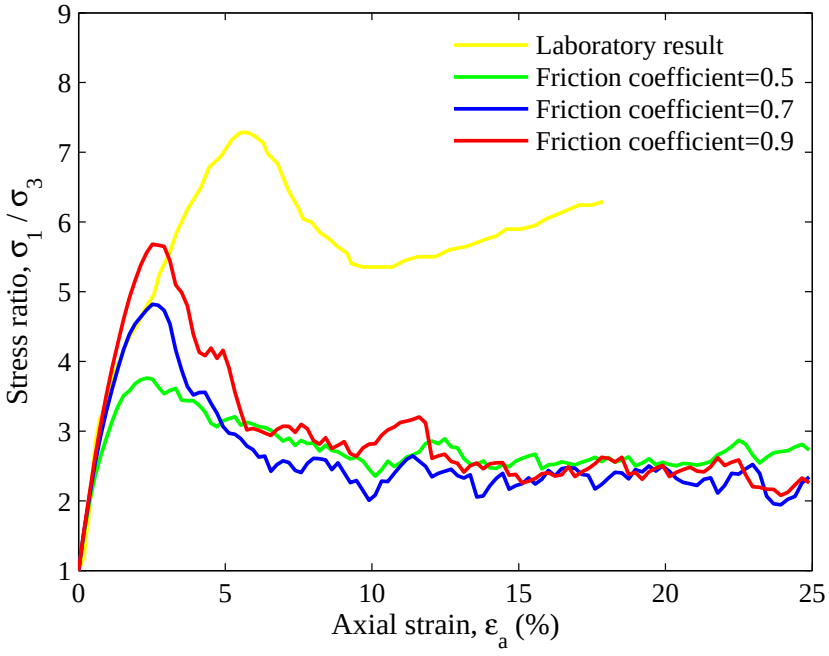

Figure 3.10: Comparison between the experimental data and simulation results (for clump samples)

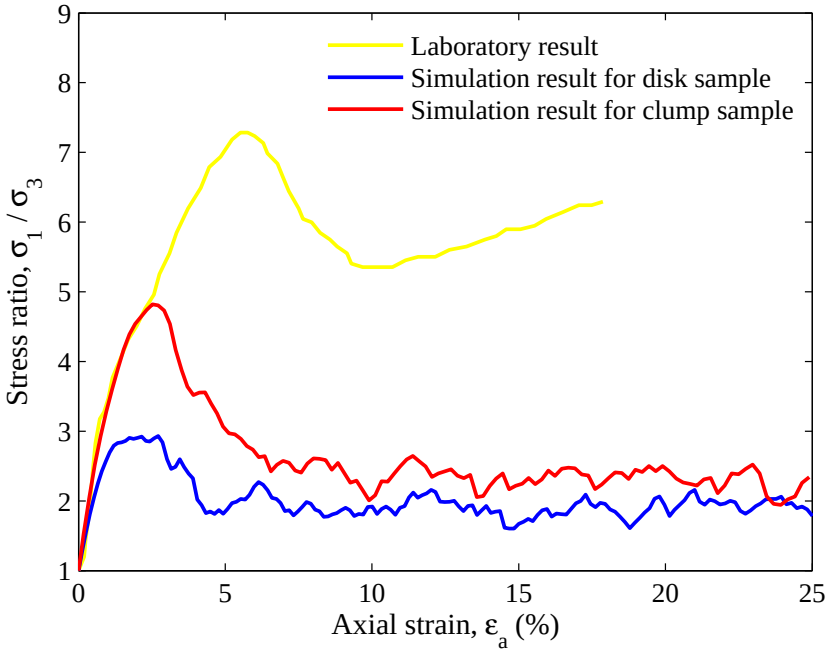

Figure 3.11: Comparison between the experimental data and simulation results (for both disc and clump samples)

3.4 Influence factors for biaxial test simulation

As described in Subsection 3.3.3, the DEM biaxial test simulation in 2D involves some factors which may have an effect on the mechanical behaviour of granular materials. The factors include particle properties such as particle stiffness and friction coefficient, the initial void ratio of the sample and the external loading condition, etc. For the disc specimen, the particle radius was selected within a range of 0.005 to 0.0075m. For the purpose of having sufficient particle numbers in the biaxial test simulation, the dimensions of the DEM specimen were chosen as 1.1×0.52m. The ratio of sample height to length in the DEM simulation is 2.1, almost the same as the laboratory tests (Alshibli and Sture, 2000). There are approximately 3200 particles filled in the rectangular vessel, which is enclosed by four rigid and massless walls. The particle number is much larger than the 2000 required for DEM biaxial test simulation, reported by Li (2006). The radius expansion method (presented in Subsection 3.3.3) was used to generate the particles, forming a sample porosity of 0.30. During particle generation, the particle friction coefficient is 0.5 and the four walls remain motionless. The friction coefficient of the walls is set as 0 to avoid the arching effect of end boundaries during shearing. A homogeneous stress field could be modelled in the granular assembly. Moreover, the particle normal stiffness is set to be equal to the shear stiffness to simplify the parameter setting. The stiffness of the lateral walls is assigned to be one-tenth of the particle stiffness, while the stiffness of loading walls (i.e. top and bottom walls) is the same as the particle stiffness. The particles have unit thickness (i.e. 1.0m). Generally, the specific gravity of soil particles ranges from 2.6 to 2.7 and it is chosen as 2.7 in the present study. The servo-control mechanism (described in Subsection 3.3.3) is applied to attain a required confining pressure during the consolidation process, i.e. $\sigma_1 = \sigma_3 = \sigma_0$. σ_0 is the required confining pressure prior to the shearing.

When the sample is being sheared, the confining pressure is kept almost unchanged by means of the servo-control. The loading is achieved by moving the top and bottom walls at a constant rate. A reasonable loading rate needs to be determined. Figure 3.12a shows the simulated results of the disc samples in terms of different loading velocities,

i.e. 0.001, 0.005, 0.01 and 0.05m/s. The particle normal and shear stiffnesses are set as 5×10^8N/m, and the particle friction coefficient assigned to be 0.7. In addition, the confining pressure is kept at 100kPa during the shearing and the sample void ratio is 0.20 when the consolidation is achieved. Note that no friction is applied to the particles during the sample consolidation. The relationship of deviatoric stress (i.e. the difference between major and minor principle stress) to axial strain, as well as the development of volumetric strain against axial strain, are plotted in Figure 3.12b. It is noted that there is a sharp increase in deviatoric stress with a rise in the loading velocity from 0.01 to 0.05m/s. The deviatoric stresses have no significant increase when the loading rate grows from 0.001 to 0.01m/s. According to the volumetric strain, there is a slight change in dilation with augmentation of the rate, especially rising from 0.001 to 0.01m/s. As discussed above, the loading rate 0.005m/s will be taken to shear the granular specimens in the following simulation tests.

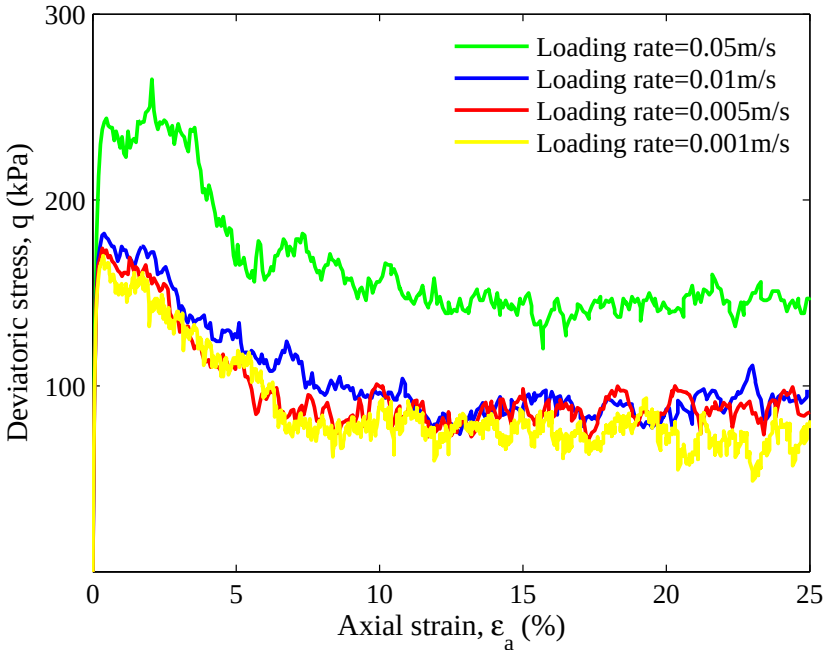

(a) Deviatoric stress versus axial strian

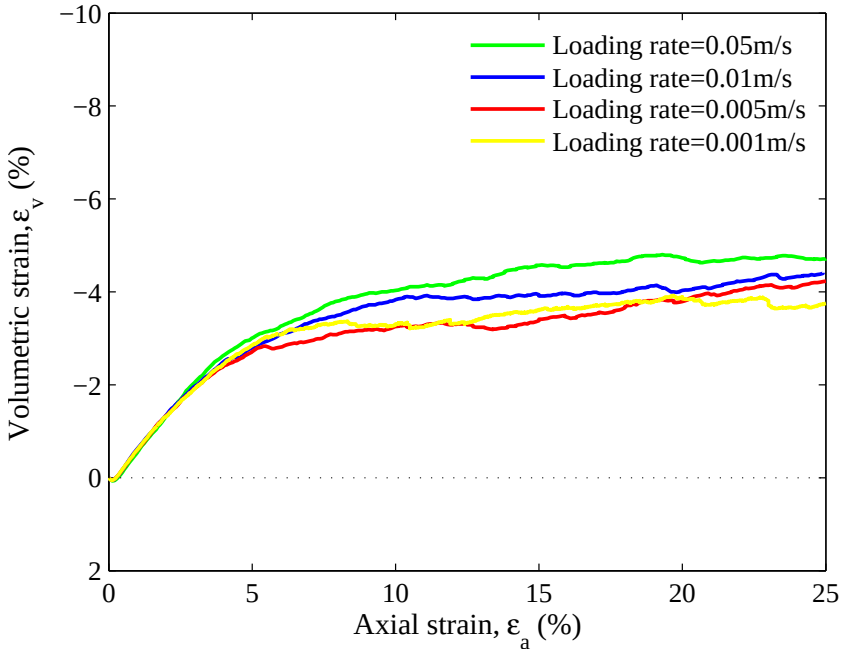

(b) Volumetric strain versus axial strain

Figure 3.12: The effect of loading rate on the mechanical behaviour of granular materials

3.4.1 Effect of particle stiffness

Particle stiffness is an important property to influence the Young's modulus (Itasca, 2004) and shear strength (Utili and Nova, 2008) of granular materials. With reference to the DEM biaxial test simulations of soil materials (e.g. Wang and Leung, 2008b; Jiang et al., 2011), the particle stiffness was generally set on the order of 1×10^8N/m. Consequently, in this subsection, the mechanical behaviour of the disc specimens is investigated in terms of different particle stiffnesses, from 5×10^7 to 5×10^8N/m, as listed in Table 3.4. The particle shear stiffness is set to be identical to the normal stiffness, which is ten times the wall stiffness to model the "soft" lateral boundaries. When the particle stiffness is assigned as 5×10^8N/m, the particle friction coefficient is taken as 0 during the consolidation process. After the target confining pressure of 100 kPa is achieved, the sample void ratio can be calculated as the initial one using Equations 3.48 and 3.59, namely 0.20. It is noted that the particle friction coefficients in consolidation can be set as 0.03 and 0.06 to obtain the same initial compaction (i.e. void ratio being 0.20) related to particle stiffnesses of 1×10^8 and 5×10^7N/m. As described in Subsection 3.3.4, the particle friction coefficient has an effect on the peak strength but not on the ultimate strength. In the present study, the particle friction coefficient is chosen to be 0.7 during the sample shearing.

Figure 3.13 shows the deviatoric stress and volumetric strain against axial strain for each sample comprising of discs with a certain particle stiffness. The initial stiffnesses (associated with Young's moduli) from the simulations in Figure 3.13a augment noticeably with the increase in the particle stiffness. There is a rapid increase in the peak strength when the particle stiffness rises from 5×10^7 to 1×10^8N/m. Nevertheless, a further increase from 1×10^8 to 5×10^8N/m has little effect on the peak strength. Similar results related to the effect of particle stiffness on shear strength in the DEM simulation can be found in Utili and Nova (2008). The ultimate strengths are quite similar, regardless of the particle stiffness. As shown in Figure 3.13b, during the shearing, the sample contracts at first and then dilates. The volumetric contraction becomes more and more inconspicuous with a rise in the particle stiffness. On the

other hand, there is an evident volumetric dilation due to increase in particle stiffness.

Particle type	Initial void ratio	Particle friction coefficient	Particle stiffness
Disc	0.20	0.7	5×10^7N/m
Disc	0.20	0.7	1×10^8N/m
Disc	0.20	0.7	5×10^8N/m

Table 3.4: The particle properties (after consolidation) and initial void ratios of the specimens for particle stiffness study

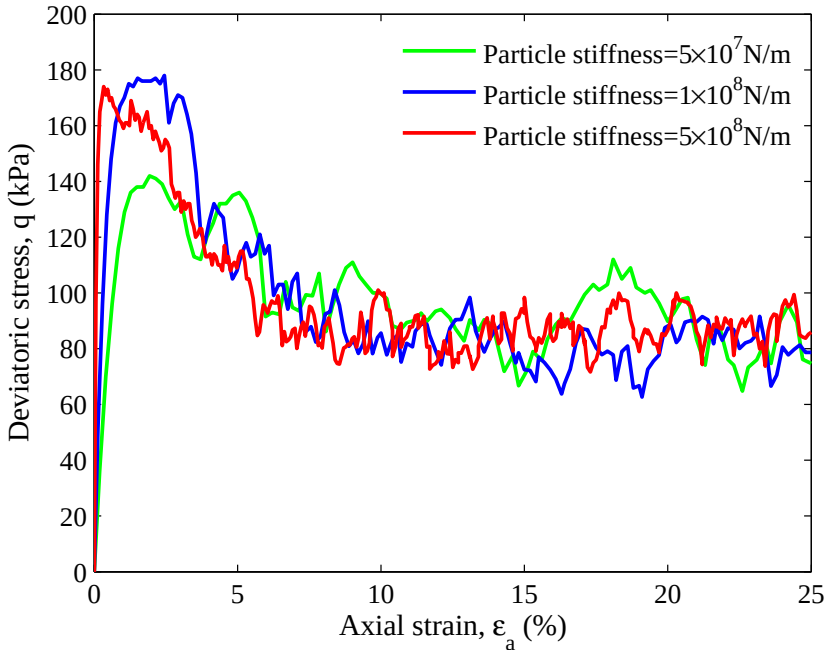

(a) Deviatoric stress versus axial strian

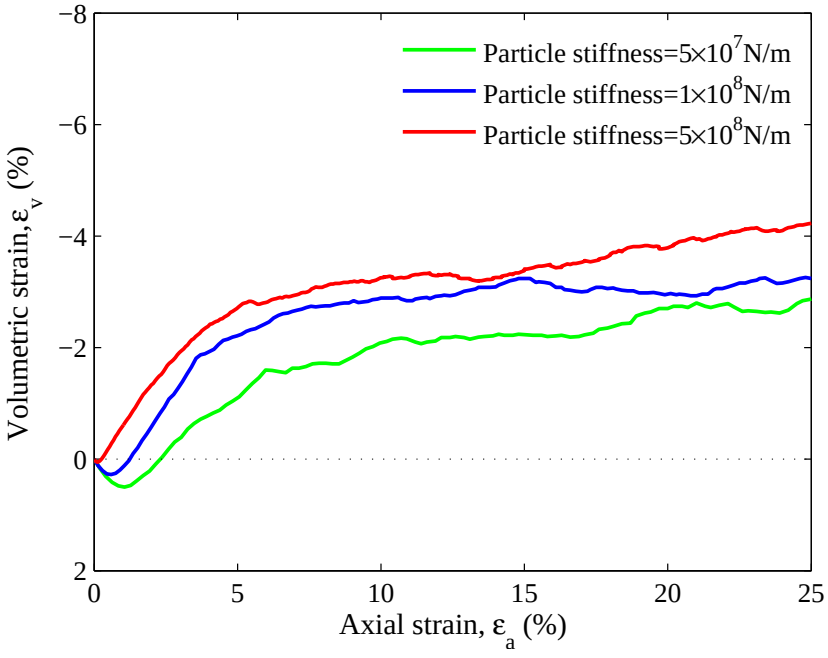

(b) Volumetric strain versus axial strain

Figure 3.13: The effect of particle stiffness on the mechanical behaviour of granular materials

3.4.2 Effect of interparticle friction

Interparticle friction plays an important role in the mechanical and deformation behaviour of a granular assembly (Geng, 2010). Biaxial test simulations in 2D were carried out on disc samples with particle friction coefficients of 0.5 and 0.9, as a supplement to the simulation test already reported. The particle normal and shear stiffnesses were both 5×10^8N/m. The consolidation process is identical to the modelling test on the sample with a particle friction coefficient of 0.7. During the consolidation, the particle friction coefficient is set as 0 and the sample void ratio is calculated as 0.20 when the desired confining pressure 100kPa is reached. After that, a particle friction coefficient of 0.5 or 0.9 is applied to the specimen particles for the sample loading. The particle parameters for sample shearing, as well as the initial void ratio of the samples, are listed in Table 3.5.

The interparticle friction has a significant effect on the peak strength, as well as the volumetric dilation but not the sample contraction, as plotted in Figure 3.14. The relationships between deviatoric stress and axial strain relating to different friction coefficients are illustrated in Figure 3.14a. There is no distinct effect of the particle friction coefficient on the initial stiffnesses of the curves, unlike the particle stiffness (shown in Figure 3.13a). The peak deviatoric stress increases significantly with the enlargement of the interparticle friction. However, the effect of interparticle friction on the ultimate strength is not significant. The results are in good agreement with previous studies (Geng, 2010). It is also noted that the deviatoric stresses reach a peak at a very small axial strain, probably owing to the high particle stiffness. During the loading, there is a volume contraction for the sample, followed by a gradual dilation (see Figure 3.14b). The sample contraction is quite insignificant, in comparison with the impending dilation. With a rise in the interparticle friction, there is a larger overall volume dilation at the end of the shear (consistent with the findings of Geng (2010)), indicating that more particle rotation restriction due to the larger interparticle friction could lead to greater overall volume dilation.

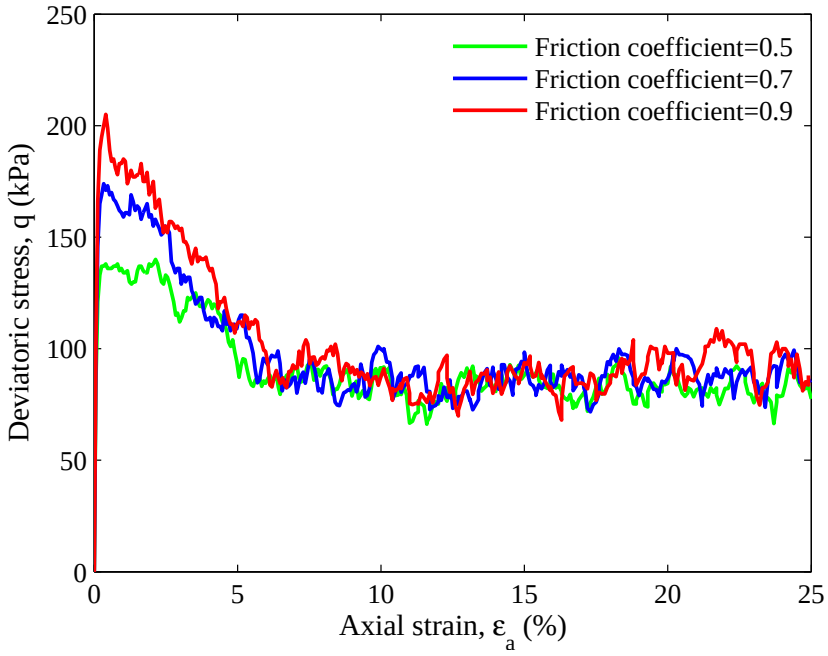

(a) Deviatoric stress versus axial strian

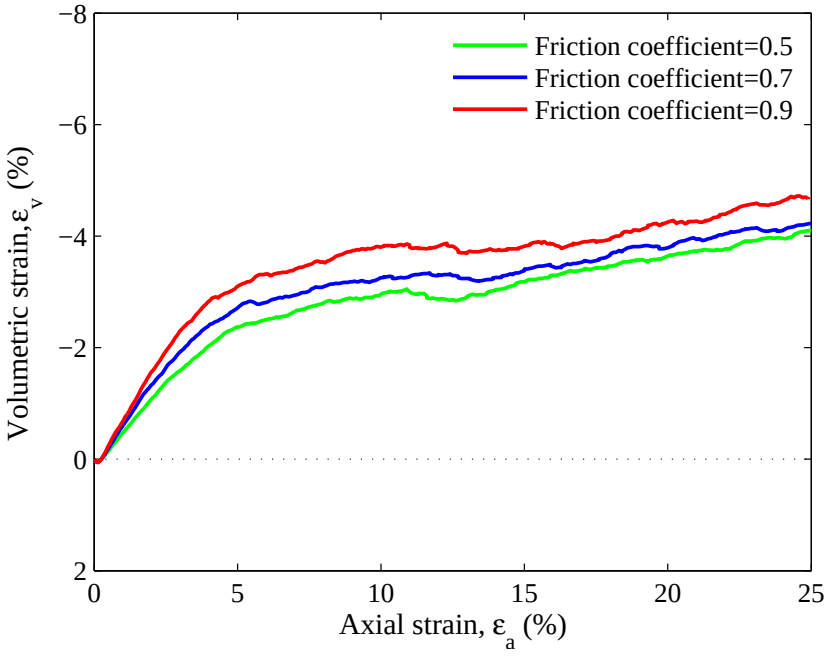

(b) Volumetric strain versus axial strain

Figure 3.14: The effect of interparticle friction on the mechanical behaviour of granular materials

Particle type	Initial void ratio	Particle friction coefficient	Particle stiffness
Disc	0.20	0.5	5×10^8N/m
Disc	0.20	0.7	5×10^8N/m
Disc	0.20	0.9	5×10^8N/m

Table 3.5: The particle properties (after consolidation) and initial void ratios of the specimens for interparticle friction study

3.4.3 Effect of particle shape

In the DEM simulations above, the particles are considered to be ideal discs, inconsistent with most real granular shapes, like sand. Generally, the actual particle is irregular and the intergranular interactions are complex. To study the influence of particle shape on the behaviour of granular materials, clumps are introduced in the DEM biaxial test simulations. Each clump is comprised of two discs with the same radius. The disc specimen is generated using the radius expansion method and then the discs are replaced by the two-disc clumps with an identical area. In this way, the particle fraction in the sample remains unchanged. The details with regard to the clump information and generation were illustrated in Subsection 3.3.3. As listed in Table 3.6, the particle stiffness is 5×10^8N/m and the friction coefficient is 0.7 during the shearing. The target confining pressure of the consolidation is 100kPa. Because the disc specimen has an initial void ratio of 0.20, different particle friction coefficients for the clump sample are assigned during the consolidation to achieve this value. It is found that a coefficient of 0.15 is required to make the clump sample have the same void ratio as that of the discs.

A comparison of the simulated results between the disc and clump samples is shown in Figure 3.15. Figure 3.15a illustrates the development of deviatoric stress against axial strain, while the relationship between volumetric strain and axial strain is plotted in Figure 3.15b. It is noted that the Young's modulus of the granular assembly is almost independent of the particle shape. With the irregular particle shape, the clump

sample presents a much larger peak and ultimate deviatoric stresses than the disc. This is probably because of the interlocking between particles and particle rotation restriction (Ting et al., 1995). After the peak point, there is a gradual reduction in strength for both of them, followed by a relatively steady state in the end. Compared to the clump particle, increasing the particle friction coefficient could only increase the peak strength but not the ultimate strength (see Figure 3.14a). At the initial stage of loading, the sample contracts slightly and then dilates significantly. It is indicated that the irregular particle shape could produce much greater overall volume dilation, just like an increase in the interparticle friction (shown in Figure 3.14b). This is possibly due to the particle rotation restriction as well. During the shearing, the shear band arises. If the particle rotation is restrained to some extent, the mutual filling among particles in the shear band, resulting in volume contraction, would be hindered.

Particle type	Initial void ratio	Particle friction coefficient	Particle stiffness
Disc	0.20	0.7	5×10^8N/m
Clump	0.20	0.7	5×10^8N/m

Table 3.6: The particle properties (after consolidation) and initial void ratios of the specimens for particle shape study

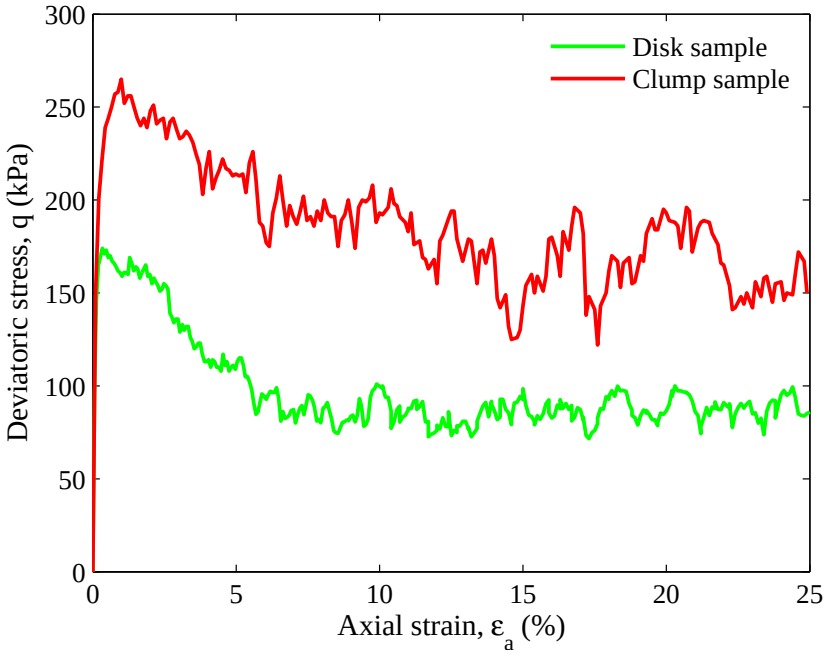

(a) Deviatoric stress versus axial strian

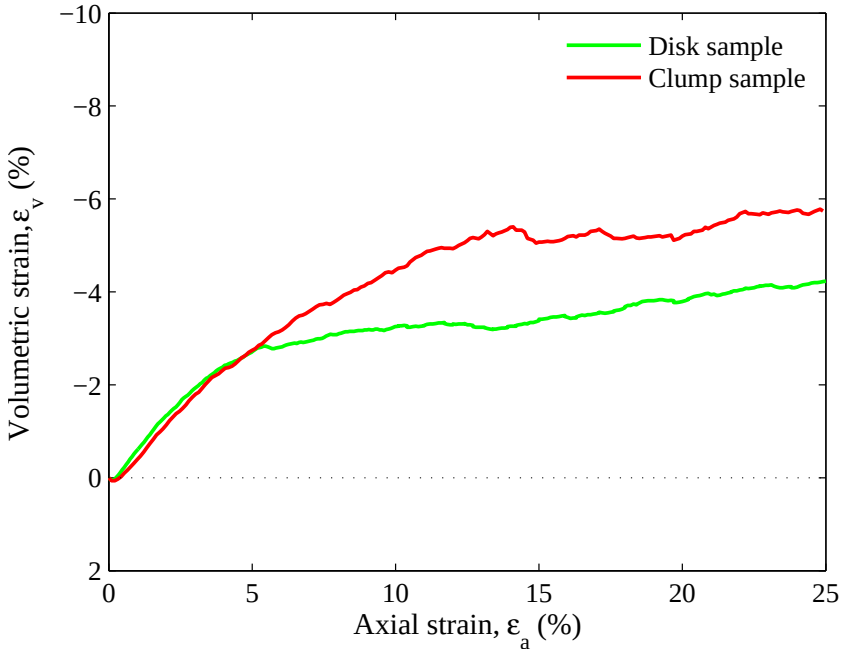

(b) Volumetric strain versus axial strain

Figure 3.15: The effect of particle shape on the mechanical behaviour of granular materials

3.4.4 Effect of initial sample void ratio

The initial compaction is of great significance to the mechanical behaviour of granular materials. In this subsection, different values of initial void ratios are investigated, which are 0.23 (denoted as a medium sample) and 0.26 (indicated as a loose sample), to complement the simulation of a void ratio of 0.20 (i.e. dense sample), already presented. It is identical for the generation of the samples with the same compaction state. The radius expansion method is used and approximately 3200 disc particles are generated in the specimens having a porosity of 0.30. At this stage, it can be ensured that no contact force occurs between particles or between particle and wall. The particle normal and shear stiffnesses are 5×10^8N/m and the target confining pressure is 100kPa before the shearing. It is noted that, when the friction coefficients are set as 0.15 and 0.7, the initial void ratios of the samples are computed as 0.23 and 0.26 respectively. After the consolidation, the friction coefficient is changed to 0.7 on the particles of all the samples. The particle properties (after consolidation) and initial condition of the specimens are listed in Table 3.7.

The results (shown in Figure 3.16) indicate that the initial void ratio has a significant effect on the peak deviatoric stress and volume deformation, but not the ultimate strength. As shown in Figure 3.16a, for the loose sample, there is a gradual increase in the strength until a relatively stable state is reached. The strengths related to the medium and dense samples rise to a peak rapidly in the beginning and then progressively reduce to a steady state. Note that the peak point of the dense sample is larger and more notable than that of the medium sample. On the other hand, the initial void ratio has little effect on the ultimate strength. The influence of the initial void ratio on the relationship of volumetric strain-axial strain is plotted in Figure 3.16b. For the loose sample, the volume contracts without any dilation during the entire shearing. In contrast, there is only a small contraction for the denser samples (i.e. medium and dense samples) and, later, the volume dilates significantly. With the reduction in the sample void ratio, the dilation of the volume becomes more and more distinct. The results related to the development of deviatoric stress and volumetric strain versus axial

strain agree well with the preceding findings (Geng, 2010).

Particle type	Initial void ratio	Particle friction coefficient	Particle stiffness
Disc	0.20	0.7	5×10^8N/m
Disc	0.23	0.7	5×10^8N/m
Disc	0.26	0.7	5×10^8N/m

Table 3.7: The particle properties (after consolidation) and initial void ratios of the specimens for sample compaction study

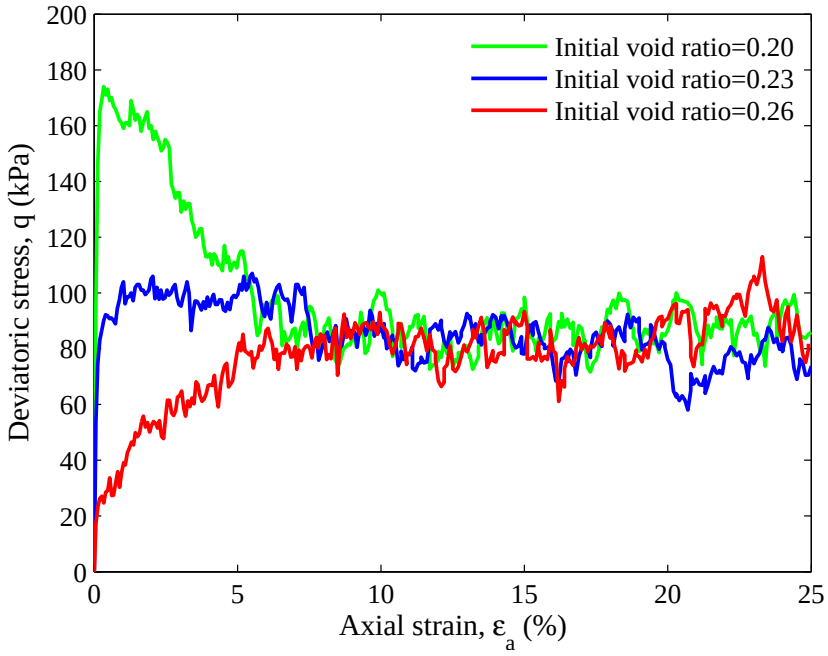

(a) Deviatoric stress versus axial strian

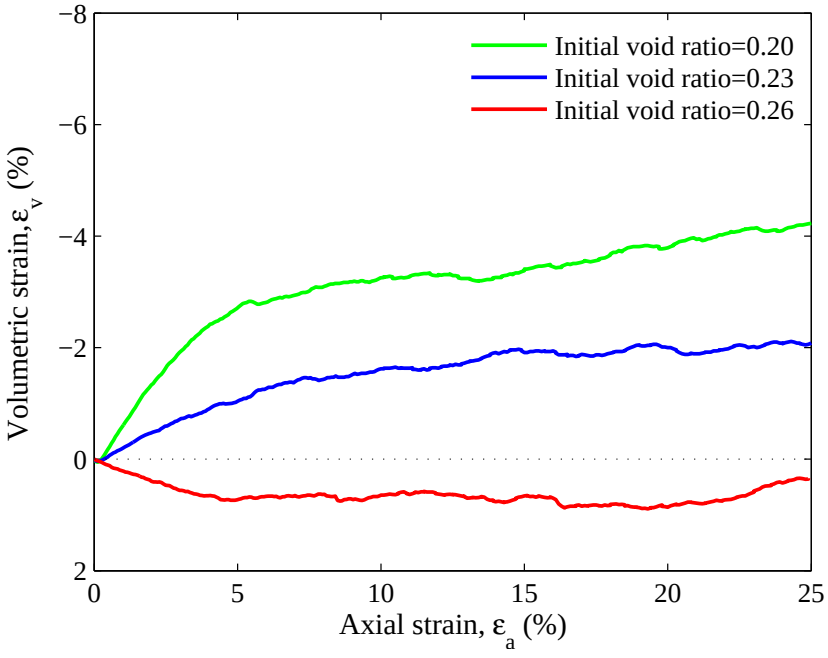

(b) Volumetric strain versus axial strain

Figure 3.16: The effect of initial void ratio on the mechanical behaviour of granular materials

3.4.5 Effect of confining pressure

The simulations described in this subsection involve numerical biaxial tests under different confining pressures of 100, 500 and 1000kPa respectively. The samples are comprised of nearly 3200 disc particles with normal and shear stiffnesses of 5×10^8N/m. During the consolidation, the particle friction coefficient is set as 0 to obtain a dense sample. The servo control is used to achieve different confining pressures by controlling the translational displacements of the lateral walls. After the consolidation, the particles of the samples are assigned a friction coefficient of 0.7. What is more, the confining pressure is kept constant during the sample shearing. The particle parameters (after consolidation) and initial consolidation conditions of the samples can be found in Table 3.8.

The effects of confining pressure on mechanical behaviour are plotted in Figure 3.17. All the deviatoric stress-axial strain curves (as shown in Figure 3.17a) have four strength stages, which are linear increase of the stress, peak strength stage, progressive strength reduction and relatively steady stage respectively. The peak strengths are reached at a small axial strain. When the confining pressure is increased from 100 to 1000kPa, there is a large augmentation for not only the peak strength but also the ultimate strength, in good agreement with the results of Sitharam (1999). Figure 3.17b shows the relationship of volumetric strain to axial strain. An initial volume compression can be found in all the curves and, later, the samples start to dilate. Under high confining pressure i.e. 1000kPa, the contraction behaviour is more notable than the others and the overall volumetric contraction develops, accompanied by the largest range of axial strain. Also, with an increase in the confining pressure, the global volume dilation gradually decreases. Similar results relating to the volumetric strain are published for the experimental tests conducted by Yamamuro and Lade (1996) and for the DEM simulations by Sitharam (1999).

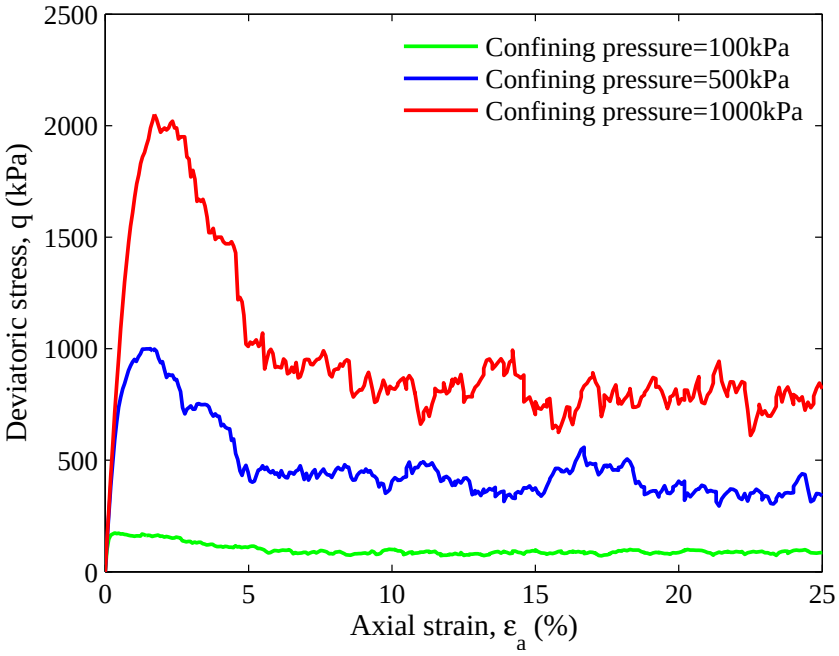

(a) Deviatoric stress versus axial strian

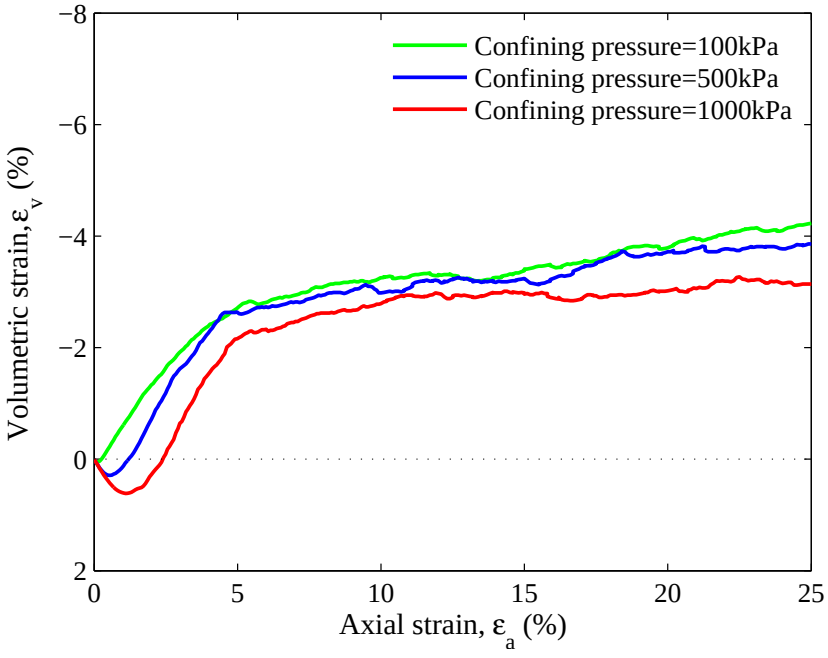

(b) Volumetric strain versus axial strain

Figure 3.17: The effect of confining pressure on the mechanical behaviour of granular materials

Particle type	Particle friction coefficient	Confining pressure	Particle stiffness
Disc	0.7	100 kPa	5×10^8N/m
Disc	0.7	500 kPa	5×10^8N/m
Disc	0.7	1000 kPa	5×10^8N/m

Table 3.8: The particle properties (after consolidation) and consolidation conditions of the specimens for confining pressure study

3.5 Summary

In this chapter, the mechanical responses and deformation characteristics of granular materials have been investigated on the basis of numerical simulation of DEM biaxial tests. The software of PFC^{2D} is used and its basic assumptions, principle theory, and general functions are introduced at the beginning. Later, the simulation procedure of the biaxial test is presented and the behaviour of a cohesionless granular assembly under monotonic loading is studied. During the compression tests, the typical stress-strain responses under constant confining pressure have four stages, i.e. linear increase in the stress, peak stress stage, progressive reduction and a comparatively stable state. The results compare well with the experimental test results in qualitative terms, especially for the samples composed of two-disc clumps. Moreover, it is found that the particle parameters have a great effect on the behaviour of the granular medium.

A series of influencing factors on the responses of granular materials have been investigated using biaxial test simulation. The factors include particle stiffness, interparticle friction, particle shape, initial void ratio of the sample, and the confining pressure. The Young's modulus is greatly influenced by the particle stiffness. In a certain range, particle stiffness also has an effect on peak strength but not ultimate strength. Similarly, with augmentation of the interparticle friction, the peak deviatoric stress increases. Moreover, particle shape and confining pressure affect not only peak strength but also ultimate strength. When the initial void ratio is enlarged sufficiently, an ultimate strength, instead of a peak one, is reached after a progressive increase.

The deformation behaviour of the granular assemblies is influenced by these factors as well. Generally, the sample volume experiences a small contraction at the beginning and then starts to dilate significantly. However, for the loose sample, the volume continues contracting until a stable global contraction is attained. As discussed above, DEM is a useful tool to simulate the biaxial test and the variation pattern of granular material properties such as Young's modulus, the peak and ultimate friction angles can also be obtained.

Chapter 4

DEM Biaxial Test Simulation for Bonded Materials

4.1 Introduction

In this chapter, the parallel bond (i.e. an application module in PFC^{2D}) is introduced in the biaxial test simulation of bonded materials. The details related to parallel bond are illustrated, including the force and moment on it and bond deformability. Later, a comparison between simulated and experimental relationships of deviatoric stress to axial strain is made as a validation of the DEM procedure. The effect of bond radius on the behaviour of granular materials is first studied. With increasing the bond radius, besides a significant growth in peak shear strength, the sample contraction and dilation become more and more evident in the shearing simulation. Also, the bond number for breakage shows significant difference during the loading when the bond radius is changed. The investigation of bond strength distribution is carried out in terms of uniform, normal and Weibull distributions. Finally, uniform bond strength and standard bond radius are introduced for subsequent simulations. Three kinds of bond strength will be used, which are 100, 300 and 500kPa. The particle friction coefficients are 0.3, 0.5 and 0.7. The simulation tests are carried out under confining pressures

of 50, 80 and 100kPa respectively. The strength parameters such as cohesion and friction angle are studied in terms of different bond strengths and sample compaction states. In addition, besides the stress-dilatancy response and bond breakage, the elastic parameters and yield stress are investigated.

4.2 The parallel-bond model in PFC^{2D}

The parallel-bond model is employed to simulate the mechanical behaviour of a piece of cementitious material of limited size, lying between two discs (Itasca, 2004). An elastic relationship between the discs is constructed by these bonds, which act in a way that is parallel with the slip model (see Subsection 3.2.3). The possibility of slippage is not eliminated, due to the existence of a parallel bond where both forces and moments are allowed to occur. A parallel bond can be regarded as a set of elastic springs with constant normal and shear stiffnesses. They are uniformly distributed over a rectangular cross-section located on the contact plane with the centre at the contact point of two particles, as shown in Figure 4.1, where the thickness of disc is set at t. Point-contact springs can also be applied to the model particle stiffness at the contact point. These two kinds of springs act in parallel with one another. Because of the parallel bond stiffnesses, a force and a moment can be caused by the relative motion at the contact. The maximum normal and shear stresses within the bond material can be calculated at the bond periphery. When either of the maximum stresses exceeds the corresponding bond strength, the parallel bond breaks. There are five parameters used in this kind of bond model, i.e. normal and shear stiffness, $\bar{k}^n$ and $\bar{k}^s$ [stress/displacement]; normal and shear strength, $\bar{\sigma}_c$ and $\bar{\tau}_c$ [stress]; and bond radius, $\bar{R}$.

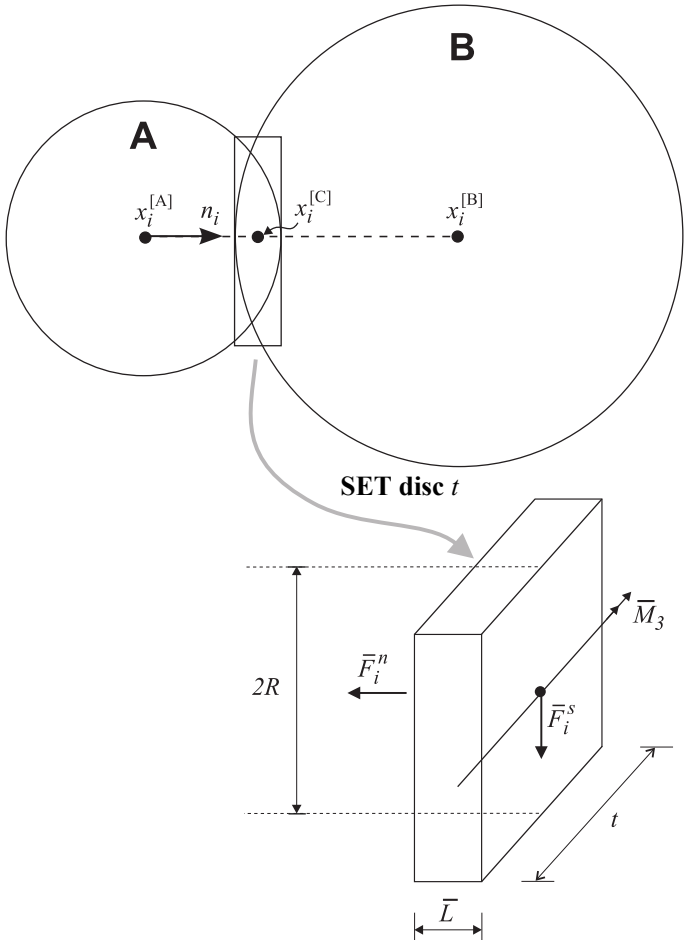

Figure 4.1: Parallel bond depicted as a cuboid of cementatious material in PFC^{2D} (Itasca, 2004)

4.2.1 Force and moment

The resultant force and moment within the parallel bond are described as $\bar{F}_i$ and $\bar{M}_3$. The force vector can be divided into normal and shear components by

$$\bar{F}_i = \bar{F}_i^n + \bar{F}_i^s \tag{4.1}$$

where $\bar{F}_i^n$ and $\bar{F}_i^s$ denote the normal and shear component vectors, respectively. These vectors and the moment vector are shown in Figure 4.1. The component vector of normal force can be described as

$$\bar{F}_i^n = (\bar{F}_j n_j) n_i = \bar{F}^n n_i \tag{4.2}$$

The initial values of $\bar{F}_i$ and $\bar{M}_3$ are set at zero when a parallel bond is formed. An elastic force and moment increment induced by the relative displacement and rotation

increment at the contacts are then added in timestep increment. The elastic normal and shear force increments, $\Delta\bar{F}_i^n$ and $\Delta\bar{F}_i^s$ at one timestep Δt are computed as

$$\begin{aligned} \Delta\bar{F}_i^n &= \left(-\bar{k}^n A \Delta U^n\right) n_i \\ \Delta\bar{F}_i^s &= -\bar{k}^s A \Delta U_i^s \end{aligned} \tag{4.3}$$

where A is the area of parallel bond cross-section, i.e. $A = 2\bar{R}t$ and the relative displacement increment ΔU_i can be expressed by the contact velocity V_i and the timestep as $\Delta U_i = V_i \Delta t$. The elastic increment of moment can be calculated as

$$\Delta\bar{M}_3 = -\bar{k}^n I \Delta\theta_3 \tag{4.4}$$

where the relative rotation increment $\Delta\theta_3$ is a function of the relative rotational velocities of particle (A) and (B), i.e. $\Delta\theta_3 = \left(\omega_3^{[B]} - \omega_3^{[A]}\right)\Delta t$, and I is the inertia moment of the bond cross-section related to an axis through the contact point and in the direction of $\Delta\theta_3$, which can be calculated as $I = \frac{2}{3}t\bar{R}^3$.

The new force and moment vectors acting on the parallel bond can be calculated via the summation between the previous values at the beginning of the timestep and the elastic force and moment increment vectors as

$$\begin{aligned} \bar{F}_i^n &\leftarrow \bar{F}^n n_i + \Delta\bar{F}_i^n \\ \bar{F}_i^s &\leftarrow \bar{F}_i^s + \Delta\bar{F}_i^s \\ \bar{M}_3 &\leftarrow \bar{M}_3 + \Delta\bar{M}_3 \end{aligned} \tag{4.5}$$

According to beam theory, the maximum tensile and shear stresses existing on the bond periphery are expressed as

$$\begin{aligned} \sigma_{max} &= \frac{-\bar{F}^n}{A} + \frac{\left|\bar{M}_3\right|}{I}\bar{R} \\ \tau_{max} &= \frac{\left|\bar{F}_i^s\right|}{A} \end{aligned} \tag{4.6}$$

When the maximum tensile or shear stress exceeds the corresponding strength, i.e. $\sigma_{max} \geq \bar{\sigma}_c$ or $\tau_{max} \geq \bar{\tau}_c$, the parallel bond breaks.

If the bond stays undamaged, the contribution of the final force and moment vectors to

the total force and moment on each of the two particles can be obtained as

$$\begin{aligned} F_i^{[A]} &\leftarrow F_i^{[A]} - \bar{F}_i \\ F_i^{[B]} &\leftarrow F_i^{[B]} + \bar{F}_i \\ M_3^{[A]} &\leftarrow M_3^{[A]} - e_{3jk}\left(x_j^{[C]} - x_j^{[A]}\right)\bar{F}_k - \bar{M}_3 \\ M_3^{[B]} &\leftarrow M_3^{[B]} + e_{3jk}\left(x_j^{[C]} - x_j^{[B]}\right)\bar{F}_k + \bar{M}_3 \end{aligned} \tag{4.7}$$

where $F_i^{[\Omega]}$ and $M_3^{[\Omega]}$ are the force and moment sums for particle (Ω), and $\bar{F}_i$ can be computed by Equation 4.1.

4.2.2 Parallel-bond deformability

The contact behaviour between two particles could be designated as an elastic beam with its two ends at the particle centres (Itasca, 2004). The loads, including the corresponding force and moment vectors acting at the individual particle centre, are applied to the beam. If two particles (A) and (B) make contact with each other, the beam radius could be described as

$$\widetilde{R} = \frac{R^{[A]} + R^{[B]}}{2} \tag{4.8}$$

and the beam length could be expressed as

$$L = 2\widetilde{R} = R^{[A]} + R^{[B]} \tag{4.9}$$

The beam cross-sectional area A and moment of inertia I could be expressed as

$$\begin{aligned} A &= 2\widetilde{R}t \\ I &= \frac{t\left(2\widetilde{R}\right)^3}{12} \end{aligned} \tag{4.10}$$

where t is the thickness of the cylindrical particle. The contact normal and shear stiffnesses can be calculated as (McGuire and Gallagher, 1979)

$$\begin{aligned} k^n &= \frac{AE_c}{L} \\ k^s &= \frac{12IE_c}{L^3} \end{aligned} \tag{4.11}$$

where E_c is the contact Young's modulus. Based on Equations 3.3 and 3.4, if the two particles (A) and (B) have the same normal and shear stiffnesses, k_n and k_s

$$\begin{aligned} k^n &= \frac{k_n}{2} \\ k^s &= \frac{k_s}{2} \end{aligned} \tag{4.12}$$

where the particle normal stiffness $k_n = k_n^{[A]} = k_n^{[B]}$ and shear stiffness $k_s = k_s^{[A]} = k_s^{[B]}$. The relation between these stiffnesses and the contact modulus can be obtained by substituting Equations 4.9, 4.10, and 4.12 into Equation 4.11

$$k_n = k_s = 2E_c t \tag{4.13}$$

denoting that the particle stiffness is independent of the particle radius and directly proportional to the contact Young's modulus.

As shown in Figure 4.1, the value of parallel-bond radius $\bar{R}$ can be assigned in PFC^{2D} via a radius multiplier $\bar{\lambda}$ times the minimum radius of two bonded particles (A) and (B)

$$\bar{R} = \bar{\lambda} \min\left(R^{[A]}, R^{[B]}\right) \tag{4.14}$$

The cross-sectional area $\bar{A}$ and inertia moment $\bar{I}$ for the parallel bond could be expressed as

$$\begin{aligned} \bar{A} &= 2\bar{R}t \\ \bar{I} &= \frac{t\left(2\bar{R}\right)^3}{12} \end{aligned} \tag{4.15}$$

Like a contact between two particles, the behaviour of the parallel-bond springs can be regarded as a beam with a height of $2\bar{R}$. The parallel-bond normal and shear stiffnesses, $\bar{k}^n$ and $\bar{k}^s$ are expressed in units of stiffness per unit area in PFC^{2D}, which can be obtained by dividing the stiffnesses of Equation 4.11 with the parallel-bond cross-sectional area $\bar{A}$

$$\begin{aligned} \bar{k}^n &= \frac{\widetilde{k}^n}{\bar{A}} = \frac{\bar{A}\bar{E}_c}{\bar{A}L} = \frac{\bar{E}_c}{L} \\ \bar{k}^s &= \frac{\widetilde{k}^s}{\bar{A}} = \frac{12\bar{I}\bar{E}_c}{\bar{A}L^3} \end{aligned} \tag{4.16}$$

where $\widetilde{k}^n$ and $\widetilde{k}^s$ are applied to the parallel bond, and used to make a difference from the corresponding stiffnesses of the particle contact, i.e. k^n and k^s in Equation 4.11, and $\bar{E}_c$ is the Young's modulus of the parallel-bond material. The relation of the stiffnesses to Young's modulus $\bar{E}_c$ can be obtained by the substitution of Equations 4.9 and 4.15 into Equation 4.16 as

$$\begin{aligned} \bar{k}^n &= \frac{\bar{E}_c}{L} \\ \bar{k}^s &= \frac{\bar{E}_c \bar{R}^2}{L\widetilde{R}^2} \end{aligned} \tag{4.17}$$

4.3 Procedure validation

4.3.1 Introduction

There are a lot of laboratory data published on naturally and artificially cemented soils (e.g. Airey, 1993; Marri, 2010). The nature of cementing agents and cement content are of significant importance to the behaviour of cemented soils. As highlighted by De Bono (2013), there have been studies on cemented soils with varied cementing agents, which are Portland cement (e.g. Marri, 2010; Schnaid et al., 2001; Wang and Leung, 2008a,b); gypsum (e.g. Huang and Airey, 1998; Wang and Leung, 2008b); lime or calcite (e.g Asghari et al., 2003; Ismail et al., 2002); and carbonates (e.g. Airey, 1993; Lagioia and Nova, 1995). Also, the effect of cement type on the behaviour of cemented materials has been studied by Ismail et al. (2002), Wang and Leung (2008b) and so on. The relationship between cement content and cohesion or friction angle has also been studied. According to Schnaid et al. (2001), there is an approximately linear increase in the cohesion of cemented sand with cement content. Nevertheless, as observed by Abdulla and Kiousis (1997) and Schnaid et al. (2001), the variation in cohesion with cement content is non-linear. The rate of increase of cohesion gradually increases with the cement content for the cemented sand. On the other hand, a specific correlation of cement content and friction angle is hard to determine (Schnaid et al., 2001). Some investigation work shows that the friction angle stays at the same

magnitude for both cemented and uncemented materials (Clough et al., 1989; Dupas and Pecker, 1979; Juran and Riccobono, 1991). However, some investigators (e.g. Schnaid et al., 2001; Wang and Leung, 2008a) have noted that a slight increase in friction angle with cement content could be observed. In contrast, some published data (e.g. Marri, 2010) has demonstrated that friction angles mildly decrease as the cement content increases.

In PFC simulations, contact bonds (e.g. Jiang et al., 2011) or parallel bonds (e.g. Camusso and Barla, 2009; Cheung and O'Sullivan, 2008) are added to the contacts between unbound particles to model the behaviour of cemented soils. The calibration work of micro-parameters for loose cemented soil has been investigated using biaxial tests by Camusso and Barla (2009). Moreover, the strain localization generated in cemented specimens was studied by Cheung and O'Sullivan (2008) and Jiang et al. (2011). It is noted that Wang and Leung (2008a,b) introduced small cementing particles to simulate the interactions between the cementing agents and the soil grains. In this way, the amount of cement content can be controlled in DEM simulation like the physical test. There have been investigations associated with the bond strength distribution in simulating the behaviour of cemented materials (e.g. De Bono, 2013; Yoon, 2007). A normal distribution of contact-bond strength is applied to obtain an optimum set of micro-parameters for modelling the physical specimen in uniaxial compression tests (Yoon, 2007). Various strength distributions of parallel bond were compared by De Bono (2013), including uniform, normal and Weibull distributions, all with the same mean value of bond strength. It was concluded that the Weibull distributions have an opportunity to yield a rounded peak strength, most similar to the stress-strain curves in experimental tests (see Marri, 2010).

According to the literature, there is a lack of systemic investigation into the mechanical behaviour of bonded materials by means of DEM. In this study, the effect of parallel-bond diameter and bond strength distribution on the response of granular materials is studied first. After that, a standard bond size and uniform bond strength is applied to a series of biaxial test simulations. The elastic parameters (i.e. Young's modulus and Poisson's ratio), primary yield stress, shear strength (i.e. friction angle and cohesion),

bond breakage and shear-dilatancy response are included in the study where sample compaction, particle friction, parallel bond strength, and confining pressure are taken into account. In addition, the correlation between bond breakage and shear dilatancy is elaborated.

4.3.2 Experimental details

Wang and Leung (2008a,b) performed drained triaxial compression tests on artificially cemented sands. Portland cement and Ottawa 20-30 sand were selected as the basic materials of cemented sands. Because the grains in Ottawa 20-30 sand were uniformly graded in size and had approximately rounded shape, they were easily modelled in DEM simulations. The grain was quartz and its size was within a range of 0.3 to 1.18mm. The specific gravity of the particle was 2.65. Cement slurry was first produced by mixing Portland cement with water at a ratio of 1:1 by weight. The artificially cemented sands were a mixture of cement slurry and Ottawa sand particles. As proposed by Ladd (1978), the mixture was compacted in 10 layers into a cylindrical sample mold to guarantee homogeneity of the specimen. The height of the specimen was 140mm and the diameter 70mm. The cement content could be calculated as the ratio of the Portland cement weight to the dry weight of the sand grains. In these experimental tests, a cement content of 3% was selected.

A CKC triaxial system (Li et al., 1988) was used in the triaxial compression tests under drained conditions. The end platens were lubricated to decrease the end effect due to friction between the specimen and the end platen. The specimen was saturated by the circulation of the deaired water under a small pressure difference of 5 to 10kPa. After that back pressure was employed to ensure the saturation of the specimen. In order to prevent significant bond breakage during consolidation and to enhance the cementation effect, three kinds of low confining pressure were applied to consolidate the cemented samples, i.e. 50, 80 and 100kPa. An axial-strain rate of 6%/h was applied for shearing. The experimental results associated with the relationship of the deviatoric stress to axial strain are plotted in Figure 4.3.

4.3.3 Details of numerical simulations

As in the simulation tests of unbonded materials in Chapter 3, a rectangle vessel with two horizontal and vertical walls is prepared, where the discs are generated by means of the radius expansion method (see Subsection 3.3.3). The wall acting as the specimen boundary is massless and rigid. The simulated sample with a height of 0.14m and a width of 0.07m has the same dimensions as the experimental one (Wang and Leung, 2008a,b). The porosity of the initially generated specimen is selected as 0.30. For the purpose of reducing the particle number, the particle diameters are scaled up 2.4 times the real grain size and uniformly graded within a range of 0.72 to 2.832mm. In this way, approximately 2800 particles are filled into the rectangular vessel. According to the work of Wang and Leung (2008a,b), the particle normal and shear stiffnesses k_n and k_s are suggested as 5×10^7N/m for quartz sand in DEM biaxial test simulations. An identical value has been used in this research. The stiffness of the lateral walls is one-tenth of that of the particle to simulate the "soft" lateral confinement in experimental tests. The top and bottom walls, acting as the loading boundaries, possess the same stiffness as the particles. The specific gravity of the particles is set at 2.65, identical to the real quartz sand. The unit thickness (i.e. 1.0m) is set for the particles. In addition, the particle friction coefficient is 0.5 during the sample generation and there is no friction between the wall and particle to prevent the arching effect of the end boundaries.

Parallel bonds can only be created at all real contacts (with nonzero overlap) and some eligible virtual contacts (Itasca, 2004). The virtual contacts are those where the intervals between two discs are less than 10^{-6} times the average radius of the two discs. So in order to install the parallel bonds in the biaxial test assembly, there should be enough real and virtual contacts generated between the discs. After specimen generation, a low isotropically compressive stress σ_{ic} (e.g. Camusso and Barla, 2009; Potyondy and Cundall, 2004) or a low vertical consolidation stress σ_{vc} (e.g. Jiang et al., 2011) within the sample needs to be achieved to create the contacts for parallel-bond installation. The reason for using small σ_{ic} or σ_{vc} is to reduce the locked-in stresses

developing after the subsequent bond-installation. In current research, prior to bond-installation, the sample is first isotropically consolidated to a relatively low confining pressure state, i.e. σ_0 = 0.5kPa (1% of the lowest confining pressure 50kPa) via the servo-control demonstrated in Subsection 3.3.3. The particle friction coefficient 0.5 remains unchanged during the entire consolidation and shearing process. The void ratio is calculated as 0.25, regarded as the initial one when the first target confining pressure of 0.5kPa is reached. After that, the parallel bonds are generated at all the particle-to-particle contacts. Note that a parallel bond can not be installed at the contact between the wall and the particle (Itasca, 2004). Five parameters need to be determined for parallel bonds, including parallel-bond normal stiffness $\bar{k}^n$, shear stiffness $\bar{k}^s$, normal strength $\bar{\sigma}_c$, shear strength $\bar{\tau}_c$ and radius multiplier $\bar{\lambda}$.

In PFC^{2D}, the value of parallel-bond radius $\bar{R}$ can be assigned by a radius multiplier $\bar{\lambda}$ using Equation 4.14. As demonstrated in Subsection 4.2.2, the behaviour of a contact between two particles can be treated as an elastic beam with its end at the particle centres. The beam cross-sectional area A can be obtained via Equation 4.10. In order to simplify the analysis, the radius of parallel bond $\bar{R}$ can be set to be equal to the beam radius $\widetilde{R}$ at the corresponding contact. So the cross-sectional area of the parallel bond $\bar{A}$ (see Equation 4.15) is equal to the beam A. Let $\widetilde{k}^n$ (see Equation 4.16) be equal to the normal stiffness k^n of the corresponding contact between particles, aiming to reduce the variable number. Hence, according to Equation 4.16, the normal stiffness of parallel bond $\bar{k}^n$ (in terms of stress/displacement) is defined to give a value equal to the ratio of the corresponding contact normal stiffness k^n (in terms of force/displacement) to the cross-sectional area of the parallel bond. Like the particle stiffness, the ratio of parallel-bond normal to shear stiffness is set at 1.0. All parallel-bond normal and shear strengths are set at 100kPa, which proves to be suitable by qualitative comparison with the experimental results (see Figures 4.3 and 4.4 in Subsection 4.3.4). When the maximum tensile or shear stress existing within the parallel bond exceeds this value, then the bond breaks. The biaxial sample properties are summarised in Table 4.1.

After the bond installation, the specimen continues to be consolidated to the second target confining pressure, i.e. 50, 80 or 100kPa. Finally, the bonded sample is sheared

by moving the top and bottom walls with a constant rate. Four loading velocities, which are 0.001, 0.005, 0.01 and 0.05m/s, were tried in order to determine a reasonable rate. The relationship of deviatioric stress q to axial strain ε_a with regard to various loading rates is plotted in Figure 4.2. This indicates that, when the rate is larger than 0.01m/s (i.e. 0.05m/s), the peak and ultimate strengths increase significantly because of the dynamic response. The quasi-static behaviour can be observed by reducing the rate to less than or equal to 0.01m/s. A loading velocity of 0.005m/s is applied to the remaining biaxial test simulations of bonded materials in this chapter.

Biaxial sample properties	
Size: height $\times$ width (m)	0.14×0.07
No. of particles	almost 2800
Initial void ratio	0.25
Particle radius (mm)	0.72-2.832
Particle friction coefficient	0.5
Specific gravity of particle	2.65
Normal stiffness of particle (N/m)	5×10^7
Shear stiffness of particle (N/m)	5×10^7
Wall friction coefficient	0
Normal stiffness of wall (N/m)	5×10^6
Shear stiffness of wall (N/m)	5×10^6
Parallel-bond normal strength (kPa)	100
Parallel-bond shear strength (kPa)	100

Table 4.1: Summary of DEM properties of the biaxial sample

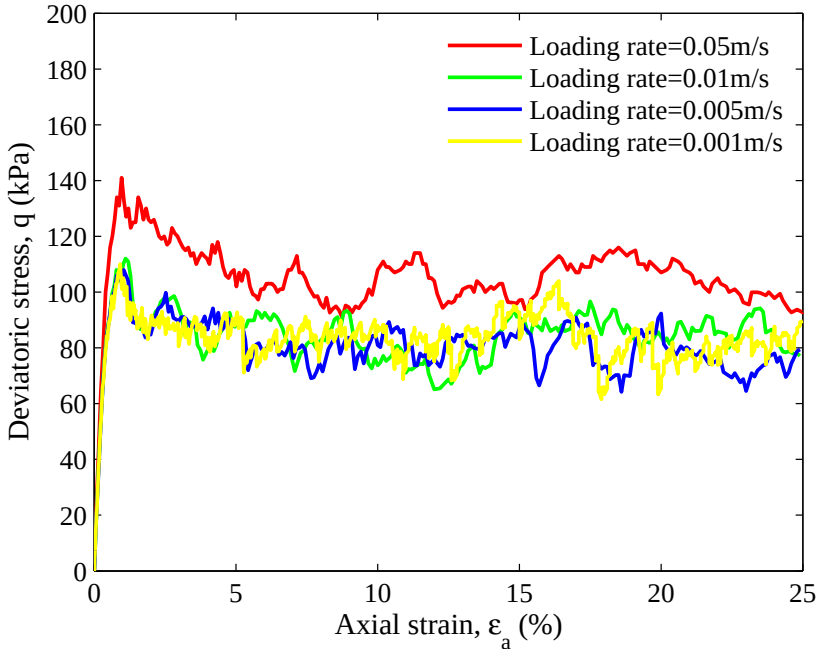

Figure 4.2: The stress-strain response for DEM biaxial test simulations with regard to various loading velocities

4.3.4 Result comparison

The stress-strain responses for Portland cement sand under various confining pressures are plotted in Figure 4.3 (Wang and Leung, 2008a). As in the biaxial results of unbonded samples, four strength stages appear during the shearing, i.e. linear increase of strength, peak stage, progressive strength reduction and a relatively steady state (i.e. confining pressure of 50kPa). Both peak and ultimate strengths are quite sensitive to the confining pressure. When increasing the lateral pressure from 50, then 80 to 100kPa, there is a notable increase in these two strengths as well as a less distinct peak strength. When the axial strain approaches 25%, the ultimate strengths with constant lateral stresses of 80 and 100kPa do not reach a steady state. Compared to the sample strength, the initial stiffness of the stress-strain curve is relatively insensitive to the lateral stress.

The DEM biaxial test simulations for mechanical responses of the bonded sample are shown in Figure 4.4. Similar to the experimental results, the four stages of stress de-

velopment are well modelled. However, unlike the laboratory tests, the ultimate steady states are attained regardless of the lateral stress, possibly owing to the brittle characteristic produced by the simulated bonds. The confining pressure is of great importance to the simulated peak and ultimate strengths. In comparison with the experimental results, both simulated peak and ultimate strengths are much lower, indicating that the simulated bond strength is smaller than the Portland cement strength. However, the strength reduction stage is well modelled because the margin of reduction is similar to the experimental observations. There is no evident change in the initial stiffness of the stress-strain curve with the increase in lateral stress, in reasonable agreement with the laboratory observations. The experimental sample produces a rounded peak stress, while the simulated specimen provides a sharp one. This is probably because the parallel bonds bring about a more brittle response than the Portland cement.

In conclusion, the mechanical behaviour of bonded materials can be replicated in a qualitative way. The initial stiffness change in the stress-strain curve with the confining pressure, the strength development versus the axial strain, as well as the effect of lateral stress on both peak and ultimate strengths, could be reflected in DEM biaxial test simulation. Hence, DEM is an effective tool to study the behaviour of bonded materials.

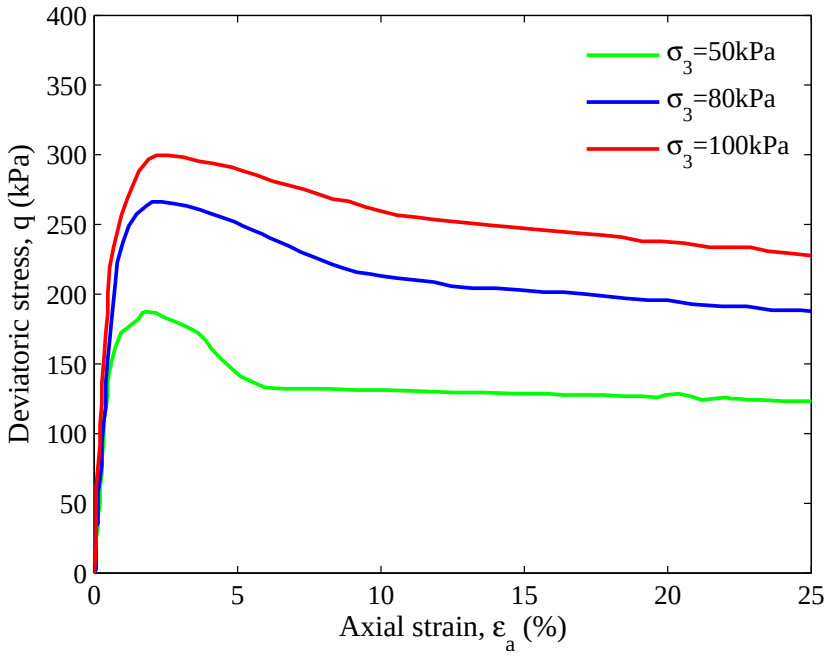

Figure 4.3: Stress-strain responses for Portland cement sand under various confining pressures (Wang and Leung, 2008a)

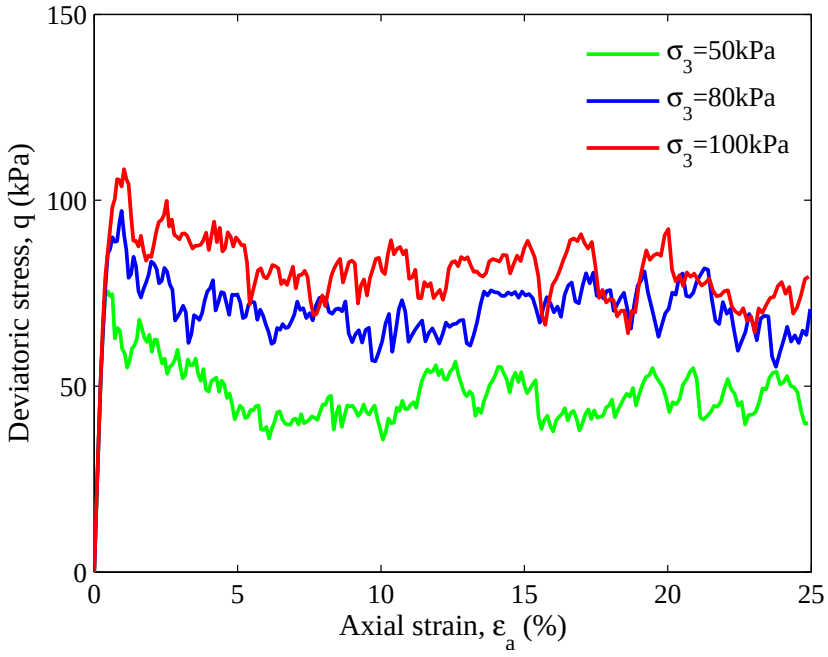

Figure 4.4: DEM biaxial test simulation for mechanical responses of bonded sample under varied confining pressures

4.4 Parallel-bond radius

The mechanical behaviour of bonded materials is closely related to bond breakage. In PFC^{2D}, the condition of parallel-bond breakage is that the maximum tensile or shear stress (i.e. σ_{max} or τ_{max}) exceeds the corresponding parallel-bond strength. σ_{max} and τ_{max} acting on the bond periphery, are strongly linked to the parallel-bond radius $\bar{R}$ (see Subsection 4.2.1). Therefore, the effect of $\bar{R}$ on the behaviour of bonded materials should not be ignored. In the current research, all the particle parameters, as well as the shearing conditions, are chosen to be equal to the simulations in Subsection 4.3.3, except for the bond stiffness, bond radius and initial void ratio. After the sample generation, the particle friction coefficient is changed from 0.5 to zero to obtain a relatively dense sample through consolidation. The sample is first isotropically consolidated to a low confining stress state (i.e. 0.5kPa) and then the initial void ratio is calculated as 0.19. Four types of sample are prepared prior to shearing, including an unbonded sample, as well as samples of parallel bonds with standard, 1.5 and 2.0 times standard bond radii.

For the unbonded sample, after achieving the low confining pressure of 0.5kPa, the sample continues to be consolidated to the target stress state, namely 80kPa. With regard to the bonded specimen, the parallel bonds are installed at all particle-to-particle contacts under the low stress state of 0.5kPa. As described in Subsection 4.3.3, each bond radius $\bar{R}$ is assigned to be equal to the beam radius $\widetilde{R}$ at the corresponding contact, denoted as the standard radius. This radius is enlarged to 1.5 or 2.0 times the standard size to study the effect of the bond radius on the behaviour of bonded materials. Based on Equations 4.15 and 4.16, $\widetilde{k}^n$ remains constant for the bonded samples with different bond radii via changing the bond normal stiffness $\bar{k}^n$. Therefore, $\widetilde{k}^n$ is controlled at all times to be equal to the normal stiffness k^n of the corresponding contact, regardless of the bond radius. After creating the bonds, the subsequent consolidation stress of 80kPa is applied to the samples. The particle friction coefficient is changed back from zero to 0.5 and then the specimens are sheared with a constant rate of 0.005m/s.

The simulated results are plotted in Figure 4.5, including the stress-strain relationship, as well as the development of volumetric strain (i.e. ε_v) and bond number versus the axial strain. The sample peak strength evidently increases as the parallel bonds are added to the contacts between particles (see Figure 4.5a). There is a further increase in peak strength with the enlargement of the parallel-bond radius from the standard size to 2.0 times the standard. However, the ultimate strength is insensitive to both bond-installing and bond radius. The initial stiffness increases significantly from unbonded to bonded materials. Nevertheless, for the bonded samples, the value of the bond radius has little effect on it. Figure 4.5b shows the relationship of volumetric strain to axial strain. The volumes of the samples contract at first, followed by a relatively notable dilation. It is noted that there is hardly any difference between the unbonded sample and the bonded one with the standard sized bonds. By increasing the bond radius, both the volume contraction and dilation become more and more evident. Compared to the dilation, the increase in contraction is not large. As highlighted by De Bono (2013), the increase in dilation is most likely owing to the increased moment resistance provided by the bonds. It prevents the particles rolling over one another. Moreover, the largest number of remaining bonds for a given axial strain (see Figure 4.5c) might logically be associated with the greatest volume dilation of the sample. In Figure 4.5c, during the shearing, there is a short steady state for the bond number, and then a rapid decrease can be observed, followed by a mild and approximately linear drop. The bond radius has a significant effect on the parallel bond number. It can be imagined that the increased bond radius reduces the number of bond breakages.

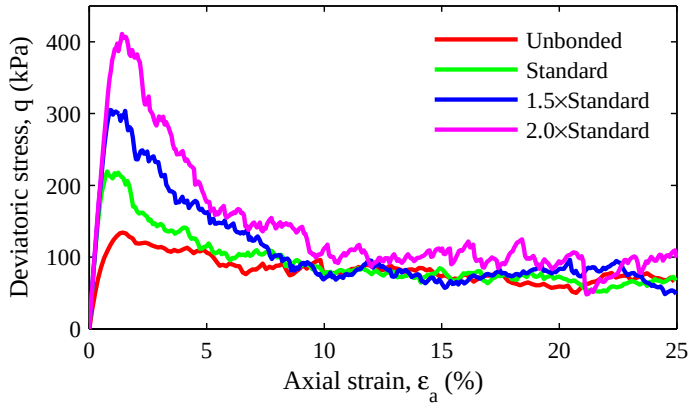

(a) Deviatoric stress versus axial strian

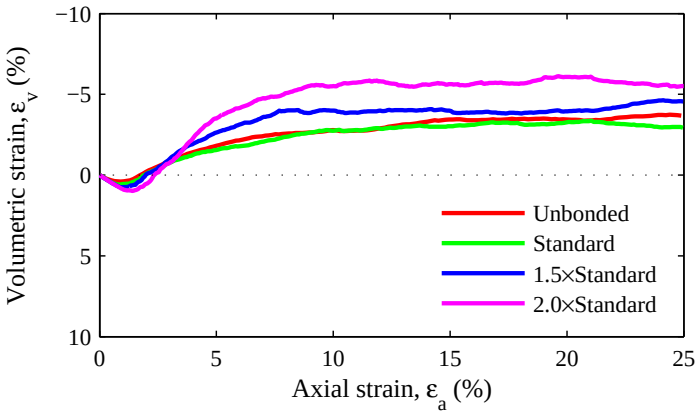

(b) Volumetric strain versus axial strain

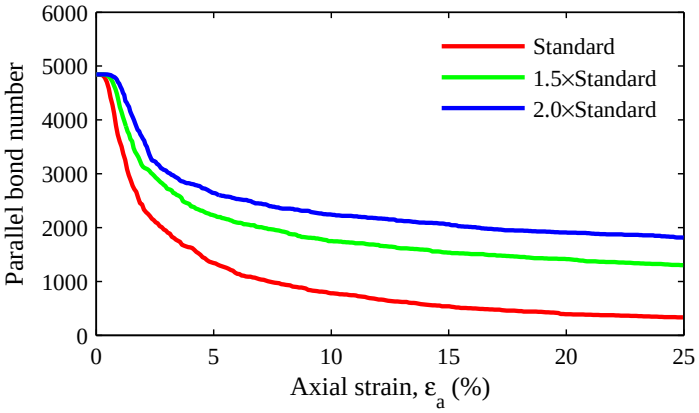

(c) Intact bond number versus axial strain

Figure 4.5: Biaxial simulation behaviour over unbonded materials, standard bond size, 1.5 and 2.0 times standard bond size, sheared under confining pressure of 80kPa

4.5 Parallel-bond strength distribution

In the biaxial test simulations described in Sections 4.3 and 4.4, parallel bonds with uniform normal and shear strengths were formed in the specimens. It is apparent from Figures 4.4 and 4.5a that quite a sharp peak strength is yielded, revealing severe brittle deformation and the start of rapid bond breakage. Based on the experimental tests, the appearance of a rounded or sharp peak strength probably depends on the confining pressure, cement agent (associated with the cementation strength) and cement content. The high confining pressure could change the behaviour of the bonded samples from brittle to ductile failure (Asghari et al., 2003; Marri, 2010). In addition, in comparison with Portland cement, gypsum-cemented samples (with weak cementation) are likely to produce a rounded peak strength, even if sheared under a very low confining stress state (Wang and Leung, 2008b). Moreover, according to Wang and Leung (2008a,b), a high cement content is prone to a sharp peak. For the purpose of replicating the ductile failure of bonded samples, as suggested by De Bono (2013), a specific distribution of bond strength, instead of strength uniformity might be adopted in DEM simulations. Therefore, the normal and Weibull distributions corresponding with the bond strength are employed in the following biaxial test simulations.

In PFC^{2D}, a random number Z can be drawn from the standard normal (or Gaussian) distribution with a mean of 0.0 and a standard deviation of 1.0, namely $Z \sim N(0,1)$. The random variable H of a general normal distribution can be obtained via Z as

$$H = (\kappa Z + \zeta) \sim N\left(\zeta, \kappa^2\right) \tag{4.18}$$

where ζ is the mean of the distribution and κ is the standard deviation. The probability density function of a normal distribution is expressed as

$$f(x, \zeta, \kappa) = \frac{1}{\kappa\sqrt{2\pi}} \exp^{-\frac{(x-\zeta)^2}{2\kappa^2}} \tag{4.19}$$

while the cumulative distribution function can be obtained as

$$F(x, \zeta, \kappa) = \frac{1}{2}\left[1 + \text{erf}\left(\frac{x-\zeta}{\kappa\sqrt{2}}\right)\right] \tag{4.20}$$

where erf is the Gaussian error function. In addition, a random number X can be drawn from a uniform distribution in the range [0.0, 1.0). The relationship of the random variable between the Weibull distribution and the uniform distribution can be described as

$$S = \lambda \left(-\ln\left(1 - X\right)\right)^{\frac{1}{k}} \tag{4.21}$$

where S is the random variable of the Weibull distribution; $\lambda > 0$ is the scale parameter of the distribution and $k > 0$ denotes the shape parameter. The probability density function of a Weibull random variable is

$$f\left(x, \lambda, k\right) = \frac{k}{\lambda}\left(\frac{x}{\lambda}\right)^{k-1} \exp^{-(x/\lambda)^k} \qquad x \geq 0 \tag{4.22}$$

while the cumulative distribution function for the Weibull distribution is

$$F\left(x, \lambda, k\right) = 1 - \exp^{-(x/\lambda)^k} \qquad x \geq 0 \tag{4.23}$$

The mean λ_{mean} of a Wellbull distribution is given by

$$\lambda_{mean} = \lambda\Gamma\left(1 + \frac{1}{k}\right) \tag{4.24}$$

where Γ is the gamma function.

The following microparameters are defined: the mean parallel-bond strength for both normal and shear directions (PBS_{mean}), and ratio of the standard deviation κ to the mean bond strength PBS_{mean} (ROSD). Note that PBS_{mean} is equal to ζ for the normal distribution and λ_{mean} for the Weibull distribution. In the normal distribution, ROSD = 0.25 and 0.40 and PBS_{mean} = 100kPa were adopted. On the other hand, for the Weibull distribution, values of shape parameter k = 0.5, 1.0 and 1.5 and PBS_{mean} = 100kPa were used. Note that PBS_{mean} is linked to both λ and k (see Equation 4.24). If k is changed, λ should be slightly adjusted to maintain the same mean λ_{mean} or PBS_{mean}. These parameters for both the normal and Weibull distributions are respectively applied to the bonded specimens. The bond radii are of standard sizes. The other parameters in the coming simulations are the same as that in Section 4.4. So the sample is dense, and the particle friction coefficient is 0.5 during shearing. After the generation of bonded samples, the distributions of bond strengths can be obtained, as

shown in Figures 4.6a and 4.6b for the normal and Weibull distributions respectively. In order to make a comparison, the simulated results in Section 4.4 for the standard bond size are introduced. Their normal and shear strengths were all 100kPa, namely uniform strength.

Comparisons between bond strength uniformity and the normal distribution of strengths are plotted in Figure 4.7. There is hardly any difference in the relationship of stress to strain between the different types of bond strength distribution, even changing ROSD from 0.25 to 0.40 (see Figure 4.7a). The initial stiffness, plus sharp peak and ultimate strengths remain almost unchanged. The behaviours of global volume contraction are quite similar with one another as well (shown in Figure 4.7b). However, some slight variations in overall sample dilation can be observed for different bond strength distributions. The number of intact bonds against axial strain is displayed in Figure 4.7c. They have a small initial steady stage and a rapid decrease stage in common. When the axial strain reaches approximately 5%, some difference at the third stage (namely the linear decrease stage) is exhibited, despite having little effect on the following stress-strain relationship (i.e. the development of ultimate strength) but probably resulting in the variations in overall sample dilation.

The results of different Weibull distributions of bond strength are compared to the simulation of uniform bond strength, as displayed in Figure 4.8. The shape parameter k has a significant effect on the initial stiffness of the stress-strain curve (see Figure 4.8a). A lower value of k produces a smaller initial stiffness (or Young's modulus), probably owing to the number of intact bonds at the beginning of the shearing (see Figure 4.8c). Moreover, a decrease in peak strength is witnessed with a reduction in the value of k from 1.0 to 0.5. Nevertheless, the ultimate strength is independent of the bond strength distribution. In the simulations, even a Weibull distribution is introduced, the rounded peak is not witnessed, inconsistent with the DEM triaxial test simulations (De Bono, 2013). According to the experimental results (Marri, 2010; Wang and Leung, 2008b), the acute peak is likely due to the low confining pressure and strong bond strength.

In spite of the significant variations in the number of intact bonds, the volumetric strains at the specimen contraction stage are similar to one another, even comparing between two different distribution types of bond strength (see Figure 4.8b). After that, the simulation with the lowest k value displays the most volume dilation for the Weibull strength distribution, despite exhibiting the fewest number of intact bonds for a given axial strain, in accordance with that in Figure 4.7, in which the fewer the remaining bonds, the greater the volume dilation for normal strength distribution. Fewer remaining bonds are observed for uniform bond strength than for normal strength distribution (i.e. ROSD = 0.40), but there is apparently no increase in volumetric dilation, an indication that the sample dilation is also affected by the bond strength distribution. As displayed in Figure 4.8c, there is an evident difference in the number of remaining bonds prior to shearing, which can be explained by the bond strength distributions before sample consolidation (see Figure 4.6b). Actually, the total number of bonds is identical in each case just after the generation of the bonded samples, regardless of bond strength distribution. However, there are many bonds with very small bond strengths, especially for the distribution with the lowest value of k and so they break during the consolidation. It is noted that, even with the largest remaining bond number just after the consolidation, the sample having uniform bond strength demonstrates the highest decrease rate of bond number during the shearing.

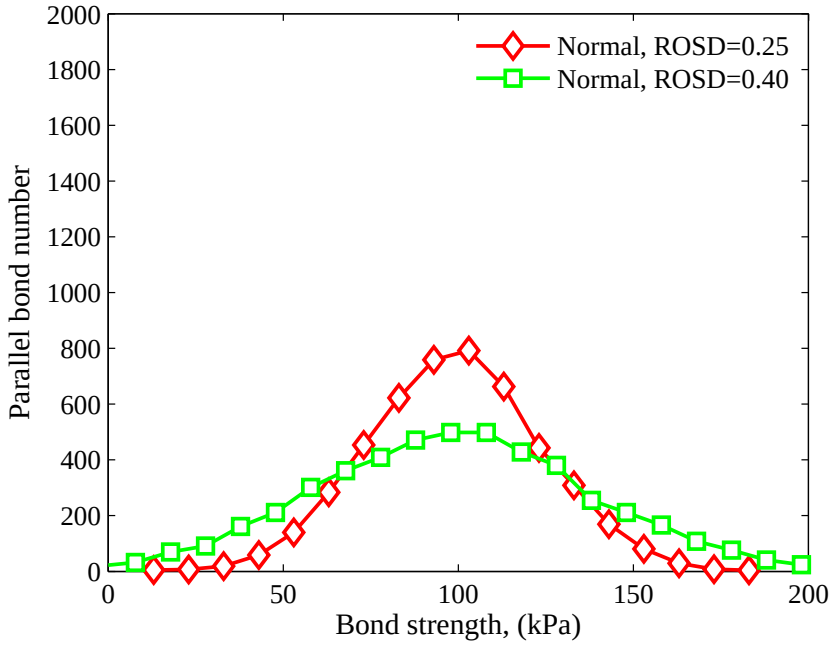

(a) Normal distribution

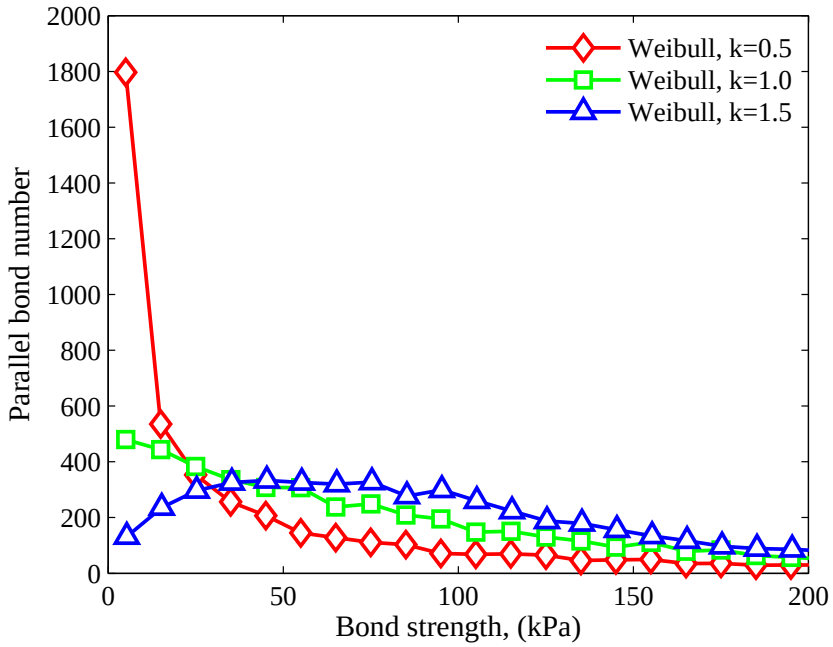

(b) Weibull distribution

Figure 4.6: Parallel bond number versus bond strength related to two kinds of bond strength distributions

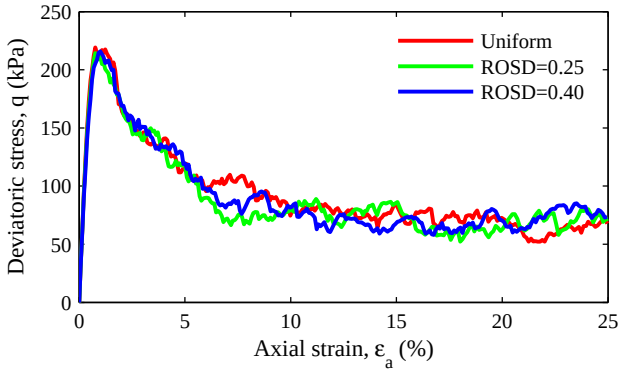

(a) Deviatoric stress versus axial strian

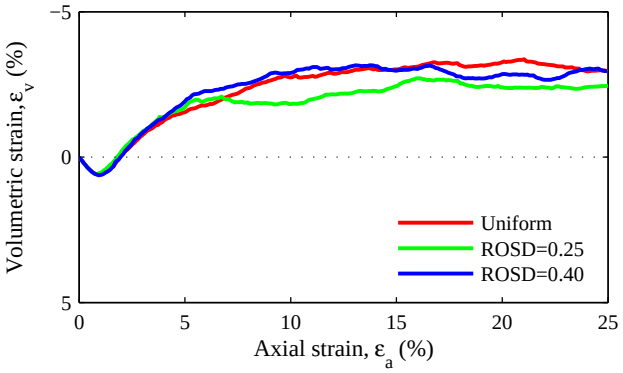

(b) Volumetric strain versus axial strain

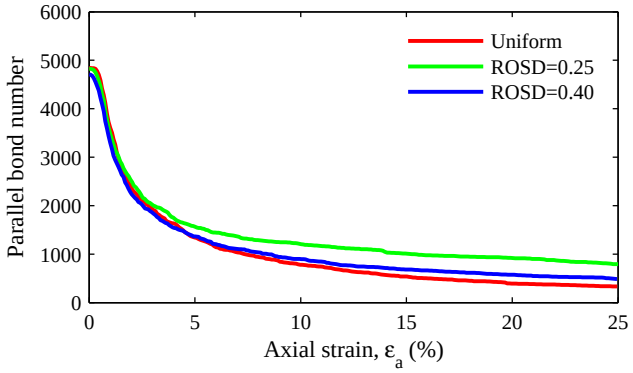

(c) Intact bond number versus axial strain

Figure 4.7: Biaxial simulation behaviour over uniform bond strength and normal distribution of bond strength (ROSD = 0.25 and 0.40), sheared under confining pressure of 80kPa

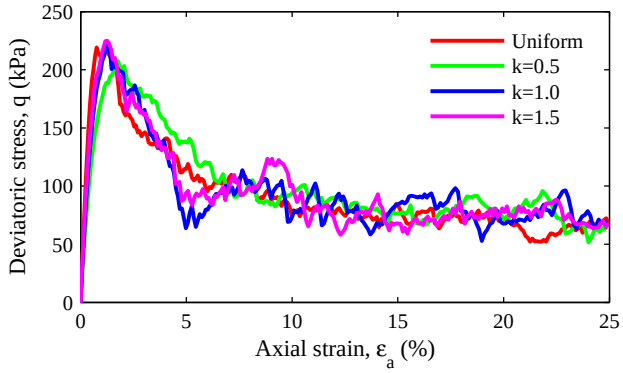

(a) Deviatoric stress versus axial strian

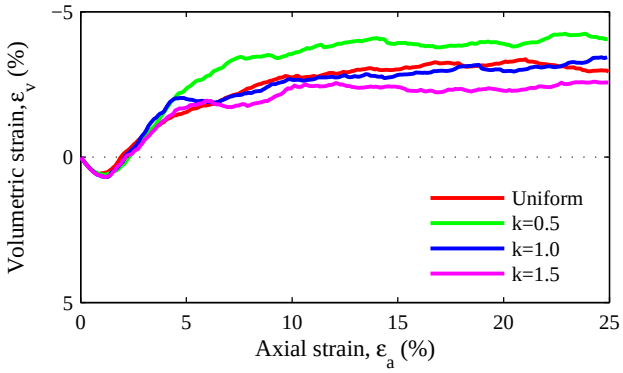

(b) Volumetric strain versus axial strain

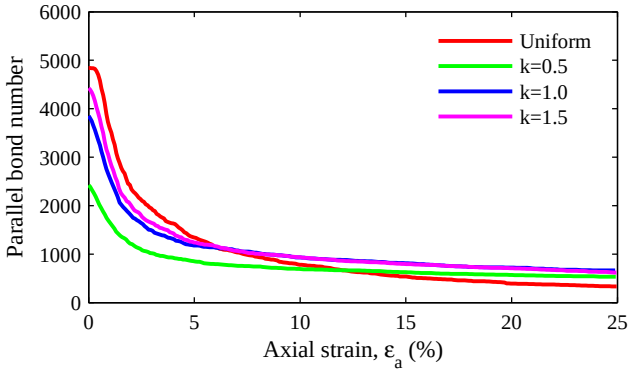

(c) Intact bond number versus axial strain

Figure 4.8: Biaxial simulation behaviour over uniform bond strength and Weibull distribution of bond strength (k = 0.5, 1.0 and 1.5), sheared under confining pressure of 80kPa

4.6 Simulation results for uniform bond strength

In this section, a series of biaxial test simulations is carried out under various confining pressures, namely 50, 80 and 100kPa. The details of the generation of unbonded samples, plus particle and sample parameters are identical to those in Subsection 4.3.3, where the particle friction coefficient μ is 0.5 prior to consolidation. After that, the unbonded samples are consolidated to a low confining stress state, i.e. 0.5kPa in which $\mu = 0$ and 0.5 are applied to obtain samples with different compaction. The void ratios can be calculated as the initial ones, which are 0.19 for the dense sample and 0.25 for the loose one. Then, parallel bonds with uniform strength are installed at all the particle-to-particle contacts and the bonded sample is created. To make a simplification of the analysis, the bond strength distribution is not considered in the following simulations. The parallel bond strengths in both the normal and shear direction are equal to one another, denoted as PBS, which is 100, 300 or 500kPa. After the creation of bonded specimens, the consolidation process is continued until the desired confining pressure is attained. At last, the particle friction coefficient is set at 0.3, 0.5 or 0.7 during the shearing. The mechanical behaviour of bonded materials is exhibited in Appendix A.

4.6.1 Elastic parameters

The deformation parameters of elastic materials are represented most often via Young's modulus (E) and Poisson's ratio (ν), applied normally in a generic sense with inelastic materials. These properties, associated with a state of plane strain, can be obtained from the results of the biaxial compression tests, where the constant lateral stress is maintained and an axial strain of $\delta\varepsilon_y$ is employed. The y-axis is aligned with the specimen axis and the loading direction. In PFC^{2D}, firstly the Young's modulus and

Poisson's ratio for a state of plane stress are calculated by

$$\begin{aligned} E' &= \frac{\delta\sigma_y}{\delta\varepsilon_y} \\ \nu' &= -\frac{\delta\varepsilon_x}{\delta\varepsilon_y} \end{aligned} \tag{4.25}$$

where the conditions of plane stress ($\sigma_z = 0$) and constant confining stress ($\delta\sigma_x = 0$) during the biaxial tests must be satisfied. After that, the elastic properties for a state of plane strain are expressed by a generic relation of plane stress to plane strain cases

$$\begin{aligned} E &= E'(1-\nu^2) \\ \nu &= \frac{\nu'}{1+\nu'} \end{aligned} \tag{4.26}$$

The initial stresses and strains are used in these calculations. Moreover, shear modulus (G), bulk modulus (K) and constraint modulus (M) can be deduced as

$$\begin{aligned} G &= \frac{E}{2(1+\nu)} \\ K &= \frac{E}{3(1-2\nu)} \\ M &= \frac{E(1-\nu)}{(1+\nu)(1-2\nu)} \end{aligned} \tag{4.27}$$

Through mechanical responses of bonded materials (see Appendix A), the axial stress, axial strain and lateral strain can be obtained. Therefore, using Equations 4.25 and 4.26, elastic constants E and ν are calculated. In this section, the development of elastic constants E and ν versus confining pressure are studied in terms of sample compaction, particle friction coefficient and parallel bond strength. Regardless of sample compaction, the installation of parallel bonds in the samples produces a significantly larger Young's modulus than the unbonded materials, although the modulus is insensitive to the bond strength over a range of 100 to 500kPa as shown in Figure 4.9. The increase in the modulus is probably due to the relatively stable structure of the bonded sample. The particle friction coefficient μ is equal to 0.5. Moreover, there is a slight increase in the modulus through raising the confining stress from 50 to 100kPa, denoting that the lateral pressure increases the initial stiffness of the stress-strain curve, in agreement with experimental findings (Marri, 2010). It is imagined that the large lateral stress prohibits the axial deformation. The effect of sample compaction on the

modulus is also investigated in terms of the unbonded (PBS = 0kPa) and bonded (PBS = 300kPa) samples, as shown in Figure 4.10. As with the creation of parallel bonds, the dense sample demonstrates an evident increase in the Young's modulus. This influence is independent of parallel bond strength. The particle friction coefficient μ is another factor to impact the elastic properties. As shown in Figure 4.11, the increase in μ from 0.3 to 0.7 brings about an increase in the Young's modulus corresponding with both dense and loose samples, particularly for the unbonded materials. However, the modulus corresponding with the dense bonded sample is independent of particle friction (see Figure 4.11b).

The lateral stress has an obvious impact on the Poisson's ratio ν for the unbonded samples, in comparison with the assemblies with parallel bonds, as shown in Figure 4.12, where the particle friction coefficient μ is 0.5. The weak structure for the unbonded sample makes it sensitive to the effect of lateral confinement. With the raising of the confining pressure, the ratio gradually decreases, in contrast to the trend of Young's modulus, showing accordance with laboratory conclusions (Marri, 2010). The Poisson's ratio corresponding with the bonded sample is independent of the parallel bond strength just like the Young's modulus. The density of the sample is of great significance to the change of Poisson's ratio as shown in Figure 4.13, where a loose sample produces a large ratio for a given confining pressure in both unbonded and bonded cases, proving that the increment of lateral strain is more sensitive to an increase of sample void ratio than the change of axial deformation. The effect of particle friction on Poisson's ratio is studied on the basis of the sample compaction and parallel bond strength (see Figure 4.14). For the loose sample, a larger particle friction brings about a bigger ratio when the friction coefficient ranges from 0.3 to 0.7. This trend is also valid for the dense unbonded samples but there is hardly any difference in the ratios for the dense samples with parallel bonds.

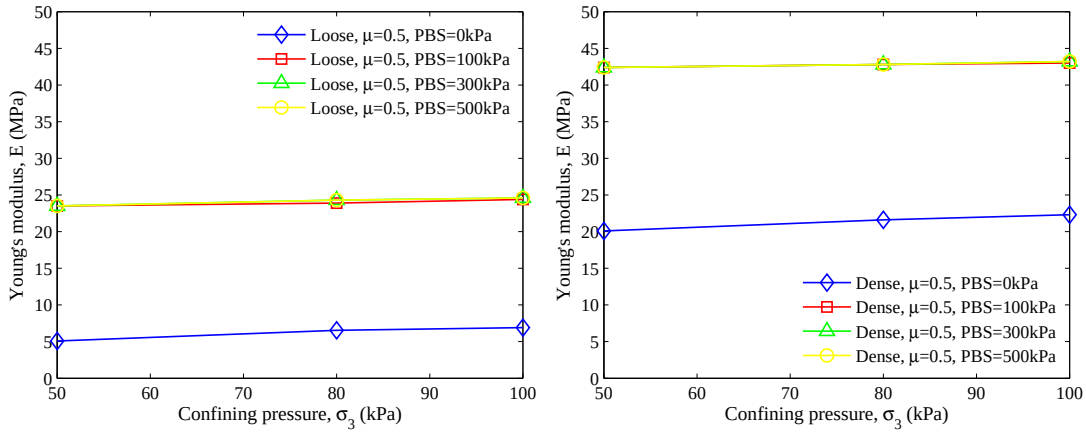

(a) Loose sample *(b) Dense sample*

Figure 4.9: Variation of Young's modulus with confining pressure and bond strength for both loose and dense samples

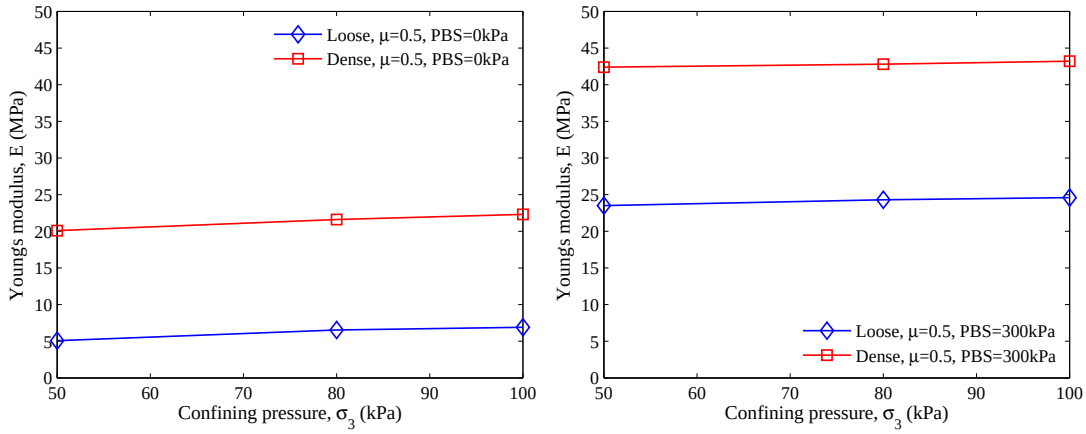

(a) PBS=0kPa *(b) PBS=300kPa*

Figure 4.10: Variation of Young's modulus with sample compaction and confining pressure for samples with different bond strengths

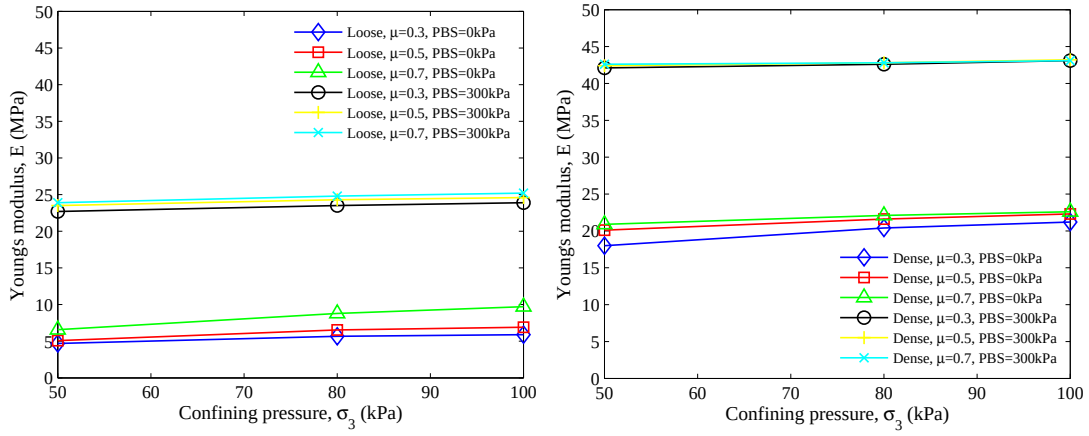

(a) Loose sample *(b) Dense sample*

Figure 4.11: Variation of Young's modulus with particle friction coefficient and confining pressure in terms of different bond strengths for both loose and dense samples

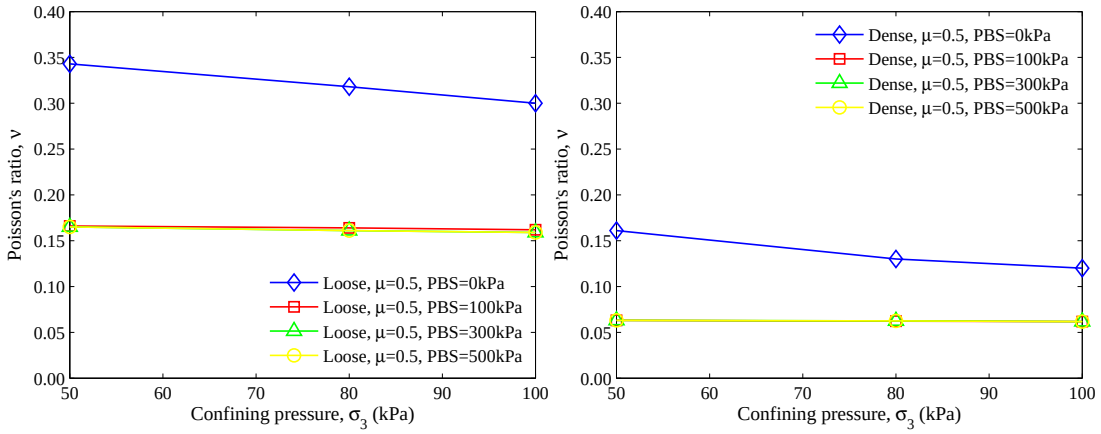

(a) Loose sample *(b) Dense sample*

Figure 4.12: Variation of Poisson's ratio with confining pressure and bond strength for both loose and dense samples

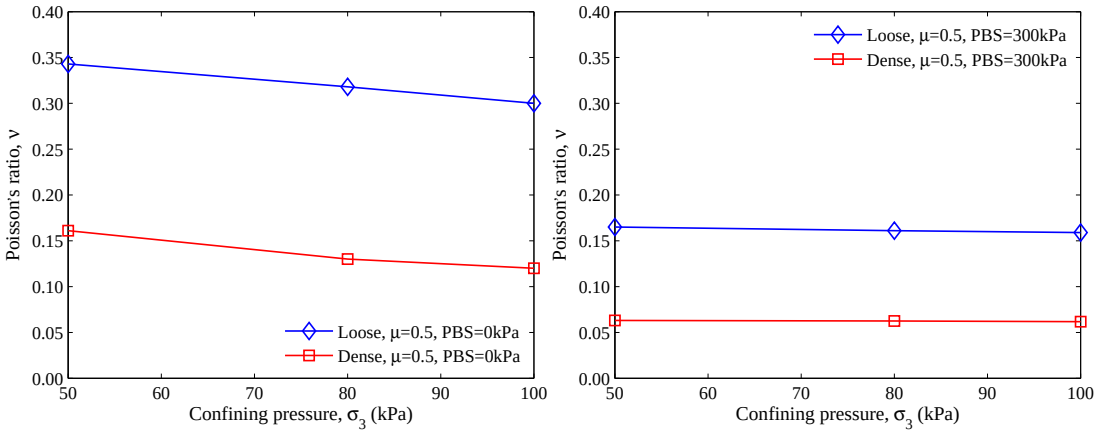

(a) PBS=0kPa *(b) PBS=300kPa*

Figure 4.13: Variation of Poisson's ratio with sample compaction and confining pressure for samples with different bond strengths

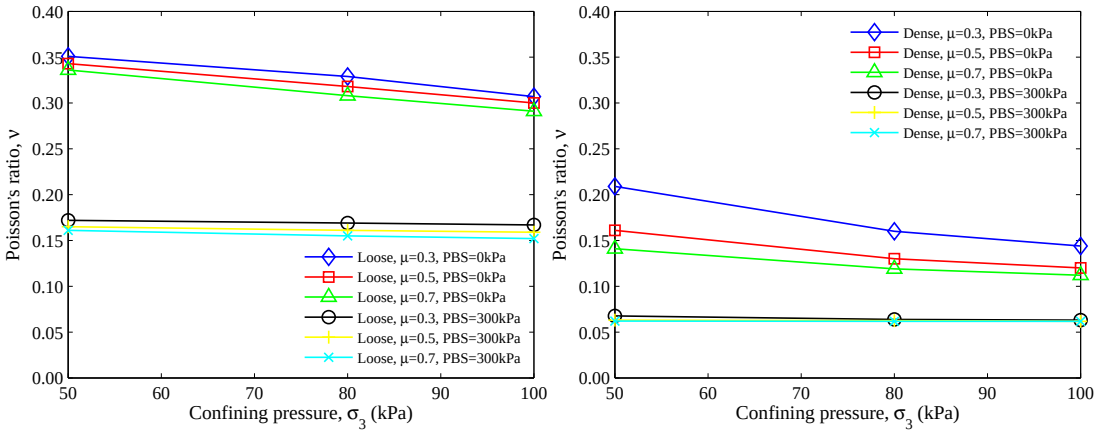

(a) Loose sample *(b) Dense sample*

Figure 4.14: Variation of Poisson's ratio with particle friction coefficient and confining pressure in terms of different bond strengths for both loose and dense samples

4.6.2 Yield stress

A yield and failure surface are most often assumed in the principle stress space for the constitutive models developed for granular materials. The yield and failure criteria are of great importance to describe the behaviour of a soil sample. Generally, the yield surface is convex and when the stress state is inside it, an elastic characteristic is seen. When the stress state is located on the surface, the yield point is attained and the material exhibits plastic behaviour. If further loading is applied on the material, the stress state will stay on the yield surface, which might change size and shape with the development of plastic strain.

In this study, the primary yield stress q_y versus the bond strength is investigated in view of the confining pressure, sample compaction and particle friction. According to Kuwano and Jardine (2007), the yielding is linked to the sharp curvature evolving in the stress-strain curve during the sample shearing. Therefore, the primary yield point can be directly obtained at the onset of the transformation from a stiff to a less stiff response, namely deviating from initial linearity (Marri, 2010; Wang and Leung, 2008b). As shown in Figure 4.15, the primary yield points are located on the stress-strain curves corresponding with the loose and dense samples with a range of parallel bond strengths. The particle friction coefficient is 0.5 and the lateral stress is 80kPa. It is believed that the breakage of bonds with large bond strength is associated with high deviatoric stress. So, following the increase in bond strength, there is a significant increase in the primary yield deviatoric stress and for the bonded sample, the position of the yield point is evidently associated with the increased axial strain.

The effect of sample compaction on the primary yield deviatoric stress over the different bond strengths is displayed in Figure 4.16, where the low void ratio clearly increases the primary yield stress for a specific bond strength. The compaction of the sample is closely related to its elastic ability. The particle friction coefficient is selected as 0.5 and the lateral stress is 80kPa. It is apparent that there is an approximately linear growth of the yield stress for the bonded samples with the raising of the parallel bond strength from 100 to 500kPa. The relationship between the confining pressure

and primary yield stress is also studied, as shown in Figure 4.17. The yield stress lacks sensitivity to the lateral stress state for both loose and dense samples. Moreover, the effect of the particle friction coefficient on the primary yield stress at a range of bond strengths is investigated, as shown in Figure 4.18. The results show that, irrespective of sample compaction, the increased particle friction is prone to the incremental yield stress corresponding with a given bond strength. A large friction coefficient hinders the rolling of particles, which may enhance the elastic limit.

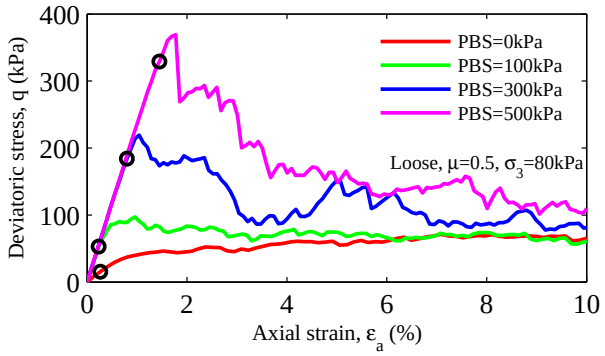

(a) Loose sample

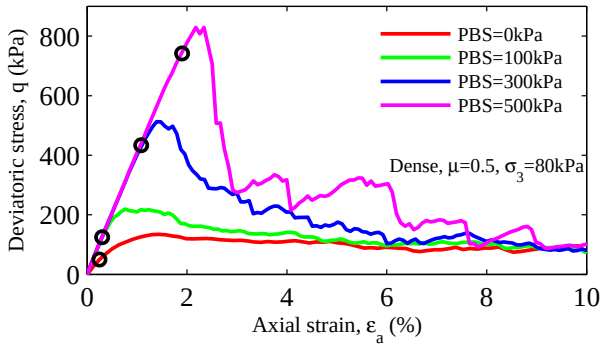

(b) Dense sample

Figure 4.15: Effect of bond strength on the location of primary yield point over particle friction coefficient 0.5 under the confining pressure 80kPa

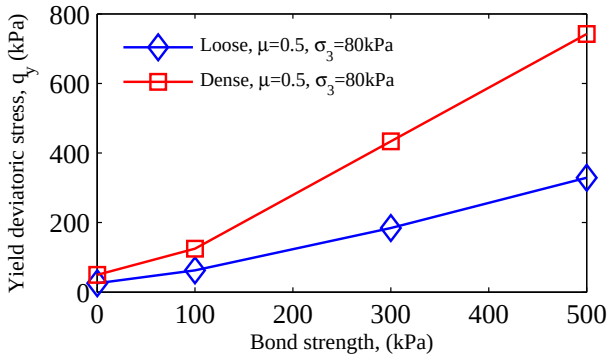

Figure 4.16: Effect of sample compaction and bond strength on yield deviatoric stress for the confining pressure 80kPa

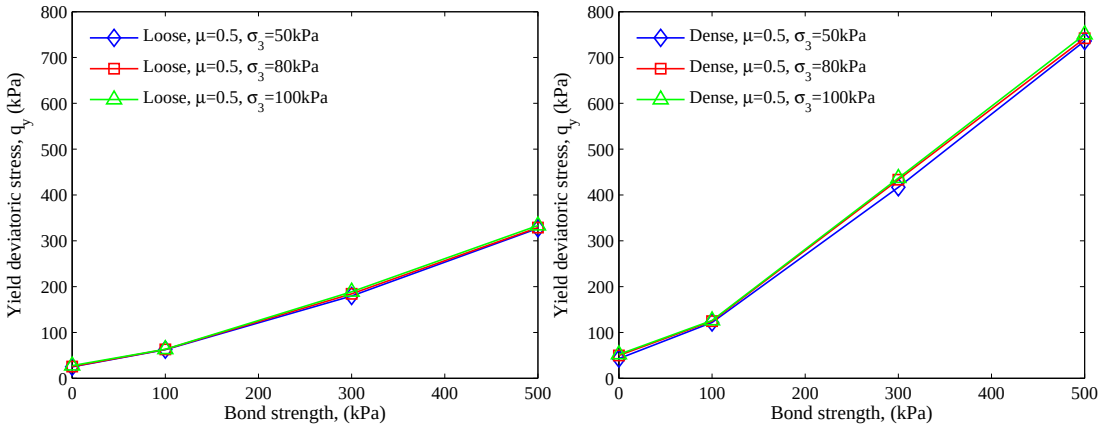

(a) Loose sample *(b) Dense sample*

Figure 4.17: Effect of confining pressure and bond strength on yield deviatoric stress for both loose and dense samples

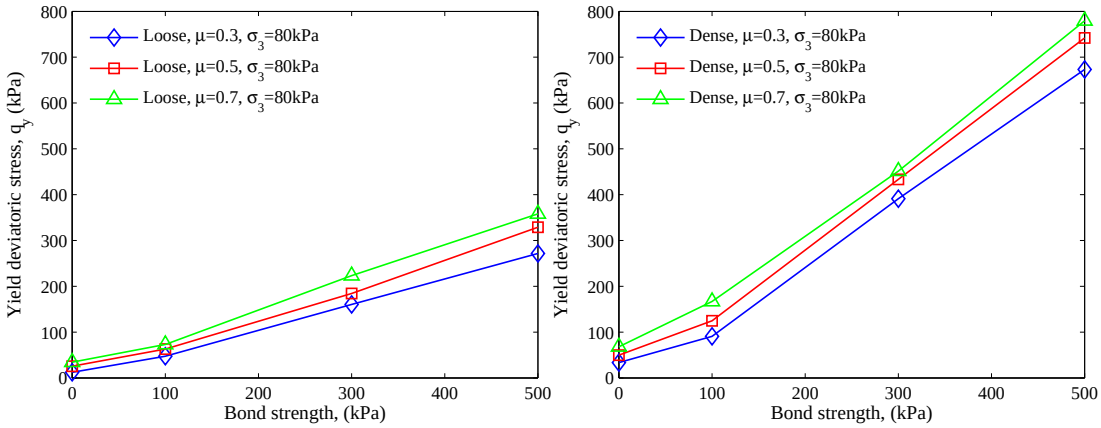

(a) Loose sample *(b) Dense sample*

Figure 4.18: Effect of particle friction coefficient and bond strength on yield deviatoric stress for both loose and dense samples

4.6.3 Shear strength

Given the cohesive-frictional nature of the bonded materials, a function associated with the cohesion and internal friction angle could be used to describe the shear strength. The peak failure data can be obtained from the modelling results, performed on bi-axial compression tests, with various parallel bond strengths and particle friction over different sample compactions under a range of confining pressures, as shown in Appendix A. After the peak failure stresses are determined, as described by Chen et al. (2010), there are two approaches to obtaining the strength parameters: cohesion intercept c and internal friction angle ϕ. The first is to get the failure Mohr-Coulomb circles directly in σ-τ plane, where σ and τ are principle and shear stress respectively as shown in Figure 4.19. Then their common tangent τ_f (i.e. failure envelope) can be drawn. The dip angle and intercept of the common tangent is the friction angle and cohesion of the material. The second method is to draw the strength line k_f through the failure points in the p-q_0 plane, shown in Figure 4.19. The strength line function would be expressed as

$$q_0 = a + p \tan \alpha \tag{4.28}$$

where q_0 is the shear stress, p indicates the mean of the major and minor principle stresses, a and α are the intercept and dip angle of the strength line. The strength line can be fitted by the least square method, and then the parameters a and α can be determined. After that, the internal friction angle and cohesion could be calculated by the following equations

$$\begin{aligned} f &= \tan \phi = \tan\left(\arcsin\left(\tan \alpha\right)\right) \\ c &= \frac{a}{\cos \phi} = \frac{a}{\cos\left(\arcsin\left(\tan \alpha\right)\right)} \end{aligned} \tag{4.29}$$

where f is the internal friction coefficient. If the first method is used, an artificial factor can not be avoided and this graphing method is not suitable. So the latter is used to determine the strength properties in this study. The Mohr-Coulomb circles, as well as the failure envelope, are shown in Figure 4.20, where the parallel bond strength is 300kPa and particle friction coefficient is chosen as 0.5 for both loose and dense samples.

The effect of sample density on the internal friction angle is investigated in terms of particle friction coefficients (see Figure 4.21). It appears that, by reducing the sample porosity, there is an apparent increase in the peak friction angle. However, it becomes less and less evident with the increase in bond strength. Generally, the friction angle decreases with the increase in parallel bond strength for the particle friction coefficient being 0.3 and 0.5. Nevertheless, when the friction coefficient is 0.7, there is a clear growth with the bond strength, rising from 300 to 400kPa, as shown in Figure 4.21c. So, a specific pattern can not be found for the relation between bond strength and friction angle, analogous to the literature (Schnaid et al., 2001) where a clear correlation of cement content and friction angle is hard to establish. On the other hand, the evolution of the friction angle versus the particle friction has been studied, as shown in Figure 4.22, in which the friction angle increases, apparently for both loose and dense samples, when the friction coefficient changes from 0.3 to 0.7. In contrast to the friction angle, the correlation between cohesion and bond strength can be clearly set up, as summarized in Figure 4.23, where, irrespective of particle friction, the increased bond strength leads to increased cohesion with a high growth rate for the dense sample. The effect of the particle friction on cohesion of the material is summarized in Figure 4.24. The cohesion remains unchanged with the increase in particle friction, except that there is a growth for the dense sample with a high bond strength (i.e. 500kPa) by increasing the friction coefficient.

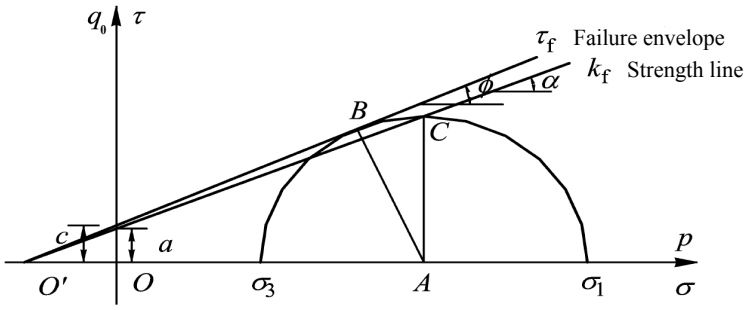

Figure 4.19: Graphics for calculating shear strength parameters of granular materials (Chen et al., 2010)

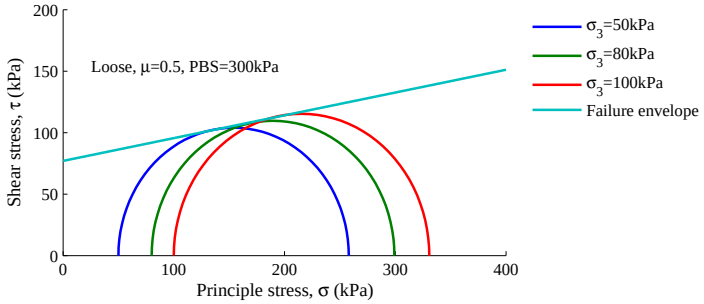

(a) Loose sample

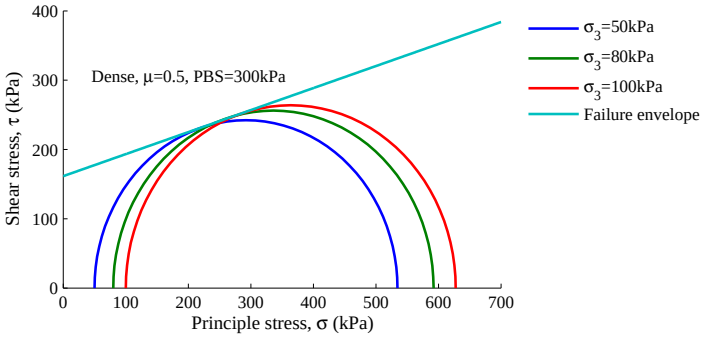

(b) Dense sample

Figure 4.20: Mohr-Coulomb circles and failure envelope for DEM biaxial test sample with bond strength 300kPa and particle friction coefficient 0.5 in terms of various confining pressures

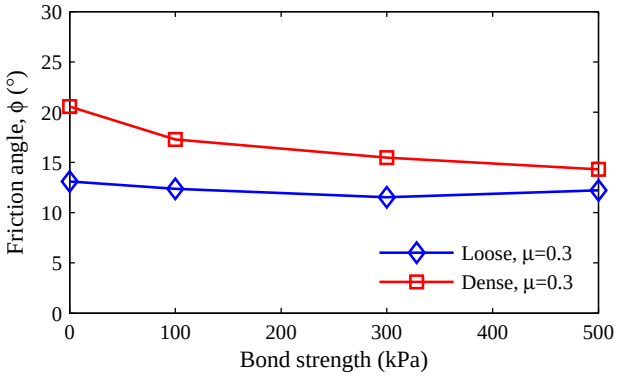

(a) μ=0.3

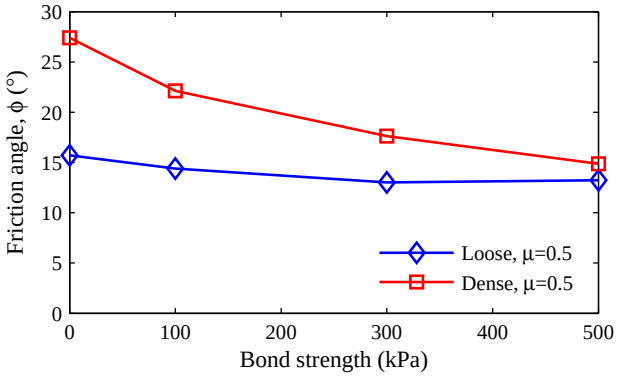

(b) μ=0.5

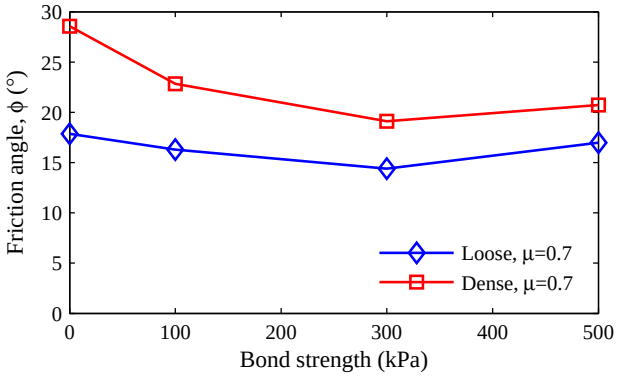

(c) μ=0.7

Figure 4.21: Variation of friction angle with sample compaction and bond strength for different particle friction coefficients

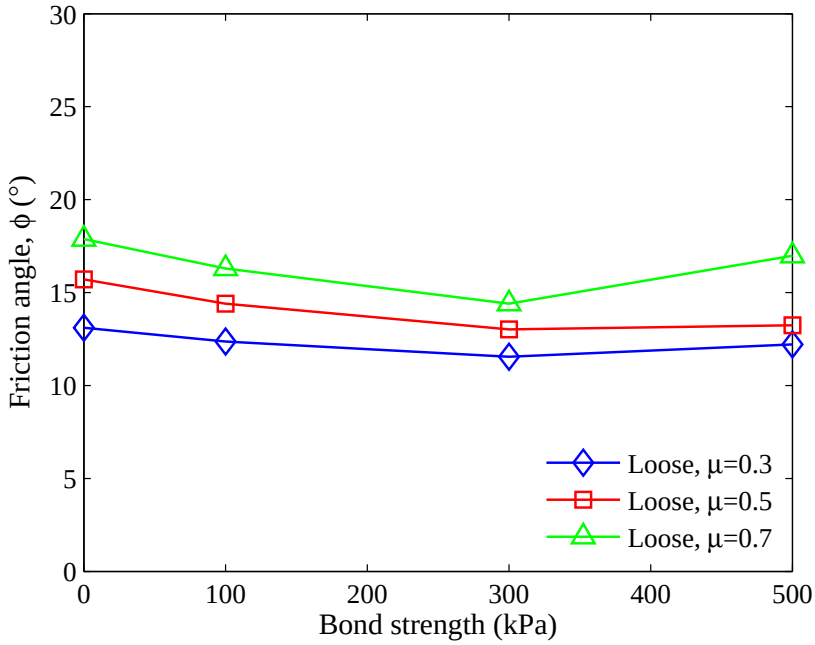

(a) Loose sample

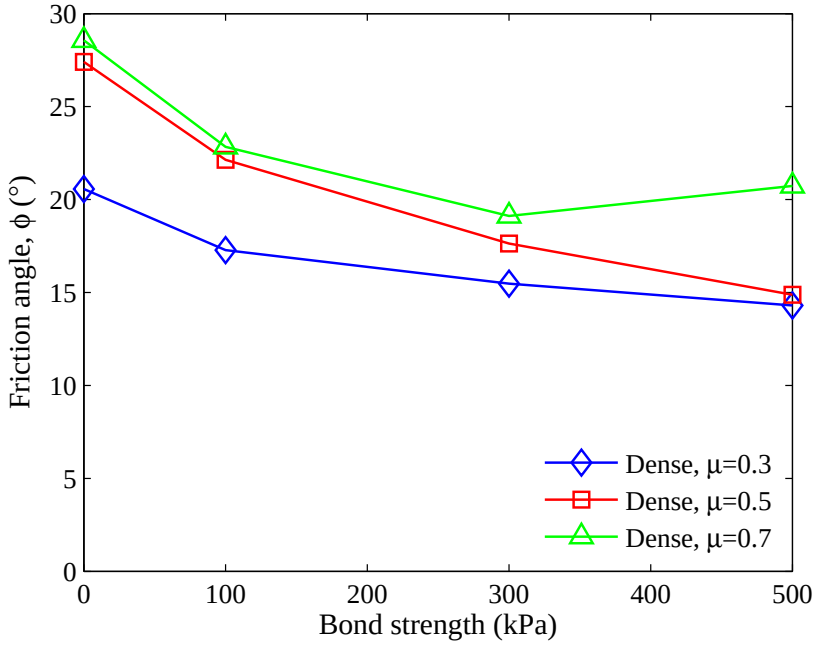

(b) Dense sample

Figure 4.22: Variation of friction angle with particle friction coefficient and bond strength for both loose and dense samples

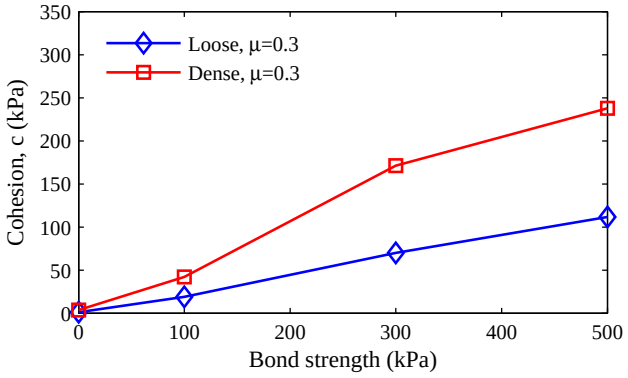

(a) μ=0.3

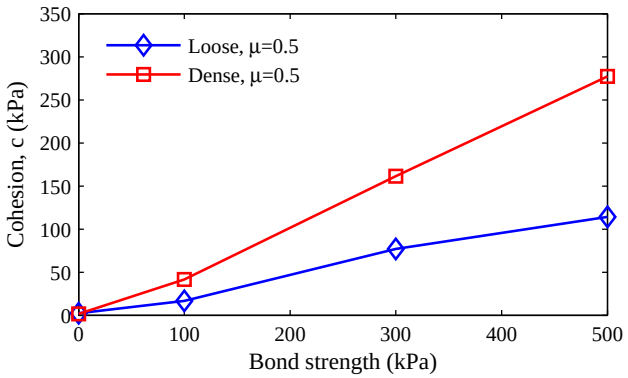

(b) μ=0.5

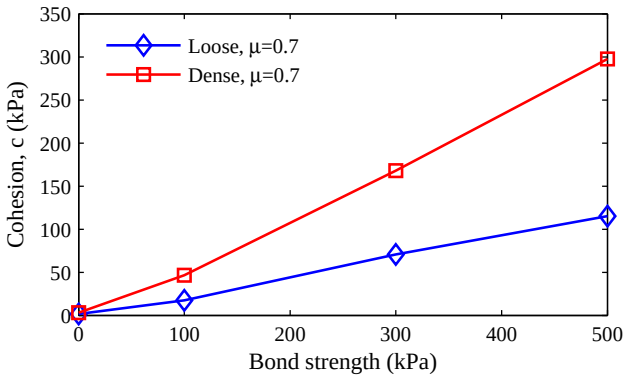

(c) μ=0.7

Figure 4.23: Variation of cohesion with sample compaction and bond strength for different particle friction coefficients

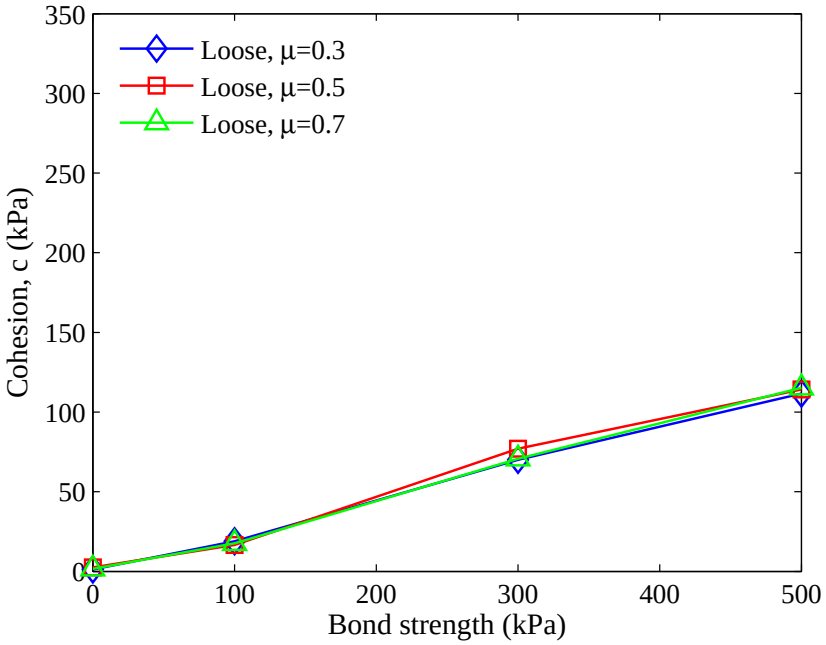

(a) Loose sample

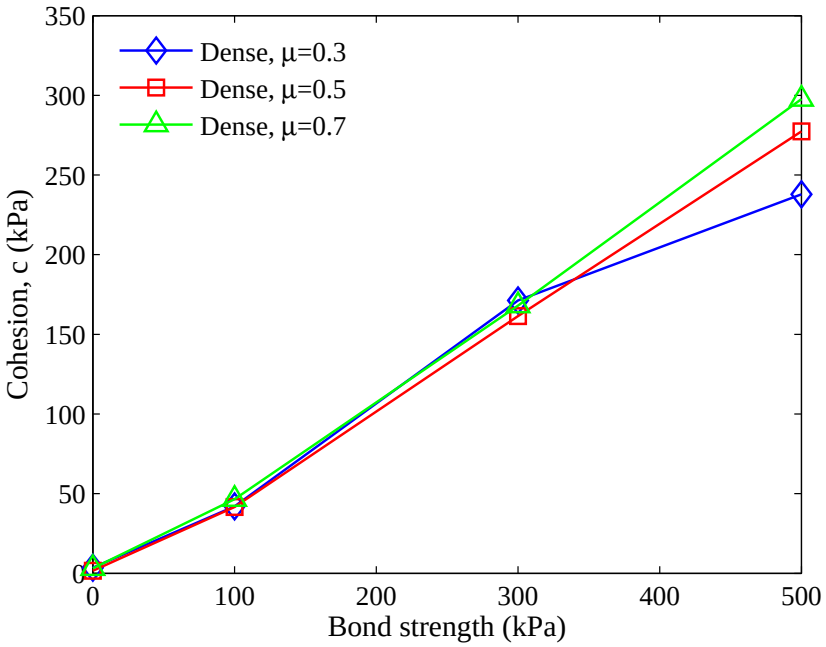

(b) Dense sample

Figure 4.24: Variation of cohesion with particle friction coefficient and bond strength for both loose and dense samples

4.6.4 Bond breakage

The mechanical behaviour of the bonded samples is closely associated with the bond breakage summarized in Figure 4.25, where the biaxial test modelling is carried out on the dense sample with bond strength 300kPa and friction coefficient 0.5 under a lateral stress of 80kPa. Generally, at the start of the shearing of the bonded sample (i.e. point A to B), the bond number remains constant, coinciding with the elastic response. Before the stress state reaches the primary yield point C, the bonds begin to break but not intensively, in agreement with the observation (Wang and Leung, 2008a). At this stage, the damage resulting from the bond breakage can be accommodated by the bonding structure through redistributing the carried load. Hence, an elastic response is retained. The bonds block the dilatancy prior to peak strength (i.e. point D). It is worth noting that the increment of axial strain is very small when loading the sample from yield point C to peak point D. During this process, the bond breakage is still mild and, therefore, further volume contraction is witnessed. The severe bond breakage starts around the peak strength (i.e. point D), denoting an occurrence of brittle failure. The volume dilation speeds up afterwards, and the large volumetric dilatancy (point E to F) is associated with the severe occurrence of bond breakage.

Given the bond strength, lateral stress state, and particle friction, the bond breakage versus axial strain for the loose and the dense samples is investigated in this subsection. The effect of confining pressure on the remaining bond number is first considered, as shown in Figure 4.26, where the particle friction coefficient μ is equal to 0.5 and bond strength 300kPa. It is worth noting that there is hardly any difference in the number of intact bonds at the initial stage and the following rapid-decrease stage. When the bonded sample continues to be sheared, the bond breakage is apparently impacted by the lateral stress, particularly for the dense sample. At this stage, the increased confinement is related to the incremental deviatoric stress, which probably causes more bond breakage for a given axial strain. In addition, the bond strength is an important property affecting the bond breakage (see Figure 4.27). By increasing the bond strength, the duration of the initial steady state rises as an indication that the high

bond strength corresponds with the large axial strain for bond breakage. In addition, the rapid-decrease stage becomes less and less intensive. The overall bond breakage develops by reducing the bond strength, especially from 300 to 100kPa. During the shearing process, most bond breakage probably takes place in the shear band for the samples with strong bond strength. On the other hand, the weak bonds are likely to break at other locations as well. The effect of particle friction on bond breakage is also studied, as demonstrated in Figure 4.28. Similar to the observations in Figure 4.26, after the rapid-decrease stage, the particle friction begins to impact the remaining bond number. Increased particle friction causes increased bond breakage.

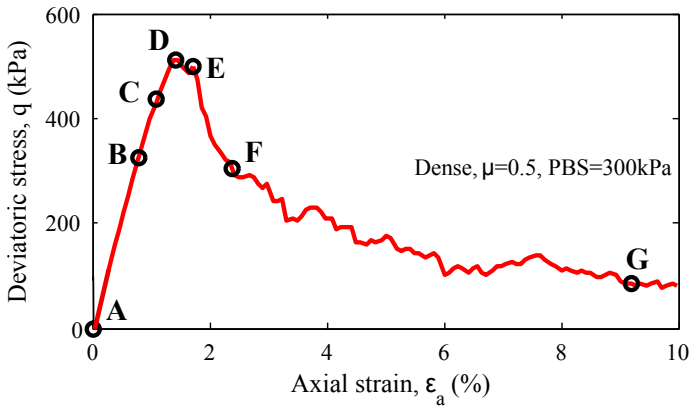

(a) Deviatoric stress versus axial strian

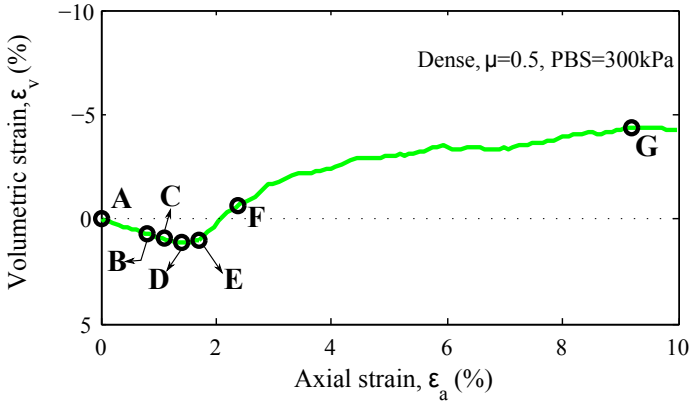

(b) Volumetric strain versus axial strain

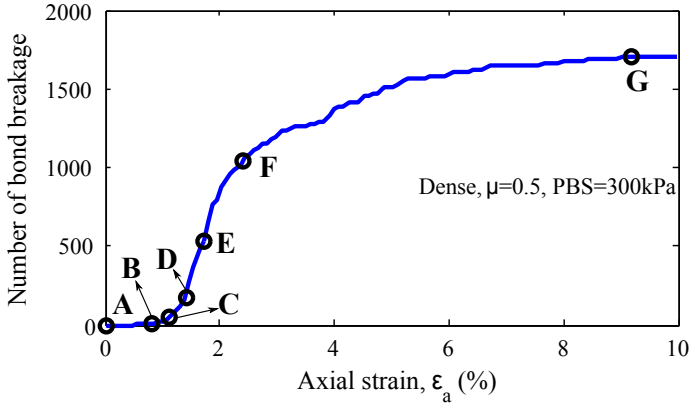

(c) Number of bond breakage versus axial strain

Figure 4.25: Results of the biaxial test simulation on the bonded sample with bond strength 300kPa and particle friction coefficient 0.5, sheared across the confining pressure 80kPa

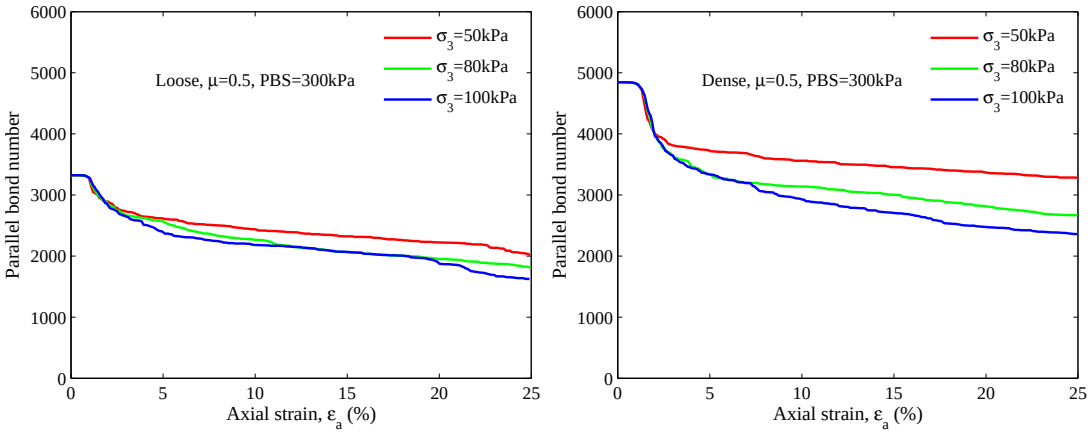

(a) Loose sample *(b) Dense sample*

Figure 4.26: Effect of confining pressure and axial strain on parallel bond number for both loose and dense samples with particle friction coefficient 0.5 and bond strength 300kPa

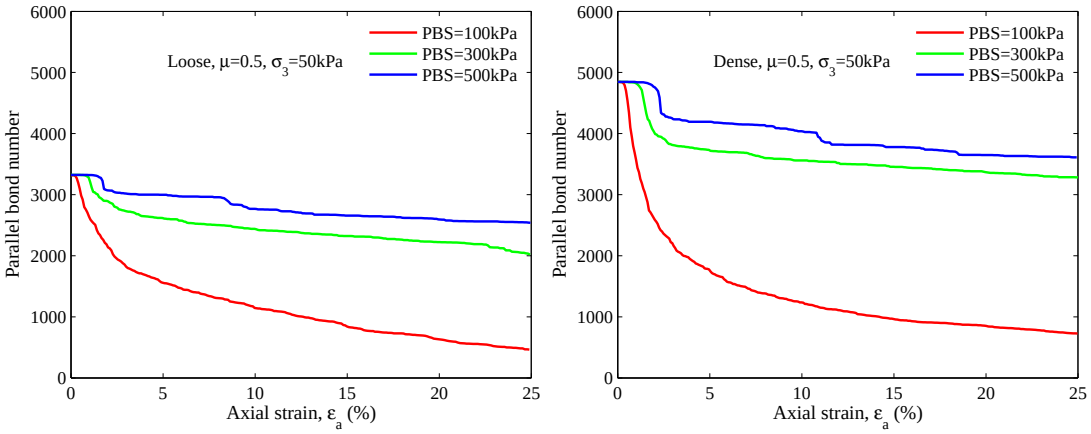

(a) Loose sample *(b) Dense sample*

Figure 4.27: Effect of bond strength and axial strain on parallel bond number for both loose and dense samples with particle friction coefficient 0.5, sheared across confining pressure 50kPa

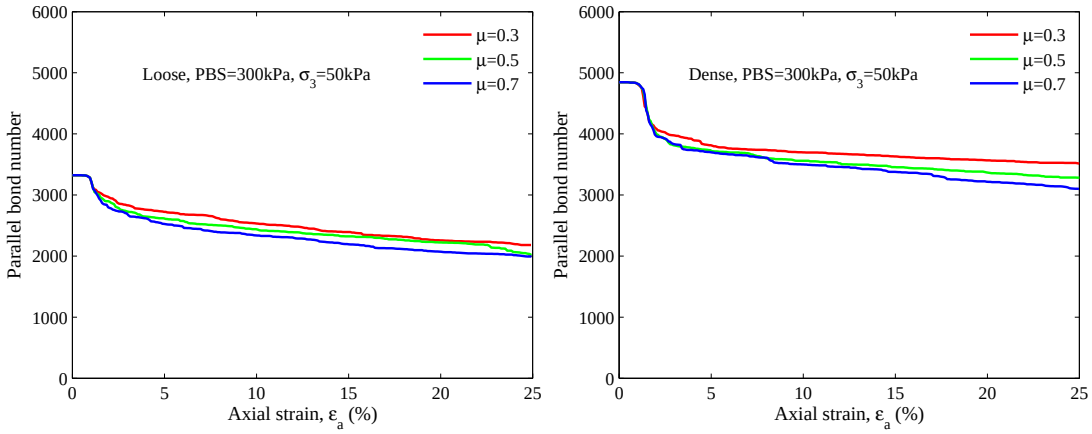

(a) Loose sample *(b) Dense sample*

Figure 4.28: Effect of particle friction coefficient and axial strain on parallel bond number for both loose and dense samples with bond strength 300kPa, sheared across confining pressure 50kPa

4.6.5 Shear-dilatancy response

After the contraction the subsequent response for a dense granular assembly is generally the expansion in sample volume, which is often known as dilation. The dilatancy, d, is defined as $(\delta\varepsilon_1 + \delta\varepsilon_3) / (\delta\varepsilon_1 - \delta\varepsilon_3)$ where $\delta\varepsilon_1$ and $\delta\varepsilon_3$ are the increments of major and minor principle strain respectively. The locations of maximum dilatancy rate are plotted in Figure 4.29a for stress-strain curves and in Figure 4.29b for volumetric strain-axial strain curves. The sample is dense, with particle friction coefficient 0.5 and parallel bond strength 100kPa. The occurrence of peak strength and maximum dilatancy is not at the same axial strain, analogous to the findings by Wang and Leung (2008a) on Portland cement sand. Such a delayed evolution of the maximum dilatancy rate is in contrast to the response of a purely frictional material, where the peak strength corresponds with the same axial strain as the maximum dilatancy rate. This indicates that the peak strength is dominated by the structure formed by the interparticle bonding.

The dependence of shear dilation on parallel bond strength, particle friction coefficient and confining pressure has been analysed on the basis of the biaxial simulation tests. The bond installation in the sample changes the behaviour of the volumetric strain as shown in Figure 4.30. The particle friction coefficient is equal to 0.5 and the lateral stress is 50kPa. For the loose unbonded sample, constant compression is observed until a relatively steady state is reached. Despite the initial contraction, the bonded sample subsequently begins to dilate, especially for the high bond strength 300 and 500kPa. As reported by Wang and Leung (2008a), during the shearing, properly sized clusters and debonded particles are generated by the bond breakage, contributing to the increase in volume dilatancy. According to the dense sample, irrespective of the bond strength, both the initial compression and the following dilation are witnessed, as demonstrated in Figure 4.30b. At the initial compression stage, the high bond strength allows bond breakage to commence at a high axial-stress state, which is related to a large elastic volume deformation. Therefore, the increased bond strength causes increased volume compression. The onset of dilation is delayed as well by increasing the bond strength. Like the loose sample, the increased bond strength leads to incremental volume dilation for the dense specimen.

The effect of particle friction on the dilatancy is explored, as shown in Figure 4.31, where the initial compression and dilatancy commencement is insensitive to the particle friction. Nevertheless, the subsequent dilation is increased with an increase of particle friction. Compared to the loose sample, the effect of the friction coefficient on dilation is obvious for the dense specimen. The increased interparticle friction hinders the rolling of clusters and debonded particles, which may contribute to the increased dilatancy. This impact is more apparent for the dense sample than the loose. On the other hand, the confining pressure has an effect on the dilation as shown in Figure 4.32. The initial compression and onset of the dilation are similar to one another, regardless of the lateral stress state. However, the initial dilatancy rate is reduced by the increase in confinement, particularly for the loose sample.

In conclusion, large overall dilatancy tends to be caused by low lateral stress and high bond strength, which contribute to low bond breakage as shown in Figures 4.26 and

4.27. Therefore, relatively low bond breakage may be linked to large dilation, probably due to the fact that more clusters, instead of debonded particles, are generated through less bond breakage. These clusters released from the bonding network bring about more volumetric dilation than the debonded particles. In contrast, the reduced bond breakage in the particle friction study (see Figure 4.28) corresponds to smaller dilation (see Figure 4.32). In this case, the high particle friction, which prohibits the rolling of clusters and debonded particles, is the dominant factor in the large dilation.

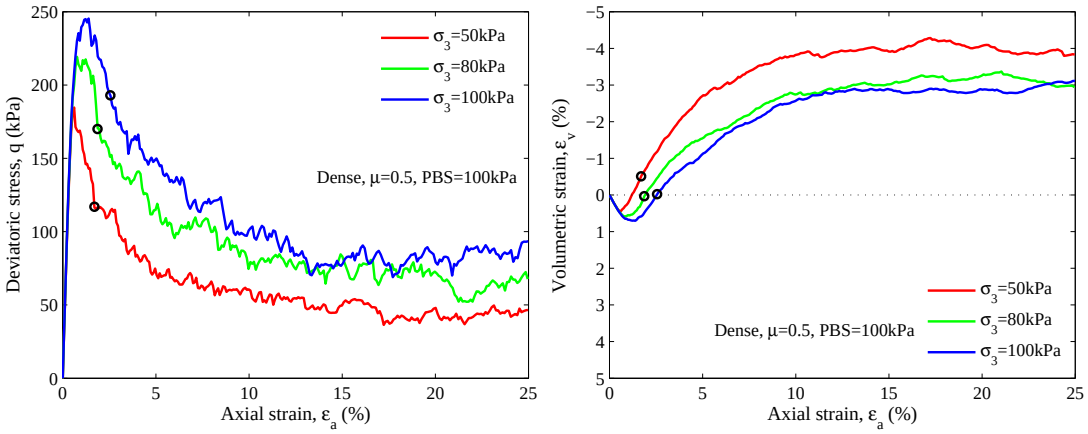

(a) Deviatoric stress versus axial strain *(b) Volumetric strain versus axial strain*

Figure 4.29: Variation of maximum dilatancy location with confining pressure for dense samples with particle friction coefficient 0.5 and bond strength 100kPa

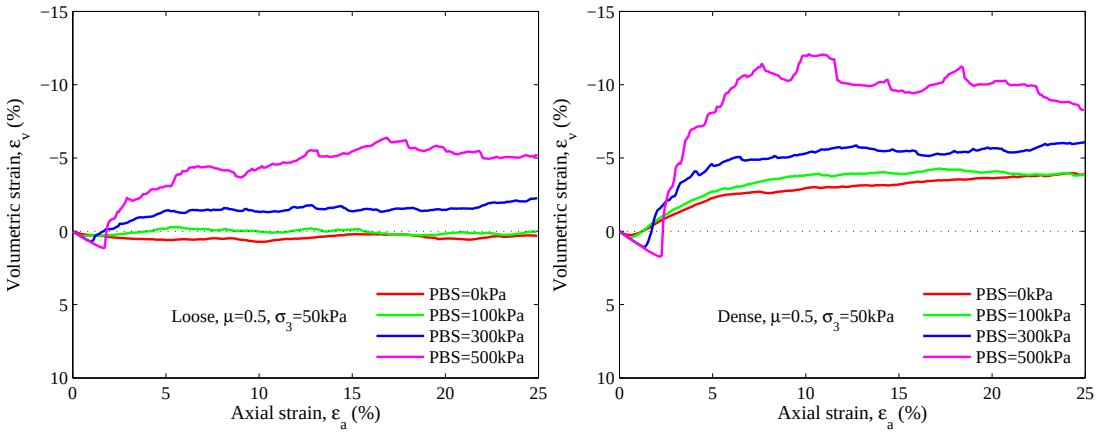

(a) Loose sample *(b) Dense sample*

Figure 4.30: Effect of bond strength and axial strain on volumetric strain for both loose and dense samples with particle friction coefficient 0.5 and confining pressure 50kPa

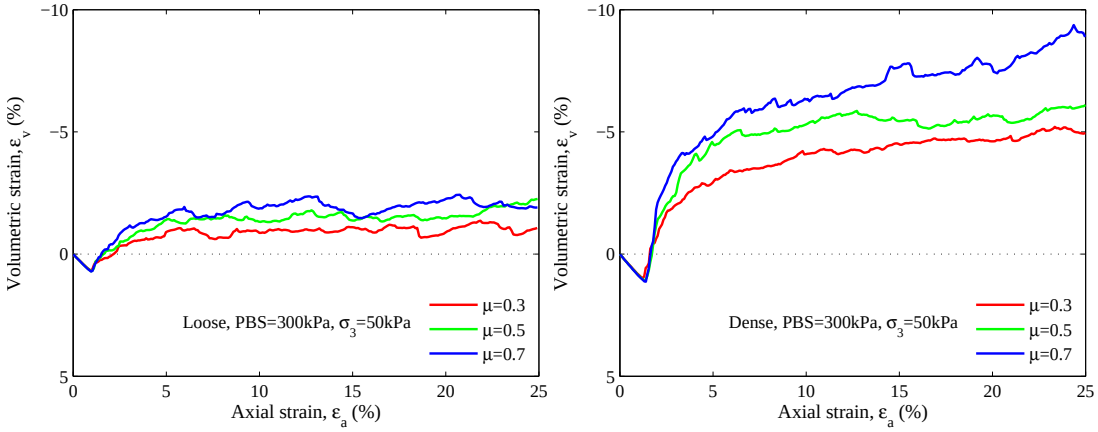

(a) Loose sample *(b) Dense sample*

Figure 4.31: Effect of particle friction coefficient and axial strain on volumetric strain for both loose and dense samples with bond strength 300kPa and confining pressure 50kPa

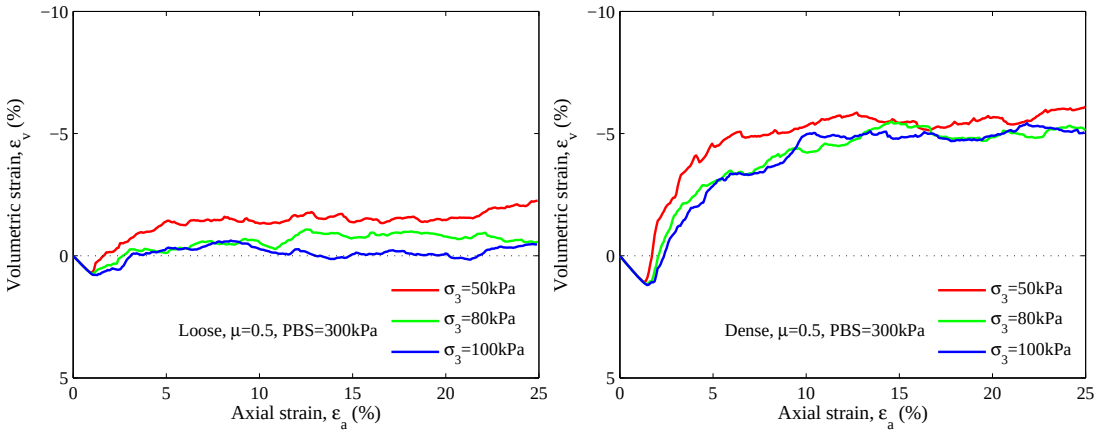

(a) Loose sample *(b) Dense sample*

Figure 4.32: Effect of confining pressure and axial strain on volumetric strain for both loose and dense samples with particle friction coefficient 0.5 and bond strength 300kPa

4.7 Summary

Biaxial compression tests have been simulated on bonded granular assemblies, and validated by comparison with laboratory findings in a qualitative way. As for the unbonded material, there exist four stages related to the development of deviatoric stress versus axial strain for the bonded specimen, i.e. linear increase stage, peak strength, stress decrease stage and a relatively steady state. The parallel bond radius has a significant effect on the peak strength, but not the ultimate strength. By increasing the bond size, peak strength rises greatly and the dilatancy response is more and more apparent. The effect of bond strength distribution on the behaviour has been studied as well. It is noted that the normal distribution produces similar mechanical responses (e.g. peak strength, ultimate strength, and volumetric contraction) to the case with uniform bond strength, except for the sample dilation and remaining bond number versus the axial strain. However, a Weibull distribution with different values of shape parameter k has been introduced to the bonded samples. A smaller initial stiffness is brought about by a lower value of k, which may be caused by a lower number of remaining bonds prior to shearing. When the parameter k is equal to 0.5, compared to the uniform bond strength, this bond distribution brings about lower peak strength. However, no difference in peak or ultimate strength is found between the uniform and Weibull bond distribution with k = 1.0 and 1.5. In addition, by increasing the k value, the overall volume dilation decreases at the ultimate stage of shearing. It is worth noting that there exits an occurrence of bond breakage during the sample consolidation, resulting from the weak bonds, which is different from the uniform and normal distributions.

A series of biaxial simulation tests has been carried out on bonded samples with uniform bond strength based on different sample compaction, particle friction coefficient, and a range of parallel bond strengths over various confining pressures. There is a significant increase in Young's modulus when adding the bond to the sample, although the modulus is insensitive to the bond strength. Moreover, the dense sample produces a larger Young's modulus than the loose. Compared to the sample compaction, the effect of particle friction and confining pressure on the modulus is not so apparent.

On the other hand, the Poisson's ratio decreases clearly for the bonded sample but, like Young's modulus, the ratio is unaffected by the bond strength. The loose sample yields a larger Poisson's ratio than the dense. Increased confinement reduces the ratio, while increased particle friction generally increases it. The primary yield stress can be obtained from the starting point of transition from a stiff to a less-stiff response. There is a linear increase in the primary yield stress for bonded samples with the increase of bond strength. Besides, this yield stress is affected by the sample density and particle friction coefficient but is independent of the confining pressures.

The strength parameters, internal friction angle and cohesion have been examined in terms of different sample compaction, parallel bond strength and particle friction. The dense sample produces a large friction angle. The friction angle decreases with the increase in bond strength, except that there is an increase for the high particle friction coefficient (i.e. 0.7) when the bond strength increases from 300 to 500kPa. Increased particle friction also yields an increased internal friction angle. The cohesion increases clearly with increased bond strength for both loose and dense samples. It is worth noting that the difference in cohesion between loose and dense samples becomes larger and larger by increasing the bond strength. Unlike the friction angle, the particle friction has hardly any effect on the cohesion, excluding the fact that the cohesion rises by increasing the particle friction for high bond strength, namely 500kPa.

Bond breakage during shearing with various confining pressures, bond strength and particle friction has been investigated. The simulation results clearly demonstrate that the number of intact bonds for a specific axial strain increases when decreasing the confining pressure and particle friction, as well as increasing the bond strength. The peak strength and the maximum dilatancy do not occur at the same axial strain, in agreement with the findings of Wang and Leung (2008a) but unlike the response of a purely frictional material where the peak strength takes place at the same axial strain as the maximum dilatancy. Bonded specimens yield a larger dilatancy than unbonded ones, probably owing to properly sized clusters and debonded particles generated by the bond breakage events (Wang and Leung, 2008a). Large overall dilatancy tends to result from high bond strength and low lateral confinement, associated with relatively

mild bond breakage. More clusters, instead of debonded particles, generated through reduced bond breakage, which probably leads to larger dilation. In contrast, smaller dilation arises from lower bond breakage in the particle friction study. The rolling of clusters and debonded particles is hindered by the high particle friction, which is probably the leading factor in the large dilation.

Chapter 5

Permanent Pavement Deformation Simulation for Unbonded Materials

5.1 Introduction

Permanent deformation in pavements for unbound materials has been investigated by means of DEM. The pavement model is first established, including the model dimensions, sample compaction condition, particle parameters and so on. Later, details of the modelling procedure are introduced. A periodic lateral boundary, instead of the wall lateral boundary is applied to the pavement simulation. The contact width between the wheel and pavement surface can be measured and then the mean contact pressure can be calculated. Also, the permanent deformation in pavements is traced for each wheel pass during the numerical simulation. After the introduction of the simulation procedure, the contact pressure distribution is studied. Compared to the vertical normal pressure, the horizontal normal pressure and resultant friction force can be disregarded. It is worth mentioning that whether stationary, translation or rolling loading, the motion mode has a negligible effect on the vertical normal pressure distribution, which can be represented by a Hertz distribution. The permanent pavement deformation versus number of wheel passes is used to make a comparison with the laboratory

results in a qualitative way.

Afterwards, the factors affecting the permanent pavement deformation are studied. Two kinds of pavement sample preparations are compared to one another, including particle radius expansion and self-weight deposition methods. In addition, the effect of wheel motion mode (i.e. translation or rolling) on permanent deformation is considered in the simulation. After that, two kinds of gravity accelerations (0.1 and 9.81m/s^2) for the pavement particles are investigated. The self-weight is found to be of great importance to the permanent deformation. Later, various wheel loads are applied to the wheel particle to study the mechanical responses of the pavement. Increased permanent deformation results from increased wheel load. Also, the initial sample compaction and particle friction coefficient have a significant effect on the behaviour of a pavement subjected to repeated wheel loading. The residual stress distributed in the pavement can be calculated on the basis of the difference between the current stress and the initial stress. The factors related to the distribution of residual stress are taken into account, which are wheel pass number and gravity acceleration as well as wheel pressure.

5.2 DEM pavement model

5.2.1 Introduction

Generally, the pavement design system can be classified into four categories, including fatigue analysis, wearing and permanent deformation design, settlement analysis and frost design. In this study, the permanent deformation of unbound granular materials is the focus of interest. With reference to Korkiala-Tanttu (2009), the permanent deformation of a pavement (i.e. rutting) can be divided into three parts, which include the wearing of the asphalt layers, compaction and shear deformations. In addition, four varied mechanisms of permanent pavement deformation have been proposed by Dawson and Kolisoja (2004), namely Modes 0 to 3. The mechanisms are comprised

of particle crushing, shear deformation, compaction, and subgrade deformation. The most common permanent deformation in pavements is a combination of these fundamental mechanisms. As summarized by Korkiala-Tanttu (2009), there are a number of material factors affecting the rutting, including grain size distribution, maximum grain size, content of fines, compaction degree, the grain shape and the surface roughness of grains. In addition, the structural factors for permanent deformation consist of the number of load repetitions, pavement structure geometry (e.g. layer thickness), the initial state of the pavement layers (e.g. anisotropy), load factors (e.g. maximum load, loading rate, and wheel type), temperature and moisture conditions, and periodical conditions (e.g. seasonal changes). In the studies on traffic-load-induced permanent deformation in pavements, it is a very complex task to take into consideration all the factors displayed above. Therefore, some factors are considered in the material parameters, some are implemented into the empirical or mechanistic-empirical calculation process, and some are disregarded.

Empirical methods are most widely used to design flexible pavements, e.g. the American Association of State Highway and Transportation Officials (AASHTO) guide. Therefore, a series of empirical equations have been put forward to calculate the rutting of a pavement subjected to repeated loading. One of them is the power equation put forward by Monismith et al. (1975), which has been commonly applied. The determination of the constants in the power equation was studied by Li and Selig (1996) where the magnitude of the applied wheel load, as well as the strength and physical state of the subgrade are taken into account in the equation. Additionally, the South African Mechanistic Design Method (SAMDM) has been applied in South Africa, which is a mechanistic-empirical design method including permanent deformation transfer functions for unbound pavement layers and the roadbed (Theyse et al., 1996). Nevertheless, the contribution of each pavement layer to the overall permanent deformation is not considered. Later, a permanent deformation model was developed to predict the displacement of individual pavement layers (Theyse, 1997). In the mechanistic-empirical framework, the linear elastic system is usually assumed for the primary response model (e.g. Monismith et al., 1977; NCHRP, 1999). In addition, a linear elastic model, in-

cluding the viscoelastic response, can be applied in the VESYS program (Kenis, 1977). However, a nonlinear finite element model is recommended by Lytton et al. (1993) after a comparison of the strengths and weaknesses between the linear and nonlinear primary models. Furthermore, an analytical-mechanical method has been proposed to calculate the permanent deformation in unbound pavement materials over some years by Korkiala-Tanttu (2009). This calculation method was generated based on the results of full-scale accelerated pavement tests along with the complementary laboratory tests and finite element calculations. The suitability of this calculation method application to Swedish roads comprising thin asphalt layers over a thick unbound granular material base has been assessed by Qiao et al. (2014). It can be used to predict the development of rutting depth in thin flexible pavements despite some overestimations. Generally, the contribution of light traffic load to rutting is ignored. Therefore, the axle load with the largest contribution to permanent deformation is the design axle load (Uzan, 2004).

A series of wheel tracking tests was carried out on various layered pavements in the laboratory by Juspi (2007). The permanent deformation in pavements was studied on the basis of the different wheel loads. Two apparent stages relating to permanent deformation were observed, i.e. a rapid deformation rate and a gradual rate of plastic deformation. According to these two stages, the permanent deformation in pavements could be classified into three categories, labelled as Types 1, 2 and 3. At the beginning of the test, there was a rapid plastic deformation and, if a gradual decrease in deformation rate followed, the permanent deformation curves were categorised as Type 1 or 2. If neither of these, the category would be Type 3. The difference between Types 1 and 2 was the deformation rate at the second stage. If the rate was very small (less than 0.001mm/pass) or zero, it was classified as Type 1, i.e. pavement shakedown. Moreover, Ravindra and Small (2008) investigated the behaviour of pavements under repeated single wheel loading. The pavements consisted of crushed concrete as base and Silica sand as subgrade. The accumulated permanent deformations were traced and the shakedown theory was validated. In general, the experimental results of the full scale road are limited by the functions of the laboratory devices and test costs. On

the other hand, a number of repeated load triaxial tests were performed on a crushed rock sample subjected to different stress states (Werkmeister et al., 2004). The permanent deformation accumulating with the repeated loading was studied. Three types of permanent deformation accumulation were found, i.e. plastic shakedown range, plastic creep response and incremental collapse. An equation was also proposed to define the stress ratio of the boundaries between these responses.

There have been a few simulation results on the pavement by means of DEM. A 3D modelled flexible pavement was established, including an asphalt layer and granular subbase and subgrade courses (Dondi et al., 2007). The model parameters were determined by a comparison between the laboratory and numerical results. The viscoelastic behaviour of the simulated pavement subjected to two circular contact patches was studied. The contact stress distributions within the simulated section were observed in terms of vertical, horizontal and shear stresses. The degradation of particles in a granular base for a flexible pavement was investigated via the PFC^{2D} program by Vallejo et al. (2006). The asphalt concrete layer was simulated by a number of particles bonded together. There was no occurrence of bond breakage during the repeatedly modelled wheel loading. The base layer was comprised of unbound particles with uniform particle size and friction coefficient. Particle crushing was only allowed to take place in the base course. It is worth mentioning that particle crushing commenced at the top of the granular base course and went on to spread towards the bottom of the base layer. In addition, the particle breakages mainly occurred during the first wheel pass and a decreasing rate was found for subsequent traffic loads. The behaviour of asphalt materials has also been satisfactorily modelled using DEM by a few pioneers (e.g. Chang and Meegoda, 1997; Collop et al., 2004; Dondi et al., 2005).

Nevertheless, these studies have concentrated only on modelling the behaviour of specimen elements but not the whole pavement layer. Besides, there have been some DEM studies focusing on the elastic-plastic behaviour of elementary specimens of unbound granular materials under quasi-static repeated loading (e.g. Garca-Rojo and Herrmann, 2005; Luding et al., 2007). The accumulated permanent deformation with the repetition of external loading was traced. The mechanical responses: shakedown (i.e. the

ceasing of plastic strain accumulation) and ratchetting (i.e. the continued accumulation of permanent deformation in each loading cycle) were observed. Reducing the particle friction coefficient or increasing the magnitude of repeated loading resulted in a transition from shakedown to ratchetting. According to the discussion above, there exists a gap in the DEM simulation of permanent pavement deformation subjected to repeated wheel loading. Therefore, the factors affecting the permanent deformation in pavements will be investigated at a grain scale.

5.2.2 Pavement preparation

In this section, the subbase layer of a pavement structure is modelled using DEM. The typical particle grading for the pavement subbase layer is plotted in Figure 5.1 (AASHTO, 1993). The particle size ranges from lower than 0.075mm to larger than 40mm. The difference between the largest and smallest particle sizes is great. The fine grains lead to a huge number of particles in DEM simulation. However, the modelled contact forces are mainly transmitted through the structure formed by the large sized particles. Therefore, it is very difficult and not necessary to model the real particle size distribution. In this study, a particle fraction (i.e. 10mm$\leq d \leq$15mm) is selected to simplify the simulation and data analysis where d is the particle size. The corresponding pavement particle radius ranges from 5 to 7.5mm, which is consistent with the biaxial test simulation for unbound granular materials (see Section 3.4). The selection of particle stiffness is important to the DEM simulation. If the particle stiffness is too great, the computation time will increase substantially, which is very disadvantageous for pavement simulation subjected to repeated wheel loading. However, it is logical that the permanent deformation in pavements is mainly induced by rearrangements of pavement particles but not by overlaps between particles. Therefore, the stiffness of pavement particles has a negligible effect on the permanent deformation. With reference to the modelled particle parameters in Section 3.4, both normal and shear stiffnesses of the pavement particles are selected as 5×10^8N/m. In addition, the specific gravity of the pavement particles is chosen as 2.7 and the particles have unit

thickness, namely 1.0m in this study.

In pavement simulation, the contact area between the vehicle wheel and pavement surface is an important factor to determine the dimensions of the modelled pavement structure. The approximate parameters for different vehicles (i.e. private car, light truck, and heavy truck) are given in Table 5.1, with wheel load, contact pressure, contact radius and tyre radius included. According to Thom (2008), the contact area is often assumed to be circular, which can be calculated on the basis of the wheel load and contact pressure (i.e. tyre pressure). In DEM simulation, the vehicle wheel is modelled using a large particle. The contact range between the wheel particle and the pavement surface is a line segment, rather than a circular area in the two-dimensional case. In this study, the radius of the wheel particle is set as 0.3m, and it is similar to the real size of the vehicle wheel. In order to simplify data analyses, the half contact width a is fixed to be approximately 0.06m by adjusting the wheel particle stiffness for different wheel loads. Sensitivity studies are performed to determine the size of the DEM pavement model. The permanent pavement deformation is mainly affected by the stress field in pavements induced by the wheel pressure. It is found that when the dimensions of the DEM pavement model are selected as $30a$ in length and $15a$ in height, a further increase in the size of the modelled region hardly affects the vehicle-induced stress field in pavements. Considering the consolidation settlement in pavement preparation, the initial size of the pavement model is 1.8m long $\times$ 1.0m high.

As in the biaxial test simulation, the particle radius expansion method (see Subsection 3.3.3) is used to prepare the pavement specimen. A rectangular vessel is built with two vertical and horizontal massless walls. The stiffness of the horizontal walls is identical to the particle stiffness, while the vertical wall stiffness is one-tenth of it (i.e. 5×10^7N/m). No friction is applied to the walls to avoid the arching effect of end boundaries. The initial friction coefficient of pavement particles for sample generation is set at 0.5. The porosity of the initial pavement sample is 0.30. Nearly ten thousand discs are generated in the sample. The consolidation process is used in order to obtain an isotropic sample. Prior to sample consolidation, the friction coefficient of the particles is changed from 0.5 to 0.7. The servomechanism (see Subsection 3.3.3)

is applied isotropically to consolidate the sample to a stress state, i.e. the confining pressure equalling 100kPa. Then, the void ratio of the sample can be calculated as the initial one, which is 0.26. After that, the pavement sample is unloaded to a stress-free state (see Figure 5.2a). The top wall boundary is removed. Then the pavement sample with a wall (rigid) lateral boundary is generated (see Figure 5.2b). If the lateral boundaries are replaced by periodic ones, the periodic boundary sample will be built (see Figure 5.2c). The reason for this boundary replacement will be described in Subsection 5.2.3. The gravity acceleration 9.81m/s^2 is introduced to the pavement particles and a large number of computation cycles are executed to make the set-up complete. It is observed that the void ratio remains unchanged (i.e. 0.26) after the gravity application, indicating that the pavement settlement induced by the self-weight stress can be disregarded. The initial pavement height can be calculated on the basis of the positions of the deleted top wall and bottom wall, which is nearly 0.92m. Afterwards, the wheel load is applied to the pavement specimen through a wheel particle (see Figure 5.2d).

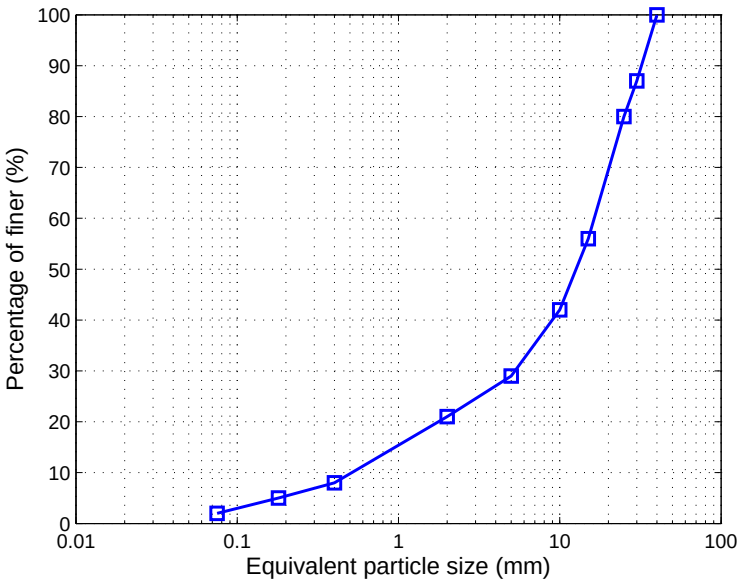

Figure 5.1: The typical particle size distribution of pavement subbase layer (AASHTO, 1993)

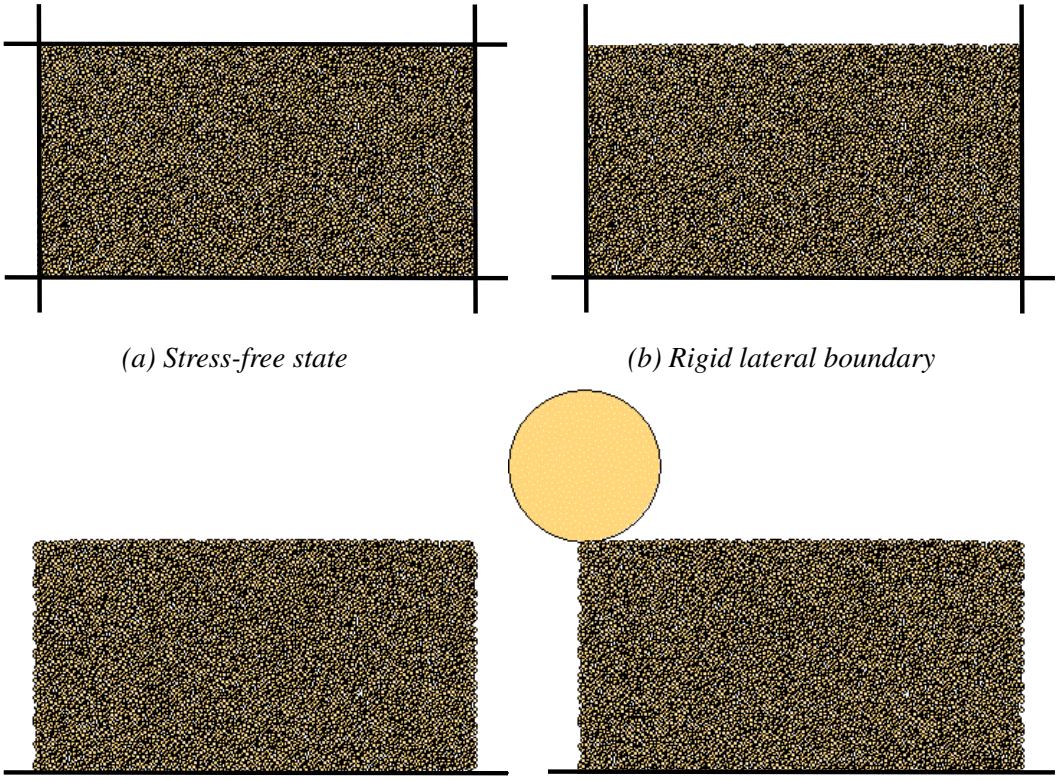

(a) Stress-free state *(b) Rigid lateral boundary*

(c) Periodic lateral boundary *(d) Pavement model*

Figure 5.2: The pavement preparation in DEM simulation

	Wheel load (kN)	Contact pressure (kPa)	Contact radius (m)	Tyre radius (m)
Private car	3	250	0.06	0.3
Truck (single tyre)	26	550	0.123	0.45
Heavy Truck (single tyre)	40	800	0.126	0.50

Table 5.1: The general parameters for varied vehicles

5.2.3 Modelling procedure

After the sample preparation, the wheel particle is produced on the top surface of the pavement (see Figure 5.2d). Compared to the pavement particles, the specific gravity of the wheel particle is set to be negligible in order to eliminate the disturbance of gravity load. A constant external force is applied to the centre of the wheel particle. Then the wheel particle will contact the pavement particles which exert the reaction forces on the wheel particle. The resultant reaction force (denoted as the contact force) can be calculated in PFC^{2D}. When its magnitude reaches the value of the external load, the modelled wheel starts to move from the left to the right boundary with a constant velocity. The travelled distance is traced all the time. When the wheel moves to the middle of the pavement surface, the contact width and contact force are measured and recorded. The pavement particles touching the wheel are first found and then their maximum and minimum coordinates in the horizontal direction are determined. The difference between these two coordinates is the contact width. The wheel continues to move until the right boundary is reached. At this time, the permanent pavement deformation is obtained and recorded.

The pavement surface consists of a number of particles with varied radii. It is neither continuous nor flat. For the purpose of determining the permanent deformation, the measured pavement surface is separated from many small fragments with a length of 0.03m in the horizontal direction. The summations of the vertical coordinate and the radius for particles belonging to each fragment could be obtained, the maximum of which is considered as the value of the corresponding vertical position of this fragmental pavement surface in DEM simulation. Therefore, the pavement surface location in the vertical direction can be calculated by averaging the position values of all the fragments. Then, the difference between the initial and current pavement surface locations is the permanent deformation.

After the first loading pass is finished, the simulated wheel goes on to move forwards. Because the lateral boundaries are periodic, the second round of repeated wheel load for the pavement sample commences. As in the case of the first wheel pass, the contact

width and contact force are determined and saved in the middle of the following wheel passes. Moreover, the permanent deformation is measured and recorded at the end of each wheel pass. As described in Subsection 2.2.4, when a wheel travels on a pavement surface, each element in the pavement structure experiences the loading and unloading processes. The vertical, horizontal and shear stress components are included and a rotation of the principle stress axes is observed. The deformation behaviour of a road pavement subjected to a moving wheel load consists of a resilient deformation and a permanent deformation.

According to Subsection 3.2.7, if the left and right boundaries are periodic in the pavement simulation, the simulated top surface of the pavement can be regarded as a circle, as shown in Figure 5.3 where the red point stands for the wheel particle and the red arrows for motion directions. The wheel moves from the left to the right boundary for each pass, meaning that the red point travels along the circle and finally returns to the original position. Consequently, all the vertical sections in the DEM pavement specimen will undergo the same stress paths of principle stress axes rotation. The pavement response is identical in the same horizontal level after each load pass. The stress state at a certain depth of pavement can be calculated through averaging all the values of stress in the corresponding cross section, which are obtained by the measurement circles in PFC^{2D}. This averaging method is beneficial to eliminate the discreteness of individual measured values. In addition, microscopic statistical analysis can be better performed on the basis of uniform pavement behaviour at the same depth.

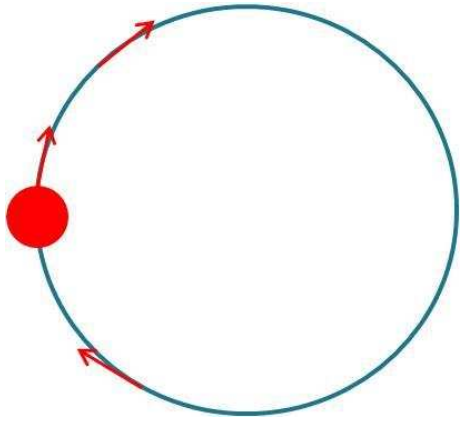

Figure 5.3: Circular boundary developed from pavement periodic lateral boundary

5.2.4 Contact pressure distribution

The traffic contact pressure could be assumed to be a Hertz or trapezoidal distribution under plane strain conditions (e.g. Yu, 2005; Yu and Hossain, 1998) while the contact loading could be simplified to a Hertz distribution acting on an elliptical or circular area in three dimensions (e.g. Ponter et al., 1985; Yu, 2005). In this subsection, the contact pressure distribution between the wheel particle and the pavement surface is studied. The individual contact forces and contact lengths between the wheel particle and each pavement particle can be determined in PFC^{2D}, as shown in Figure 5.4. Individual contact forces include normal force F_n and friction force F_s. The normal force can be divided into a horizontal normal force F_{nx} and a vertical normal force F_{ny}. It is assumed that stress is uniformly distributed on each contact width and then the value of the individual contact stresses can be calculated. The pavement model with periodic boundary is used to determine the contact pressure distribution, as shown in Figure 5.5.

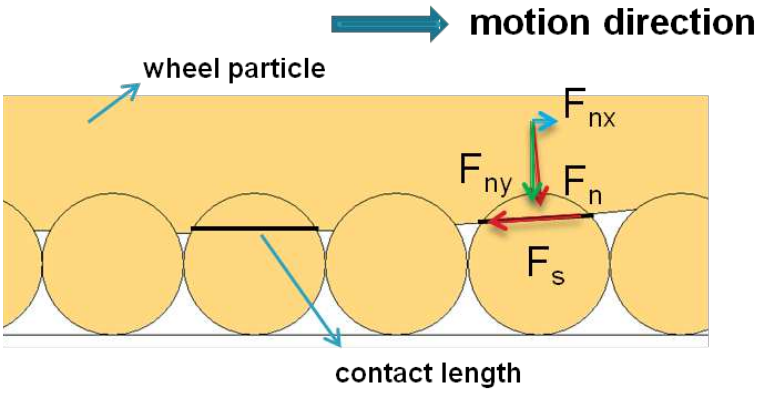

Figure 5.4: Contact forces between wheel and pavement particles

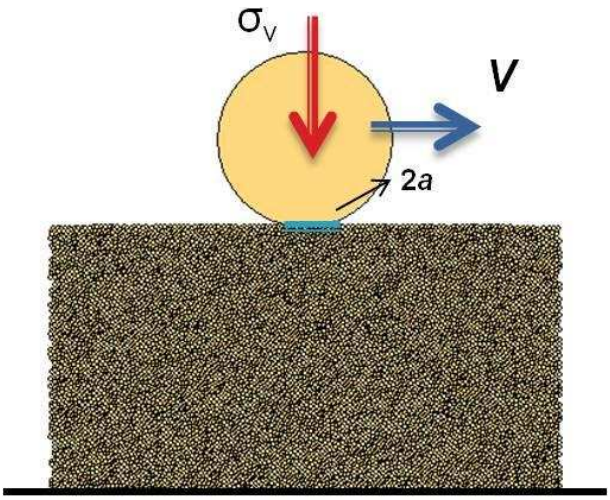

Figure 5.5: The pavement model with periodic lateral boundary

There are three kinds of wheel loads exerted on the pavement model, namely stationary wheel load, translational and rolling wheel load. In this study, the wheel particle is subjected to a concentrated force F_v in the centre, which is 700N. The wheel particle stiffness is selected as 4×10^4N/m and then the contact width $2a$ is kept at nearly 0.06m. For static loading, the friction coefficient of the wheel particle has a negligible effect on the contact pressure distribution, based on sensitivity studies. Hence, the friction coefficient of the wheel particle is assigned as zero in the case of static loading. In order to facilitate the data analysis, there is also no friction between the wheel and pavement particles for translational wheel load. The translational velocity V remains unchanged during the wheel movement, which is 0.5m/s. When the pavement model is subjected to rolling wheel load, a constant angular velocity ω_0 is applied on the wheel particle, which makes the wheel move on the pavement surface with a constant linear velocity V_0. The linear velocity is selected as 0.5m/s and the corresponding angular velocity can be calculated on the basis of the equation: $V_0 = \omega_0 \times r$ where r is the radius of the wheel particle, i.e. 0.3m. In this case, the friction coefficient for the wheel particle is set as 0.7, identical to the pavement particles. Therefore, the sliding friction coefficient between the wheel and pavement surface is 0.7, which is consistent with the situation of a dry pavement surface in practice. The linear velocity is traced in the simulation and can be kept at 0.5m/s.

The normal contact pressure between the wheel particle and pavement particles is divided into the vertical and horizontal components. The vertical component for stationary loading is plotted in Figure 5.6a, and Figure 5.6b illustrates the normal contact pressure distribution in the horizontal direction, which is antisymmetrical. Compared to the vertical component, the horizontal is quite small. For both the maximum values, the horizontal component is nearly 5% of the vertical. For the sake of simplification of the simulation, the horizontal normal pressure is not taken into consideration. The normal pressure distributions in the vertical direction for various wheel loads are described in Figure 5.7, where normal contact pressure is measured when the wheel particle moves to the middle of the pavement surface for the moving loading. With regard to the stationary loading, the wheel particle is generated in the middle pavement surface and subjected to external loading. The contact pressure is obtained. It is noted that there is no significant difference between stationary, translation and rolling loadings, which is in good agreement with the findings of Marwick and Starks (1941). The DEM simulation result is also compared to the Hertz distribution, showing a good agreement (see Figure 5.8). Since friction exists between the wheel particle and the pavement surface for rolling loading, the rolling resistance coefficient C_{rr} can be calculated on the basis of the formula: $F = C_{rr}N$ where F is the rolling friction force, and N is the vertical normal force. In this study, the resultant friction force can be measured, which is nearly 20N, and the applied force is 700N. The rolling resistance coefficient is calculated, and its value is 0.029. In comparison with the normal contact pressure, the friction stress can be disregarded.

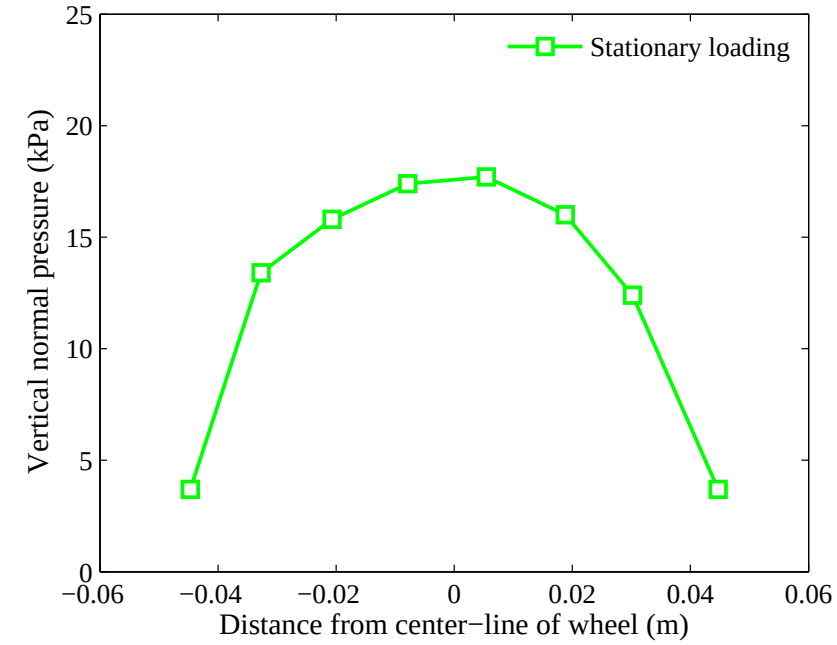

(a) Vertical normal pressure

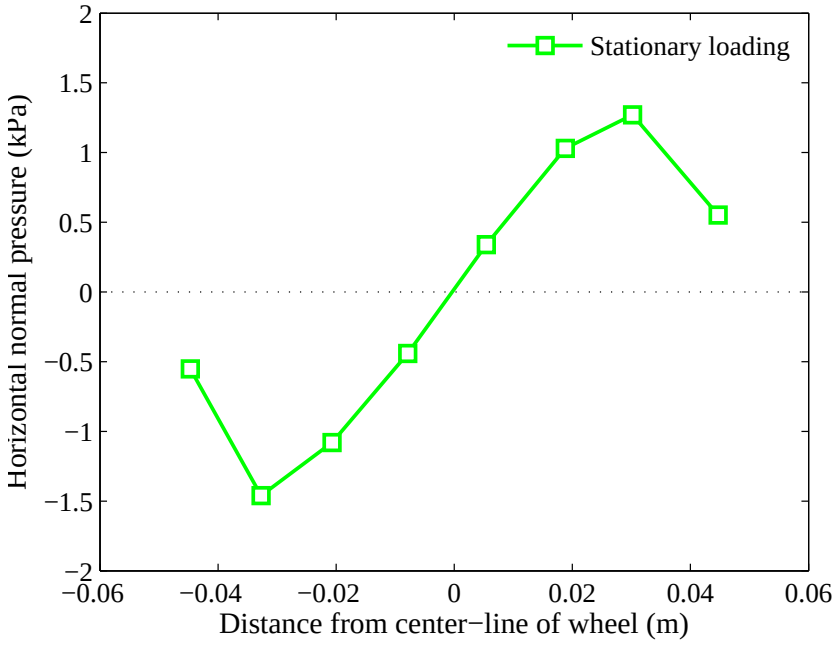

(b) Horizontal normal pressure

Figure 5.6: The vertical and horizontal normal pressure distributions for stationary loading

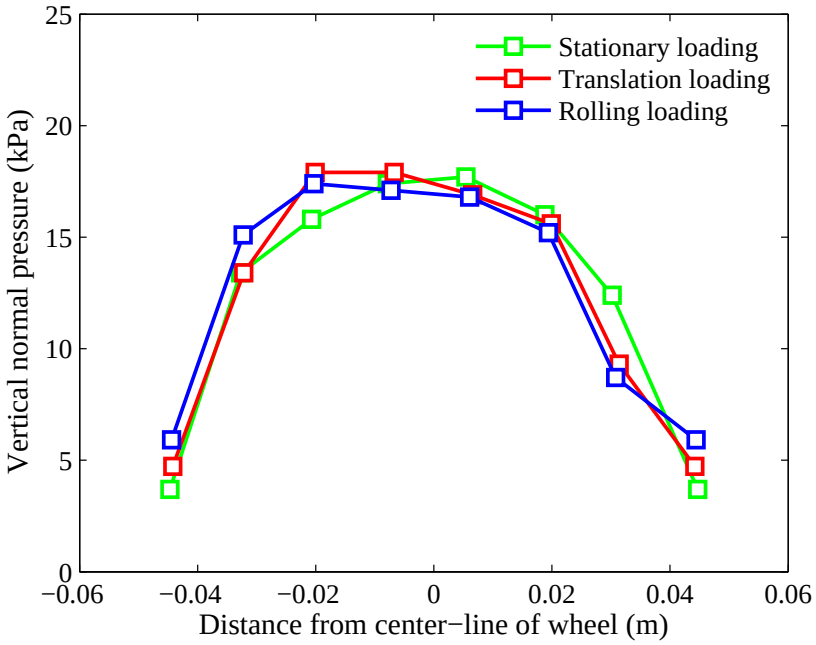

Figure 5.7: Comparison among various wheel loads for vertical normal pressure

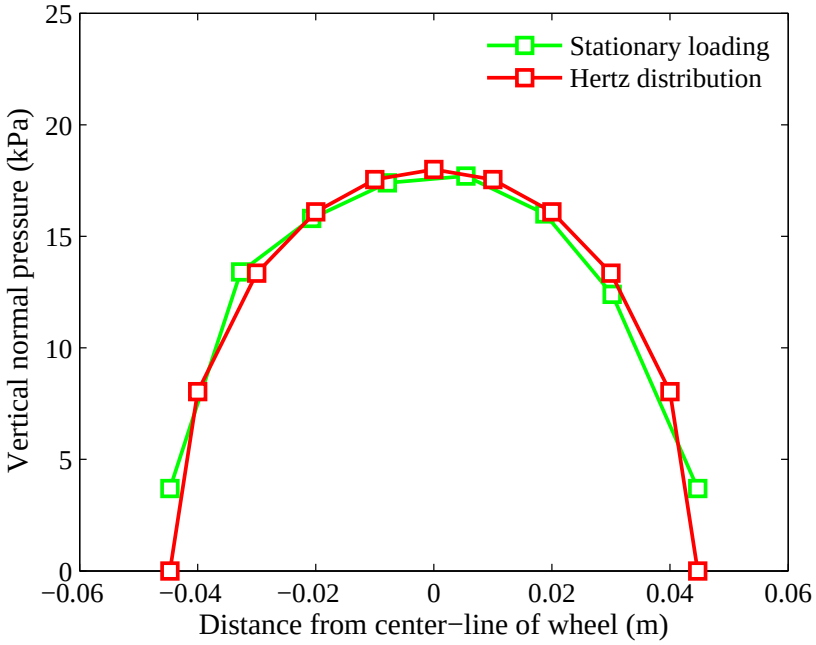

Figure 5.8: Comparison between simulated result and Hertz distribution for vertical normal contact pressure

5.2.5 Procedure validation

5.2.5.1 Periodic boundary

In this study, two different boundary conditions are used to simulate the process of wheel loading. The first one is to use walls to model the left and right pavement boundaries (i.e. rigid lateral boundary), while the second substitutes periodic boundaries for walls as the lateral borders in DEM simulations. A comparison is made as a validation of the application of the periodic boundary. For the periodic boundary, if only one vertical section in the pavement goes through the complete process of loading and unloading, the entire pavement model will experience it. The size of the DEM pavement model with periodic lateral boundaries is determined on this basis. Provided that the pavement model with a rigid lateral boundary has the same size as the periodic boundary model, only the vertical section in the middle undergoes the entire process of loading paths after each load pass. For the purpose of studying the pavement response, the length of the pavement model with the rigid lateral boundary is enlarged from $30a$ to $40a$. The middle section with a length of $10a$ (i.e. 0.6m) can experience the complete loading path. Its surface is used as the measured pavement surface to study the permanent deformation of the pavement. In contrast, in the case of the periodic lateral boundary, the entire pavement surface is treated as the measured surface. The measurement method for permanent deformation in pavements has been presented at the beginning of Subsection 5.2.3.

The preparation of the rigid boundary pavement is analogous to the periodic boundary sample and all the particle parameters for different pavement samples are identical (see Subsection 5.2.2). The initial height of pavement vessel remains 1.0m. The particle radius expansion method is employed to generate the pavement sample with rigid lateral boundary, which includes approximately fourteen thousand particles. Afterwards, the sample is isotropically consolidated to the target stress state of 100kPa. The void ratio is measured as the initial one, which is 0.26, identical to that of the periodic model (see Subsection 5.2.2). Later, the pavement model is unloaded to a stress-free state.

In the periodic situation, the top and two vertical walls are removed and a periodic boundary is introduced as the lateral boundary. According to the rigid lateral boundary, just the top wall is deleted (see Figure 5.2b). Finally, the gravity acceleration of 9.81m/s^2 is applied to the pavement particles. At this time, the height of the pavement sample is measured, which is nearly 0.95m, larger than 0.90m (i.e. $15a$) as required for pavement simulation.

A concentrated load of 700N is exerted at the centre of the wheel particle. Both normal and shear stiffnesses of the wheel particle are set as 4×10^4N/m in order to achieve an approximate contact width of 0.06m. The friction coefficient of the pavement particles remains 0.7 during the moving wheel load. In the rigid boundary case, the wheel particle is generated on the top of the left boundary, which will be removed after it travels along the pavement surface to the right boundary. Then one load pass is finished, and a new wheel particle is created to repeat this loading process. The concentrated load applied on the wheel particle is kept constant during the wheel movement. It is worth mentioning that the motion mode is a translation with a constant velocity of 0.5m/s. There is no friction between the wheel and pavement particles. Consequently, the pavement simulation is simplified. The effect of translation velocity on permanent deformation in pavements will be investigated in Subsection 5.3.1.

A comparison of permanent deformation between periodic and rigid lateral boundary is plotted in Figure 5.9, where there is not much difference between these two boundary conditions at a low number of wheel passes. Later, some difference develops with a similar variation in the rate of deformation. This deformation difference is probably due to the different measurement ranges for pavement surface displacement but not the varied boundary conditions. When the wheel pass number ranges from 100 to 200, the average diversity ratio of permanent deformation is approximately 5%. Hence, the periodic boundary can be used to investigate pavement behaviour subjected to repeated wheel loading. Because the stress paths are identical for the periodic boundary after each load pass in the same cross section, it will be beneficial to obtain the pavement stress distribution using measurement circles and to perform microscopic statistical analysis in the future. In addition, the contact width and contact force are recorded for

each of the load passes. The average contact width is nearly 0.10m and the measured contact force is 700N.

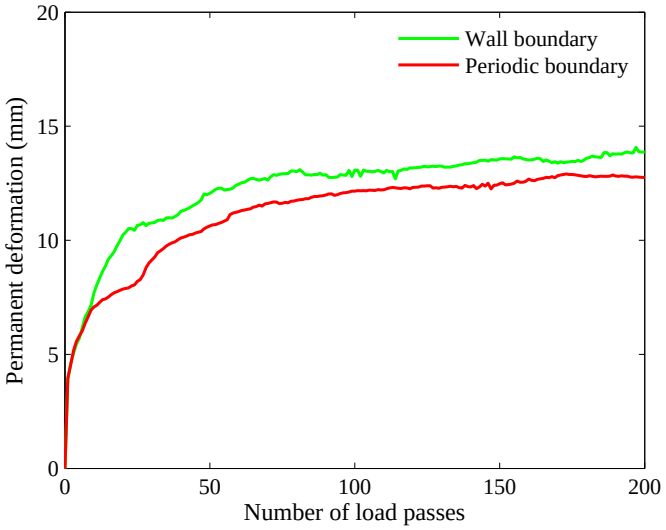

Figure 5.9: Comparison of permanent deformation between periodic and rigid lateral boundary

5.2.5.2 Permanent deformation

The permanent deformation in pavements was investigated in a small wheel tracker developed formerly to study the rutting resistance of asphalt slabs (Brown et al., 2008). The pavement specimens were prepared in a mould 400mm long $\times$ 280mm wide $\times$ 250mm deep. The apparatus (see Figure 5.10) has a 200mm diameter steel wheel with a solid rubber tyre of 50mm width through which a constant load is applied to the test samples. The wheel load was exerted by a weight hanger and a lever arm. An electric motor was used to drive the sample mould to reciprocate relative to the wheel. The reciprocation rate was controlled by the motor speed and was set at 40 passes per minute. The surface permanent deformation was measured by an LVDT. The test material, Portaway sand, was poorly graded and the maximum particle size was 6mm. It was compacted in three layers within the mould by a vibrating hammer. In order to obtain a dense sample, the optimum water content was used for the sands. It is worth mentioning that the wheel load was bidirectional rather than unidirectional because of the limitation of the test apparatus. The latter reflects the real situation

in a road pavement and smaller rut depth is caused than in the case of the former (Brown and Chan, 1996). The wheel load tests were carried out on the top of a 1.5mm thick rubber sheet in order to minimize the drying of the test specimens. Otherwise, they quickly became dry, especially on the surface and the charateristics of the sand specimen were changed. For the sake of determining the contact area between the wheel and the sample surface, the tyre was inked and subjected to static loading on a piece of graph paper placed on the soil surface. The contact area was measured through the footprint generated on the paper. The rolling resistance coefficient was also determined, which was 0.08. The measurement details were described by Juspi (2007). The test results corresponding to permanent deformations are plotted in Figure 5.11a, where two wheel loads were applied in the tests, which were 79 and 104N respectively. The corresponding mean contact pressures were calculated as 111 and 127kPa based on the measured contact areas.

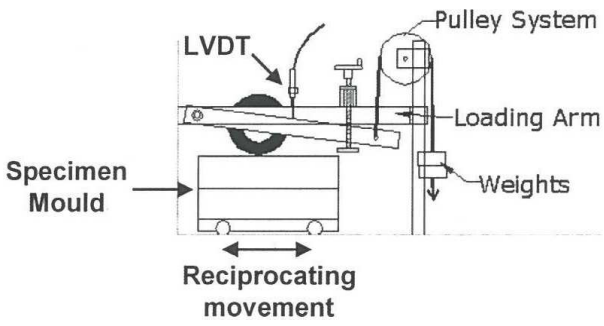

Figure 5.10: The wheel tracking apparatus (Brown et al., 2008)

For the DEM pavement simulation in two dimensions, the lateral boundary is periodic. The details about the particle parameters and pavement preparation are described in Subsection 5.2.2. The motion mode of the simulated wheel is rolling with the constant angular rate of 1.667rad/s. Like the pavement particles, the friction coefficient of the wheel particle is 0.7. The applied wheel loads are 200 and 700N and the corresponding stiffnesses of wheel particles are assigned as 1×10^4 and 4×10^4N/m. The contact widths between the wheels and the pavement surfaces are measured in the middle of individual wheel passes. The average contact widths can be calculated, which are both approximately 0.10m for the wheel loads of 200 and 700N. Therefore, the related mean contact pressures are computed as 2.0 and 7.0kPa. The modelled permanent de-

formations are demonstrated in Figure 5.11b. In the laboratory tests, there is a rapid plastic deformation rate for both of the contact pressures at first. When the contact pressure is relatively low, namely 111kPa, the plastic deformation rate gradually decreases to nearly zero after 1000 wheel passes, regarded as pavement shakedown (see Figure 5.11a). A continuing nonzero deformation rate is observed for a high wheel pressure, namely 127kPa. Similarly, an early rapid plastic deformation rate is seen, regardless of wheel pressure, in the DEM pavement simulation. The deformation rate reduces to nearly zero for a wheel pressure of 2.0kPa and an approximately constant rate is found for the relatively large wheel pressure, i.e. 7.0kPa. Because of the limitation of computation speed, the simulated wheel loading stops at pass 800, which takes more than one month using a standard computer. The computer processor is Intel(R) Core(TM) i3-2120 CPU 3.30GHz 3.30GHz and the installed memory (RAM) is 4.00GB. In conclusion, the pavement behaviour can be well simulated using DEM in a qualitative way. Like the laboratory results, the rapid early rate and the subsequent lower rate (i.e. nearly zero or nonzero) of rutting are replicated in the numerical simulation. Pavement shakedown (i.e. no further accumulation of permanent deformation) and ratchetting (i.e. continued accumulation of plastic deformation) are both reflected in the numerical results.

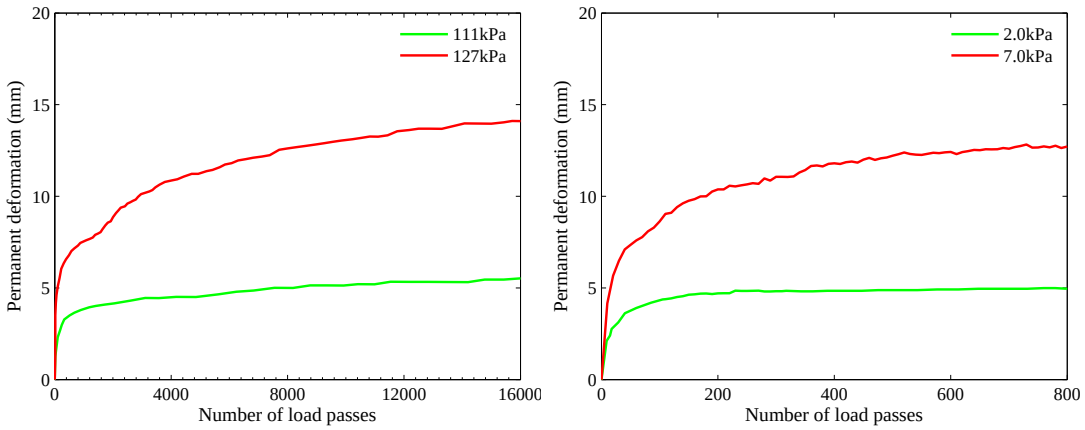

(a) Laboratory results (Brown et al., 2008) *(b) Simulation results*

Figure 5.11: The permanent deformation versus wheel pass

5.3 Factors affecting permanent deformation

5.3.1 Wheel velocity

A large wheel velocity tends to bring about the dynamic behaviour of a pavement by which the rutting will be affected. As referred to in previous investigations (e.g. Juspi, 2007; Ravindra and Small, 2008; Vallejo et al., 2006), the influence of wheel velocity is always disregarded, even in the study of a quasi-static pavement phenomenon (i.e. shakedown). Therefore, the effect of wheel velocity on permanent deformation is investigated in the present research. A reasonable velocity is determined to satisfy the quasi-static response of the pavement and to study the effect of the other factors on pavement behaviour. The particle parameters and pavement model are described in Subsection 5.2.2, where the particle radius expansion method is applied to create the pavement model. The periodic lateral boundary is introduced, and the gravity acceleration for pavement particles is 9.81m/s^2. The friction coefficient corresponding with the pavement particles is 0.7. The motion mode of the wheel is translation and three different wheel rates are taken into consideration, namely 0.5, 1.0 and 1.5m/s. The friction coefficient of the wheel particle is set at zero and therefore, there is no friction between wheel and pavement surfaces. Two different wheel loads are exerted on the centre of the wheel particle, i.e. 200 and 700N and their corresponding stiffnesses of the wheel particles are set at 1×10^4 and 4×10^4N/m. The mean contact pressures $\bar{p}$ are calculated as 2.0 and 7.0kPa, based on the average contact widths, both of 0.10m, which are identical to the wheel rolling situation (see Subsection 5.2.5).

The modelled results relating to permanent deformation are presented in Figure 5.12. Irrespective of the wheel velocity, a large rate of plastic deformation commences at first, and then the rate gradually decreases until an approximately steady rate is reached. There is no difference in permanent deformation for different wheel velocities at a low number of wheel passes. After that, a correspondingly high wheel velocity (i.e. 1.5m/s) produces a small permanent deformation for a given number of wheel passes, whereas a decrease in wheel velocity from 1.0 to 0.5m/s has a negligible effect

on the rutting. It seems that the final approximately constant rate of plastic deformation is independent of the wheel velocity, noting that the constant deformation rates are all nearly zero for a mean contact pressure of 2.0kPa while a continued accumulation of rutting is observed for a contact pressure of 7.0kPa. The deformation rate in units of millimetres per 100 passes is shown in Figure 5.13, where a rapid decrease in the deformation rate is observed prior to pass 200 for both wheel pressures. The deformation rate is nearly equal to zero from pass 500 to 800 for the low contact pressure of 2.0kPa. The relatively constant deformation rate starts from pass 400 for the contact pressure of 7.0kPa, although with some fluctuations. In conclusion, when the wheel rate is less than or equal to 1.0m/s, the permanent deformation is largely unaffected and, therefore, the quasi-static response can be reflected in the numerical study. A rate of 0.5m/s is selected to study the other factors affecting the permanent deformation response in following subsections.

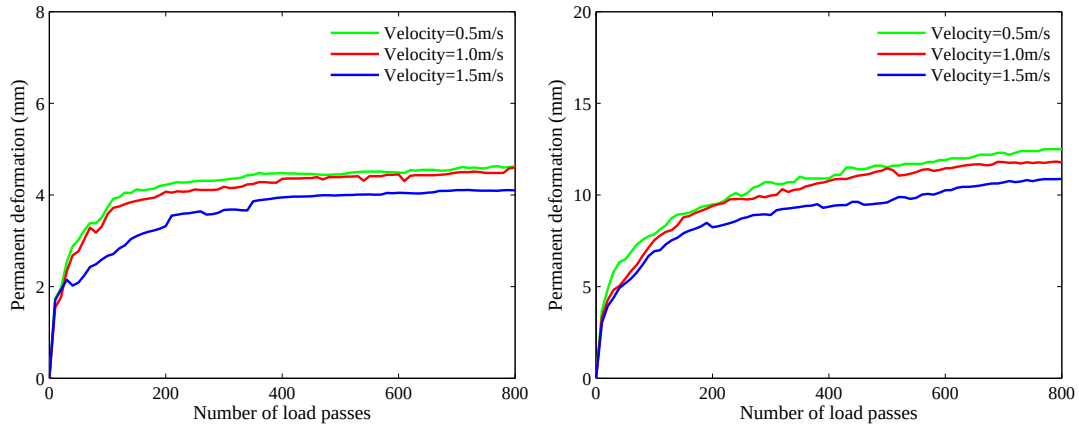

(a) $\bar{p}$=2.0kPa *(b) $\bar{p}$=7.0kPa*

Figure 5.12: Comparison of permanent deformation with varied wheel velocities

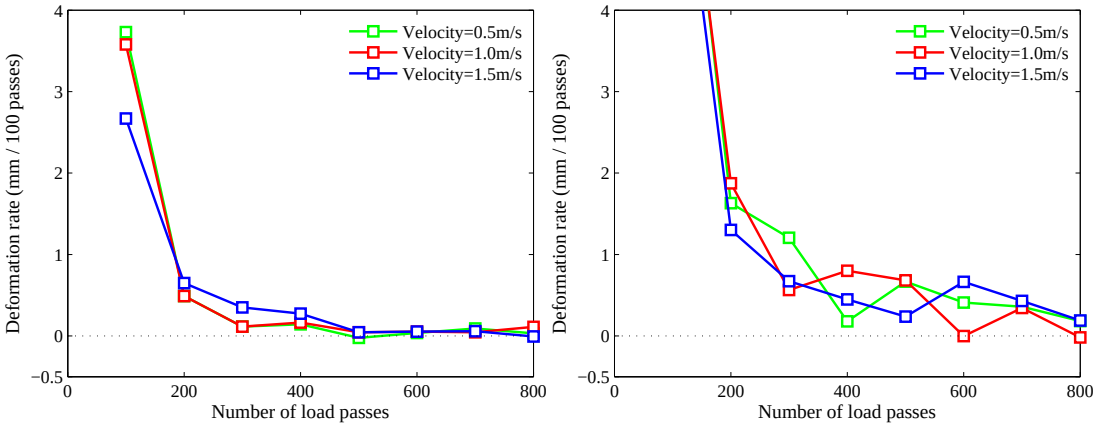

(a) $\bar{p}$=2.0kPa *(b) $\bar{p}$=7.0kPa*

Figure 5.13: Comparison of permanent deformation rate with varied wheel velocities

5.3.2 Specimen preparation

As described in Subsection 5.2.2, the pavement specimen is created using the particle radius expansion method. Afterwards, the specimen is isotropically consolidated to a required stress state (i.e. 100kPa), and then isotropically unloaded to a stress-free state so as to eliminate the disturbance of anisotropy in the sample preparation. Nevertheless, the initial structure corresponding with practical materials in geotechnical engineering tends to be anisotropic, especially for non-circular grains, the long axis of which is highly directional.

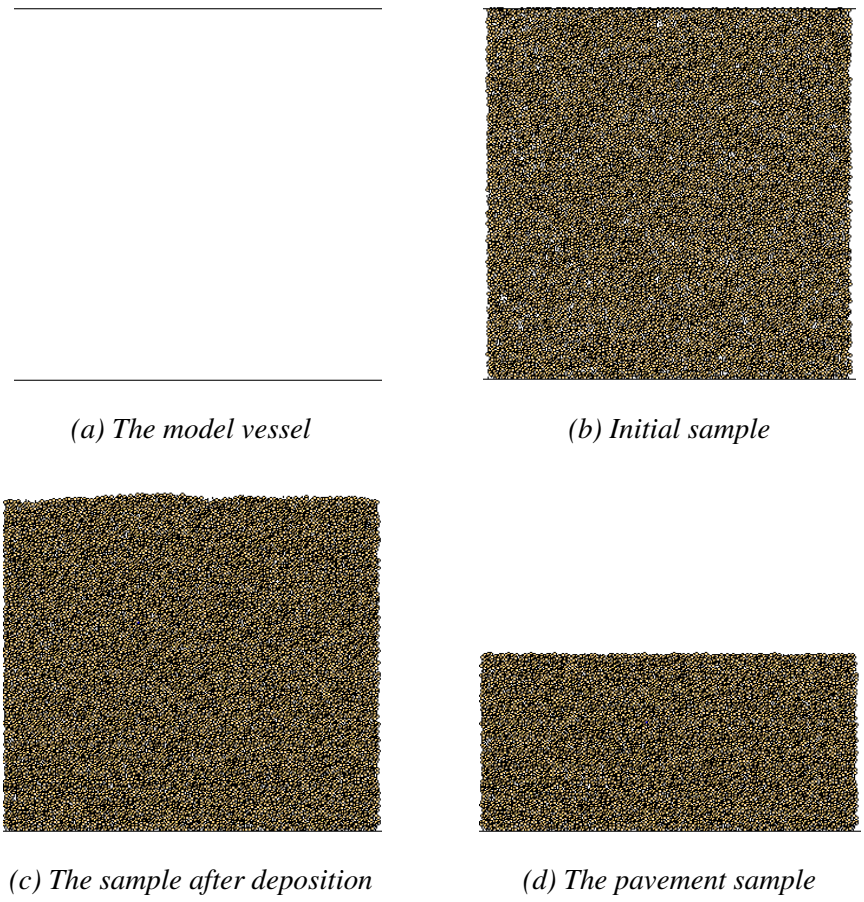

(a) The model vessel *(b) Initial sample*

(c) The sample after deposition *(d) The pavement sample*

Figure 5.14: The pavement sample prepared by gravity deposition method

In order to study the effect of sample anisotropy on rutting, another kind of sample preparation is employed, namely the gravity deposition method. The sample generated using this method will possess an initial anisotropic fabric, even though the particles are of circular shape. According to Li (2006), the preparation process is described as

follows:

1. Create a vessel with a height double that of the pavement specimen, where particles are randomly generated using the radius expansion method. The generated particle number should be more than the number of sample particles. In the present study, the size of the vessel is 1.8m long $\times$ 2.0m high and its lateral boundary is periodic (see Figure 5.14a). The porosity for particle generation is 0.30 and there exist nearly twenty thousand particles in the vessel, as shown in Figure 5.14b. The particle and wall parameters are the same as those in Subsection 5.2.2.

2. Assign a gravitational acceleration g=9.81m/s^2 to each particle. Adjust the local damping coefficient (see Subsection 3.2.6) from the default value (i.e. α=0.7) to a low value of 0.157 so as to model the energy loss in gravity deposition. The deposition time is calculated on the basis of the free fall formula $t = 1.2\sqrt{2h/g}$, where h is the height of vessel. All the boundaries are fixed at this stage. Different particle friction coefficients (i.e. 0.4, 0.5 and 0.6) were tried to generate a specimen with a target void ratio. The sample after gravity deposition is plotted in Figure 5.14c.

3. Reset the position of the upper boundary based on the required specimen size and delete all the particles lying outside the boundaries (see Figure 5.14d). The height of the specimen is selected as 0.95m, which is analogous to the initial height of the sample generated using the expansion method. It is observed that, when the particle friction coefficient is 0.5 at the second stage, the sample has the same void ratio (i.e. 0.26) as the previous sample in Subsection 5.2.2. Adjust the friction coefficient of the particles to 0.7 and restore the damping coefficient to the default value. The specimen has approximately eleven thousand particles.

The wheel stiffnesses and wheel loads are consistent with those in Subsection 5.3.1. Therefore, the corresponding mean wheel pressures are 2.0 and 7.0kPa respectively. The motion mode of the wheel is selected as translation with a constant velocity of

0.5m/s. The friction coefficient of the wheel particle is set at zero. The modelled permanent deformations versus the number of wheel passes are shown in Figure 5.15. When the wheel pressure is 2.0kPa, the sample preparation has a significant effect on the rutting. Compared to the expansion method, the sample generated with the deposition method exhibits a smaller permanent deformation for a given number of wheel passes but with a relatively large constant deformation rate in the end. This difference is probably due to the induced anisotropy possessed by the pavement sample. On the other hand, the permanent deformations exhibit a similar variation pattern for a wheel pressure of 7.0kPa. There exists hardly any difference in the surface deformation between the varied methods of sample preparation. This suggests that the effect of initial anisotropy on permanent deformation is restricted to a relatively low wheel pressure. The changes in deformation rate with wheel passes are displayed in Figure 5.16. There is a gradual decrease in the deformation rate prior to pass 400 for the pavement sample generated using the deposition method (see Figure 5.16a). In comparison, the initial decrease is relatively drastic for the expansion method, which is observed before pass 200. The deformation rates change in a similar pattern for a high wheel pressure, although with some fluctuations (see Figure 5.16b) where the final deformation rates are both obviously nonzero, as an indication of the occurrence of pavement ratchetting. The pavement model created by the expansion method is used in subsequent subsections.

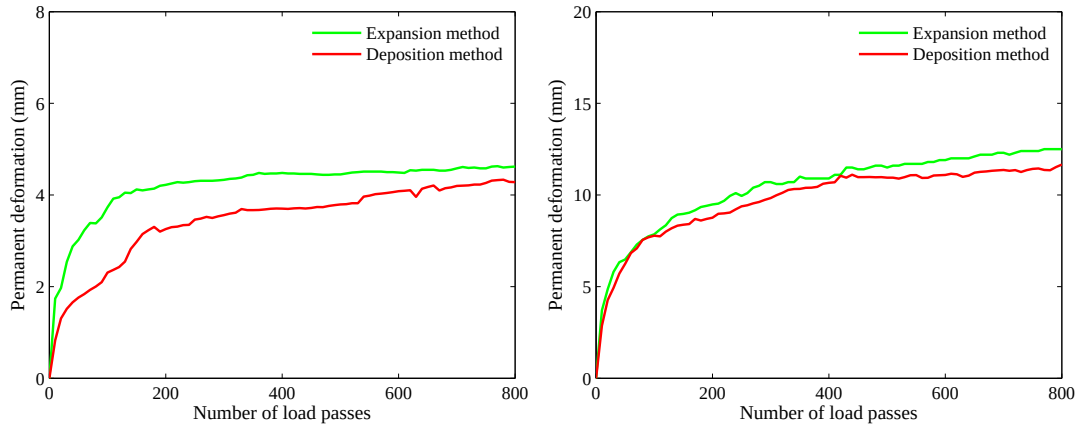

(a) $\bar{p}$=2.0kPa *(b) $\bar{p}$=7.0kPa*

Figure 5.15: Comparison of permanent deformation between different sample preparation methods

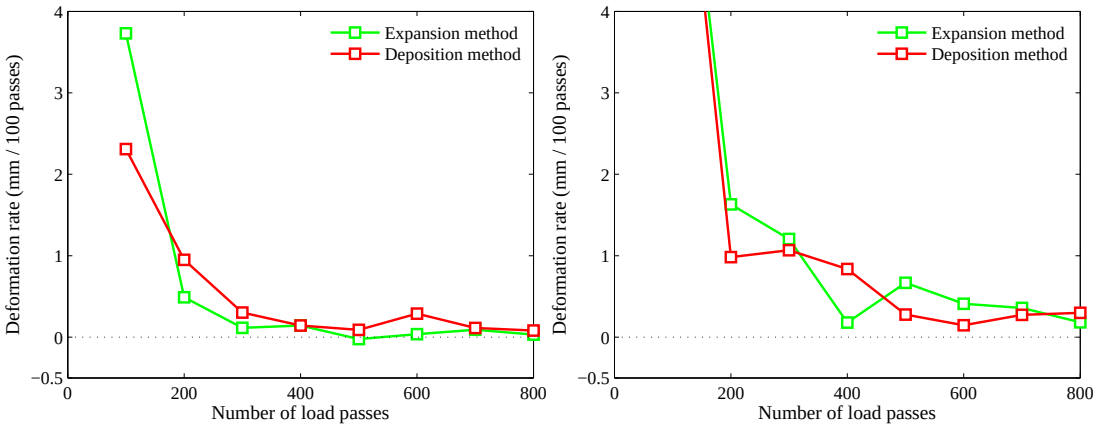

(a) $\bar{p}$=2.0kPa *(b) $\bar{p}$=7.0kPa*

Figure 5.16: Comparison of permanent deformation rate between different sample preparation methods

5.3.3 Wheel motion mode

In DEM simulation, the translation of the wheel is a simplified mode of movement, when the friction between the wheel and the pavement surface is not taken into consideration. As demonstrated in Subsection 5.2.4, an insignificant difference in the vertical stresses under stationary, translational and rolling wheel loads was found. The rolling resistance coefficient is quite small, namely 0.029 when the friction coefficients of the wheel and pavement particles are both 0.7. In this subsection, the effect of the motion mode (i.e. translation and rolling) on permanent deformation is studied. The angular rate for rolling is 1.667rad/s. Since the modelled wheel radius is 0.3m, the corresponding linear velocity is 0.5m/s. The velocity for translation is set at 0.5m/s. The mean contact pressures are applied to the wheel, namely 2.0 and 7.0kPa. The wheel friction coefficient is zero for translation and 0.7 for rolling. The parameters of the pavement particles and the pavement sample are shown in Subsection 5.2.2.

The simulated results relating to permanent deformation are shown in Figure 5.17, where all the deformations increase rapidly at first followed by a gradual decrease in the deformation rate until a relatively steady rate is achieved. When the wheel pressure is 2.0kPa, an apparent difference in rutting between these two motion modes is observed, although neither of the permanent deformations continues to accumulate after pass 200. The deformation difference is probably due to the friction between wheel and pavement surface induced by wheel rolling. Under the correspondingly large wheel pressure, namely 7.0kPa, the pavements exhibit similar permanent deformations regardless of motion mode. Therefore, the effect of motion mode on permanent deformation is limited to a low wheel pressure, but the ultimate steady rate of deformation is not affected. The variation in deformation rate with number of wheel passes is described in Figure 5.18, where the patterns are alike for a given wheel pressure. It is worth mentioning that pavement shakedown takes place for a wheel pressure of 2.0kPa while ratchetting is observed with a high wheel pressure since the accumulations of rutting do not cease.

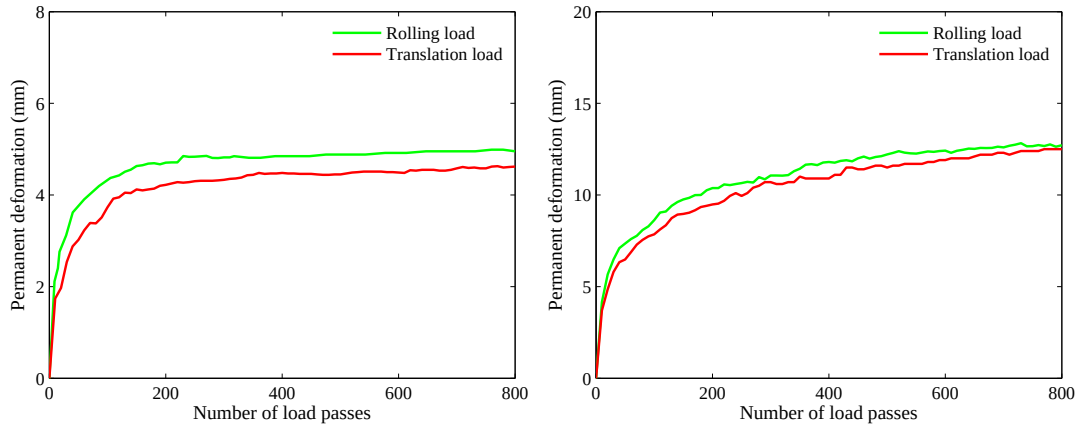

(a) $\bar{p}$=2.0kPa *(b) $\bar{p}$=7.0kPa*

Figure 5.17: Comparison of permanent deformation between different wheel motion modes

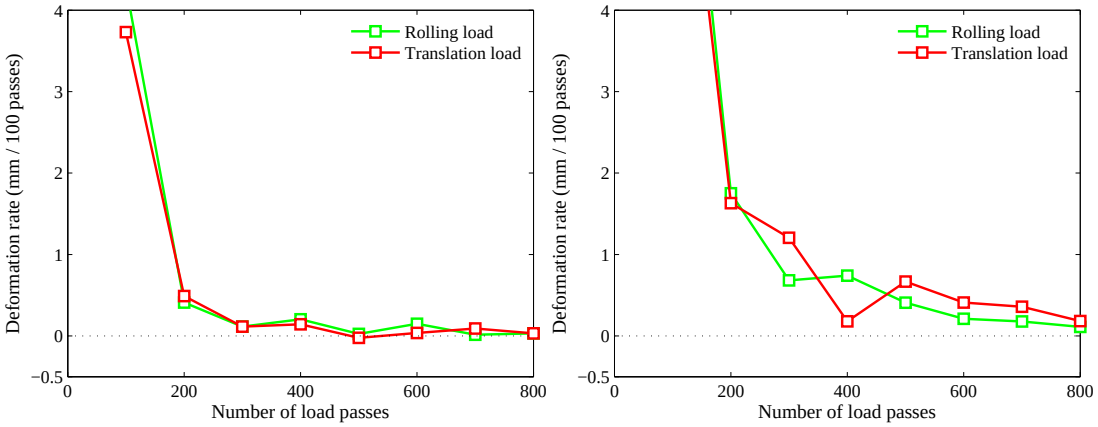

(a) $\bar{p}$=2.0kPa *(b) $\bar{p}$=7.0kPa*

Figure 5.18: Comparison of permanent deformation rate between different wheel motion modes

5.3.4 Gravity acceleration

The initial stress field distributed in the pavement is likely to have an impact on the permanent deformation. Also, in order to alleviate the effect of initial stress field on the residual stress distribution (see Section 5.4), the study on pavements with a low gravity stress field is necessary. After the pavement sample is unloaded to a stress free state during the sample preparation, two gravity accelerations (i.e. 0.1 and 9.81m/s^2) are applied to the pavement particles to model different self-weight stress fields. It is found that the void ratio is hardly affected by the gravity stress, which is 0.26 for both, after the preparation of the pavement sample. The other parameters of the pavement particles and the pavement sample are kept unchanged, as seen in Subsection 5.2.2. The pavements are subjected to translational wheel loads. The mean contact pressures are 2.0 and 7.0kPa as well. The effect of the initial stress field on permanent pavement deformation is shown in Figure 5.19. With the increase in gravity stress, the permanent deformation decreases significantly. Although the applied wheel pressure is small, namely 2.0kPa, the ultimate deformation rate is evidently nonzero for the pavement with a low initial stress field. Pavement shakedown does not take place. Similarly, subjected to a high wheel pressure of 7.0kPa, the pavement with low self-weight stress exhibits a relatively large permanent deformation and ultimate deformation rate. The deformation rate against the number of wheel passes is shown in Figure 5.20. It is noted that the pavement with a low gravity stress field generally displays a continued decrease in deformation rate, irrespective of wheel pressure. Nevertheless, in general, its deformation rate for a specific pass is obviously larger than that for the pavement with a high initial stress field.

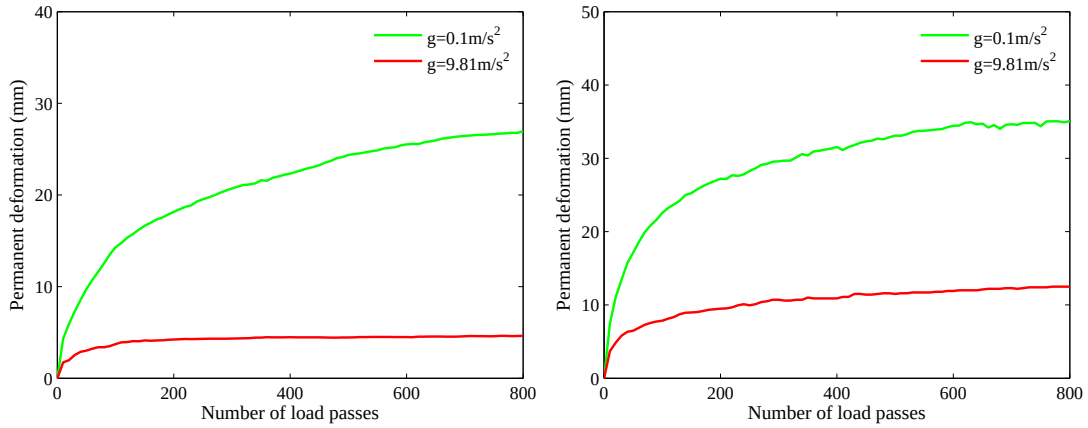

(a) $\bar{p}$=2.0kPa *(b) $\bar{p}$=7.0kPa*

Figure 5.19: Comparison of permanent deformation between samples with varied self-weight stress fields

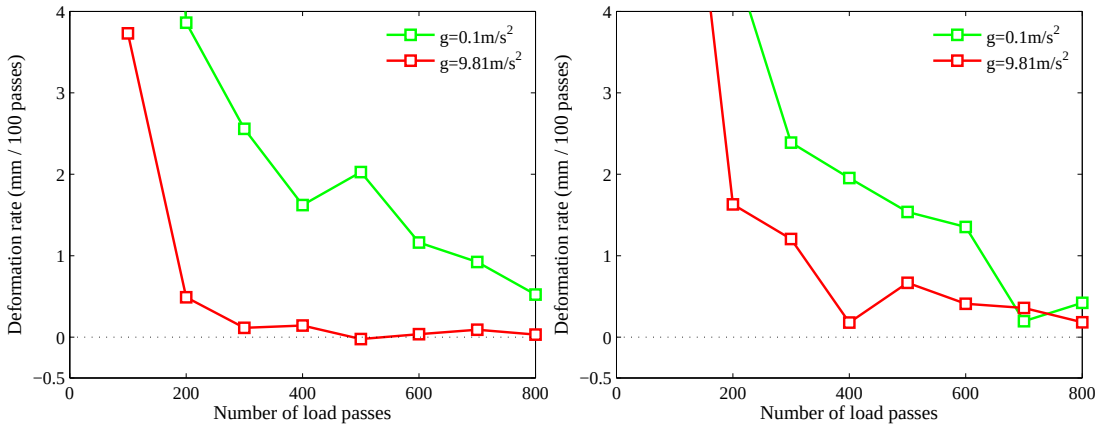

(a) $\bar{p}$=2.0kPa *(b) $\bar{p}$=7.0kPa*

Figure 5.20: Comparison of permanent deformation rate between samples with varied self-weight stress fields

5.3.5 Wheel pressure

The wheel pressure has a direct effect on permanent deformation in pavements. Two kinds of pavement samples with gravity accelerations of 0.1 and 9.81m/s^2 are studied. The details about the translational wheel load, wheel stiffness, contact width and contact pressure are listed in Table 5.2.

Gravity acceleration (m/s^2)	Wheel load (N)	Wheel stiffness (N/m)	Contact width (m)	Contact pressure (kPa)
0.1	50	2.5×10^3	0.10	0.5
	100	5×10^3	0.10	1.0
	200	1×10^4	0.10	2.0
	700	4×10^4	0.10	7.0
	2000	1×10^5	0.112	17.8
9.81	100	5×10^3	0.10	1.0
	200	1×10^4	0.10	2.0
	700	4×10^4	0.10	7.0
	900	5×10^4	0.10	9.0
	2000	1×10^5	0.112	17.8
	3000	1.5×10^5	0.118	25.5

Table 5.2: The details about the wheel and its contact information

The permanent deformation for a specific number of wheel pass increases with the increase of mean contact pressure regardless of the initial stress field in the pavement (see Figure 5.21). When the gravity acceleration is 0.1m/s^2, the ultimate deformation rate is nonzero, even if the contact pressure is very low, namely 0.5kPa. On the other hand, the pavements with high gravity stress demonstrate different responses to the varied contact pressures. When the mean contact pressure is not large enough (i.e. 1.0 and 2.0kPa), there is no further accumulation of permanent deformation, as an indication of shakedown. An approximately constant deformation rate is finally observed for the relatively high wheel pressure. Generally, when the contact pressure is low,

a further increase in wheel pressure will bring about a large increment of permanent deformation. With high mean contact pressure, the increment induced by increasing wheel pressure is less and less apparent. It is worth mentioning that the pavement deformation grows with more apparent fluctuations at higher contact pressure. This is because the large wheel pressure tends to cause a correspondingly uneven pavement surface. The variation of deformation rate with wheel pass number is plotted in Figure 5.22. Generally, the deformation rate for low gravity acceleration is larger than that for pavements with high gravity stress. When the contact pressure is large enough, the deformation rate fluctuates significantly, owing to the uneven pavement surface.

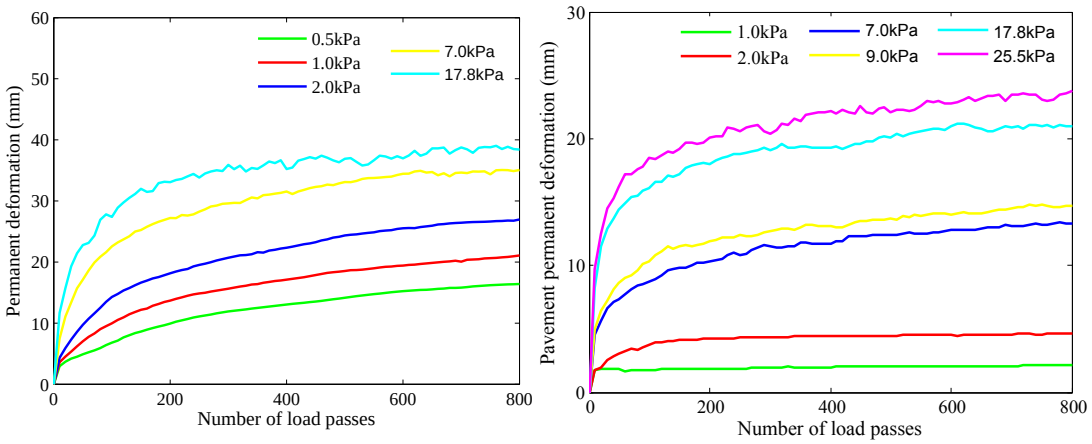

(a) g=0.1m/s^2 *(b) g=9.81m/s^2*

Figure 5.21: Comparison of permanent deformation among various moving wheel loads

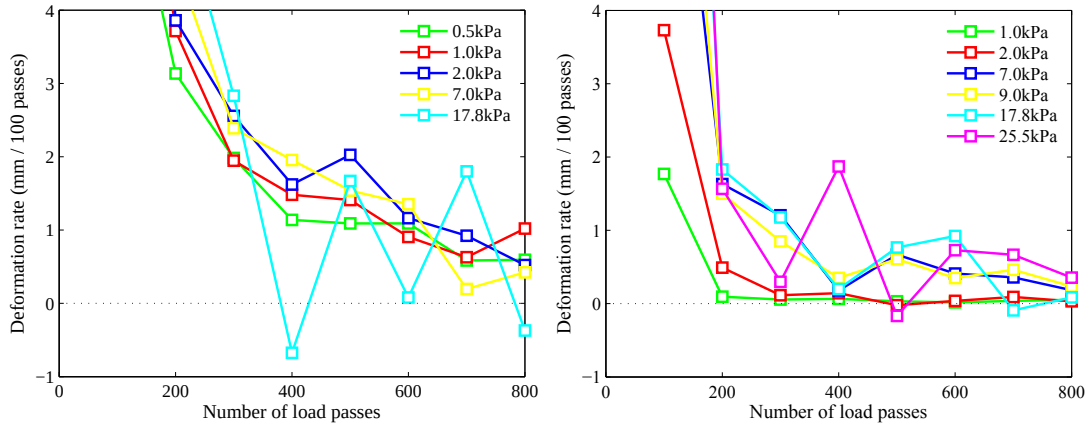

(a) g=0.1m/s^2 *(b) g=9.81m/s^2*

Figure 5.22: Comparison of permanent deformation rate among various moving wheel loads

5.3.6 Initial sample void ratio

It is well known that the sample void ratio can have a great influence on pavement behaviour. In this study, a dense sample with a void ratio of 0.23 is added to make a comparison with the previous sample, which is relatively loose with a void ratio of 0.26. The particle friction coefficient is a critical property to generate a relatively dense sample. The initial friction coefficient is 0.5 when the sample is created using the radius expansion method. The friction coefficient is changed to 0.2 during the consolidation and unloading processes. Afterwards, it is adjusted to 0.7. The gravity acceleration of 9.81m/s^2 is applied to the particles and plenty of calculation cycles are executed until there is no occurrence of extra settlement. Then the void ratio is calculated, which is 0.23. The motion mode is translation and the applied contact pressures are 2.0 and 7.0kPa. Compared to the previous sample, the dense sample demonstrates a much smaller permanent deformation, even though the void ratio is merely reduced by 0.03 (see Figure 5.23). With regard to the dense sample, the pavement surface is evidently uneven after the wheel load since the curve of permanent deformation develops with dramatic fluctuations. Figure 5.24 shows the deformation rates developing with the number of wheel loads. The initial deformation rate for the dense sample is much lower than that for the previous sample, regardless of the wheel contact pressure. The ultimate deformation rates are both nearly zero with a low contact pressure of 2.0kPa. Generally speaking, subjected to a relatively high wheel pressure, the loose sample produces a greater deformation rate than the dense one.

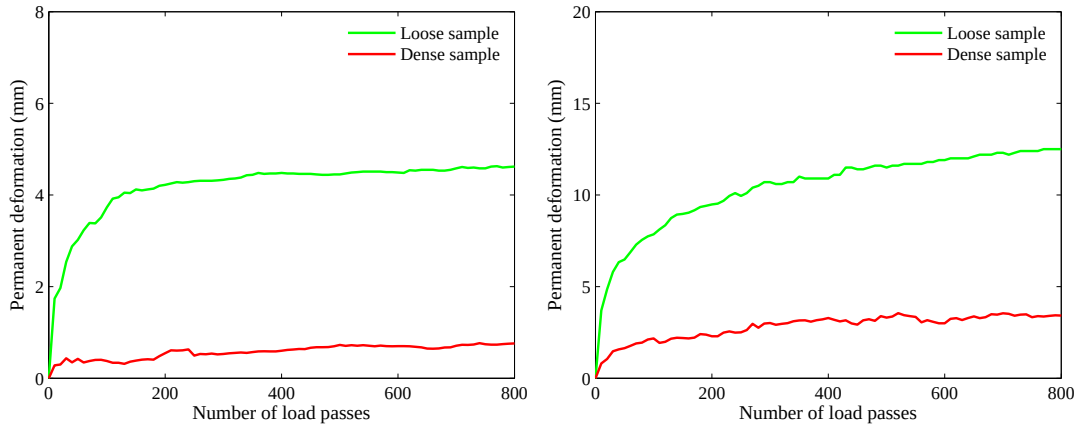

(a) $\bar{p}$=2.0kPa *(b) $\bar{p}$=7.0kPa*

Figure 5.23: Comparison of permanent deformation between samples with different compaction states

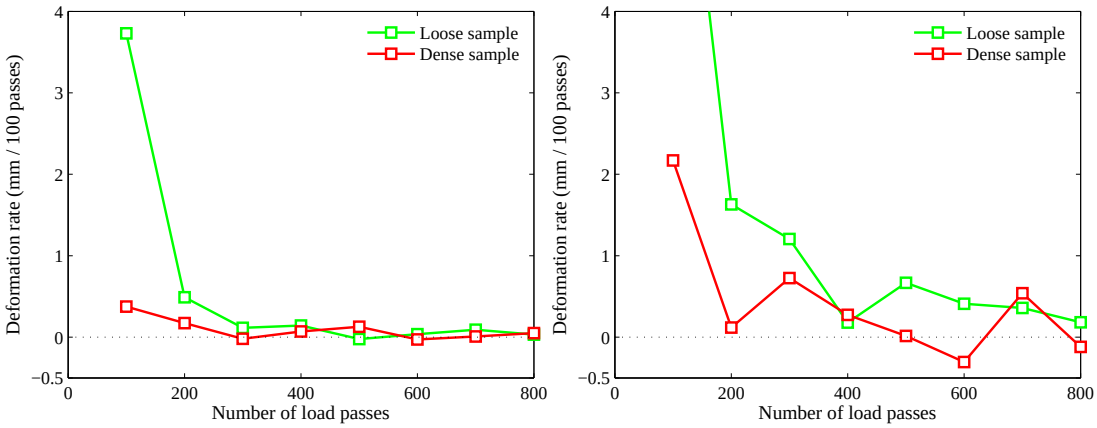

(a) $\bar{p}$=2.0kPa *(b) $\bar{p}$=7.0kPa*

Figure 5.24: Comparison of permanent deformation rate between samples with different compaction states

5.3.7 Interparticle friction

The friction coefficient μ depicts an inherent property of granular particles, which may affect the mechanical behaviour of pavement. As studied in Subsection 3.4.2, the interparticle friction has a significant influence on the peak strength and volumetric strain of granular materials. The friction coefficients of 0.5 and 0.9 are introduced as a complement to the simulation with the coefficient of 0.7. During pavement preparation, when the consolidation and unloading processes are finished, the friction coefficient is changed from 0.7 to 0.5 or 0.9. Afterwards, the gravity acceleration 9.81m/s^2 is applied to the pavement particles to model the self-weight stress field. It is found that the effect of the friction coefficient on the void ratio of the pavement sample can be ignored at this stage, all being at 0.26. The results corresponding to the development of permanent deformation with number of wheel passes are shown in Figure 5.25. The rutting is obviously affected by the interparticle friction coefficient. The decreased friction coefficient is responsible for the increased permanent deformation at both contact pressures, i.e. 2.0 and 7.0kPa. In addition, the friction coefficient affects the ultimate deformation rate for low contact pressure. When the coefficient is small (i.e. 0.5), the permanent deformation continues to accumulate, in contrast to the others with high coefficients (see Figure 5.25a). The change in the deformation rate with number of wheel passes is displayed in Figure 5.26, where the rate decreases rapidly prior to pass 200, regardless of contact pressure. At a wheel pressure of 7.0kPa, the deformation rates are similar to one another, despite some fluctuations.

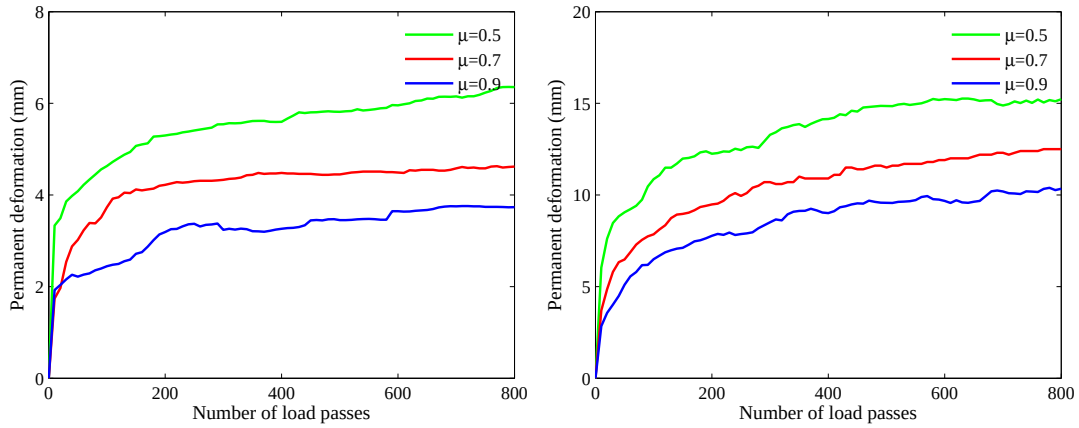

(a) $\bar{p}$=2.0kPa *(b) $\bar{p}$=7.0kPa*

Figure 5.25: Comparison of permanent deformation among samples with different particle friction coefficients

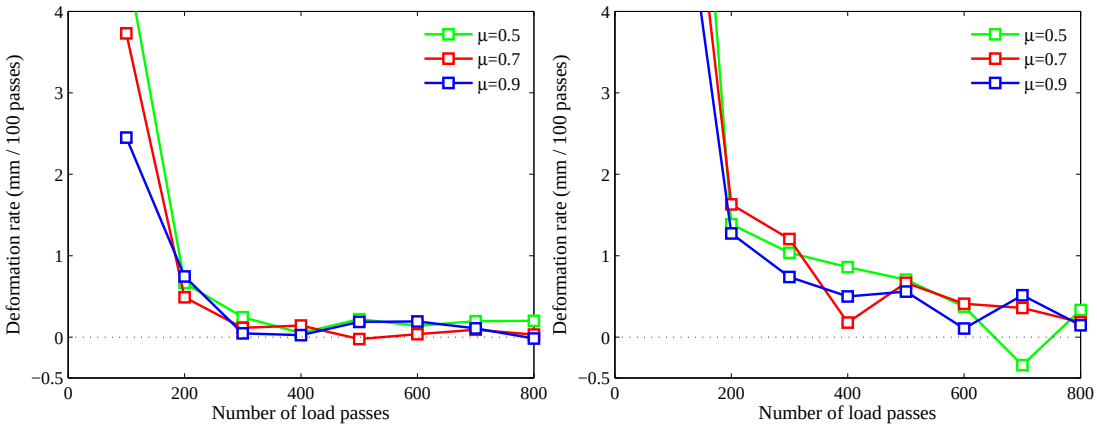

(a) $\bar{p}$=2.0kPa *(b) $\bar{p}$=7.0kPa*

Figure 5.26: Comparison of permanent deformation rate among samples with different particle friction coefficients

5.4 Residual stress

In DEM simulation, the stress field in the pavement can be obtained using measurement circles, the details of which are described in Subsection 3.2.4. The initial stress distribution and the stress field after moving traffic load are measured first. The difference between them is the residual stress field. The critical point in this method is to determine the measurement circle size. If the measurement circle is too small, there are insufficient interparticle contacts within it. This could affect the computational results for stress tensors. When its radius is quite large, there would be fewer measurement circles positioned within the pavement and then the measurement results would not embody local stress diversification. Hence, for the sake of getting the stress fields within the pavement model, a reasonable sized measurement circle should be selected. Four types of measurement circles with different radii are applied to get the self-weight stress distributions in vertical and horizontal directions within the pavement model. The circle radii are 0.005, 0.01, 0.02 and 0.03m respectively. At the same horizontal level, an array of measurement circles is positioned from the left pavement boundary to the right. The interval between two circles is the circle radius. In theory, the stress state is independent of the travel (horizontal) direction because of the periodic boundary. Hence, the self-weight stresses at a certain height could be obtained by averaging the results of all the measurement circles, which are at the corresponding horizontal level. The initial pavement sample has been studied. The measured results are plotted in Figure 5.27 where it is shown that, if the radius of measurement circle is selected as 0.02m, it will be large enough to reflect the stress variation with the pavement depth. As a result, a reasonable radius of measurement circle, which is 0.02m, is selected for use. It is notable that the fluctuations corresponding with horizontal self-weight stress are larger than the vertical. That is probably because the vertical stress field is primarily influenced by the porosity distribution in the pavement. If the sample is homogenous, the fluctuations of vertical stress distribution will be gentle. On the other hand, the horizontal gravity stresses are affected by the sample structure. The diversity of local structures induced by the discreteness of the pavement sample may be responsible for the evident undulations of the self-weight stress in the horizontal

direction.

The stress distribution obtained using the measurement circle method will be validated via theoretical solutions. The vertical gravity stress σ_{zz} is calculated by $\sigma_{zz} = \rho g h$ where ρ is the density of pavement sample and h is pavement depth. The density ρ is computed approximately as 2.14×10^3kg/m^3 based on particle specific gravity, which is 2.7 in the present study and the void ratio of the sample (with a value of 0.26) as the sample is assumed to be uniform. As shown in Figure 5.28, the measured data is in good accordance with the analytical results when the gravity accelerations are 0.1 and 9.81m/s^2. Consequently, the measurement circle can be employed to analyse the stress field distributed within the DEM pavement sample.

The residual stress is obtained on the basis of the difference between the present total stress (after trafficking) and the initial stress. Their distributions with pavement depth are plotted in Figures 5.29 and 5.30, where different wheel pass numbers (100, 300, 500 and 700) are considered. The applied wheel load is 700N and the corresponding mean contact pressure is 7.0kPa. In general, there is no obvious difference between the initial stress and various later stresses, indicating that the residual stress is not large in comparison with the initial stress. The calculated residual stress distribution with pavement depth is shown in Figures 5.31 and 5.32. It is noted that the vertical residual stresses are nearly zero, compared to the horizontal residual stress, regardless of the self-weight stress field. This is in good agreement with the constraint condition for residual stress, i.e. ϱ_{zz}=0. The results also show that the residual stress is independent of the wheel pass number, indicating that the residual stress has been fully developed. Although there is a continued increase in permanent deformation with wheel pass, the quantities corresponding with the interparticle contacts (e.g. contact force and contact vector) are not affected. Therefore, the contact-related residual stress is not changed with increasing wheel passes. Obvious fluctuations for horizontal residual stress are exhibited, owing to the diversity of local pavement structures.

The effect of wheel pressure on horizontal residual stress has been investigated for wheel pass 100 and 500, as shown in Figure 5.33 and 5.34. Three kinds of contact

pressures are considered, which are 2.0, 7.0 and 17.8kPa respectively. With a gravity acceleration of 0.1m/s^2, although with some undulations, the horizontal residual stress is independent of the applied wheel pressure. The fully developed horizontal residual stress is not sufficient to prevent the increase of plastic strain in pavements, even if the wheel pressure changes from 17.8 to 2.0kPa. Therefore ratchetting is observed (see Figure 5.21a). On the other hand, a larger wheel pressure (e.g. 17.3kPa) induces a more evident residual stress distribution when the large self-weight stress field is applied to the pavement sample. This indicates that the large wheel pressure causes great changes in the contacts in the DEM pavement model. When the wheel pressure is 2.0kPa, pavement shakedown is observed (see Figure 5.21b) since the permanent deformation can be inhibited by the horizontal residual stress. Moreover, the initial gravity stress field has a great impact on the horizontal residual stress distribution. The applied wheel pressure is 7.0kPa. As demonstrated in Figure 5.35, horizontal residual stress is obvious for large initial gravity stress. The greater interparticle contact forces induced by large gravity acceleration are clearly responsible for the high residual stress.

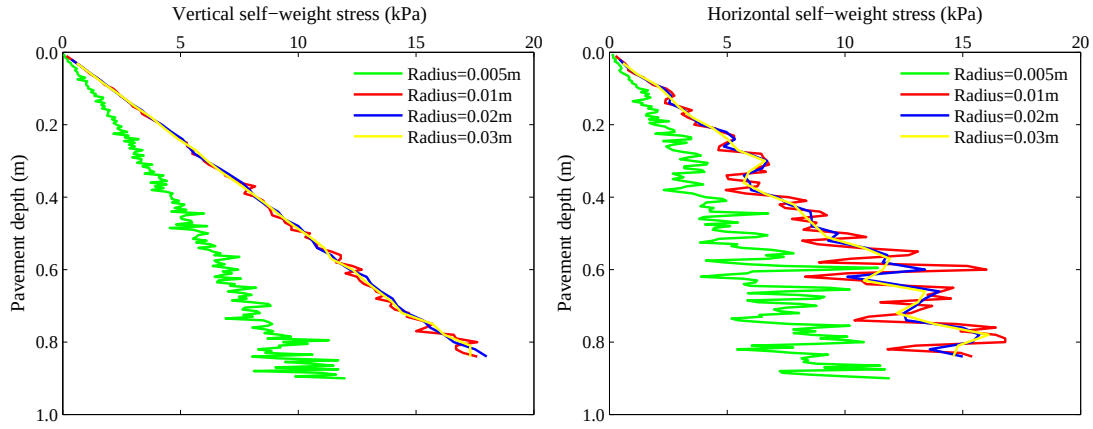

(a) Vertical self-weight stress *(b) Horizontal self-weight stress*

Figure 5.27: Self-weight stress versus pavement depth for different sized measurement circles

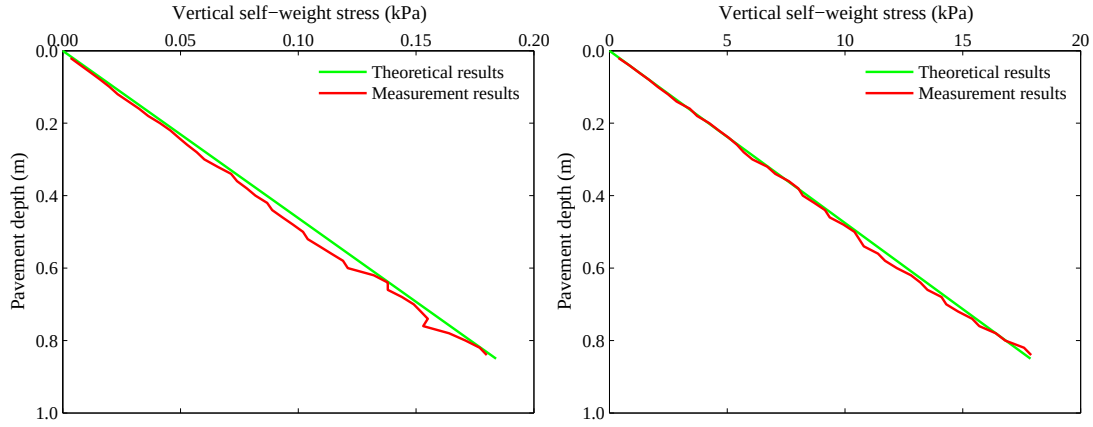

(a) g=0.1m/s^2 *(b) g=9.81m/s^2*

Figure 5.28: Self-weight stress comparison between theoretical solutions and measurement results in terms of different gravity accelerations

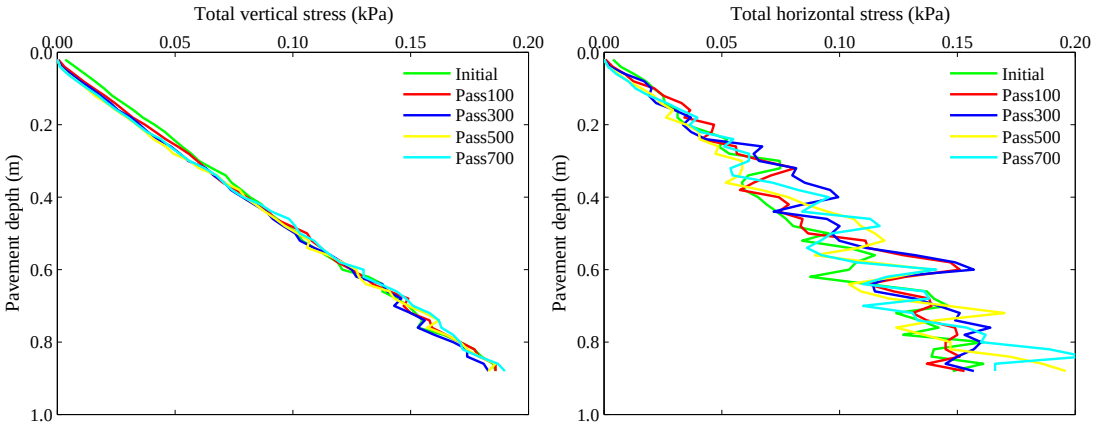

(a) Total vertical stress *(b) Total horizontal stress*

Figure 5.29: The total stress distribution versus pavement depth for gravity acceleration of 0.1m/s^2

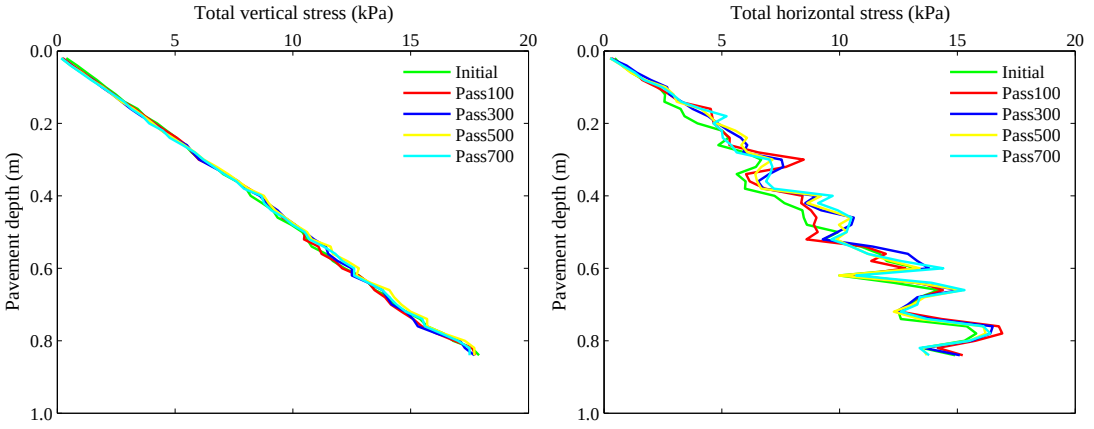

(a) Total vertical stress *(b) Total horizontal stress*

Figure 5.30: The total stress distribution versus pavement depth for gravity acceleration of 9.81m/s^2

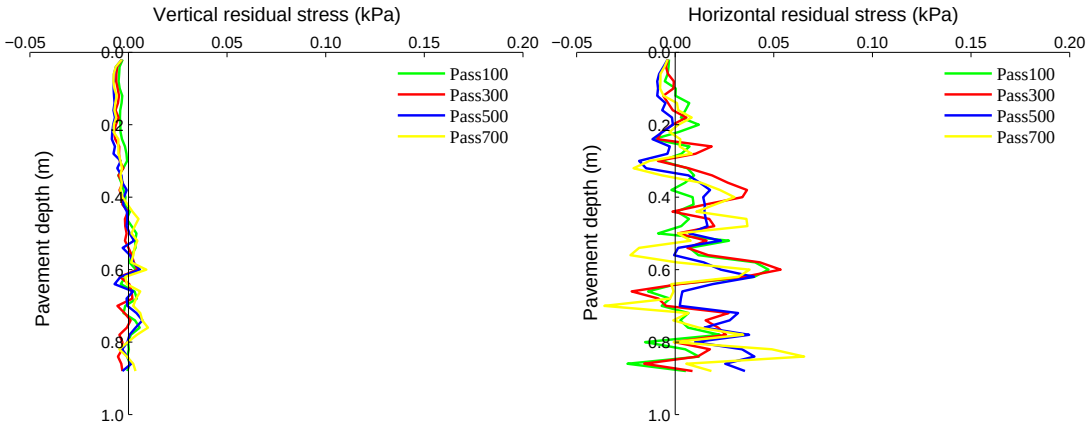

(a) Vertical residual stress *(b) Horizontal residual stress*

Figure 5.31: The effect of wheel pass on residual stress distribution for gravity acceleration of 0.1m/s^2

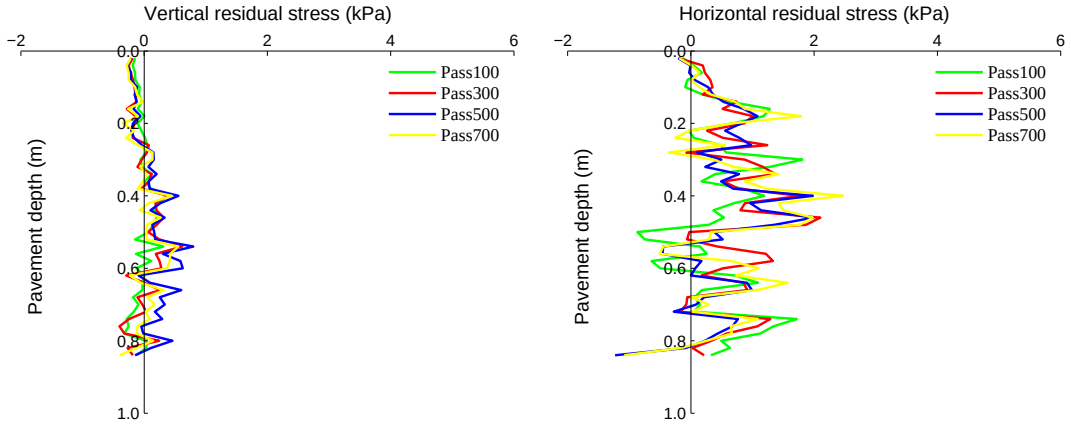

(a) Vertical residual stress *(b) Horizontal residual stress*

Figure 5.32: The effect of wheel pass on residual stress distribution for gravity acceleration of 9.81m/s^2

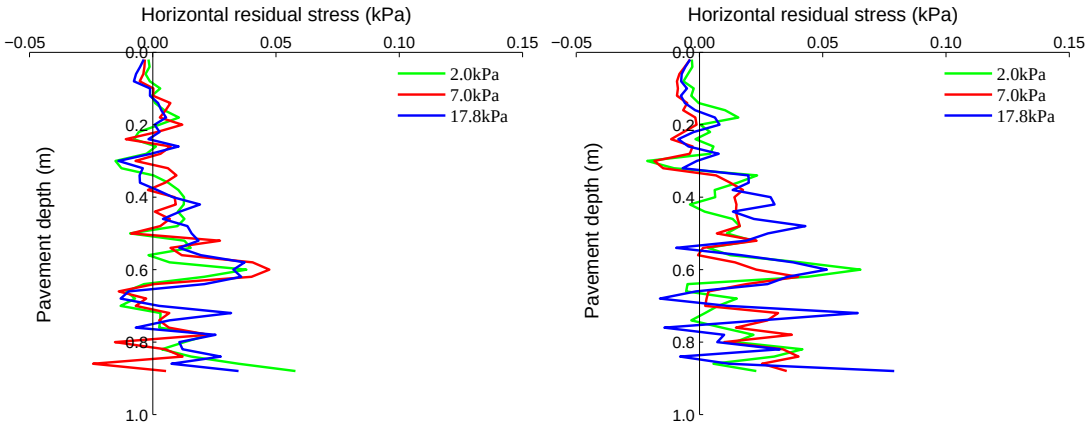

(a) Pass 100 *(b) Pass 500*

Figure 5.33: The effect of wheel pressure on residual stress distribution for gravity acceleration of 0.1m/s^2

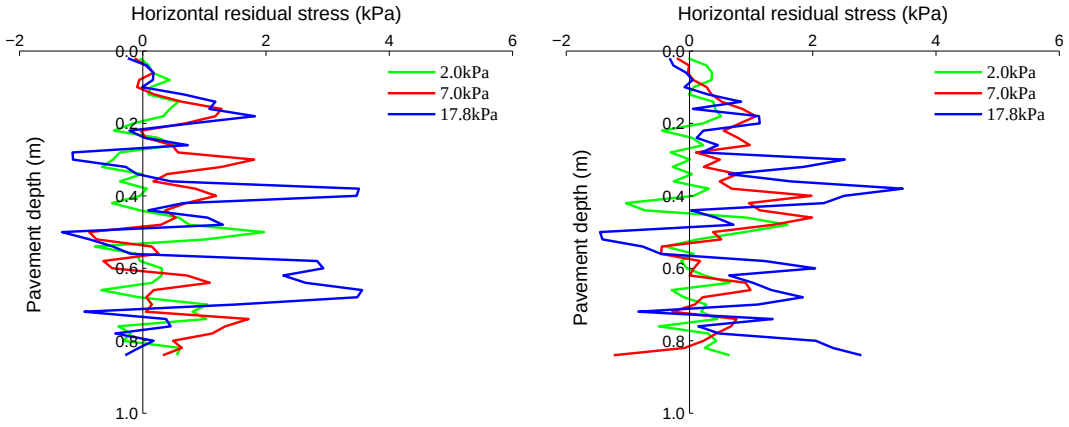

(a) Pass 100 *(b) Pass 500*

Figure 5.34: The effect of wheel pressure on residual stress distribution for gravity acceleration of 9.81m/s^2

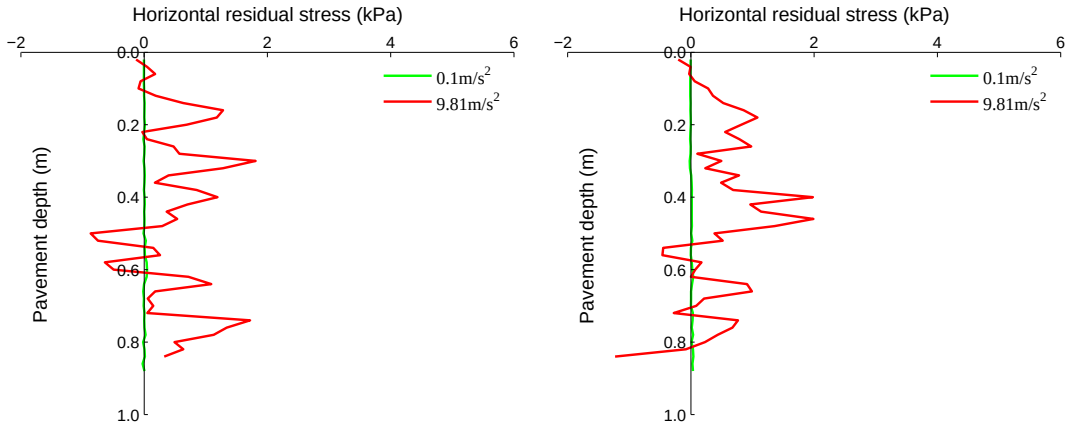

(a) Pass 100 *(b) Pass 500*

Figure 5.35: The effect of gravity stress on residual stress distribution for wheel pressure of 700N

5.5 Summary

A DEM pavement model has been generated to study permanent deformation under a moving wheel load. The modelling procedure is introduced in detail. The contact force, as well as contact width between wheel particle and pavement surface, are measured and recorded in the middle of each wheel pass. In addition, the permanent deformation in pavements is calculated after individual wheel passes. Afterwards, the contact pressure distribution between wheel particle and pavement surface is taken into consideration. Stationary, translational and rolling wheel loads are applied to the wheel respectively. It is found that the motion mode has a negligible effect on the contact pressure distribution, which can be assumed as a Hertz distribution. The measured rolling resistance coefficient is quite small, namely 0.029. The periodic lateral boundary has also been compared to the rigid lateral boundary as a validation. The results show that a periodic boundary can be employed to model the permanent pavement deformation. In the same cross section, the pavement undergoes an identical stress path because of the periodic boundary. Therefore, the acquisition of the pavement stress

distribution via measurement circles and the performance of microscopic statistical analysis will be beneficial. The simulated pavement surface deformation is obtained to make a comparison with laboratory test results. The permanent deformation increases rapidly for a number of initial wheel passes and then gradually decreases to a steady deformation rate. Generally, two kinds of pavement behaviour are observed, i.e. pavement shakedown (the ceasing of permanent deformation accumulation) and ratchetting (the continuous accumulation of permanent deformation). These results are consistent with the laboratory findings.

The factors affecting the rutting have been investigated. The effect of wheel velocity on rutting is first considered. Three kinds of translational velocities are compared to one another, including 0.5, 1.0 and 1.5m/s. The large velocity (i.e. 1.5m/s) brings about a relatively small permanent deformation. When the rate is less than 1.0m/s, the variation in rutting with wheel velocity can be disregarded. A wheel velocity of 0.5m/s is selected for the studies into other factors. In addition, two kinds of sample preparation are taken into consideration, which are the particle radius expansion method and the gravity deposition method. The sample prepared with the gravity deposition method exhibits a smaller surface deformation for a given wheel pass number, although the difference in rutting can be ignored when the wheel pressure is relatively large, namely 7.0kPa. A nonzero ultimate deformation rate is also observed, even for low wheel pressure (i.e. 2.0kPa) if the sample is generated using the gravity deposition method. These characteristics are probably due to the initial anisotropy of the sample induced by the gravity deposition method. It is noted that the effect of sample anisotropy on rutting is particularly sensitive to relatively low wheel pressure. Next, different motion modes are introduced, i.e. translation and rolling. The permanent deformation is affected by the motion mode at low wheel pressure although the steady deformation rate remains unchanged.

The gravity stress field in the pavement has a significant impact on permanent deformation. A relatively large permanent deformation and steady deformation rate are observed for a pavement with low self-weight stress. It is noted that the pavement with low gravity stress field displays a nonzero constant deformation rate even for a low

wheel pressure of 2.0kPa. Irrespective of the initial stress field, the rutting increases with the rise in mean contact pressure. The pavements with high gravity stress exhibit different responses to the varied contact pressures, i.e. pavement shakedown and ratchetting. When the gravity acceleration is low, i.e. 0.1m/s^2, the constant deformation rate is nonzero, even if the contact pressure is very low (e.g. 0.5kPa). Apparent fluctuations are observed for high contact pressure, because of the induced uneven pavement surface. Generally, the deformation rate for a specific wheel pressure is large for low gravity acceleration. The permanent deformation is also significantly affected by the initial sample void ratio. With a slight decrease in the ratio from 0.26 to 0.23, the pavement exhibits a much smaller permanent deformation. In addition, for the dense sample, the pavement surface is obviously uneven after trafficking. Varied particle friction coefficients are also investigated, which are 0.5, 0.7 and 0.9 respectively. With a reduction in the friction coefficient, the permanent deformation increases significantly. When the coefficient is 0.5, the permanent deformation continues to accumulate for low wheel pressure, in contrast to cases of high self-weight stress.

The stress after trafficking and initial stress can be obtained by means of measurement circles. The difference between them is the residual stress. The measured stress components at the same cross section are averaged as the stress values at the corresponding pavement height. Regardless of the self-weight stress field, the vertical residual stresses are nearly zero, which is in good accordance with theoretical analysis. The horizontal residual stress is independent of the wheel pass number. Generally, the wheel pressure has a negligible effect on the horizontal residual stress for a pavement with low self-weight stress, whereas larger horizontal residual stress is caused with a greater wheel pressure (e.g. 17.3kPa) for a pavement with a large self-weight stress field. Pavement shakedown is observed if the accumulation of plastic strain can be inhibited by the horizontal residual stress. Otherwise, ratchetting will occur. The horizontal residual stress is obviously affected by the initial gravity stress. A large initial gravity stress corresponds to evident horizontal residual stress.

Chapter 6

Permanent Pavement Deformation Simulation for Bonded Materials

6.1 Introduction

Parallel bonds have been introduced to the interparticle contacts (i.e. actual and eligible virtual contacts) in DEM simulation so as to model the permanent pavement deformation for bonded materials. Details of the pavement sample and the modelling procedure, which are analogous to the simulation of a pavement with a rigid lateral boundary, are exhibited in Subsection 5.2.5. The bonds are applied to the entire pavement structure and then a single-layered pavement is built. The factors affecting the pavement permanent deformation, i.e. wheel pressure and initial gravity stress have been investigated. Mean contact pressures from 42 to 254kPa are selected for pavement particles with gravity acceleration of 0.1m/s^2 while pressures of 85 and 169kPa are applied to a pavement with a normal self-weight stress field (i.e. g=9.81m/s^2). It is noted that the initial self-weight stress, rather than wheel pressure, has an effect on the permanent deformation.

On the other hand, a double-layered pavement composed of an asphalt concrete layer

(i.e. upper layer) and a granular layer has also been constructed. The asphalt concrete layer is modelled by the bonding particles. Three thicknesses for the upper layer are considered, i.e. 0.10, 0.15 and 0.20m, while the total height of the flexible pavement remains constant, i.e. approximately 0.95m. The effect of bonded layer thickness on rutting is studied. The deformation rate versus wheel pass number is also presented. The friction coefficient of particles in the granular layer also has a significant effect on the permanent deformation. In the present study, coefficients of 0.5, 0.7 and 0.9 are included. In addition, the permanent deformation is apparently affected by the wheel pressure. Finally, there is a comparison of the permanent deformation between unbound and double-layered pavements. The double-layered pavement produces a smaller permanent deformation when subjected to identical contact pressure. The residual stress induced by plastic deformation is investigated. It is affected by the following factors: wheel pass number, particle friction coefficient, thickness of the upper layer and wheel pressure.

6.2 DEM pavement model

6.2.1 Pavement specimen

The preparation of the pavement specimen is totally identical to the preceding method used in Subsection 5.2.2, where the particle radius expansion method is employed to generate the sample. A rectangular vessel is built by two horizontal and vertical walls in which the particles are created. The parameters of the pavement particles and walls are also the same as those of the previous pavement study. The pavement particle radius is in the range of 5.0-7.5mm. The particles have unit thickness (i.e. 1m). The specific gravity of the particles is 2.7. Both normal and shear stiffnesses of particles are chosen as 5×10^8N/m. The horizontal walls have the same stiffness as the particles, while the stiffnesses of vertical walls are one-tenth of those of the horizontal walls. As in the former research, the particle friction coefficient for the initial pavement sample

is 0.5 and the porosity of the sample is 0.30. There is no friction between wall and pavement particles. After the particles are generated, the particle friction coefficient is changed from 0.5 to 0.7. The pavement sample is isotropically consolidated to a required stress state (i.e. 100kPa) and then isotropically unloaded to a stress free state. The top wall is removed and two vertical walls act as the rigid lateral boundary of the pavement sample. In order to alleviate the effect of initial stress field on the residual stress distribution (see Section 5.4), it is also necessary to carry out studies on pavements with a low gravity stress field. Therefore, the gravity acceleration (i.e. 0.1 or 9.81m/s^2) is applied to the pavement particles. Once there is no further settlement, the parallel bonds are added to the interparticle contacts. The single-layered pavement is created such that the parallel bonds are installed at all the actual and eligible virtual contacts in the pavement. Nearly twenty-one thousand parallel bonds are generated for pavements with varied self-weight stress fields. When the parallel bonds are merely added to the contacts belonging to the upper part of the pavement, the double-layered pavement is generated, as shown in Figure 6.1. Therefore, the double-layered pavement is comprised of an upper bonded layer (identified by the red colour) and a simulated granular base (denoted by the yellow colour).

Figure 6.1: Double-layered pavement sample

As noted in Section 4.2, there are five parameters for parallel bonds, namely normal and shear strength, $\bar{\sigma}_c$ and $\bar{\tau}_c$ [stress]; normal and shear stiffness, $\bar{k}^n$ and $\bar{k}^s$ [stress/displacement] and bond radius, $\bar{R}$. In order to simplify the analyses, the bond breakage is not allowed during DEM pavement simulations. Consequently, the bond strength should be large enough. The uniform strength distribution is adopted and $\bar{\sigma}_c$

and $\bar{\tau}_c$ are selected as 600kPa. Each bond radius, $\bar{R}$ is assigned to be equal to the radius of the homologous elastic beam $\widetilde{R}$, which is conceived on the basis of the behaviour of the interparticle contact. The normal stiffness of parallel bond $\bar{k}^n$ is given the value equivalent to the ratio of normal stiffness of the corresponding contact k^n to the cross-sectional area of parallel bond $\bar{A}$. The parallel-bond shear stiffness is set to be the same as the normal one. The details of the value assignments of $\bar{R}$, $\bar{k}^n$ and $\bar{k}^s$ are discussed in Subsection 4.3.3.

It is found that the periodic lateral boundary is not suitable for the study of pavements with bonded materials. Because of the apparent existence of force concentrations at the lateral boundary, the distribution of residual stress in the pavement will be seriously disturbed. However, when the pavement sample is entirely comprised of unbonded particles, these force concentrations are not observed. Therefore, the wall lateral boundary is applied in the present study. In this situation, a confinement effect due to rigid lateral boundaries must be acknowledged. Some discussion of the difference expected between the rigid lateral boundary and periodic boundary has been performed in Subsection 5.2.5. As discussed in Subsection 5.2.5, the pavement size is not less than $40a$ long $\times$ $15a$ high. The half contact width a is chosen as 0.06m. Considering the pavement settlement during preparation, the initial height of the specimen vessel is set at 1.0m. When the preparation is finished, the pavement height can be calculated, which is nearly 0.95m. The vessel length is $40a$, i.e. 2.4m. After the preparation, the void ratio of the pavement is also calculated as 0.26, identical to the pavement samples in Subsections 5.2.2 and 5.2.5.

6.2.2 Modelling procedure

As in the description in Subsection 5.2.5, a wheel particle with radius of 0.3m is generated on the top of the left boundary, and a concentrated load is exerted at the centre of it. There is no friction between the wheel particle and the pavement surface. Afterwards, the wheel moves on the pavement surface with a constant translation velocity (i.e. 0.5m/s). When the wheel particle gets to the right boundary, the wheel will be

removed and one wheel pass is achieved. This process is repeated for the following wheel passes. The contact force, as well as the contact width between the wheel particle and the pavement surface, are measured and recorded when the wheel moves at the middle of the pavement surface. Also, after individual wheel passes are completed, the pavement surface deformation is obtained and saved. The middle section of the pavement surface with a length of $10a$ (i.e. 0.6m) is used to study the permanent deformation. The measurement methods corresponding to the contact width and permanent deformation are described in Subsection 5.2.3.

6.3 Single-layered pavement structure

6.3.1 Permanent deformation

A variety of wheel loads have been applied to the wheel particle to study the permanent pavement deformation. The stiffnesses of the wheel particle are adjusted for varied wheel loads to keep a nearly constant contact width (namely 0.12m). There are four wheel pressures for a low gravity stress field (g=0.1m/s^2), which are 42, 85, 169 and 254kPa. Two wheel pressures are applied (i.e. 85 and 169kPa) to the wheel particle when a high self-weight stress field (g=9.81m/s^2) is used in the pavement sample. The detailed information is displayed in Table 6.1. It is found that the permanent deformation in pavements can be negligible, even though the wheel pressure increases from 42 to 254kPa or the gravity acceleration of pavement particles changes from 0.1 to 9.81m/s^2. This is because parallel bonds at interparticle contacts significantly inhibit the particle arrangement that mainly causes the permanent pavement deformation.

Gravity acceleration (m/s^2)	Wheel load (kN)	Wheel stiffness (N/m)	Contact width (m)	Contact pressure (kPa)
0.1	5	2.5×10^5	0.118	42
	10	5×10^5	0.118	85
	20	1×10^6	0.118	169
	30	1.5×10^6	0.118	254
9.81	10	5×10^5	0.118	85
	20	1×10^6	0.118	169

Table 6.1: The detailed information about the wheel and wheel-related contact for single-layered pavement

6.3.2 Residual stress

The initial stress field and stress distribution after the wheel load can be obtained via measurement circles provided in PFC^{2D}, as discussed in Subsection 5.4. The details of the measurement circle are depicted in Subsection 3.2.4. The gravity acceleration for pavement particles is $0.1 m/s^2$. The residual stress is calculated through subtracting initial stress from current stress. The effect of wheel pass number on residual stress distribution is plotted in Figure 6.2, where the wheel pressure is 169kPa. Compared to the horizontal residual stress (see Figure 6.2b), the residual stress in the vertical direction can be neglected, as shown in Figure 6.2a, in good agreement with theoretical analysis (see Subsection 2.3.3). The maximum horizontal residual stress is near the pavement surface, which is consistent with the findings of Wang (2011). With the rise in number of wheel load passes (from 100 to 300), the horizontal residual stress clearly increases, especially the maximum value. Although there is no obvious accumulation of plastic normal strain (see Subsection 6.3.1), further load applications probably cause an increase in plastic shear strain, which may contribute to the development of horizontal residual stress. The effect of wheel pressure on horizontal residual stress was investigated (see Figure 6.3). There are three wheel pressures, namely 85, 169 and 254kPa and pass numbers 100 and 300 are considered. Given a specific load

pass number, the high wheel pressure gives rise to large horizontal residual stress. The increased wheel pressure possibly leads to an increase of plastic shear strain, which may be responsible for the increase in residual stress. In addition, it is noted that the maximum residual stress is most sensitive to the wheel pressure.

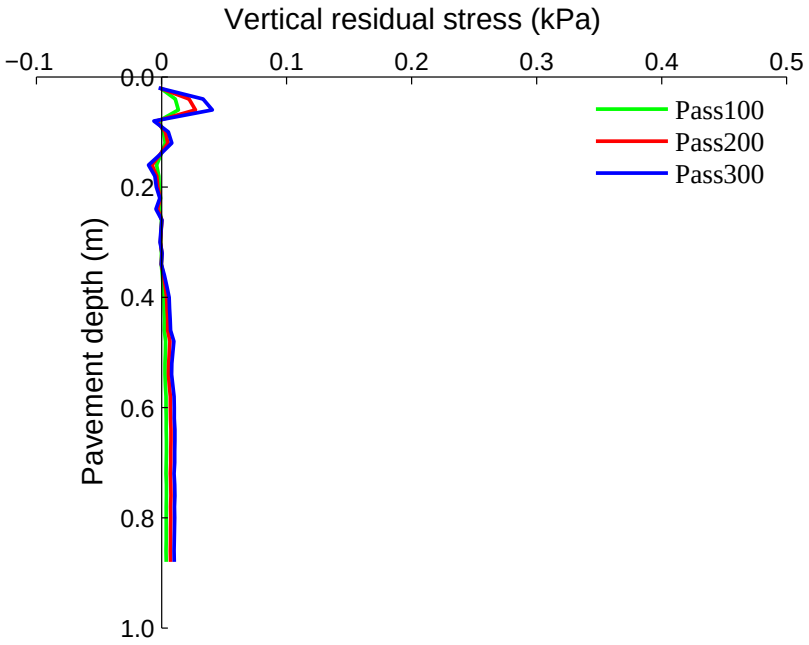

(a) Vertical residual stress

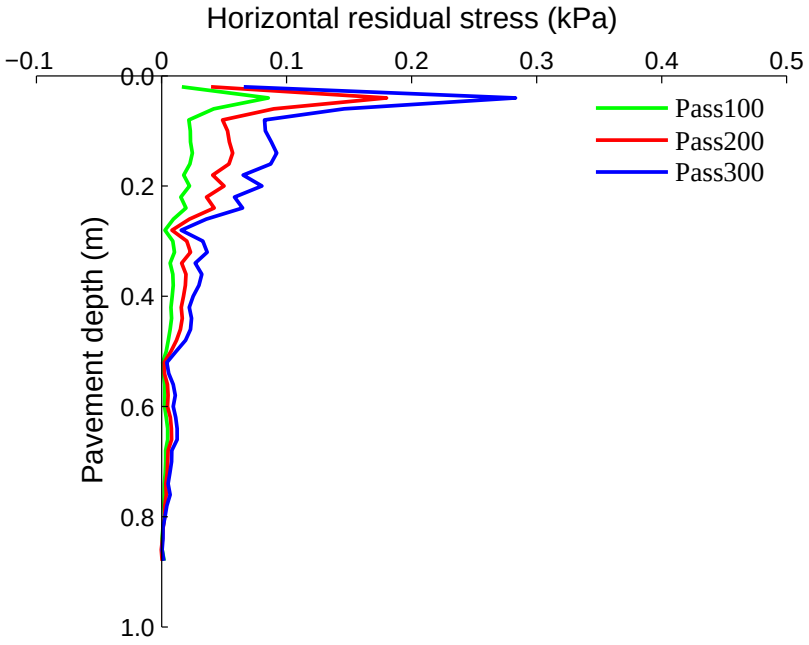

(b) Horizontal residual stress

Figure 6.2: Effect of wheel pass on residual stress distribution in single-layered pavement

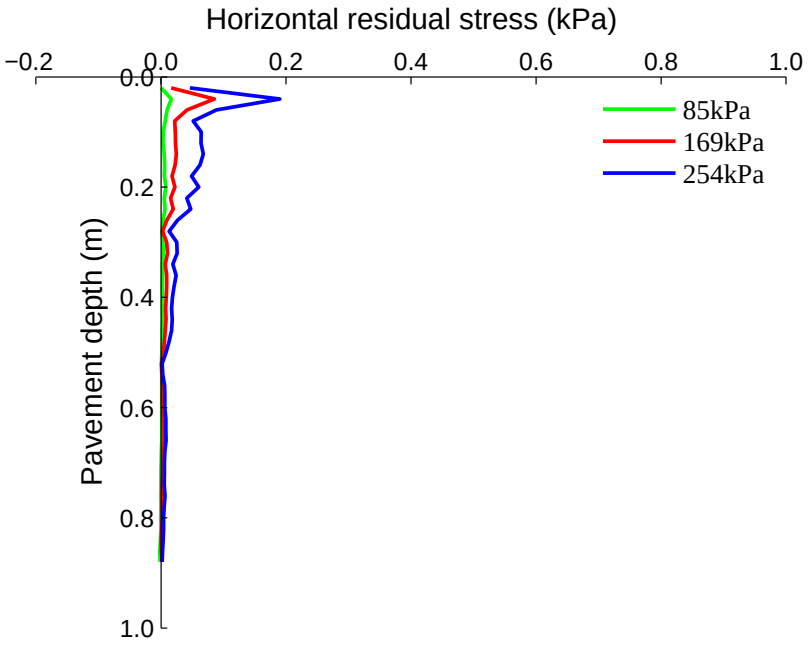

(a) Pass100

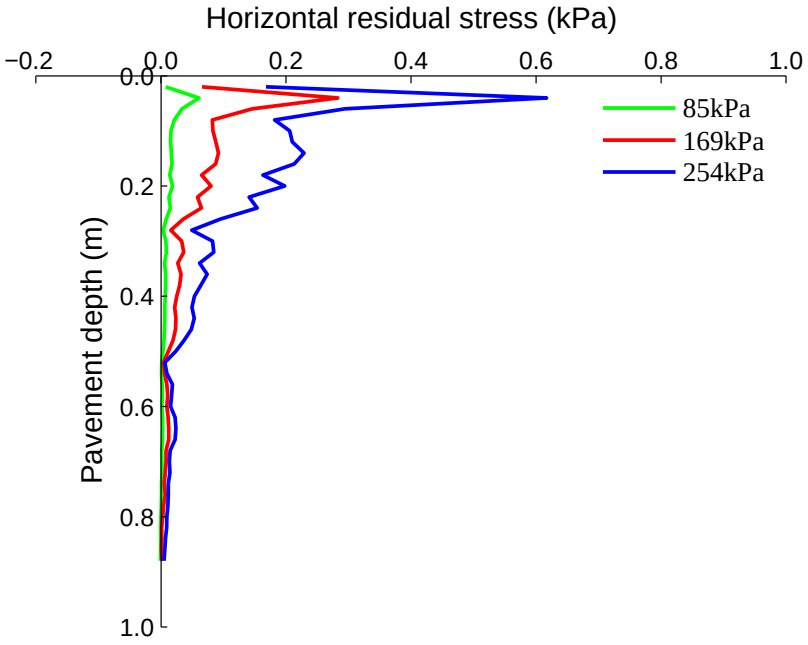

(b) Pass300

Figure 6.3: Effect of wheel pressure on horizontal residual stress distribution in single-layered pavement

6.4 Double-layered pavement structure

6.4.1 Permanent deformation

6.4.1.1 Thickness of simulated asphalt layer

For a double-layered pavement structure, the upper layer is the simulated asphalt concrete, which is composed of particles and parallel bonds existing at the interparticle contacts. The second layer is considered as a granular base. As discussed in Subsection 6.2.1, the parameters of the particles in these two layers are identical. During the repeated loading, the friction coefficient of the pavement particles is 0.7. Both normal and shear strengths of the parallel bonds are so large that no breakage of bonds is observed during the simulation. The gravity acceleration is assigned as 0.1m/s^2. Three thicknesses for the upper layer are studied, i.e. 0.10, 0.15 and 0.20m. The corresponding numbers of parallel bonds are nearly 2300, 3600 and 4700. The aggregate thickness of the pavement sample remains unchanged, which is approximately 0.95m. The wheel load is selected as 1000N. Both the normal and shear stiffnesses of wheel particle are 5×10^4N/m. The average contact width between wheel and pavement surface is calculated, namely 0.10m and then the corresponding mean contact pressure is computed as 10.0kPa.

It is found that the thickness of the upper layer has an obvious impact on the pavement permanent deformation, as shown in Figure 6.4. The pavement with a thick (simulated) asphalt layer produces a small permanent deformation, as an indication that the asphalt layer prohibits the permanent deformation to some extent. When the thickness of the upper layer increases from 0.15 to 0.20m, the decrease in plastic deformation is relatively evident. The development of the permanent deformation rate (in units of millimetres per 50 passes) with the number of load passes is displayed in Figure 6.5. It is noted that the initial deformation rates are different for varied thicknesses of the upper layers. The rate decreases rapidly in the beginning and there is hardly any difference between the rates after wheel pass 150.

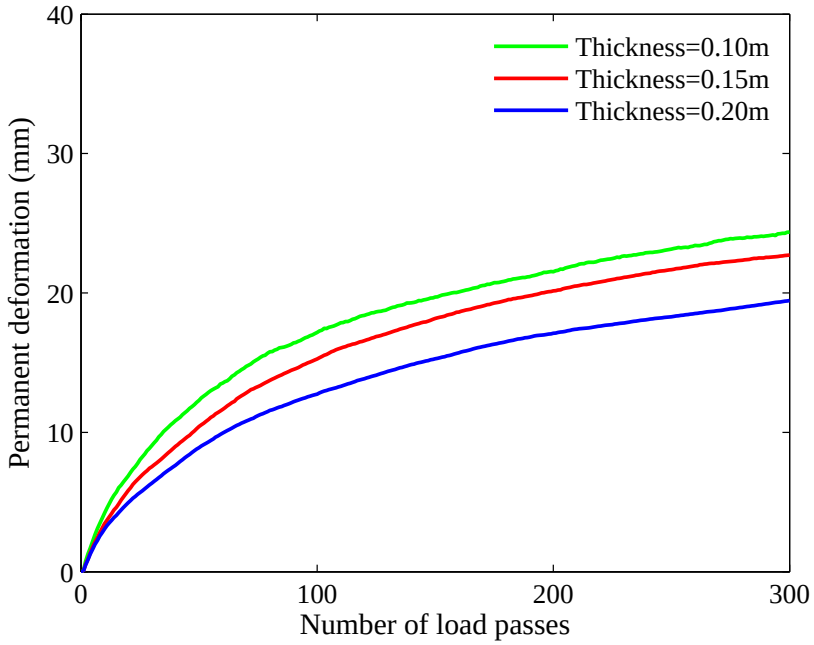

Figure 6.4: Effect of upper layer thickness on permanent deformation in double-layered pavement

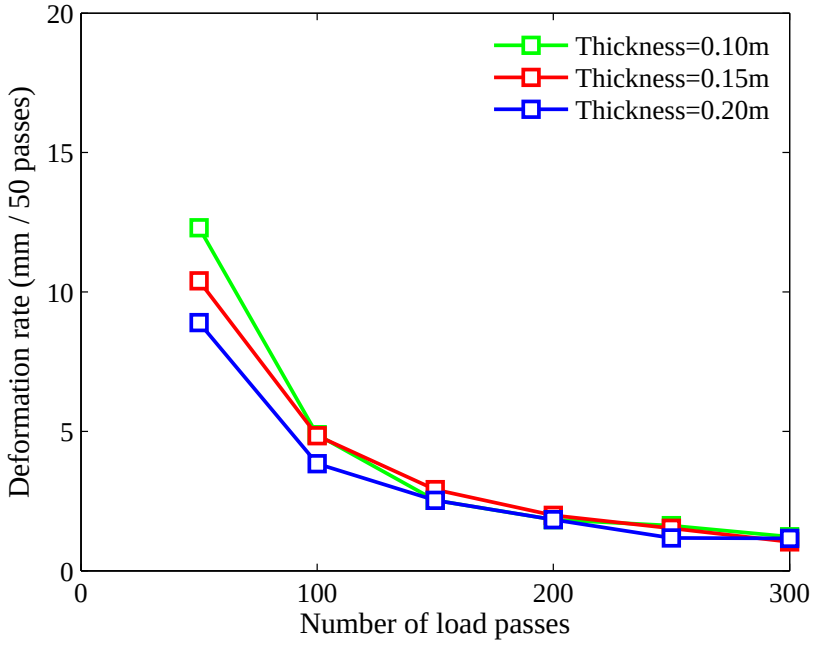

Figure 6.5: Effect of upper layer thickness on permanent deformation rate for double-layered pavement

6.4.1.2 Particle friction coefficient

As noted in Subsection 6.3.1, the permanent deformation is limited for pavements composed of bonding particles. However, a considerable plastic deformation is observed for the double-layered pavement, as discussed above. Therefore, the deformation mainly comes from the granular base. It is therefore logical that the friction coefficient of particles in the granular base may have an effect on the permanent deformation. The thickness of the simulated asphalt layer is selected as 0.15m. The friction coefficient of the particles in the upper layer is 0.7. Three friction coefficients for the granular base are studied, which are 0.5, 0.7 and 0.9 respectively. The gravity acceleration is 0.1m/s^2. The mean wheel pressure is 10.0kPa. The development of permanent deformation with number of load passes is plotted in Figure 6.6. The effect of the friction coefficient on permanent deformation is apparent. The small friction coefficient is associated with large permanent deformation. The change in the permanent deformation rate during the simulation is demonstrated in Figure 6.7. A large initial rate is observed for the small friction coefficient. The deformation rates are similar to one another after pass 100. Therefore, the effect of particle friction on permanent deformation is restricted to the initial stage of repeated loading. There is a continuous accumulation of permanent deformation since the deformation rate is still nonzero after 300 passes.

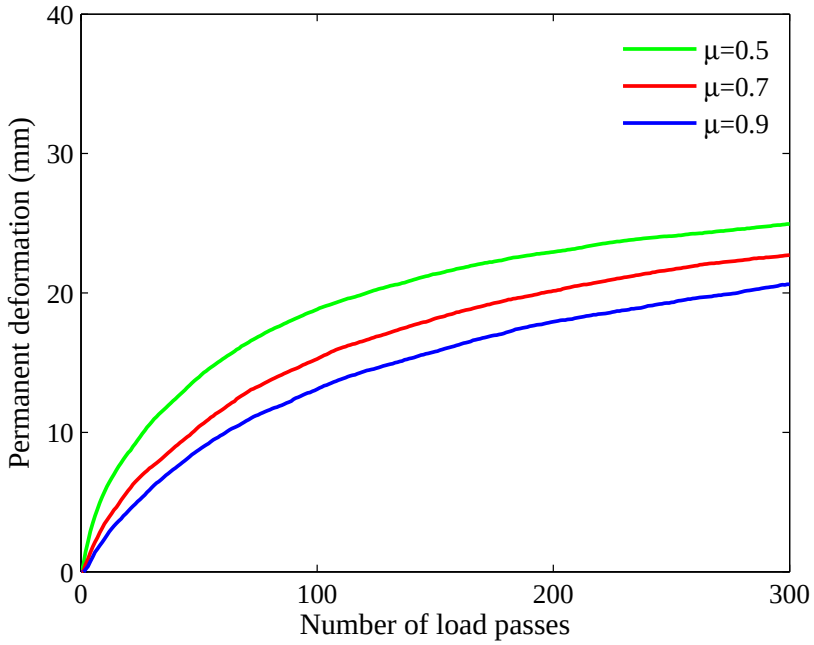

Figure 6.6: Effect of interparticle friction on permanent deformation in double-layered pavement

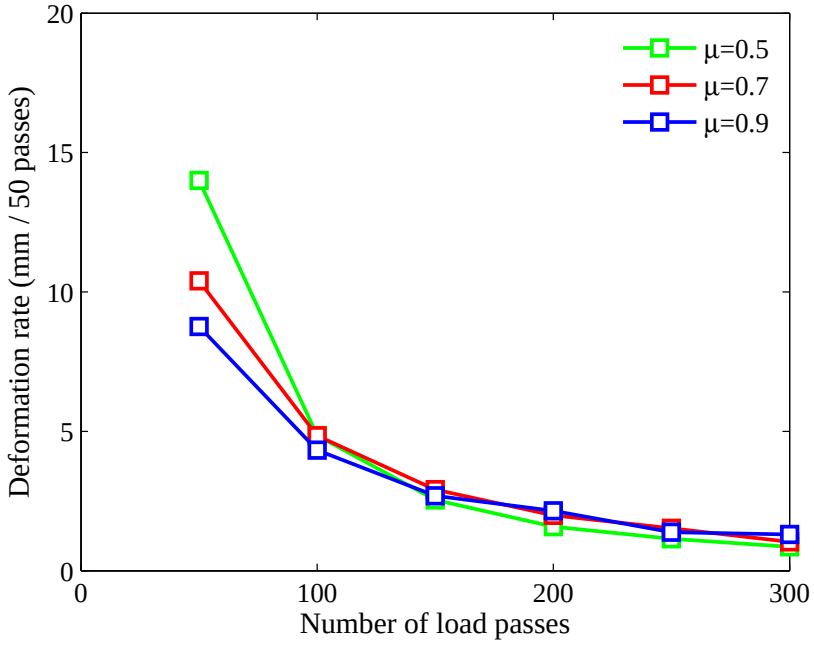

Figure 6.7: Effect of interparticle friction on permanent deformation rate for double-layered pavement

6.4.1.3 Wheel pressure

Different wheel loads have been applied to the pavement structure, which are 700, 1000 and 1500N respectively. The corresponding stiffnesses of the wheel particle (both normal and shear components) are 4×10^4, 5.5×10^4, and 7.5×10^4N/m respectively. The average contact widths between the wheel and pavement surface are calculated, namely 0.10, 0.10 and 0.118m. Therefore, the mean wheel pressures are 7.0, 10.0 and 12.7kPa, as shown in Table 6.2. The gravity acceleration is 0.1m/s^2. The friction coefficient of the pavement particle is 0.7. The thickness of the upper layer is 0.15m. The development of permanent deformation with number of load passes is plotted in Figure 6.8. The wheel pressure has a significant effect on the permanent deformation. When the contact pressure increases, there is an increase in the plastic deformation for a specific number of wheel passes. The permanent deformation rate against the load pass number is shown in Figure 6.9. Generally, the deformation rate decreases dramatically in the first 100 wheel passes. Afterwards, a gradual decrease is observed. When the pass number is 300, the deformation rate remains nonzero. There is no sign of the occurrence of pavement shakedown. The initial deformation rate increases with the rise in wheel pressure, whereas, after pass 100, the convergence of the deformation rate curves commences.

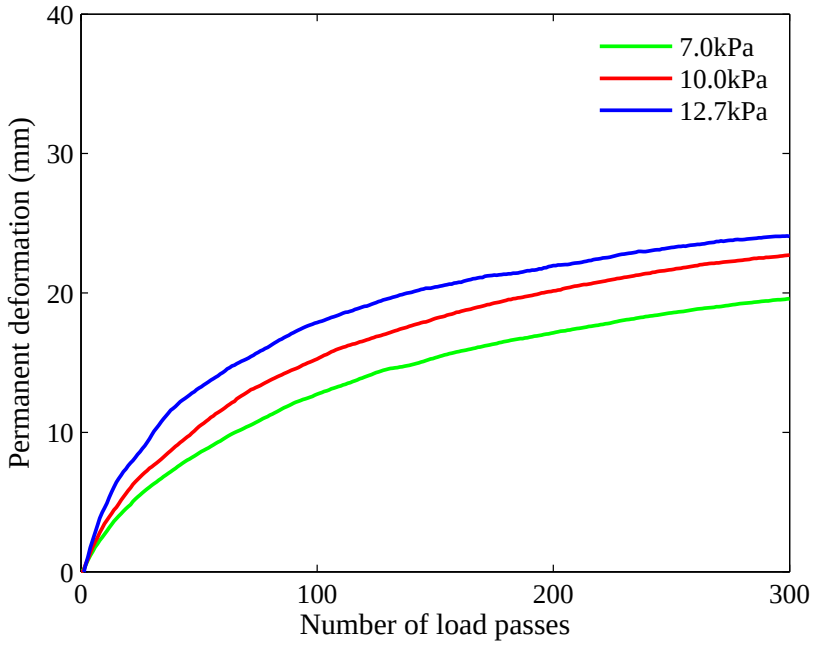

Figure 6.8: Effect of wheel pressure on permanent deformation in double-layered pavement

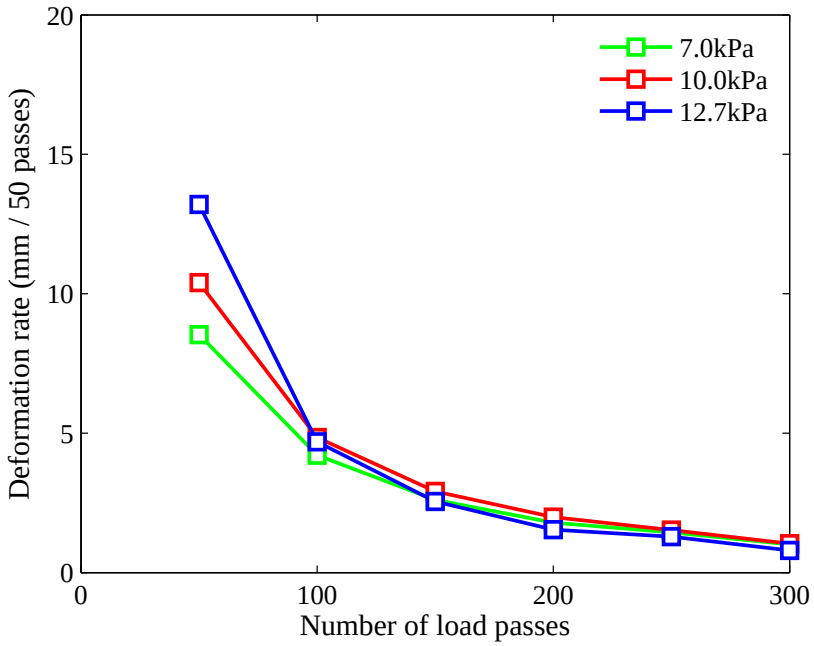

Figure 6.9: Effect of wheel pressure on permanent deformation rate for double-layered pavement

Gravity acceleration (m/s^2)	Wheel load (N)	Wheel stiffness (N/m)	Contact width (m)	Contact pressure (kPa)
0.1	700	4.0×10^4	0.10	7.0
	1000	5.5×10^4	0.10	10.0
	1500	7.5×10^4	0.118	12.7

Table 6.2: The detailed information about the wheel and wheel-related contact for double-layered pavement

6.4.1.4 Comparison with unbound pavement

As described in Section 5.3, the permanent deformation for an unbound pavement was investigated. A comparison between unbound and double-layered pavements is now made. For the unbound pavement, the lateral boundary is periodic and consequently the entire pavement surface is measured for determining the permanent deformation. The length of the unbound pavement is $30a$, i.e. 1.8m. On the other hand, for the double-layered pavement, the middle surface with a length of 0.6m is used to measure the plastic pavement deformation due to the restriction of the rigid lateral boundary. Based on the analysis in Subsection 5.2.5, a comparison of permanent deformation between these two varied pavements is feasible. The friction coefficient of the pavement particles is 0.7 and the gravity acceleration is $0.1 m/s^2$. The initial height of the pavement is approximately 0.95m and the void ratio is 0.26. The thickness of the simulated asphalt layer is 0.15m. A mean contact pressure of 7.0kPa is applied.

The permanent deformation developing with wheel load number is shown in Figure 6.10. The upper bonded layer has an apparent effect on the permanent deformation. Compared to the unbound pavement, the pavement deformation is restricted by the asphalt layer. The deformation curve is smooth for the double-layered pavement, probably because the pavement surface composed of bonding particles is flat after each wheel pass. The deformation rate was also studied, as shown in Figure 6.11. The initial deformation rate for unbound pavement is relatively large. Both the deformation

rates decrease rapidly prior to pass 100. After pass 150, the curves of the deformation rates converge, as an indication that the effect of the modelled asphalt layer on permanent deformation is confined to the opening stage of repeated loading.

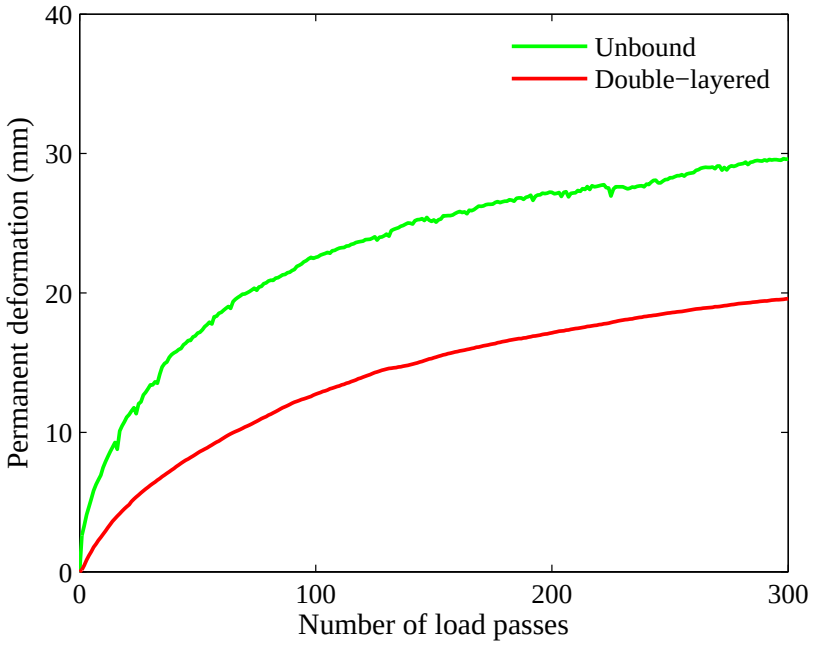

Figure 6.10: Comparison of permanent deformation between unbound and double-layered pavements

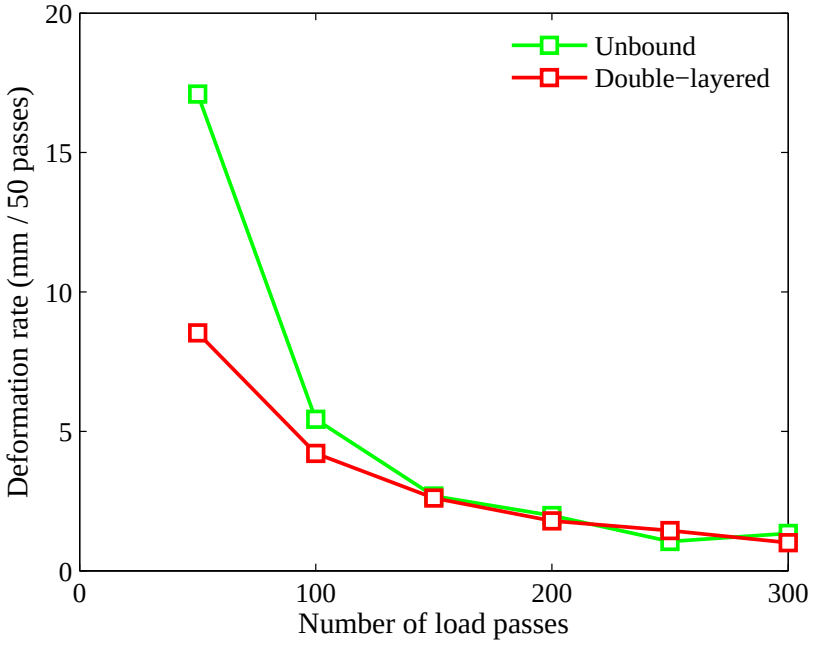

Figure 6.11: Comparison of permanent deformation rate between unbound and double-layered pavements

6.4.2 Residual stress

In this section, the residual stress for double-layered pavement is analysed. The measurement circle is used to obtain the residual stress in individual pavement layers. As discussed in Subsection 6.4.1, the pavement with a low self-weight stress field (i.e. g=0.1m/s^2) is studied. The factors affecting the residual stress distribution are taken into consideration, namely wheel pass number, wheel pressure, thickness of the simulated asphalt layer and particle friction coefficient.

6.4.2.1 Wheel pass number

With the increase in the number of wheel passes, the permanent deformation constantly accumulates. The residual stress is closely associated with the plastic strain. As a result, it is logical that the residual stress will develop continuously with the ongoing accumulation of plastic deformation. The friction coefficient of the pavement particle is selected as 0.7. The thickness of the upper layer is 0.15m and the mean wheel pressure is chosen as 10.0kPa. The residual stress distribution with pavement depth is demonstrated in Figure 6.12. The horizontal residual stress fields in the individual pavement layers are shown in Figure 6.12b, where the residual stresses are not continuous at the interface between the varied pavement layers. Compared to the unbound layer, the horizontal residual stress is quite large in the simulated asphalt layer. This is because of the cohesion of the bonded material. After the wheel load, large contact and bond forces can be generated at interparticle contacts. The large deformation in the unbound layer also induces the high residual stresses in the bonded layer. The horizontal residual stress increases from the pavement surface and then a maximum value is rapidly reached. Afterwards, a nearly constant decrease in residual stress is observed in the bonded layer. Although the permanent deformation is mainly attributed to the compaction of the unbound layer, horizontal residual stress in the unbound layer is not apparent. The effect of wheel pass number on horizontal residual stress is merely confined to the upper layer. As the number of wheel passes increases from 100 to

300, a growth in the maximum residual stress is observed, which is probably due to the incremental plastic normal and shear strains. Compared to the horizontal residual stress, the residual stress in the vertical direction can be disregarded (see Figure 6.12a), in accordance with the equilibrium condition for a traction free surface in Subsection 2.3.3.

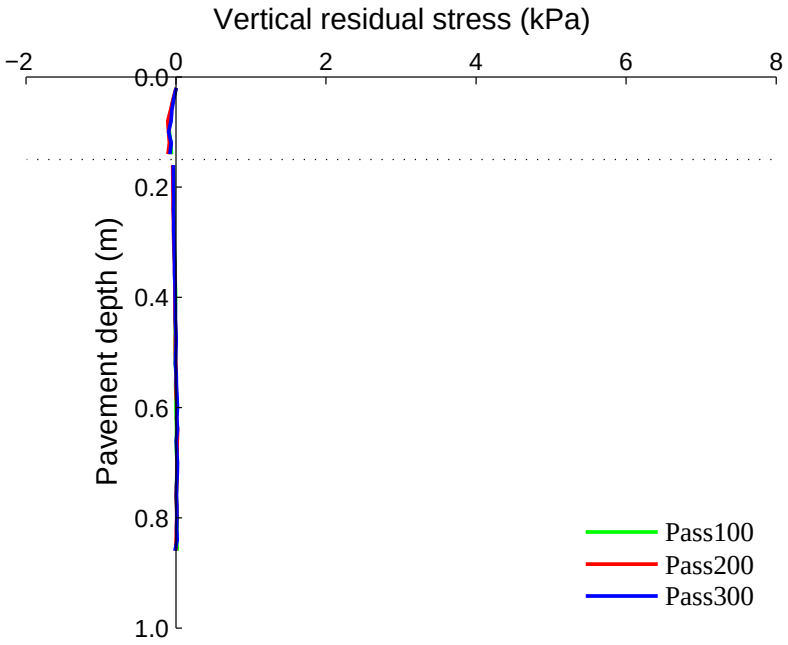

(a) Vertical residual stress

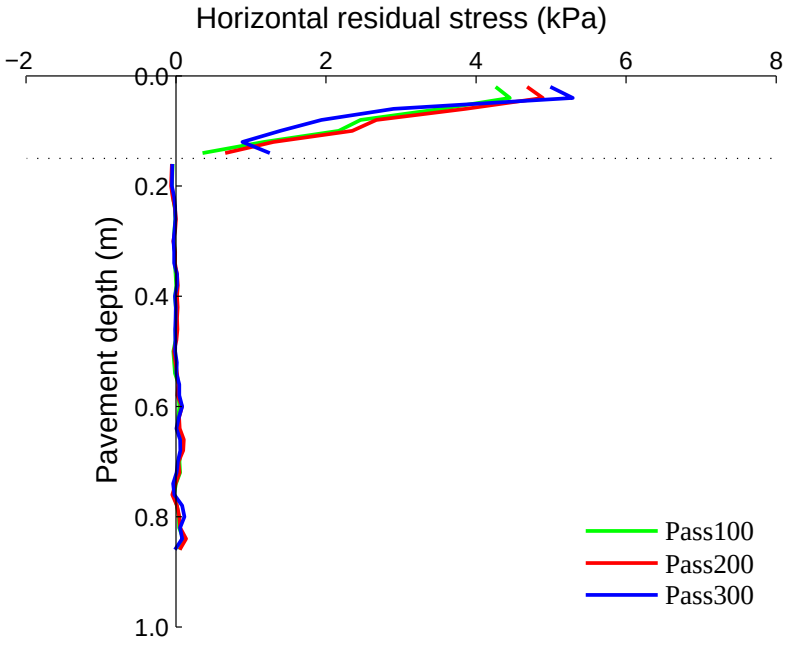

(b) Horizontal residual stress

Figure 6.12: Effect of wheel pass on residual stress distribution in double-layered pavement

6.4.2.2 Wheel pressure

Large plastic normal and shear strains can be induced by high wheel pressure. Therefore, the residual stress distribution may be affected by the wheel pressure. The thickness of the simulated asphalt layer is 0.15m, and the friction coefficient of the pavement particles is 0.7. There are three types of contact pressures applied to the pavement structure, namely 7.0, 10.0 and 12.7kPa. The horizontal residual stress developing with the pavement depth is demonstrated in Figure 6.13, where the pass numbers 100 and 300 are considered. In the bonded layer, the effect of wheel pressure on the residual stress is quite evident. The increased wheel pressure gives rise to an increase of residual stress distributed close to the pavement surface. As the residual stress is caused by the plastic deformation, the large plastic deformation corresponding with the high wheel pressure is possibly responsible for the apparent residual stress. The residual stress in the unbound layer is hardly affected by the wheel pressure. Compared to the bonded layer, the residual stress in the simulated granular base is nearly zero. Because the base course is comprised of unbounded particles, the interlocking effect is not evident during the simulation. Although a large relative displacement might exist between the unbound particles, the formation of a large contact force may be difficult. In contrast, in the simulated asphalt layer, the contacting particles are bonded together and, therefore, the interlocking effect is very strong. A small interparticle displacement may lead to large residual stress.

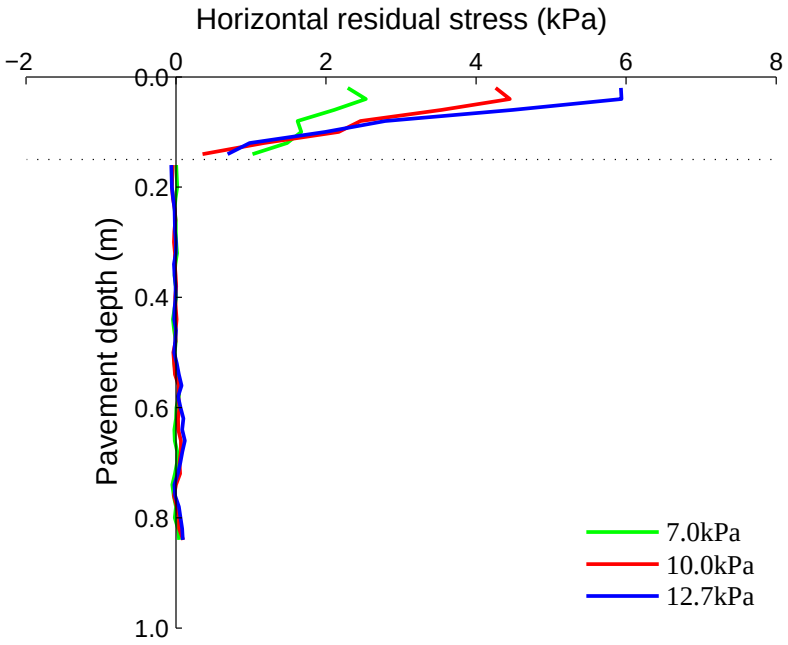

(a) Pass100

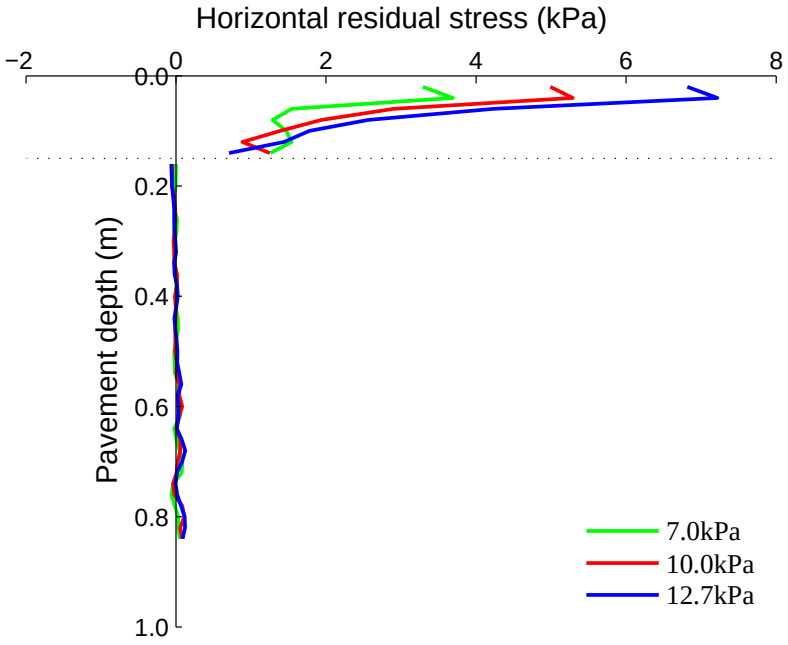

(b) Pass300

Figure 6.13: Effect of wheel pressure on horizontal residual stress distribution in double-layered pavement

6.4.2.3 Upper layer thickness

The thickness of the upper bonded layer has a significant impact on permanent pavement deformation, as discussed in Subsection 6.4.1. As a result, the bonded layer thickness is regarded as an influence on the horizontal residual stress distribution. Three thicknesses are applied to the simulated asphalt layers, namely 0.10, 0.15 and 0.20m. The friction coefficient of the pavement particles is 0.7 and the mean wheel pressure is 10.0kPa. After wheel pass 100 and 300, the wheel particle is removed from the right rigid lateral boundary. A certain number of calculation cycles are executed until a relatively stable stress state is reached in the pavement model. The difference between the current and initial stress is the residual stress. The development of horizontal residual stress with pavement depth is demonstrated in Figure 6.14. With the growth in pavement depth, the residual stress increases to a maximum value at first and then gradually decreases within the bonded layer. When the upper layer thickens, the maximum residual stress decreases evidently, probably due to the reduced permanent deformation. It is noted that the residual stress is mainly distributed in the first layer, irrespective of the varied thicknesses of upper layers. The residual stress in the unbound layer is hardly affected by the upper layer thickness.

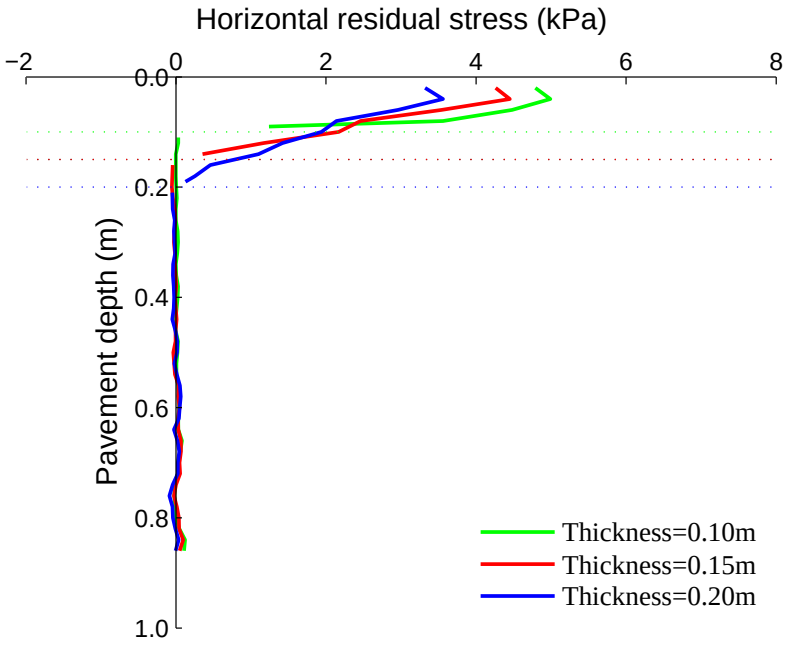

(a) Pass100

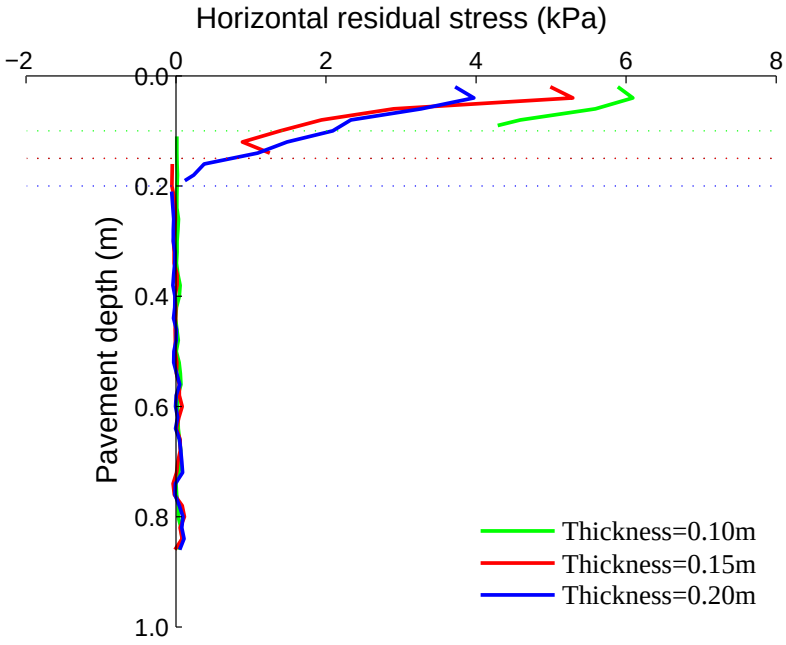

(b) Pass300

Figure 6.14: Effect of upper layer thickness on horizontal residual stress distribution in double-layered pavement

6.4.2.4 Interparticle friction

The contacting particles in the upper layer are bonded together and then their relative displacements after repeated wheel loading are seriously limited. Therefore, the effect of interparticle friction on permanent deformation is restricted to the unbound layer. As mentioned above, the residual stress field is closely influenced by the plastic deformation. The particle friction in the unbound layer is consequently assumed to have an effect on the residual stress. The friction coefficient of the particles in the upper layer is 0.7 and the coefficients in the base course are 0.5, 0.7 and 0.9 respectively. The thickness of the upper layer is selected as 0.15m and the mean wheel pressure is 10.0kPa. The horizontal residual stresses after wheel pass 100 and 300 are shown in Figure 6.15. The development pattern for residual stress with pavement depth is unchanged, irrespective of particle friction. Generally, an increase in residual stress is observed, followed by a broad decrease within the bonded layer. The maximum residual stress increases with the reduction of the particle friction coefficient. The effect of interparticle friction on residual stress in the unbound layer remains negligible.

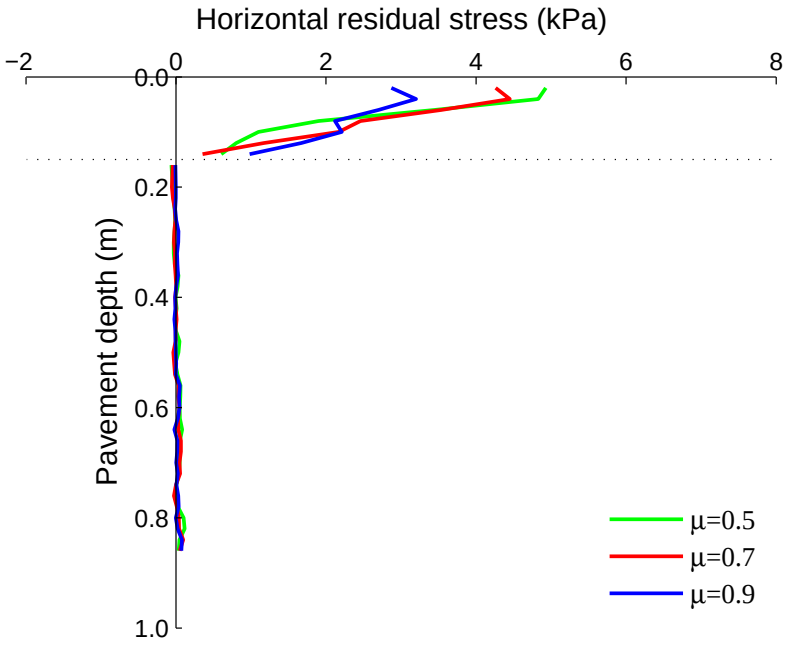

(a) Pass100

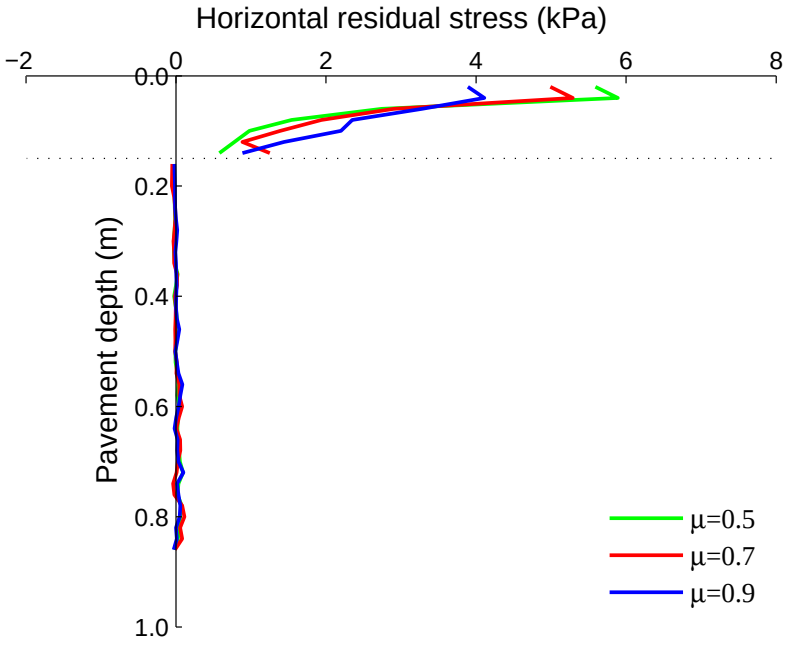

(b) Pass300

Figure 6.15: Effect of interparticle friction on horizontal residual stress distribution in double-layered pavement

6.5 Summary

Two kinds of pavement samples have been generated for the study of permanent deformation. The first is the single-layered pavement of bonded materials. The parallel bonds are created at all the interparticle contacts. The latter is a double-layered pavement, which is comprised of a simulated asphalt layer and a granular base. The parallel bonds are merely added to the upper part of the pavement to model the asphalt concrete. A rigid lateral boundary is introduced in the pavement simulation. Translation motion with a constant velocity (i.e. 0.5m/s) is applied to the wheel particle. There is no friction between the wheel and pavement surface. For the single-layered pavement, the deformability is significantly limited by parallel bonds at interparticle contacts. The permanent deformation can be disregarded, even for the high wheel pressure or the low initial stress field in the pavement.

The residual stress distributed in a single-layered pavement can be obtained through a measurement circle. With the pavement depth, the horizontal residual stress increases rapidly to a peak value near the pavement surface. When the load pass number changes from 100 to 300, the horizontal residual stress evidently grows, particularly at the peak point. Although plastic normal strain is not obviously accumulated, the development of residual stress is probably caused by incremental plastic shear strain. In contrast, the residual stress in the vertical direction can be ignored, consistent with theoretical analysis. Given a specific number of wheel passes, high wheel pressure produces a large horizontal residual stress. The increase of wheel pressure may lead to increased plastic shear strain, which possibly causes the increase in residual stress.

In the case of a double-layered pavement, the factors affecting the permanent pavement deformation have been investigated, namely upper layer thickness, the particle friction coefficient and wheel pressure. Generally, a considerable plastic deformation is involved in the simulation of a double-layered pavement. Since the deformation capacity is extremely limited for bonded materials, the pavement deformation is mainly attributed to compaction of the granular base. Besides, the deformation rate decreases

drastically at first and then a gradual decline is exhibited with load pass number. After pass 300, the rate remains nonzero, indicating no sign of the occurrence of pavement shakedown. The initial deformation rate is affected by the factors listed above, whereas, after a certain number of wheel passes, the curves of the deformation rates converge. This indicates that the effect of these factors on permanent deformation is mostly confined to the opening stage of repeated loading.

The simulated asphalt layer is able to restrict the deformation of a pavement subjected to repeated wheel loading. A small permanent deformation is observed for the pavement with a thick bonded layer. The initial deformation rate also becomes smaller when the upper layer is thickened. In addition, the friction coefficient of particles in the granular base has a significant effect on permanent deformation. It is found that a large particle friction coefficient is able to inhibit permanent deformation and the corresponding initial rate of deformation is reduced. In addition, when the wheel pressure is increased, an increase in the permanent deformation as well as the initial deformation rate is caused. Finally, the permanent deformation for double-layered pavement was compared to the unbound pavement. The unbound pavement produces a larger permanent deformation, whereas the ultimate deformation rates are comparable with one another.

The residual stress distributed in a double-layered pavement was investigated. Generally speaking, the horizontal residual stress increases to a peak from the pavement surface, followed by a progressive decrease with depth into the upper bonded layer. The residual stresses are not continuous at the interface between different pavement layers. There is negligible residual stress in the granular base, probably due to the weak interlocking effect between unbound particles. It is difficult for a big contact force to arise, even if a large relative displacement takes place between particles in the unbound layer. In contrast, the interlocking effect is very strong in the simulated asphalt layer, where the contacting particles are bonded together. Even a small inter-particle displacement possibly causes large residual stress.

The residual stress is closely related to the plastic deformation. The factors affect-

ing the permanent deformation therefore have an effect on residual stress. With the increase in wheel pass number, there exists an increase of the peak of the horizontal residual stress. In addition, high wheel pressure gives rise to a large permanent deformation for a specific wheel pass number, resulting in a rise in the maximum residual stress. Moreover, as the upper layer thickens, the peak of horizontal residual stress reduces. The interparticle friction in the unbound layer also affects the residual stress distribution within the upper layer. The relatively small permanent deformation induced by a high friction coefficient is associated with an increased peak residual stress.

Chapter 7

Micro-analysis of the DEM Pavement Simulation

7.1 Introduction

The probabilistic characteristics of contact forces in DEM pavement simulations have been investigated. The unbonded pavement model is divided into several layers and the thickness of each layer is set at 0.10m. The normal and tangential contact forces between two contacting particles, described by the probability density distribution, are then evaluated. The factors most likely to affect the probability density distribution are studied: pavement layer, the number of wheel passes, wheel pressure, initial void ratio and particle friction coefficient.

On the other hand, the layer thickness for both single- and double-layered pavements is chosen to be 0.15m. The forces existing in the bonded layers are comprised of contact forces between particles and the forces in parallel bonds. In both cases, the forces can be classified into normal and shear forces. The development of probability density distribution according to pavement layer and number of wheel passes is investigated. Moreover, the effect of wheel pressure on the probability distribution is included in the

microscopic analysis.

Apart from the probability analysis of the contact forces, for unbonded pavements, the sliding contact ratios are analysed using the pavement layering method. The contact slippage can be determined on the basis of the ratio of the tangential to normal contact force. Lastly, the particle displacements are analysed for both unbonded and bonded pavements. The factors affecting the particle displacement, e.g. wheel pass number and wheel pressure, are evaluated.

7.2 Unbonded pavement structure

7.2.1 Introduction

When ordinary solids are subjected to uniform loads, the induced stresses are distributed homogeneously all over the materials. However, this approach is not suitable for granular materials, which are comprised of discrete macroscopic particles. For such systems, force chains and spatially inhomogeneous stress distributions are generally presented. Most of the stresses are transmitted through the material along the force chains containing the large interparticle forces. The probability density distribution of the contact forces allows us to analyse these stresses in a quantitative way (Liu et al., 1995).

Experimental studies on these distributions have been performed, for example by Liu et al. (1995), Mueth et al. (1998), Makse et al. (2000) and Blair et al. (2001) where the carbon paper method was employed to measure the forces at the boundary. On the other hand, the forces on the individual particles at the bottom boundary have been obtained using a high precision electronic balance (Løvoll et al., 1999). Because of the limitations of experimental tests, the force measurement is generally confined to the normal component of forces at the boundary. Also, stationary bead packs were used in most of these experimental tests. Generally speaking, the distribution is nearly uniform

or possibly reaches a small peak at the small contact forces and exhibits an exponential decay at large forces (e.g. Løvoll et al., 1999; Blair et al., 2001). Nevertheless, a Gaussian-type distribution is found for high pressures (Makse et al., 2000).

Different analytical models have been presented to explain the probability distributions. A famous model is the q model, proposed by Liu et al. (1995) and demonstrated further by Coppersmith et al. (1996). The q model is a simple scalar model and captures the primary characteristics of probability distribution at large contact forces: $P(F/\bar{F}) \propto exp(-dF/\bar{F})$ in which d is a positive constant, F is normal force and $\bar{F}$ is mean normal force. However, this model merely takes the normal contact force into consideration and is not suitable to predict the power-law behaviour for probability distribution at forces below the mean force. Another approach is the maximum entropy method, presented by Rothenburg (1980) to study the quasi-static deformation in granular materials. Later, Bagi (1997) and Kruyt (2003) employed it to describe the probability distribution for contact forces. The characteristic of exponential decay for probability distribution was revealed by Bagi (1997). It is worth mentioning that the probability distribution for both normal and tangential components associated with contact forces was studied by Kruyt (2003), agreeing with many of the DEM simulation results in a qualitative way.

Many numerical studies of probability distribution for contact forces have been carried out generally using the discrete element method (e.g. Radjai et al., 1996; Thornton, 1997; Thornton and Antony, 1998; Makse et al., 2000; Kruyt, 2003). The internal contact forces and tangential forces can be measured by means of such discrete element simulations. These forces are not easily obtained by direct measurements in experimental tests. A qualitative comparison between simulation and experimental results can be made. The factors affecting the probability distribution have been studied: confining pressure, Young's modulus of particle, interparticle friction and so on. According to Makse et al. (2000), there is little difference between the distributions for normal contact forces at low confining pressures. A similar pattern is observed for the system of hard-spheres (i.e. with large Young's modulus) (Thornton and Antony, 1998). The change in the distribution with various low consolidation pressures is re-

flected in soft-sphere packs. Furthermore, the dependence of probability distribution on the interparticle friction is presented by Thornton (2000). Simulations by Radjai et al. (1996) predict the independence of the probability distribution from sample size and particle size distribution. On the other hand, the probability distribution for the contact force at a fixed contact orientation was considered by Kruyt (2003). It is worth mentioning that the present simulations are generally conducted on element tests. Different shear stages have a significant effect on the distributions (e.g. Thornton and Antony, 1998; Kruyt, 2003).

As discussed above, the nature of the internal force network is of significant importance to an understanding of the behaviour of granular materials. The probability density distribution of contact forces provides one with an illuminating insight into the observed properties of granular materials. At present, these studies focus mostly on element tests, rather than a physical structure. Therefore, the analysis of probability distribution will be applied here to pavement simulations.

7.2.2 Normal contact force

Differing from element tests, the stress paths are diverse at different depths in an unbonded pavement. However, because of the periodic boundary, the pavement elements at the same depth experience an identical stress path (see Subsection 5.2.3). Therefore, after being generated, the pavement is divided into several layers to perform the micro-analysis. The pavement particles are identified by the number of the individual layers and this identity information is not changed with the pavement deformation during wheel loading. Since the particle identities are determined, the microscopic information, such as normal contact force in the individual layers, can be obtained in PFC^{2D}. The friction coefficient of the pavement particles is 0.7. The gravity acceleration is 9.81m/s^2. The void ratio of the pavement sample is 0.26. Details of the unbonded pavement have been described in Subsection 5.2.2. The motion mode of the wheel particle is translational movement with a constant velocity of 0.5m/s.

The effect of the thickness of individual layers needs to be determined first. The interval of normal contact force (denoted as x_n) is set initially at 2N and three kinds of layer thickness (denoted as h) are considered, i.e. 0.08, 0.10 and 0.12m. The results of the top two layers for the initial pavement sample are demonstrated in Figure 7.1. The distributions of normal contact forces are affected by the layer thickness, whereas the variation trend generally remains unchanged. A peak is observed at a small normal contact force. Subsequently, a rapid decrease stage follows and then the decrease rate gradually decays. The thickness of the pavement layer was chosen as 0.10m. The interval of the contact force may also have an effect on the probability distribution. A reasonable interval needs to be determined. The intervals of 1, 2 and 3N are studied, as shown in Figure 7.2. When the interval is small (i.e. 1N), there are many fluctuations in the distribution. If the interval is too large, some information might be concealed, as seen in Figure 7.2b where, for the interval of 3N, there is no increase in the proportion of the normal-force contacts with the increase of the normal contact force. Consequently, the interval of the normal contact force is selected as 2N.

The factors affecting the probability distribution have been studied: pavement layer, number of wheel passes, wheel pressure, the initial void ratio and interparticle friction. Note that the distributions in Figures 7.3-7.8 are all related to the condition after the wheel load has been removed. The top four layers of the pavement are considered. The development of the distribution is sensitive to the pavement layer, as shown in Figure 7.3, where the initial sample, as well as the samples after load pass 100 and 500, are considered. The applied wheel pressure is 2.0kPa. Generally, the peak of the distribution decreases as the pavement depth increases, especially from the top to the second layer. Since the self-weight stress increases with the pavement depth, the proportion of the contacts with small normal forces will decrease accordingly. On the other hand, there will exist a slightly increased proportion of the contacts with large forces as the pavement depth rises. These trends seem insensitive to the wheel pass number. Moreover, for the initial pavement sample, the maximum contact forces are 117, 263, 377 and 417N respectively for the pavement layers from the top to the fourth layer. Compared to the other layers, the probability density for the top layer decreases

rapidly with the increase in contact force. Given a specific normal contact force within the range of zero to 50N, the probability density generally decreases with the pavement depth, apart from the top layer.

The effect of wheel pass number on the probability distribution for the top layer is shown in Figure 7.4. It is noted that this effect is clearest at the peak, which occurs at a small contact force. Therefore, the development of the distribution with wheel pass number is investigated more fully for contact forces from zero to 50N, as shown in Figure 7.5. Compared to the initial pavement sample, there is a reduction in the peak for the pavements subjected to a number of repeated wheel loadings. This phenomenon is noted for the top four layers studied. It is probably because during the wheel loading, there is a decrease in the small contact forces for different pavement layers. However, in the first two layers, the reduction of the peak is not obvious for low number of wheel passes (i.e. 100 and 300).

In order to make a comparison between different wheel pressures, a relatively large wheel pressure of 7.0kPa was added to the previous study. The comparison of probability density is made after the wheel pressure is removed at wheel pass 100, as shown in Figure 7.6. As in the study of wheel pass number, the effect of wheel pressure on the distribution is confined to the small contact forces. In the first two layers, there is little change in the distribution whereas an increase in the peak value is observed for the large wheel pressure (i.e. 7.0kPa) in the third layer. The reverse pattern is found in the fourth layer. Although the pavement demonstrates a large deformation when subjected to a large wheel pressure (see Subsection 5.3.5), there is no significant variation in the probability distribution, particularly for the top two layers. In addition, there is no fixed pattern to describe the effect of wheel pressure on the peak value of the distribution.

A dense pavement sample has been studied as a supplement to the study of the initial void ratio. The initial void ratio for the dense sample and the previous sample are 0.23 and 0.26 respectively. The number of wheel passes is 100. The variation in probability distribution with contact force is demonstrated in Figure 7.7, where the maximum

difference between the loose and dense samples is at the peak, at small normal contact forces. In the dense sample, the proportion of contacts with small contact force is less than those in the loose sample. This applies to the top four layers of pavement. That is probably because the large self-weight stress in the dense sample reduces the proportion of small contact forces.

The interparticle friction has an effect on the probability density distribution. Three friction coefficients of the pavement particles are considered, which are 0.5, 0.7 and 0.9 respectively. Note that the friction coefficient for the previous sample is 0.7. In comparison with the coefficient of 0.5, the proportion of small-force contacts for a large coefficient (i.e. 0.9) is reduced (see Figure 7.8). However, when the coefficient of 0.7 is taken into consideration, a fixed pattern for the distribution can not be found. A relatively stable structure is formed in the pavement when the friction coefficient is large enough (i.e. 0.9). Therefore, a greater number of large normal contact forces can be produced than for other samples during the wheel loading.

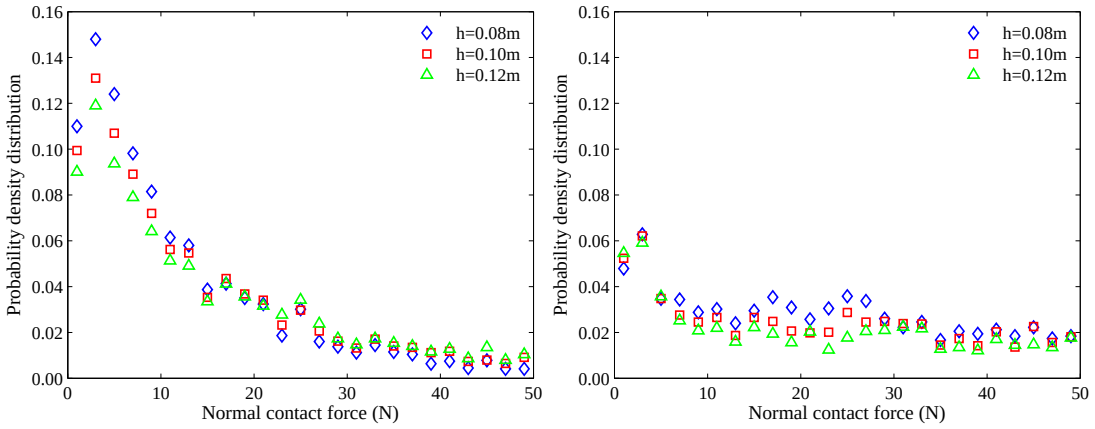

(a) Layer 1 *(b) Layer 2*

Figure 7.1: Effect of layer thickness on the probability density distribution of the normal contact force for the unbonded pavement

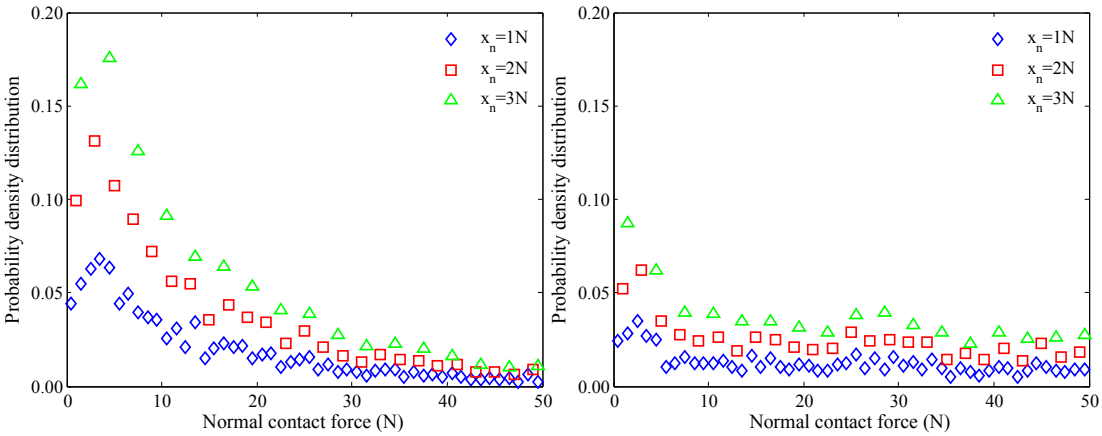

(a) Layer 1 *(b) Layer 2*

Figure 7.2: Effect of force interval on the probability density distribution of the normal contact force for the unbonded pavement

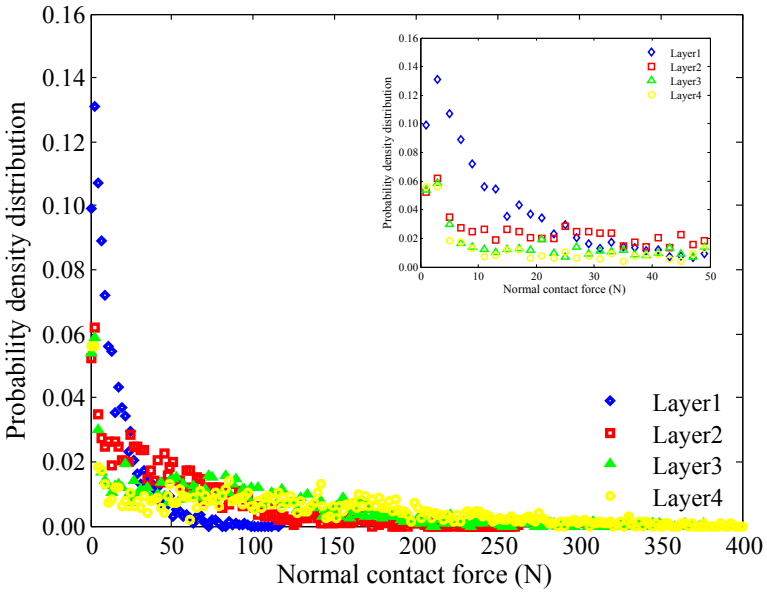

(a) Initial sample

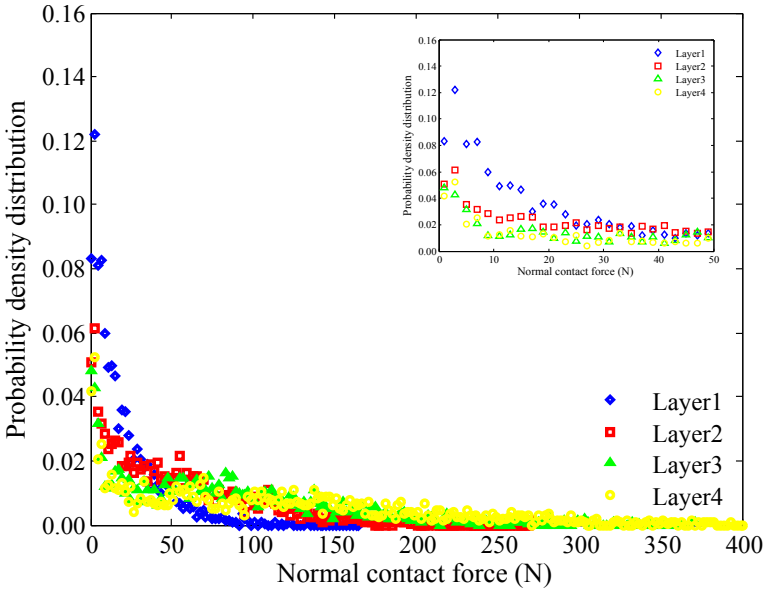

(b) Pass 100

Figure 7.3: Effect of pavement layer on the probability density distribution of the normal contact force for the unbonded pavement

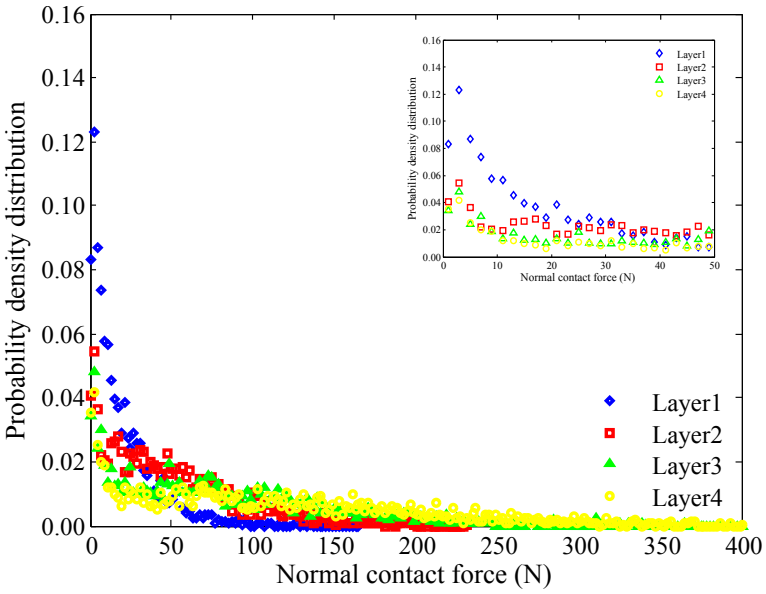

(c) Pass 500

Figure 7.3: Effect of pavement layer on the probability density distribution of the normal contact force for the unbonded pavement

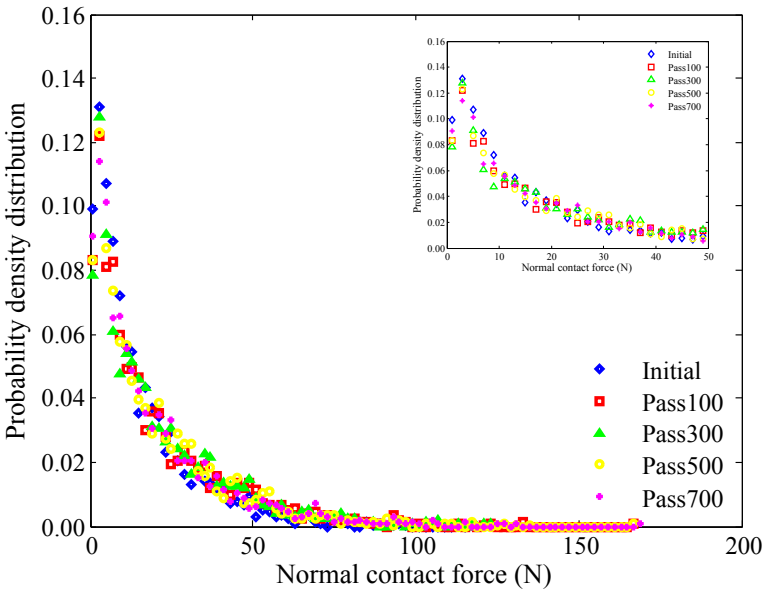

Figure 7.4: Effect of wheel pass number on the probability density distribution of the normal contact force for the unbonded pavement (for layer 1)

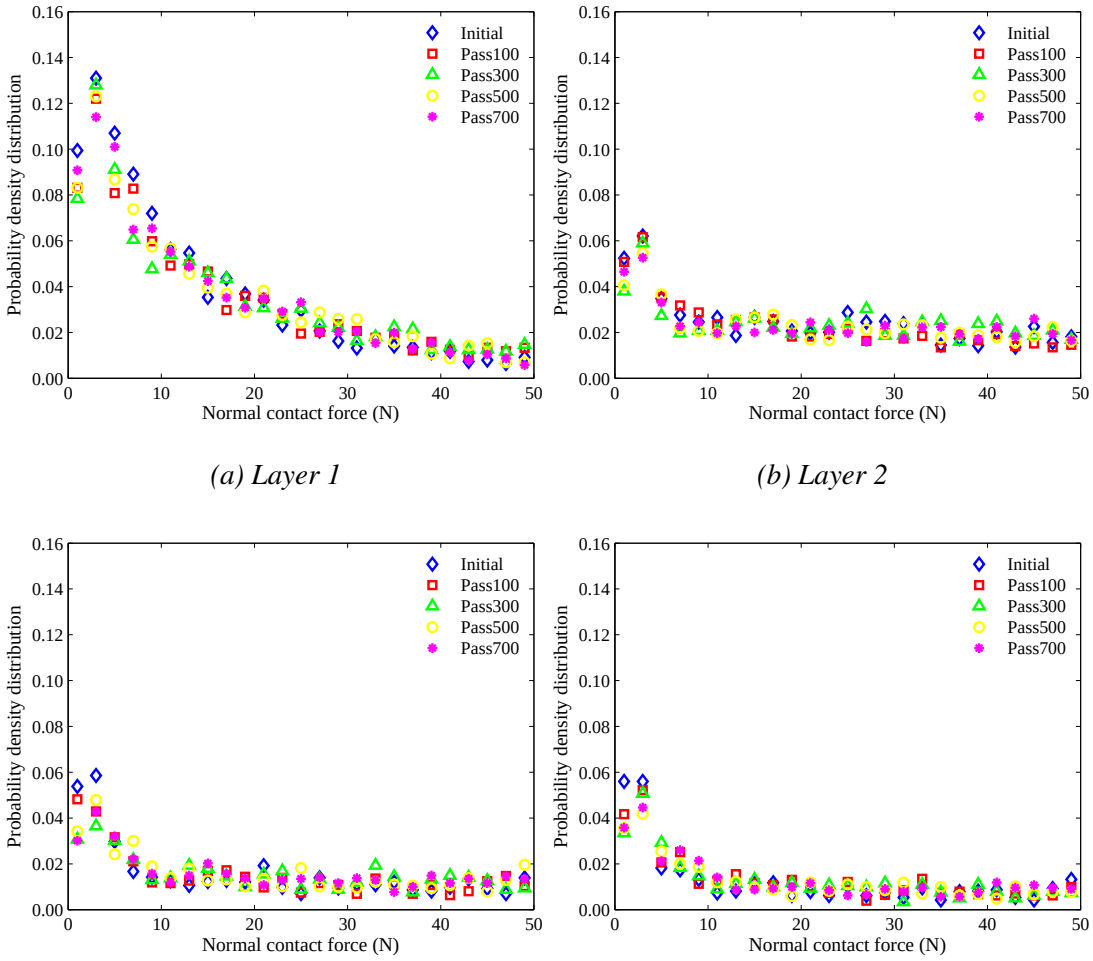

(a) Layer 1 *(b) Layer 2*

(c) Layer 3 *(d) Layer 4*

Figure 7.5: Effect of wheel pass number on the probability density distribution of the normal contact force for the unbonded pavement

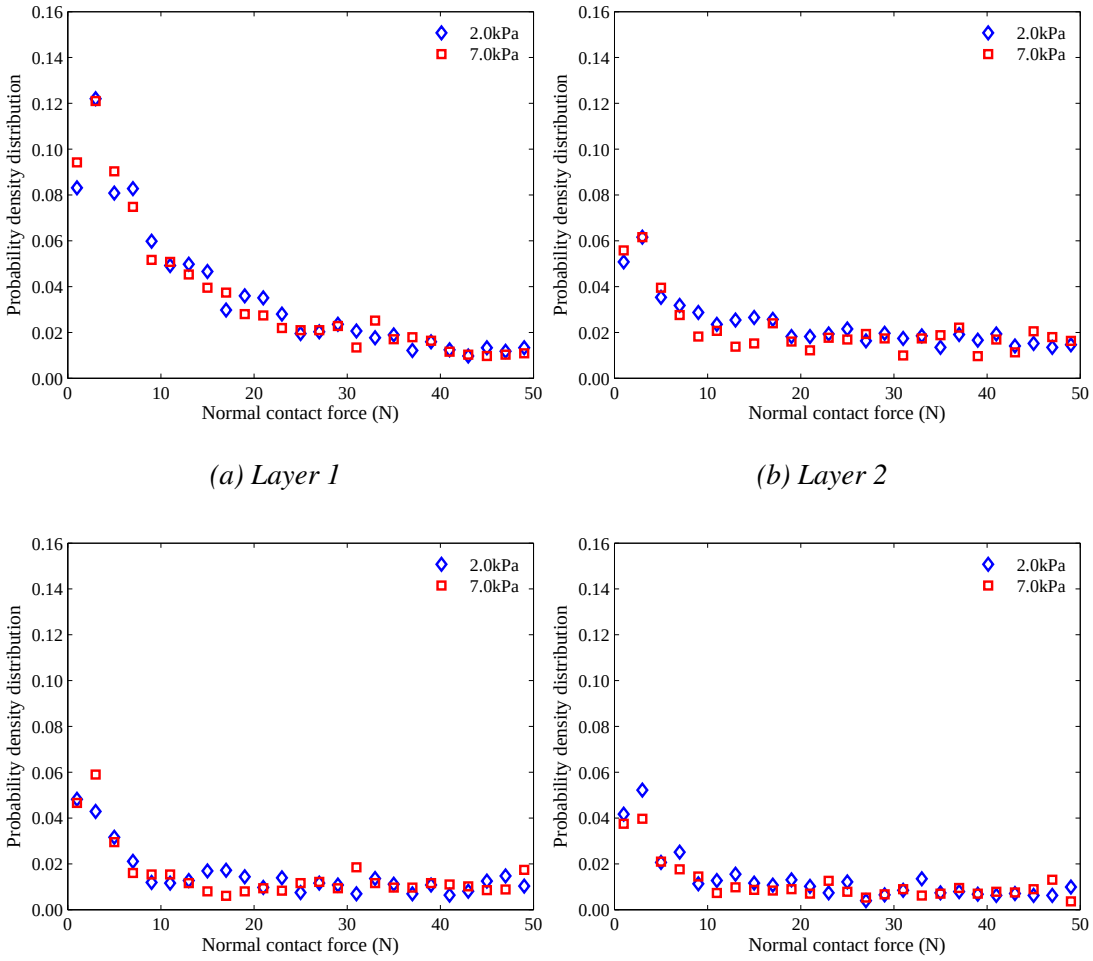

(a) Layer 1

(b) Layer 2

(c) Layer 3

(d) Layer 4

Figure 7.6: Effect of wheel pressure on the probability density distribution of the normal contact force for the unbonded pavement

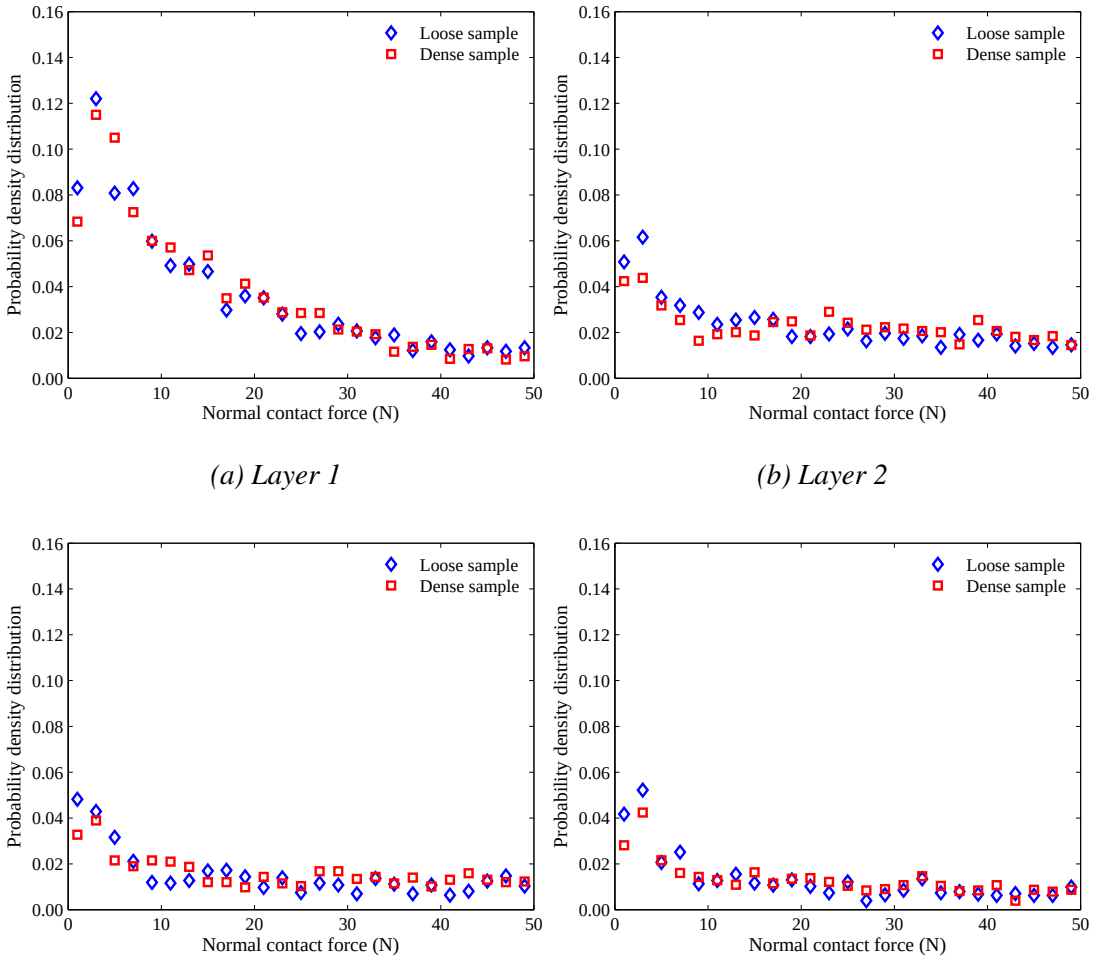

(a) Layer 1 *(b) Layer 2*

(c) Layer 3 *(d) Layer 4*

Figure 7.7: Effect of initial void ratio on the probability density distribution of the normal contact force for the unbonded pavement

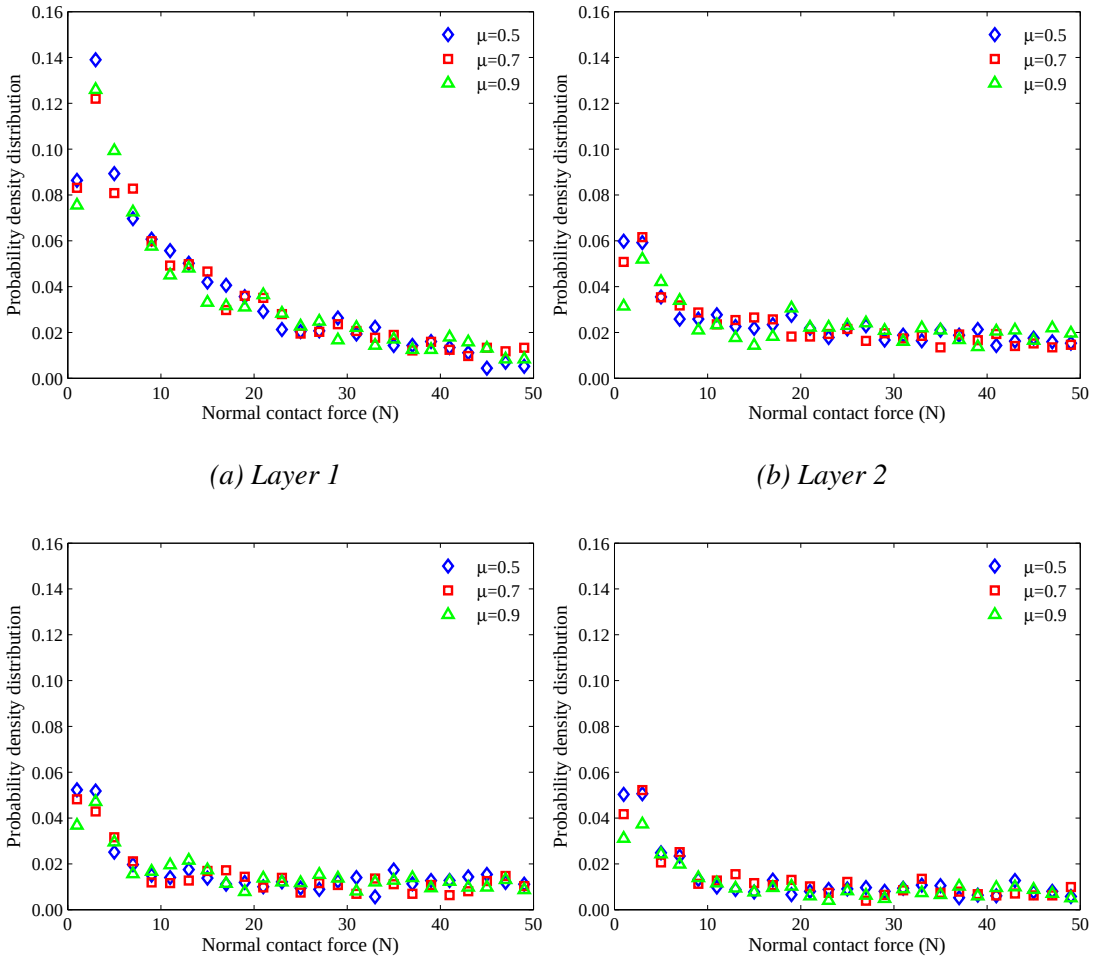

(a) Layer 1 *(b) Layer 2*

(c) Layer 3 *(d) Layer 4*

Figure 7.8: Effect of particle friction coefficient on the probability density distribution of the normal contact force for the unbonded pavement

7.2.3 Tangential contact force

As in the study on the normal contact force, the layering method is employed to analyse the probability distribution of the tangential contact forces. A feasible thickness for the pavement layer needs to be determined first. Three kinds of thickness (i.e. h) are considered, which are 0.08, 0.10 and 0.12m respectively. Details of the unbonded pavement are described in Subsection 7.2.2. It is worth mentioning that, in PFC^{2D}, the tangential force is a positive value if it makes the particle rotate or develop a rotation trend in a counterclockwise direction. Otherwise, the force is a negative value. In this way, the positive or negative sign does not stand for the magnitude of the tangential force, which depends on the absolute value of the force.

The probability distribution for the tangential contact forces is shown in Figure 7.9 where the interval of the tangential force (denoted as x_t) is set at 2N. Generally speaking, a peak for the distribution is observed at small tangential forces. There is a rapid drop from the two sides of the peak point. After that, a gradual decrease follows until the probability density approaches zero. With the increase in the layer thickness, only the peak of the distribution is slightly affected. There is a small reduction of the peak when increasing the thickness from 0.08 to 0.12m. As in the case of the normal contact force, the layer thickness for the tangential force is selected as 0.10m. On the other hand, the interval of the tangential contact force has a significant effect on the distribution, as shown in Figure 7.10 where three intervals are applied, i.e. 1, 2 and 3N. When the interval is enlarged, a significantly increased probability density is observed near the peak. Nevertheless, the development pattern is not affected. The interval of the tangential force is chosen as 2N in order to be consistent with that in the study of the normal forces.

The factors affecting the probability distribution have been studied such as pavement layer, number of wheel passes, wheel pressure, and so on. Note that the distributions in Figures 7.11-7.16 are all related to the condition after the wheel load has been removed. The probability distributions for the tangential forces in the different layers are shown in Figure 7.11 where the initial sample and the samples after wheel passes 100

and 500 are included. The distribution is obviously affected by the initial self-weight stress (see Figure 7.11a), especially near the peak, i.e. at small tangential forces. The probability density near the peak decreases with the pavement depth, particularly from the top layer to the second layer. That is because the increased gravity stress with pavement depth reduces the proportion of the contacts with small tangential forces. This pattern is not changed after the wheel loading, as shown in Figures 7.11b and 7.11c. For the initial pavement sample, the extremum in absolute terms increases with the depth of the pavement. The negative extrema for the top four layers are -26, -58, -134 and -180N respectively while the positive extrema are 34, 66, 102 and 162N.

The effect of wheel pass number on the probability distribution has also been studied, as shown in Figure 7.12. The wheel pressure is 2.0kPa and the top layer is selected. It is worth mentioning that the variation in the distribution with the pass number is generally confined to the contacts with small tangential forces. Therefore, the range from -10 to 10N for the tangential force is studied further. The distributions are given in Figure 7.13 in terms of the number of wheel passes and various pavement layers. In general, there is a reduction in the peak when the initial sample is subjected to a number of repeated wheel loads. It can be concluded that the external wheel load reduces the proportion of the contacts with small tangential forces. However, this law is not obvious for pass 100, except for the top layer.

A comparison of the distribution between the wheel pressures of 2.0 and 7.0kPa was performed (see Figure 7.14). This also focuses on the small tangential forces. The number of wheel passes is 100. In the top three layers, the distribution is insensitive to the wheel pressure. However, a reduction in the peak is observed for the fourth layer, when the wheel pressure changes from 2.0 to 7.0kPa. This is probably due to the fact that the large wheel pressure still has an effect on the distribution at depth in the pavement. However, near the pavement surface, the distribution of the tangential forces is independent of the wheel pressure. As described in Subsection 5.2.5, two kinds of pavement response (i.e. shakedown and ratchetting) are observed when the unbonded pavement with high self-weight stress experiences different wheel pressures. However, there is no significant change in the probability density distribution of the

contact force (see Figures 7.6 and 7.14). The residual stress distribution (see Figure 5.34a) changes with wheel pressure, which is probably caused by large contact forces even with smaller proportion in comparison with small contact forces.

A dense sample was added to study the effect of initial void ratio on the probability distribution. As described in Subsection 7.2.2, the initial void ratios for the dense and loose samples are 0.23 and 0.26. A slight decrease in the peak is observed for the dense sample, except for the top layer (see Figure 7.15). The decrease is more obvious for the fourth layer than the other two layers. The large gravity stress induced by the dense sample may reduce the proportion of contacts with small tangential forces. This effect is particularly noticeable at depth in the pavement.

The tangential contact force is affected by the particle friction coefficient. Therefore, it is likely that the friction coefficient may have an effect on the probability distribution. Three friction coefficients are considered, which are 0.5, 0.7 and 0.9 respectively. The distributions for the tangential forces are shown in Figure 7.16. A specific pattern can be summarized. With an increase in the particle friction coefficient, the peak of the distribution decreases. With the increase in the friction coefficient, interparticle slippages are easily inhibited and the internal structure in the pavement is more and more stable. Consequently, during repeated wheel loading, the interparticle friction for some contacts may increase, instead of the slippages of these contacts. If the interparticle contact slides, the slippage will slowly stop after the removal of the wheel load, which probably causes an increase in the proportion of the contacts with small tangential forces.

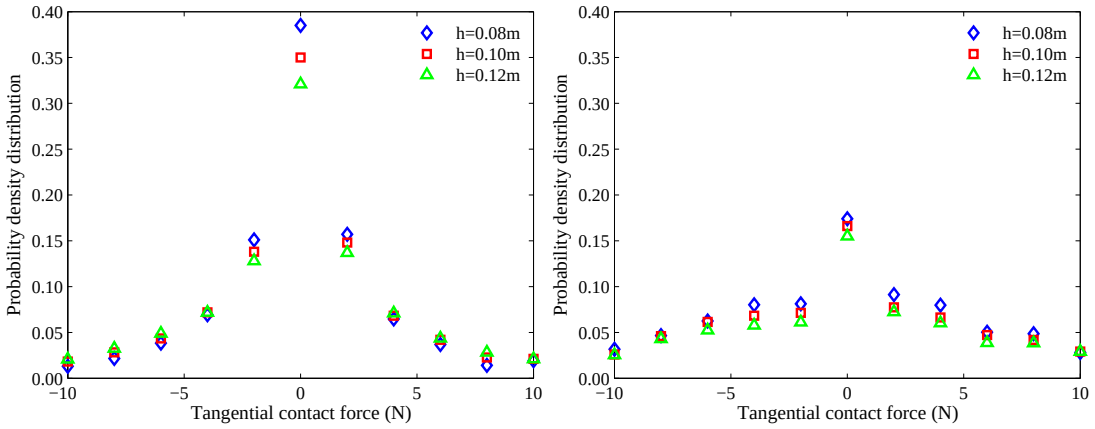

(a) Layer 1 *(b) Layer 2*

Figure 7.9: Effect of layer thickness on the probability density distribution of the tangential contact force for the unbonded pavement

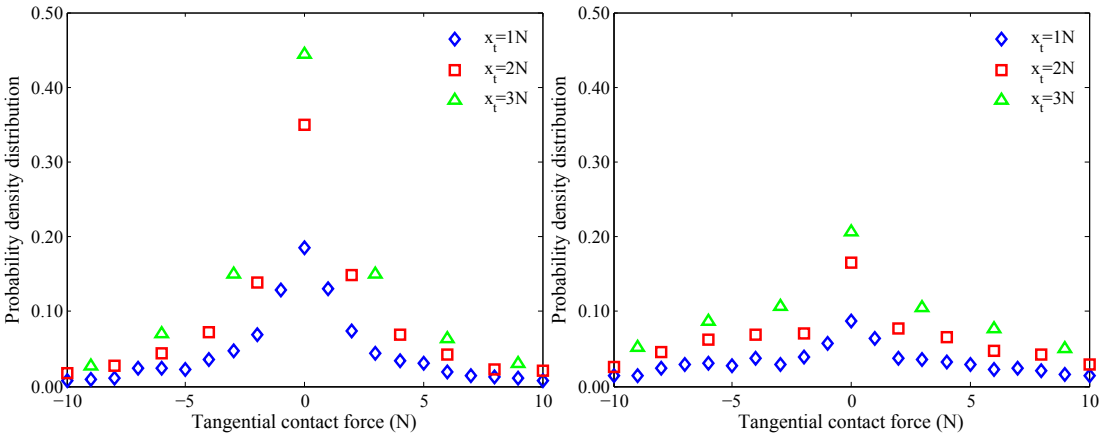

(a) Layer 1 *(b) Layer 2*

Figure 7.10: Effect of force interval on the probability density distribution of the tangential contact force for the unbonded pavement

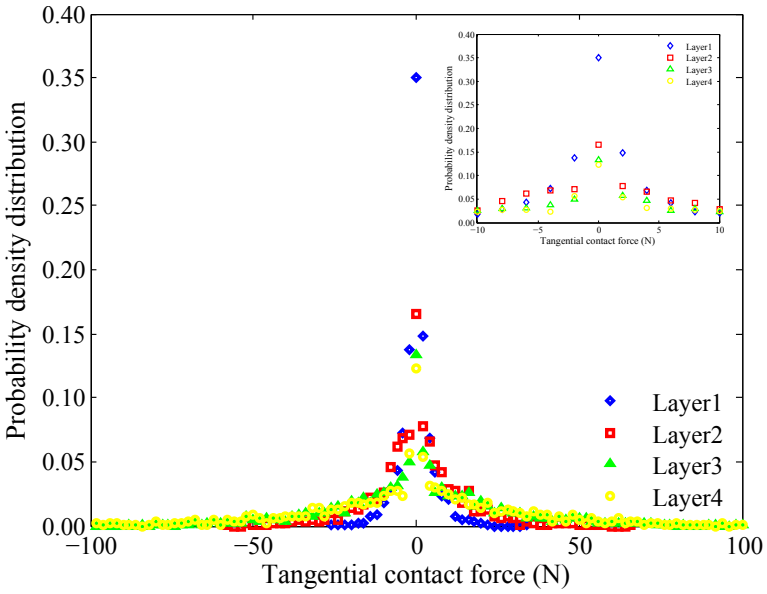

(a) Initial sample

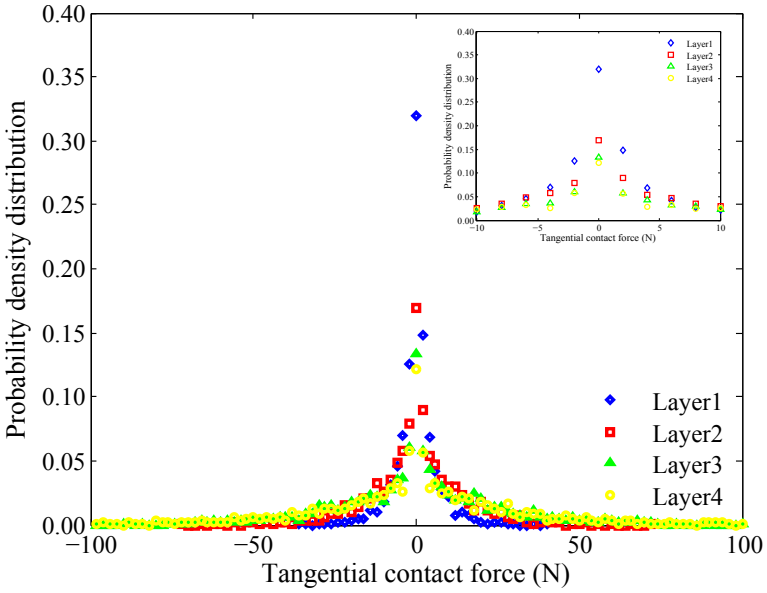

(b) Pass 100

Figure 7.11: Effect of pavement layer on the probability density distribution of the normal contact force for the unbonded pavement

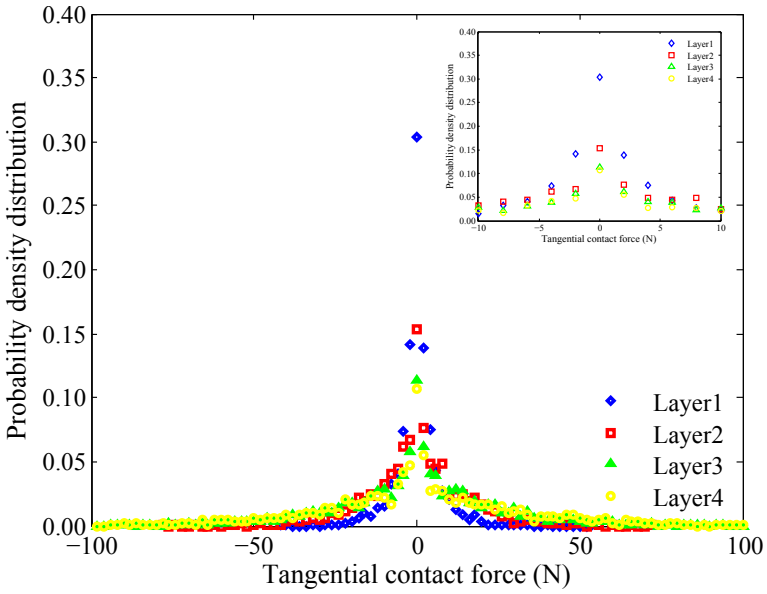

(c) Pass 500

Figure 7.11: Effect of pavement layer on the probability density distribution of the tangential contact force for the unbonded pavement

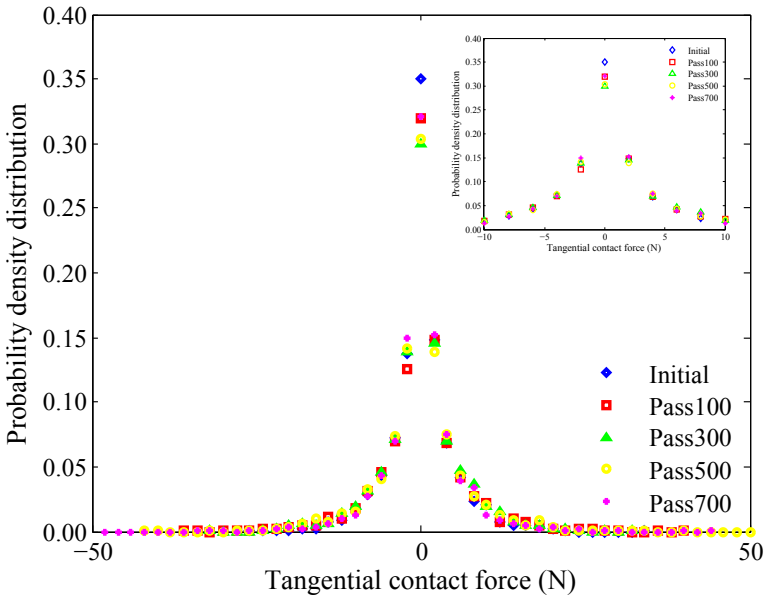

Figure 7.12: Effect of wheel pass number on the probability density distribution of the tangential contact force for the unbonded pavement (for layer 1)

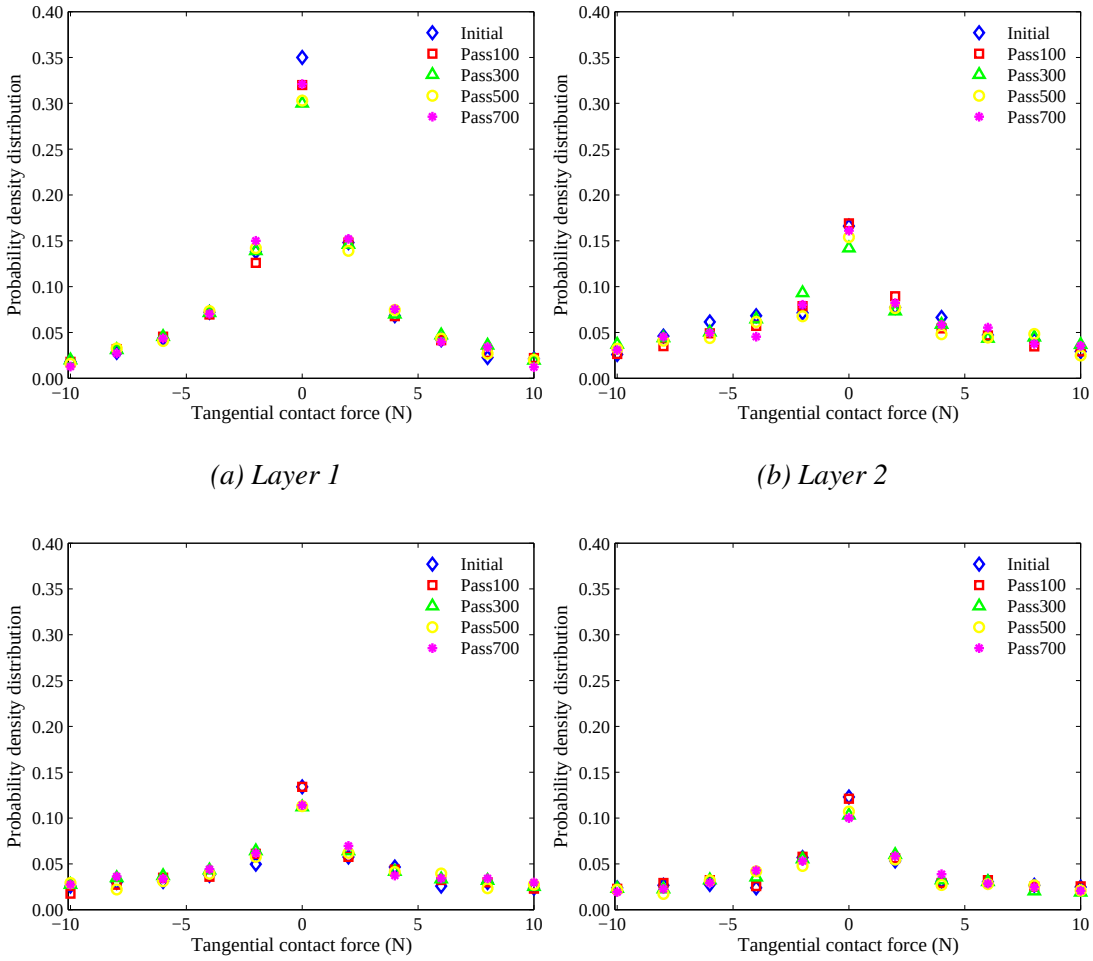

(a) Layer 1 *(b) Layer 2*

(c) Layer 3 *(d) Layer 4*

Figure 7.13: Effect of wheel pass number on the probability density distribution of the tangential contact force for the unbonded pavement

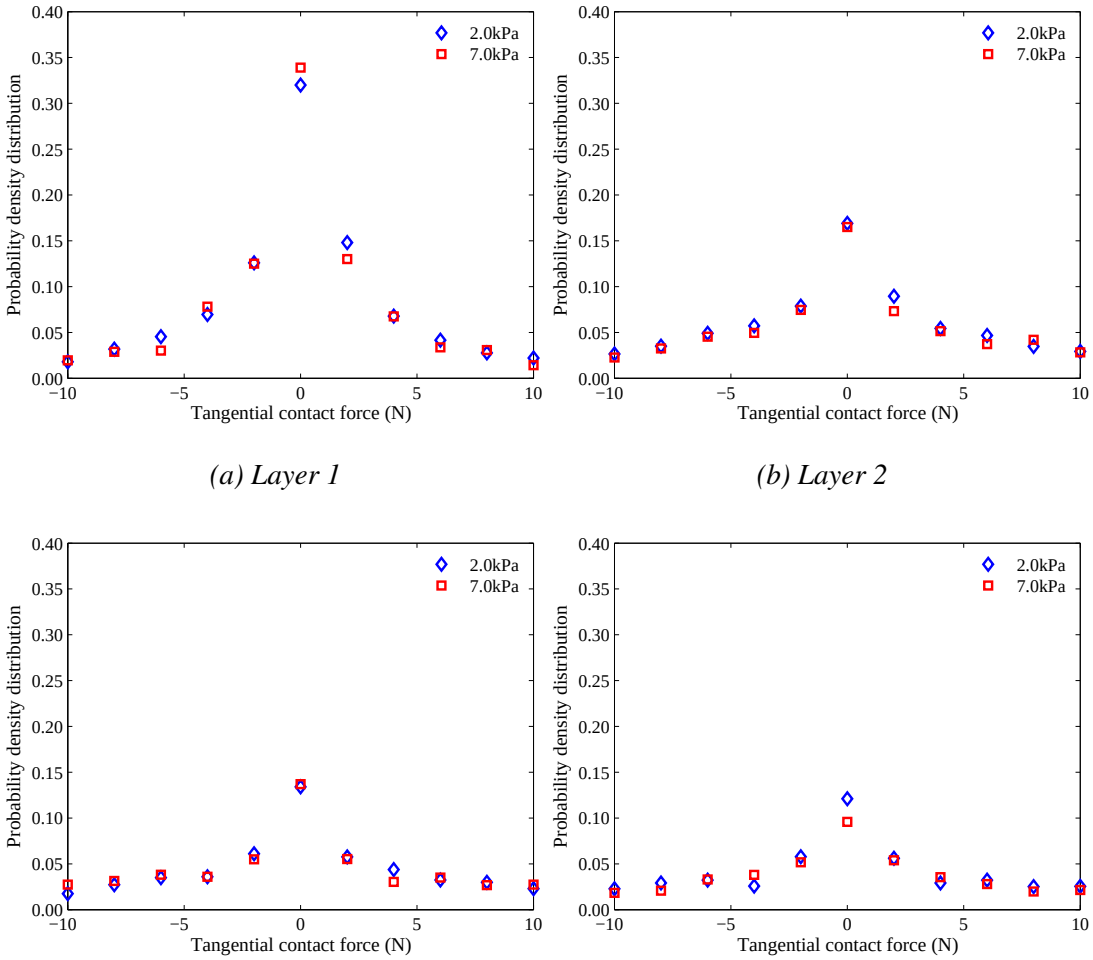

(a) Layer 1

(b) Layer 2

(c) Layer 3

(d) Layer 4

Figure 7.14: Effect of wheel pressure on the probability density distribution of the tangential contact force for the unbonded pavement

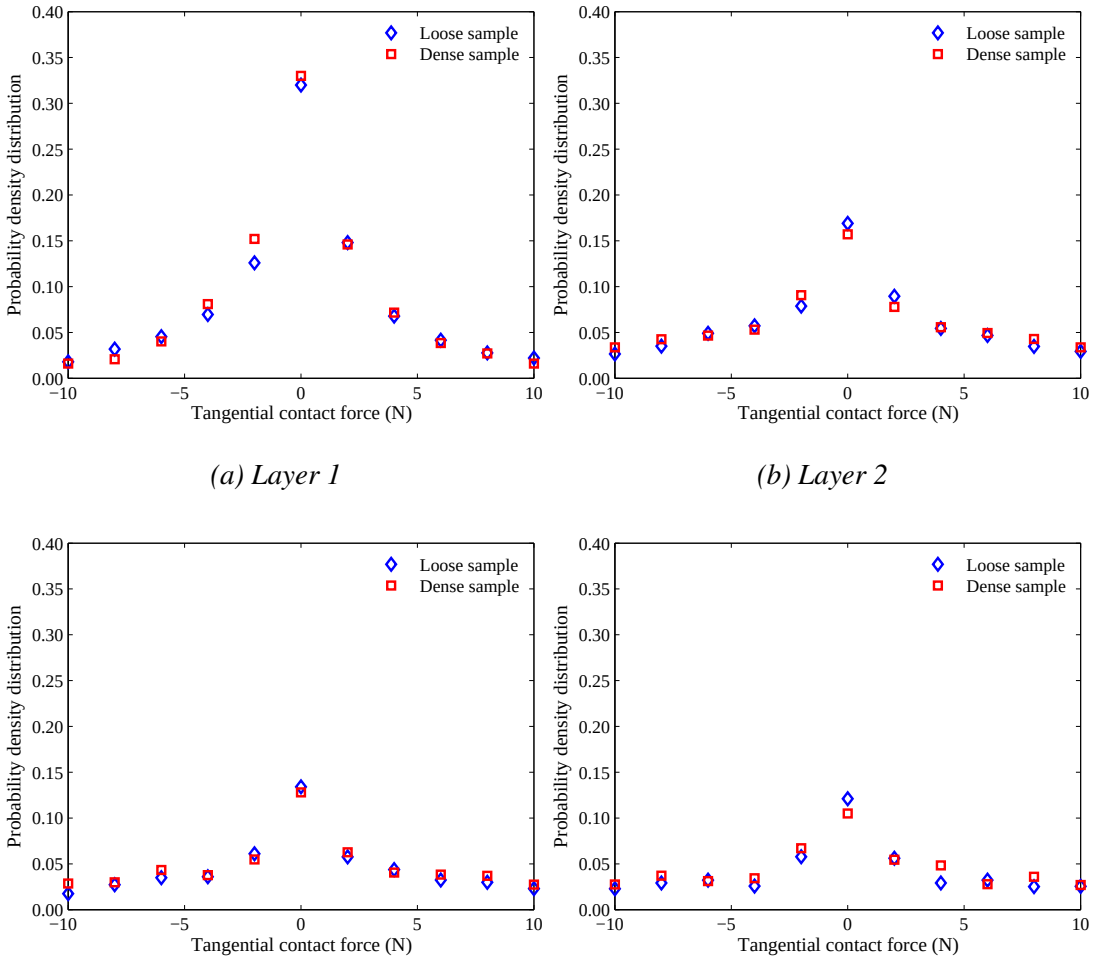

(a) Layer 1 *(b) Layer 2*

(c) Layer 3 *(d) Layer 4*

Figure 7.15: Effect of initial void ratio on the probability density distribution of the tangential contact force for the unbonded pavement

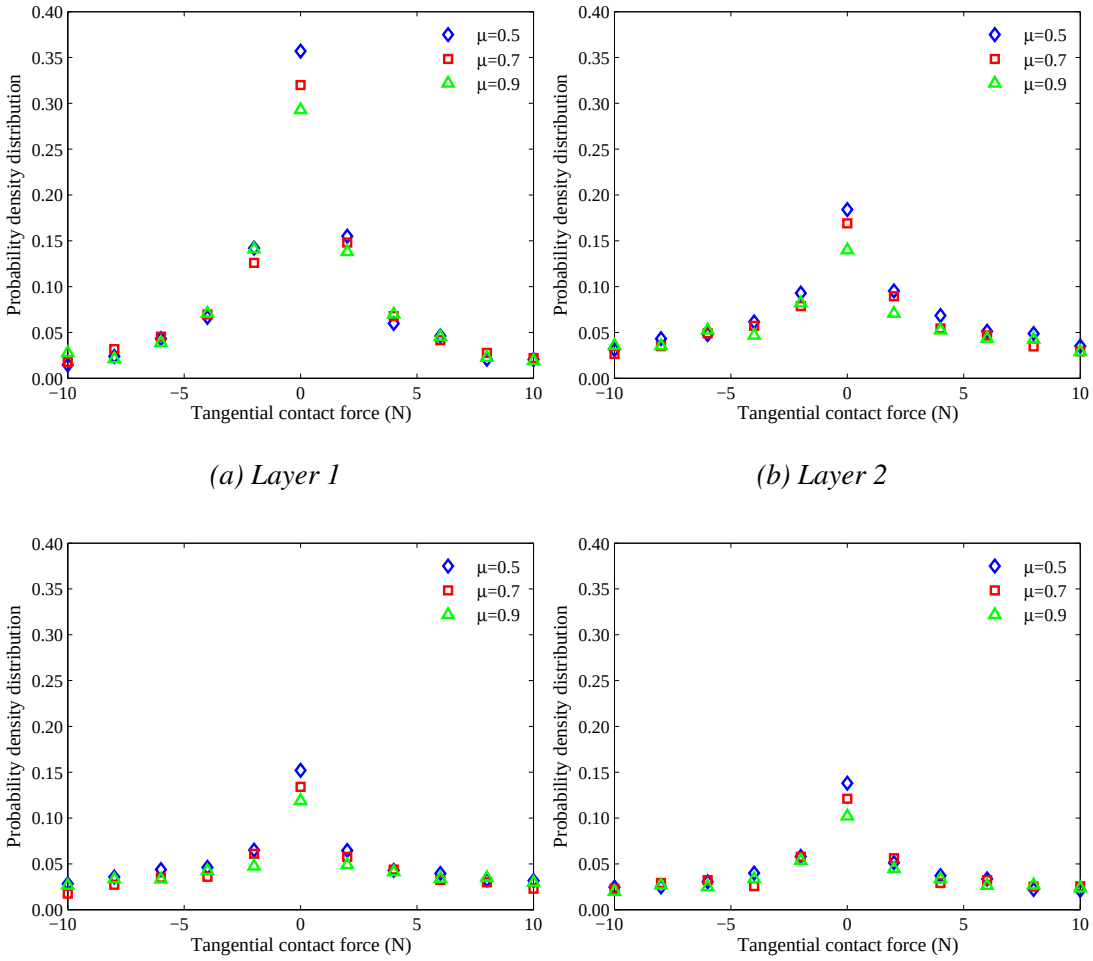

(a) Layer 1 *(b) Layer 2*

(c) Layer 3 *(d) Layer 4*

Figure 7.16: Effect of particle friction coefficient on the probability density distribution of the tangential contact force for the unbonded pavement

7.2.4 Sliding contact ratio

As described in Subsection 7.2.2, the initial pavement sample was uniformly divided into several layers. The thickness of the individual layers is 0.10m. Each layer can be considered as an assemblage of a number of pavement particles that are never changed during repeated wheel loading. The sliding contacts in each layer can be determined on the basis of the slip model (see Subsection 3.2.3). The sliding contact ratio for individual layers is defined as the ratio of sliding contact number to total contact number in each layer. Details of the pavement sample are described in Subsection 7.2.2. After trafficking, the sliding contact ratios are calculated.

The variation in the sliding contact ratio is studied in terms of the various pavement layers and the wheel passes, as shown in Figure 7.17. When the wheel pressure is relatively low, i.e. 2.0kPa, given a specific number of wheel passes, the ratio for the top layer is generally larger than that of the other three layers (see Figure 7.17a). However, there is no specific pattern to describe the relationship among the ratios for the layers from number 2 to 4. On the other hand, subjected to the wheel pressure of 7.0kPa, the pavement produces a decreasing sliding contact ratio with the pavement depth, from the top to the second layer in particular (see Figure 7.17b). This indicates that, with pavement depth, the effect of the wheel pressure on the contact slippage is gradually weakened. For the low wheel pressure, beneath the top layer, this effect is so weak that it is difficult to distinguish the variation of the ratio in different layers. The ratio of the sliding contacts is quite small. The maximum is nearly 0.015 for the relatively low wheel pressure and is less than 0.04 for the high wheel pressure. Another factor affecting the sliding contact ratio is the number of wheel passes. During repeated wheel loading, some fluctuations of the ratio are observed. There is no continuous decrease or increase in the ratio with number of wheel passes.

A comparison of the sliding contact ratio between different wheel pressures has been studied, as shown in Figure 7.18. In the top three layers, on the whole, a large ratio corresponds with high wheel pressure for a given wheel pass number. Nevertheless, the difference is not significant in the fourth layer, indicating that high wheel pressure has

a weak effect on the contact slippage in this layer. On the other hand, the initial gravity stress may have an effect on the contact slide. Two kinds of gravity accelerations are considered, which are 0.1 and 9.81m/s^2. The preparation of the sample in the low self-weight stress field is described in Subsection 5.3.4. The applied wheel pressure is 2.0kPa. As shown in Figure 7.19, a large ratio of the sliding contacts is associated with low self-weight stress in the top four layers. This is probably due to the small contact normal forces induced by the low gravity stress. The tangential contact force corresponding with the contact slippage is reduced accordingly.

Compaction of the pavement is considered likely to affect the contact slippage. A dense sample has therefore been added to the study. The initial void ratios for the loose and dense samples are 0.26 and 0.23. The wheel pressure is 2.0kPa. The effect of the sample compaction on the contact slippage is demonstrated in Figure 7.20. Compared to the dense sample, a large permanent pavement deformation is produced in the loose sample, which may play an important role in the contact slippage. Consequently, a large ratio of the sliding contacts is generally observed for the loose sample. Moreover, the particle friction coefficient is a direct factor affecting contact sliding. Friction coefficients of 0.5 and 0.9 have been added to study the contact slippage. In the top two layers, the ratio of the sliding contacts is quite large for the low friction coefficient (i.e. 0.5) at wheel pass 100 (see Figure 7.21). After that, the ratio reduces to values similar to those for the high friction coefficients. This indicates that, when the friction coefficient is reduced from 0.9 to 0.5, contact sliding is affected at wheel pass 100, but is merely confined to the top two layers. Generally speaking, there is no specific pattern to summarise the effect of the friction coefficient on the contact slippage. During wheel loading, the fluctuation of the ratio is severe for a friction coefficient of 0.5 in the top layer.

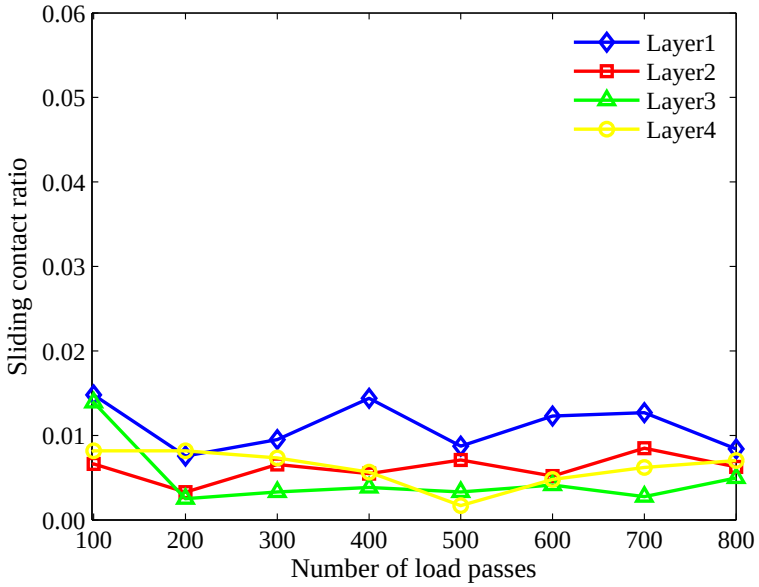

(a) 2.0kPa

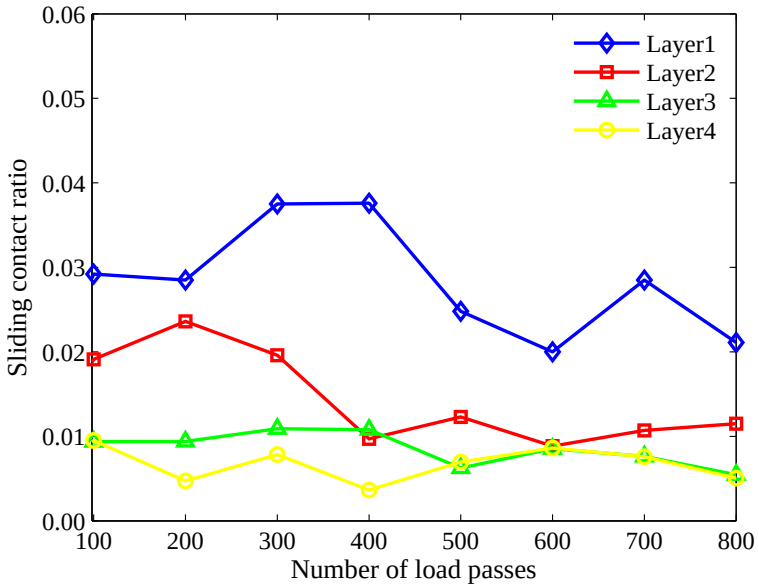

(b) 7.0kPa

Figure 7.17: Effect of pavement layer on the sliding contact ratio for the unbonded pavement

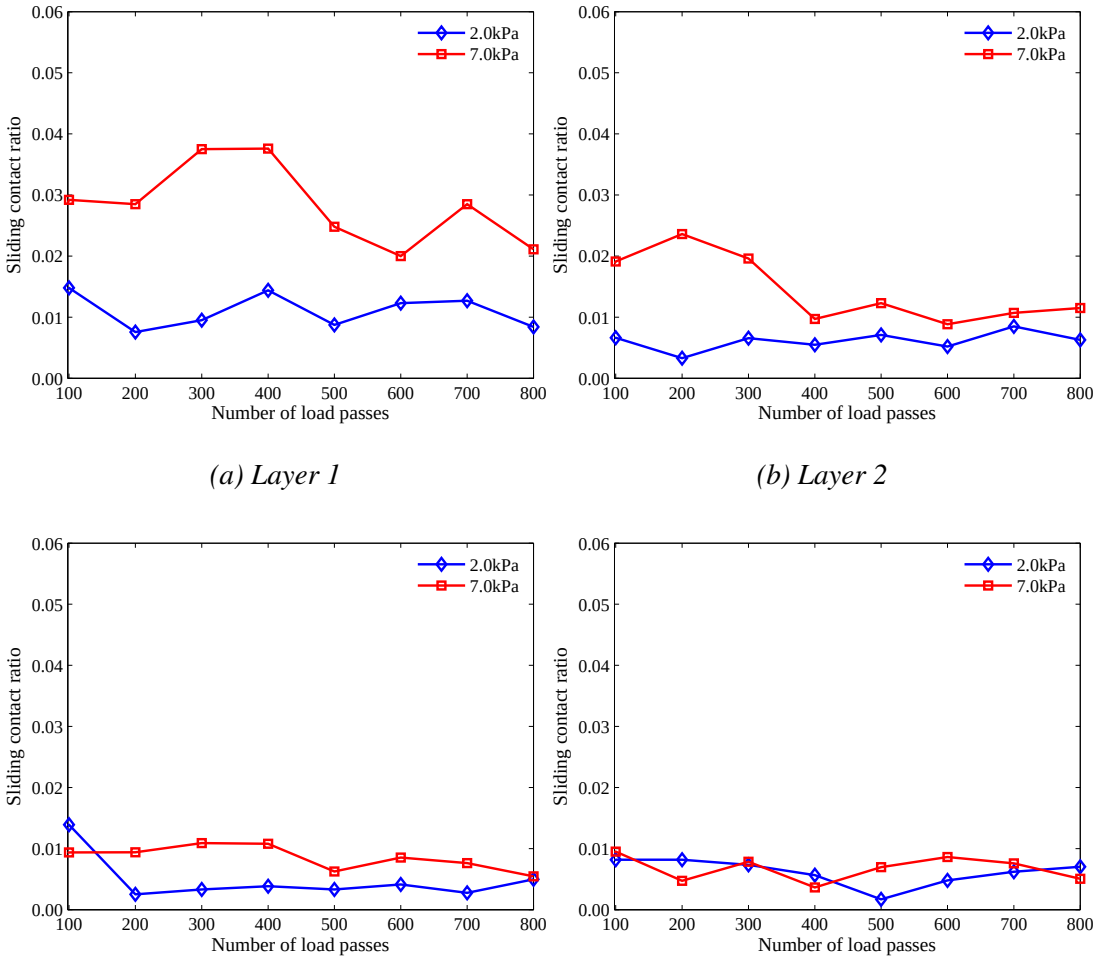

(a) Layer 1 *(b) Layer 2*

(c) Layer 3 *(d) Layer 4*

Figure 7.18: Effect of wheel pressure on the sliding contact ratio for the unbonded pavement

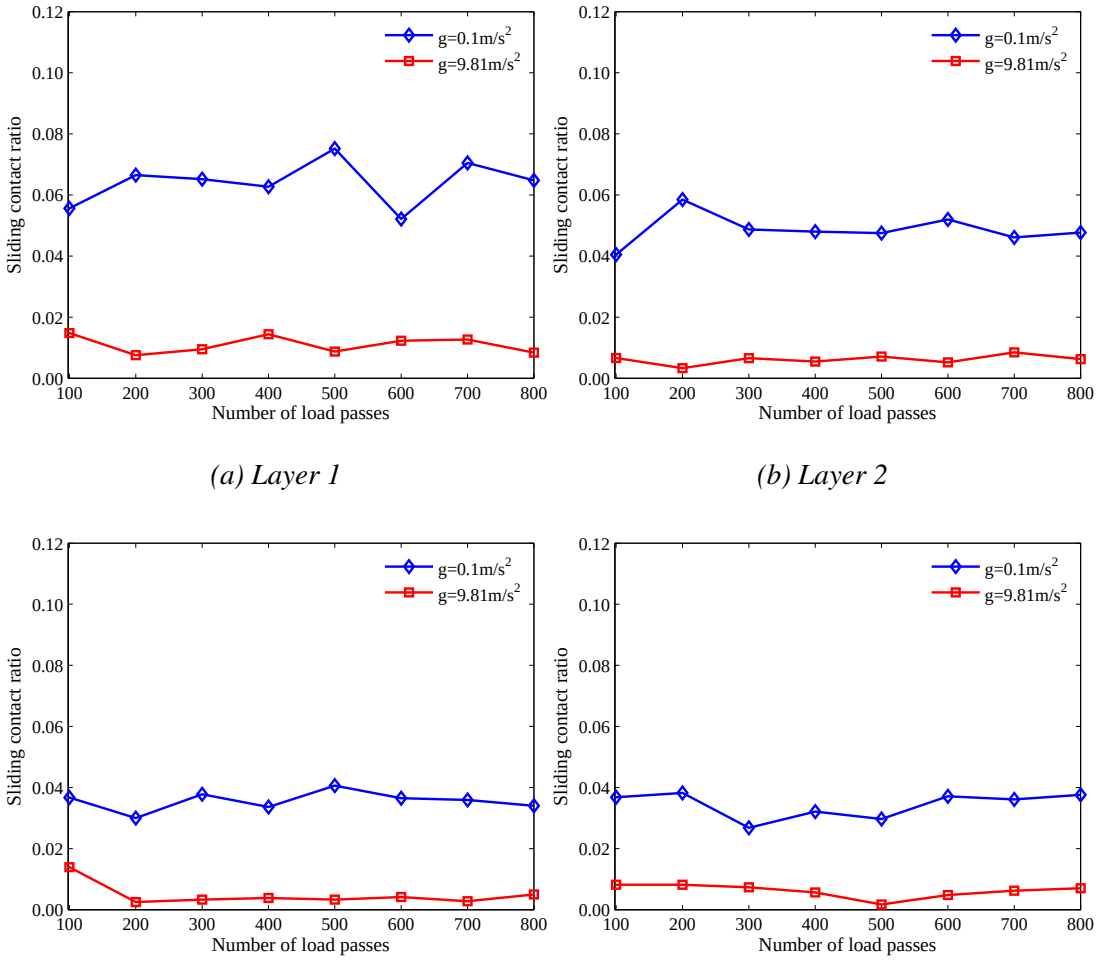

(a) Layer 1

(b) Layer 2

(c) Layer 3

(d) Layer 4

Figure 7.19: Effect of self-weight stress field on the sliding contact ratio for the unbonded pavement

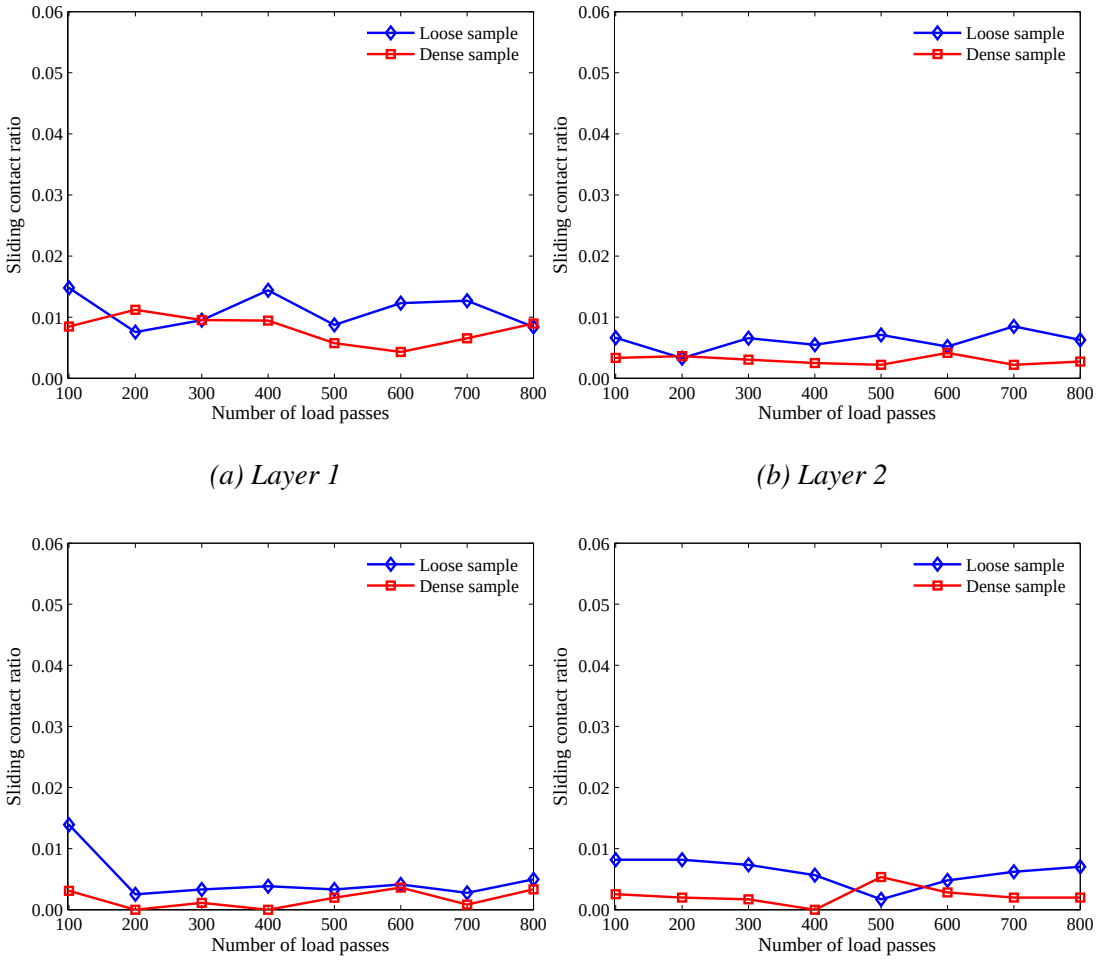

(a) Layer 1 *(b) Layer 2*

(c) Layer 3 *(d) Layer 4*

Figure 7.20: Effect of initial void ratio on the sliding contact ratio for the unbonded pavement

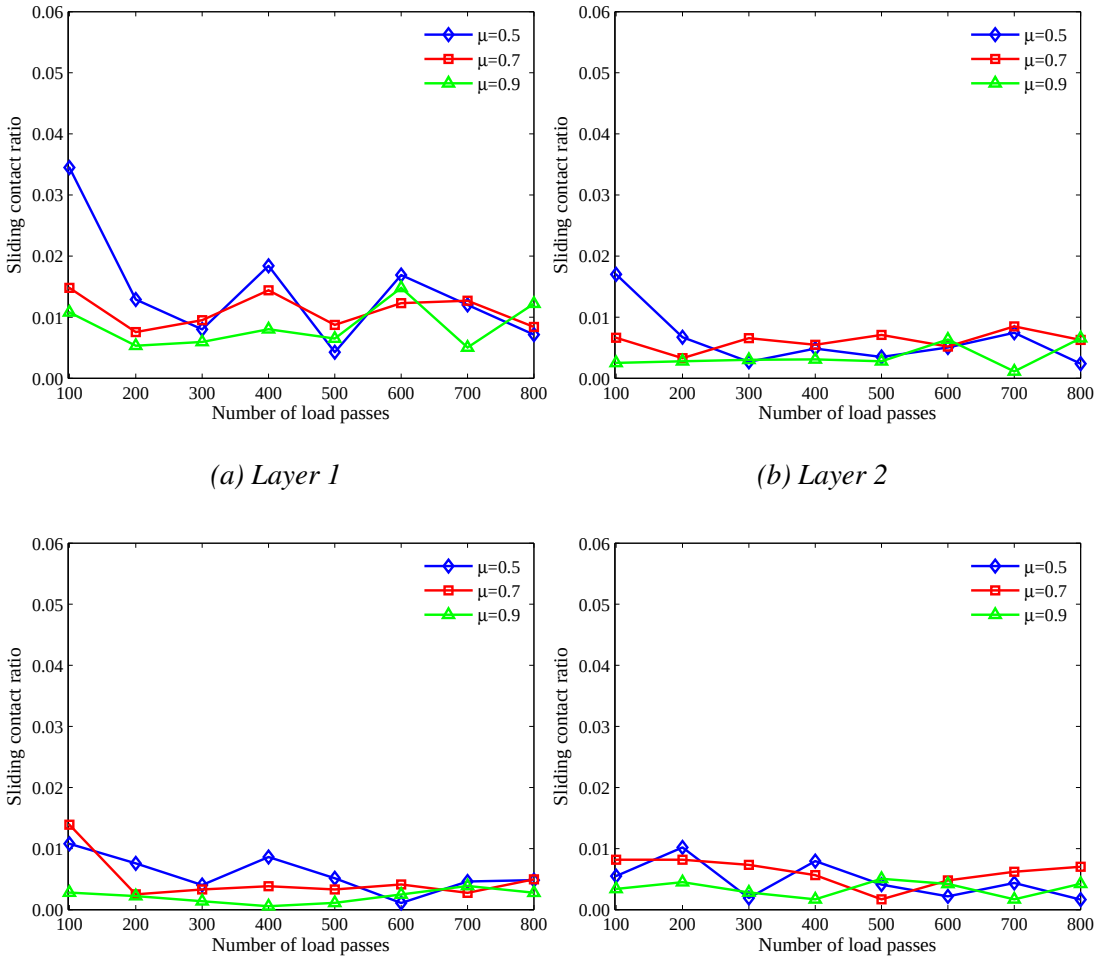

(a) Layer 1

(b) Layer 2

(c) Layer 3

(d) Layer 4

Figure 7.21: Effect of particle friction coefficient on the sliding contact ratio for the unbonded pavement

7.2.5 Pavement particle displacement

The displacement vectors of the pavement particles can be obtained in PFC^{2D} after the wheel load is removed. In Figure 7.22, the gravity acceleration of the pavement particles is 9.81m/s^2. The wheel pressure is 2.0kPa and the number of wheel passes is 100. The motion mode of the wheel particle is translation with a velocity of 0.5m/s. Relatively large particle displacements are generally observed near the pavement surface. Nevertheless, their directions are diverse. The maximum displacement is 1.43×10^{-2}m. It is worth mentioning that all the displacement vectors deep in the pavement are in nearly the same direction. These vector directions are approximately in line with the translational direction of the external wheel load. As the permanent pavement deformation further accumulates at wheel pass 500, there is a general increase in the displacement vectors even deep in the pavement, as shown in Figure 7.23. However, the maximum displacement slightly decreases to 1.39×10^{-2}m.

Large permanent deformation in the pavement is induced by high wheel pressure. Therefore, the wheel pressure may logically have an effect on particle displacement. A high wheel pressure of 7.0kPa has been evaluated after 100 wheel passes. Compared to the low wheel pressure (see Figure 7.22), the relatively large displacements for the high wheel pressure are widely distributed, rather than merely located near the pavement surface (see Figure 7.24). The maximum displacement increases to 2.41×10^{-2}m. The vector directions deep in the pavement are still almost coincident with the motion direction of the wheel particle.

On the other hand, permanent deformation is significantly affected by the initial gravity stress. Consequently, gravity acceleration is probably another factor affecting particle displacement. A low gravity acceleration of 0.1m/s^2 has been added to the previous study. The wheel pressure is 2.0kPa and the wheel pass number is 100. Compared to the particle displacements shown in Figure 7.22, there is a wide distribution for the relatively large particle displacements in the low self-weight stress field (see Figure 7.25). The directions of the displacement vectors near the pavement surface are almost downward, unlike those in the high gravity stress field. Also, the directions of

the vectors deep in the pavement are diverse rather than in accordance with the translational direction of the wheel. The maximum particle displacement is 2.44×10^{-2}m.

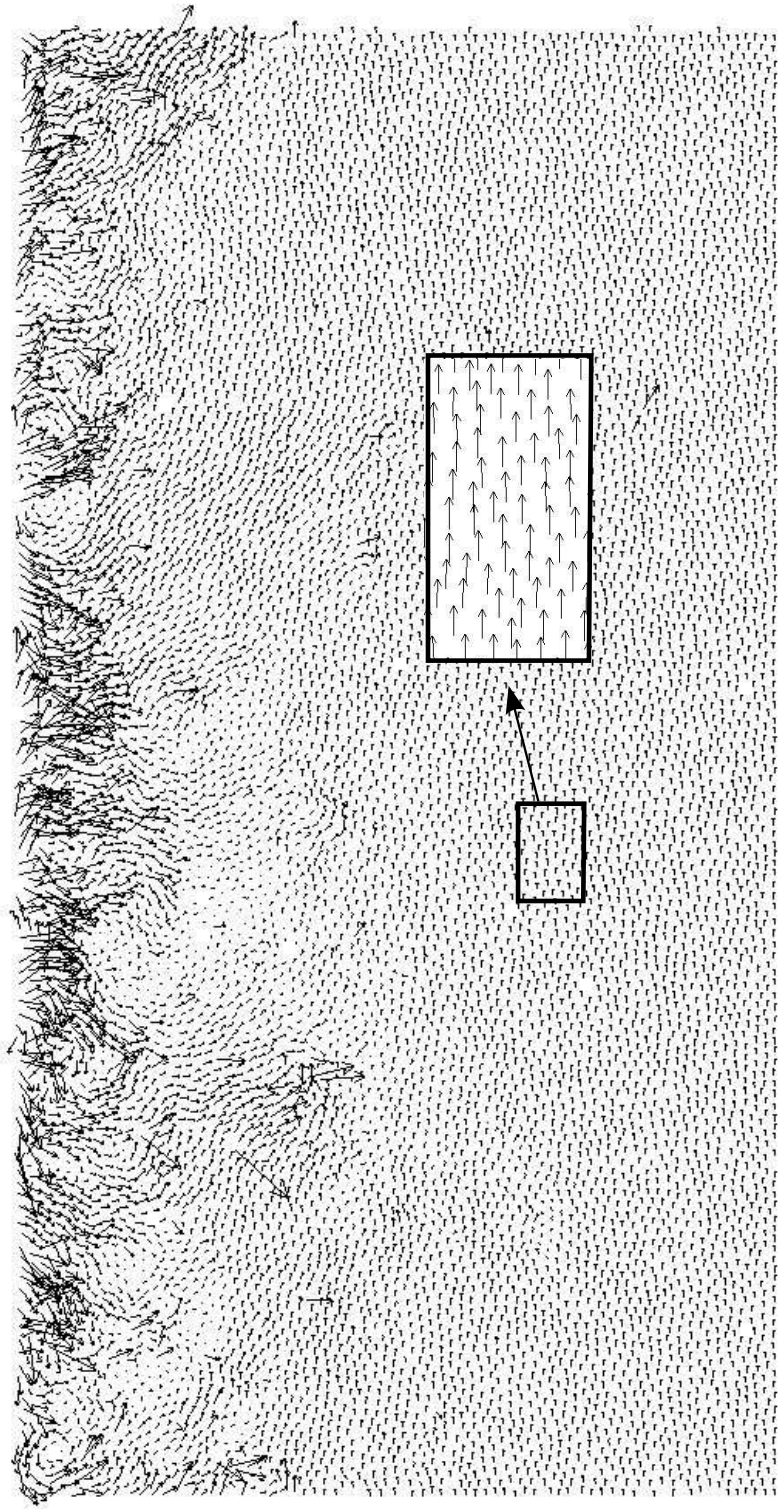

Figure 7.22: Total particle displacement after wheel pass 100 for gravity acceleration of 9.81m/s^2 and wheel pressure of 2.0kPa (maximum displacement $= 1.43\times10^{-2}m$)

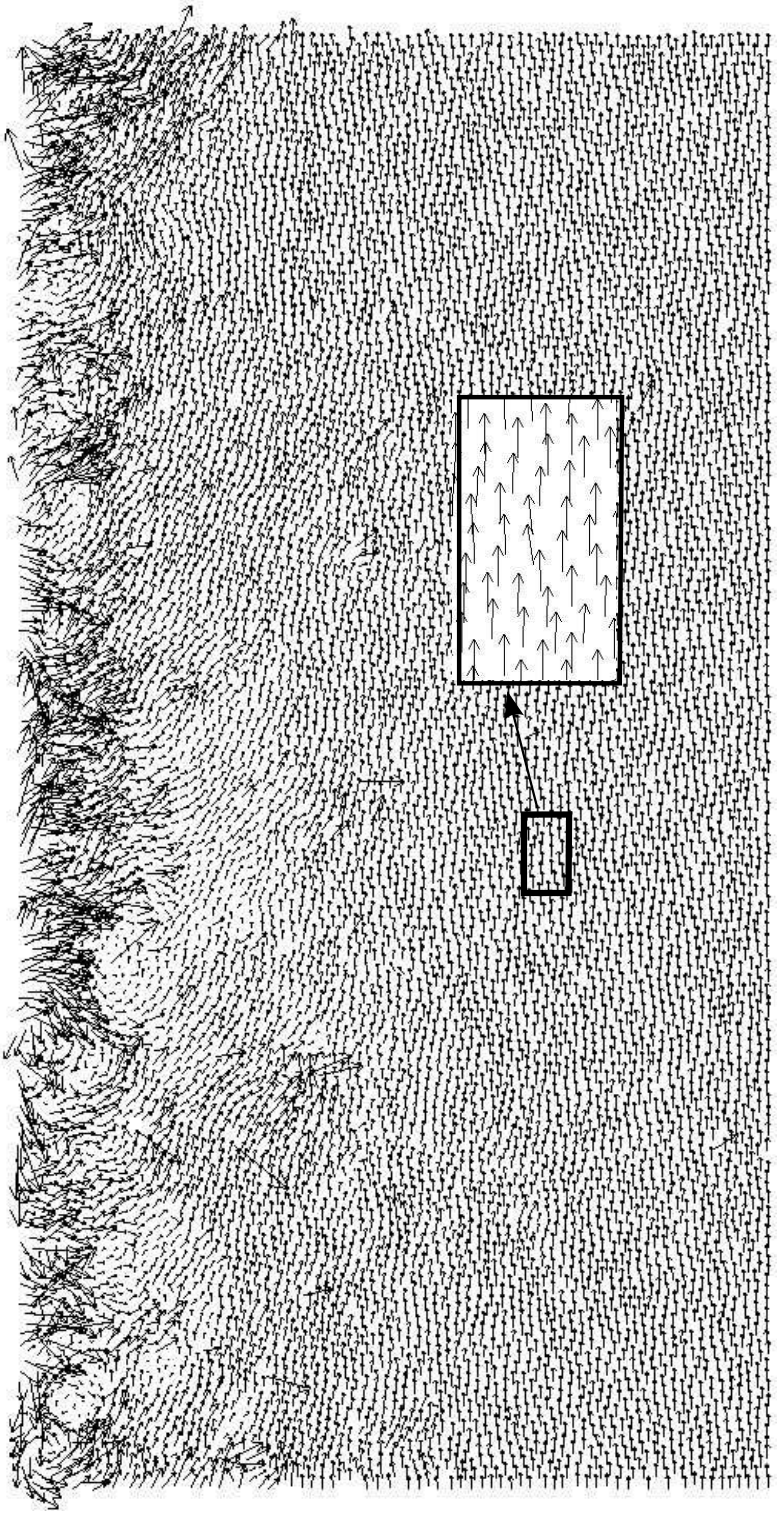

Figure 7.23: Total particle displacement after wheel pass 500 for gravity acceleration of $9.81 m/s^2$ and wheel pressure of 2.0kPa (maximum displacement $= 1.39 \times 10^{-2} m$)

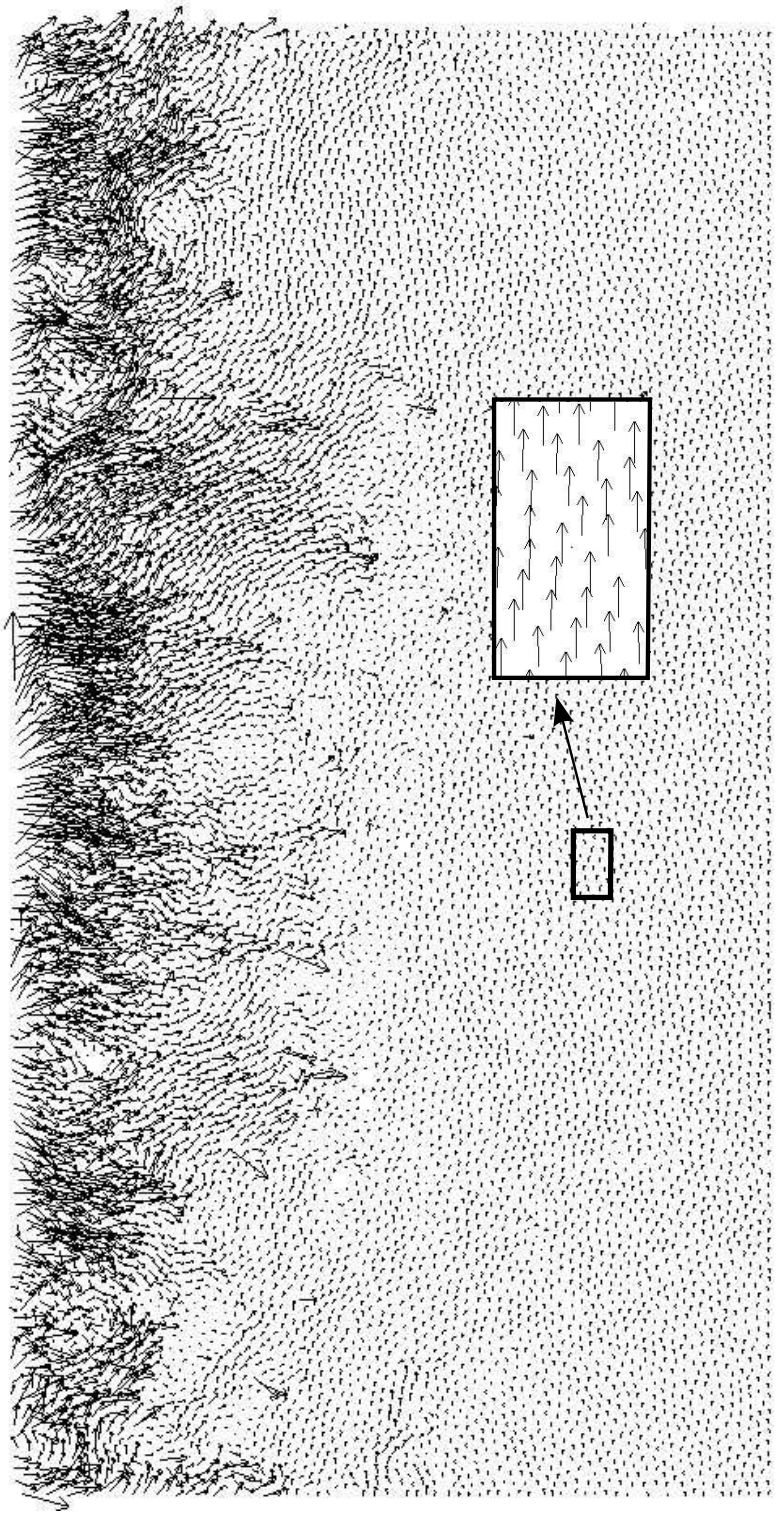

Figure 7.24: Total particle displacement after wheel pass 100 for gravity acceleration of 9.81m/s^2 and wheel pressure of 7.0kPa (maximum displacement $= 2.41\times10^{-2}m$)

Figure 7.25: Total particle displacement after wheel pass 100 for gravity acceleration of 0.1m/s^2 and wheel pressure of 2.0kPa (maximum displacement = 2.44×10^{-2}m)

7.3 Bonded pavement structure

The periodic lateral boundary is not suitable to model the bonded pavement structure, because severe force concentrations can arise at the lateral boundary, which have a negative effect on the stress distribution in the pavement. Consequently, the rigid lateral boundary is introduced in the bonded pavement simulation. As discussed in Subsection 5.2.5, the size of the bonded pavement is 2.4m long $\times$ 0.95m high. The middle pavement section with a length of 0.6m is able to go through the complete stress path induced by the external wheel load. Therefore, micro-analysis is performed on this section. The thickness of the layer for analysis is 0.15m, which is identical to that of the simulated asphalt layer in the double-layered pavement. The gravity acceleration is 0.1m/s^2 and the initial void ratio of the pavement sample is 0.26. The interparticle friction coefficient is 0.7. Details of the single- and double-layered pavements have been presented in Subsection 6.2.1.

7.3.1 Single-layered pavement

For the single-layered pavement, the microscopic properties for the individual layers are studied, which are the normal contact force, tangential contact force, normal bond force and tangential bond force respectively. The probability density distribution is employed to carry out the micro-analysis. The interval of the force has to be determined first. The wheel pressure is 169kPa and the number of wheel passes is 100. Three intervals, i.e. 0.1, 0.2 and 0.3N are considered. The change regulation of the distribution for all the microscopic properties discussed above is not altered when these three intervals are employed. Thus, the interval of 0.2N is applied in the following studies. The factors affecting the probability distribution taken into account, are pavement layer, wheel pass number and wheel pressure. These distributions are all related to the condition after the wheel load has been removed.

7.3.1.1 Normal contact force

The gravity stress increases with pavement depth. Therefore, the probability distributions of the normal contact forces probably differ for the various pavement layers. The wheel pressure is 169kPa and different wheel pass numbers are considered, namely 100, 200 and 300. For the initial pavement sample, the contact proportion with small forces in the top layer is significantly larger than those in the other three layers, as shown in Figure 7.26a. With the pavement depth, there is a decrease in the contact proportion with small forces. The extremum of the normal contact force increases with pavement depth. These values from the top to the fourth layers are 1.7, 3.7, 5.3 and 6.9N respectively (see Table 7.1). After the pavement is subjected to wheel pressure, the difference between the distributions for the different layers is significantly altered, as shown in Figure 7.26b, 7.26c and 7.26d. Compared to the other three layers, the proportion of small contact forces for the top layer is obviously small. The extrema for the normal contact forces are shown in Table 7.1. Contrary to the initial pavement sample, the largest extremum corresponds to the top layer when the wheel pressure is applied to the pavement.

As discussed above, the probability distribution is severely affected by the wheel pressure, for the top layer in particular. According to the studies on the residual stress (see Subsection 6.3.2), the variation in the stress is almost confined to a pavement depth of 0.3m. Consequently, the top two layers are studied by micro-analysis. As shown in Figure 7.27, a decrease in the contact proportion with small forces is observed with wheel pass number, especially from the initial stage to pass 100. As in the previous study, the permanent vertical deformation is limited. The variation in the distribution is probably due to the accumulation of the plastic shear strain. During repeated wheel loading, the distribution of the normal contact force in the top layer tends to be uniform. For the top two layers, the extrema for the normal contact forces generally increase with number of wheel passes, as shown in Table 7.1. For example, in the top layer, they are 1.7, 11.3, 23.3 and 35.5N respectively.

The wheel pressure is an important factor affecting the distribution of the normal con-

tact force. Four different wheel pressures are selected, namely 42, 85, 169 and 254kPa. The wheel pass numbers are 100 and 300. The top two layers are studied. The probability distribution is demonstrated in Figure 7.28. With the increase in the wheel pressure, the contact proportion with small contact forces decreases, particularly for the top layer. Therefore, the wheel pressure has a significant effect on the probability distribution. That may be because of the large plastic shear strain induced by the high wheel pressure. The extrema are given in relation to the wheel pressure and the pavement layer, as shown in Table 7.2. In the top layer, the extrema evidently increase with the increase of the wheel pressure. Nevertheless, the variation in the extremum for the second layer is not so obvious.

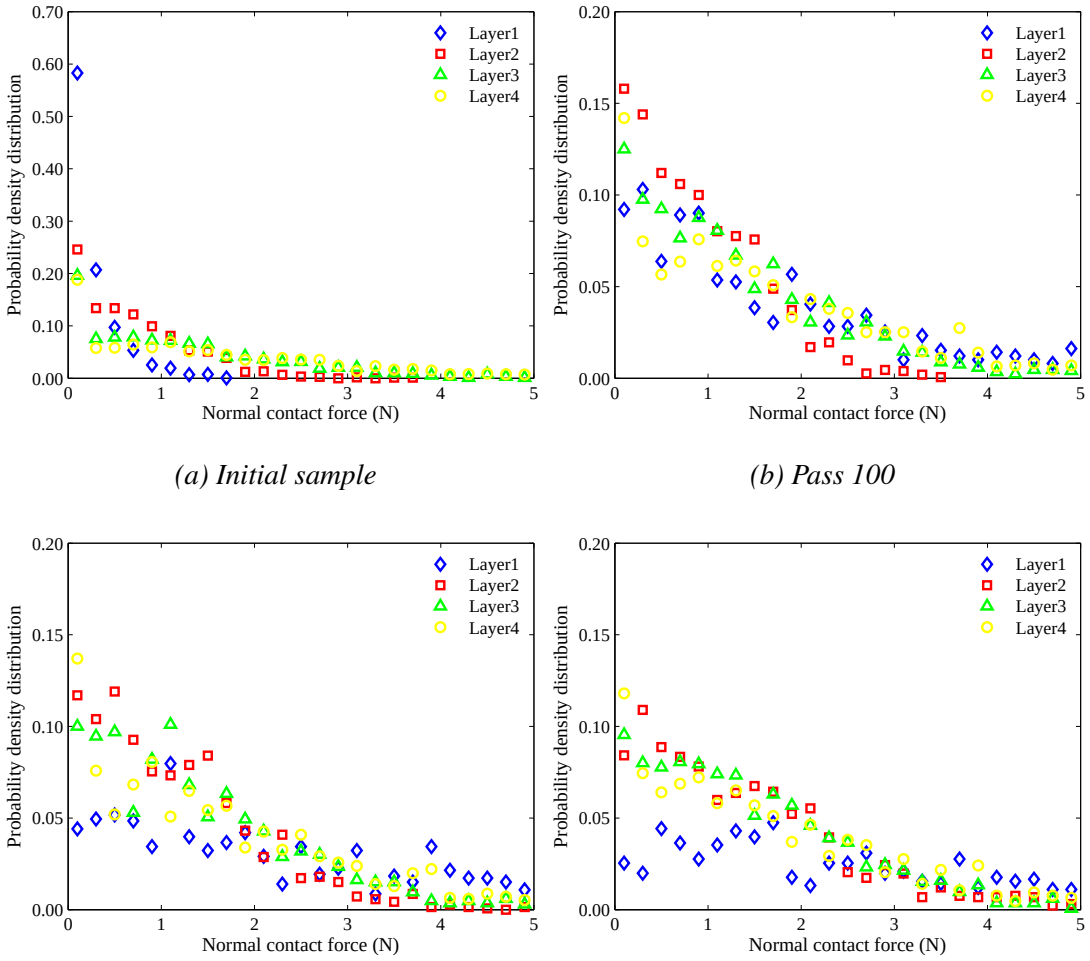

(a) Initial sample *(b) Pass 100*

(c) Pass 200 *(d) Pass 300*

Figure 7.26: Effect of pavement layer on the probability density distribution of the normal contact force for the single-layered pavement

Extremum	Pavement layer	Initial	Pass 100	Pass 200	Pass 300
Positive	1	1.7	11.3	23.3	35.5
	2	3.7	3.5	5.3	7.1
	3	5.3	4.9	5.1	5.3
	4	6.9	6.7	6.9	6.9

Table 7.1: Variation in the extremum of the normal contact force with the pavement layer and wheel pass number for the single-layered pavement (the unit of the contact force: N)

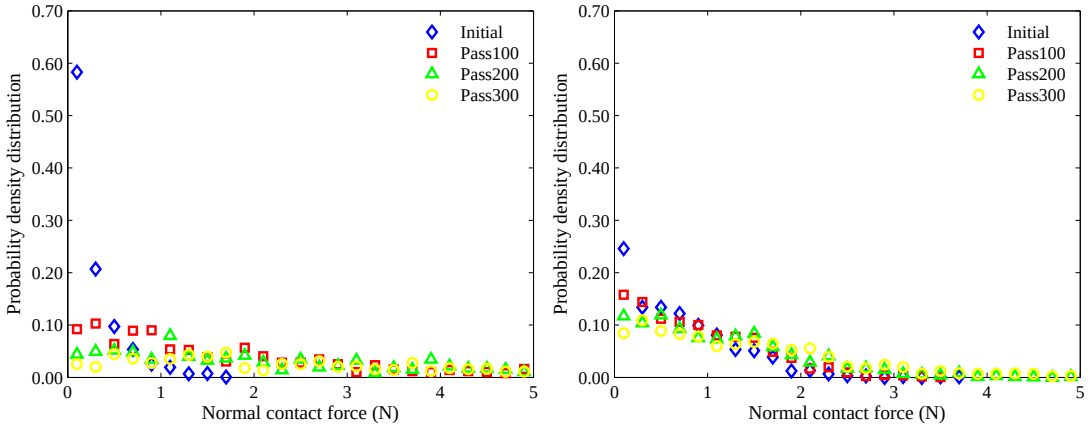

(a) Layer 1 *(b) Layer 2*

Figure 7.27: Effect of wheel pass number on the probability density distribution of the normal contact force for the single-layered pavement

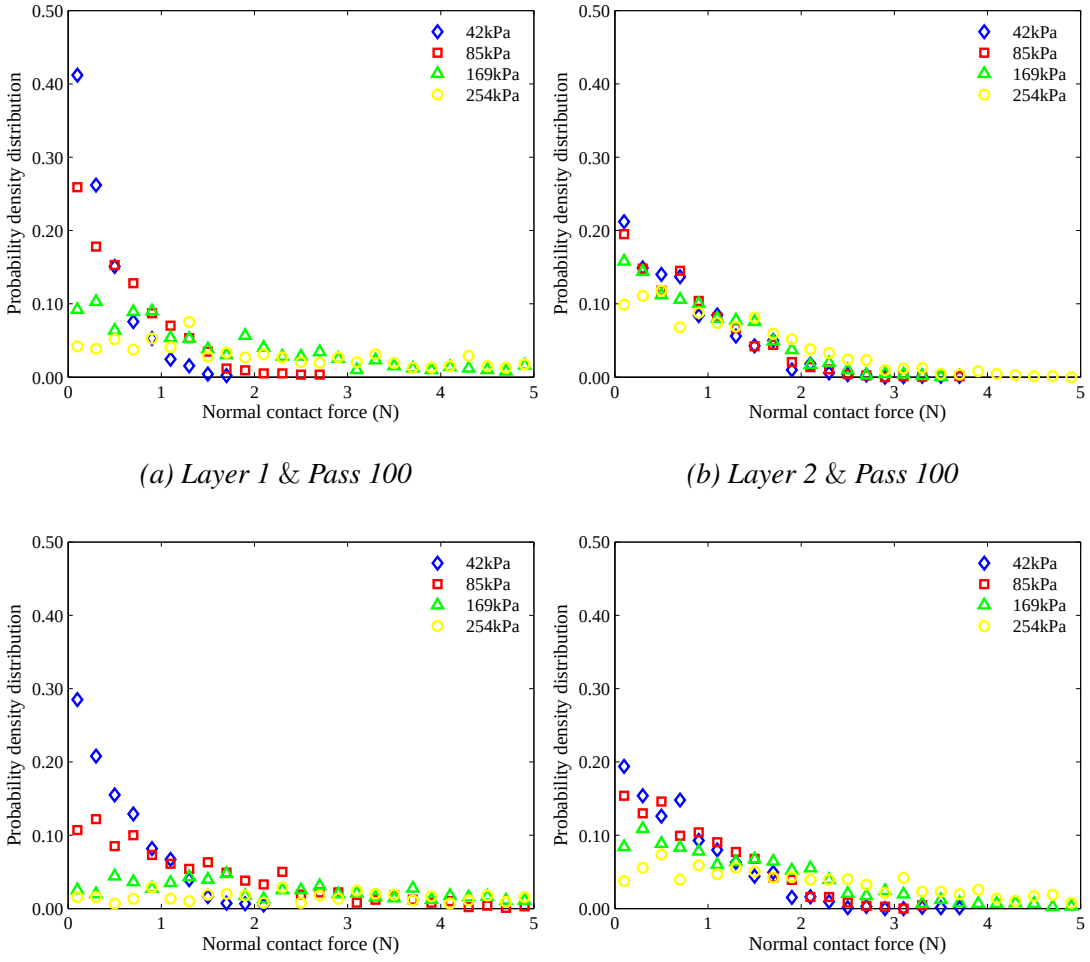

(a) Layer 1 & Pass 100

(b) Layer 2 & Pass 100

(c) Layer 1 & Pass 300

(d) Layer 2 & Pass 300

Figure 7.28: Effect of wheel pressure on the probability density distribution of the normal contact force for the single-layered pavement

Extremum	pavement layer	Wheel pressure (kPa)	Pass 100	Pass 300
Positive	1	42	1.7	2.1
		85	2.7	8.3
		169	11.3	35.5
		254	26.3	81.3
	2	42	3.7	3.7
		85	3.7	3.3
		169	3.5	7.1
		254	5.9	14.3

Table 7.2: Variation in the extremum of the normal contact force with the wheel pressure for the single-layered pavement (the unit of the contact force: N)

7.3.1.2 Tangential contact force

The distribution of the tangential contact force has been investigated in terms of the pavement layer and wheel pass number, as shown in Figure 7.29. The wheel pressure is 169kPa. As discussed in Subsection 7.2.3, the positive or negative sign does not denote the magnitude of the tangential force, which is determined by the absolute value of the force. Generally speaking, there exists a peak at small tangential forces. With the increase in the force, the probability density gradually decreases. For the initial pavement sample, the contact proportion with small forces decreases with pavement depth (see Figure 7.29a). Furthermore, the extremum in absolute terms increases from the top to the fourth layer, as illustrated in Table 7.3. For example, the negative extrema are -0.6, -0.8, -1.4 and -2.2N for the different layers. This is probably because of the progressive increase in gravity stress with pavement depth. After the pavement is subjected to a number of repeated wheel loads (i.e. pass 200 and 300), the peak of the distribution in the top layer is lower than those in the other three layers. There is hardly any difference between the contact proportions with small forces in the layers from the second to the fourth. Generally speaking, after wheel passes 100, 200 and

300, the absolute extremum in the top layer is larger than those in the other three layers (see Table 7.3).

The number of wheel passes has a significant effect on the probability distribution of the tangential force, as shown in Figure 7.30 where the top two layers are considered. With the increase in the number of wheel passes, the peak of the distribution decreases, especially at the initial stage of the repeated loading. This indicates that the wheel pressure reduces the proportion of small-force contacts. For the top two layers, there is a general increase in the absolute extremum with repeated loading (see Table 7.3). That is probably due to the accumulation of plastic shear strain.

On the other hand, the probability distribution of the tangential force is obviously affected by the wheel pressure, as demonstrated in Figure 7.31. The wheel pressures are 42, 85, 169 and 254kPa respectively. For the top layer, after wheel pass 100 or 300, the large wheel pressure significantly reduces the proportion of the contacts with small forces. A mild decrease in the peak of the distribution is observed for the second layer when the wheel pressure is increased from 42 to 85kPa. If the wheel pressure is further increased, an evident decrease in the peak will take place. As displayed in Table 7.4, in the top layer, there is an increase in the absolute extremum with increase of wheel pressure. The effect of the wheel pressure on the absolute extremum in the second layer is less apparent.

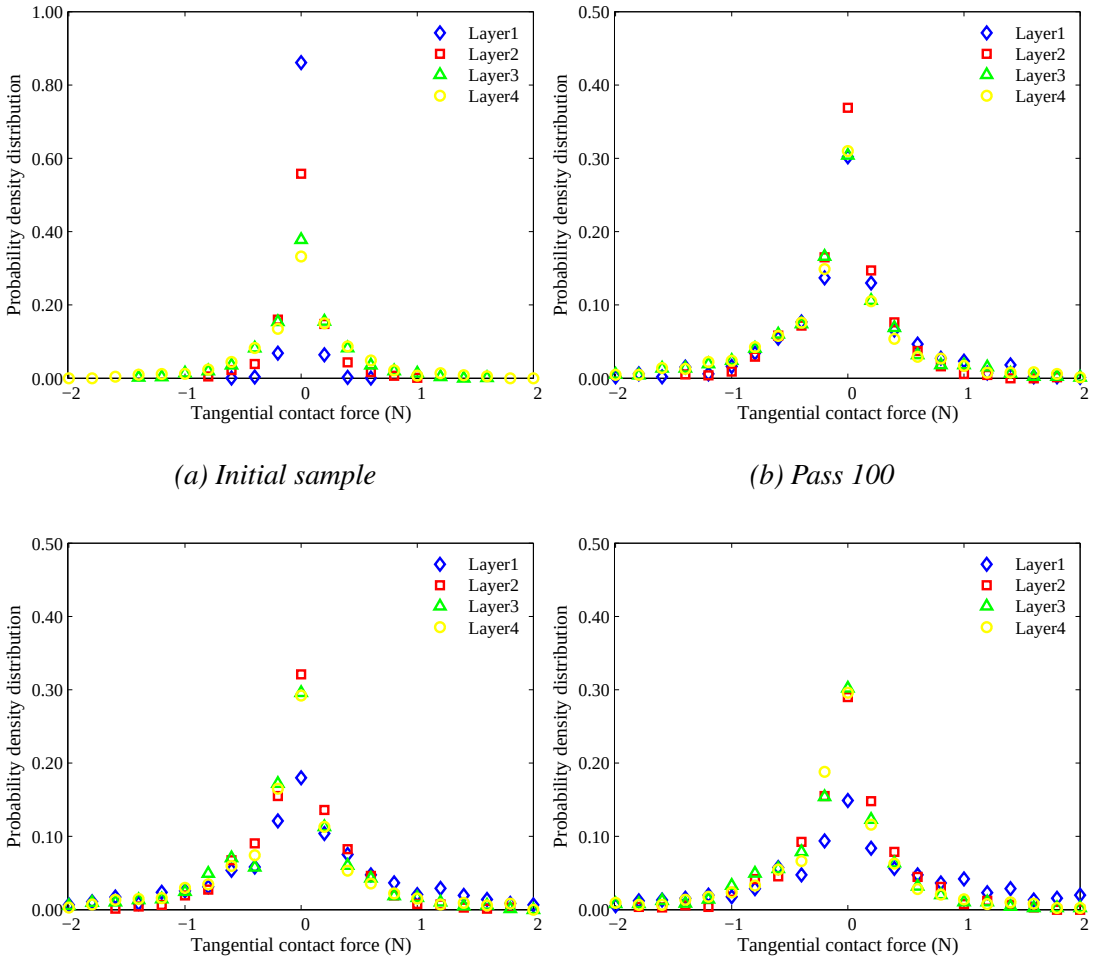

(a) Initial sample *(b) Pass 100*

(c) Pass 200 *(d) Pass 300*

Figure 7.29: Effect of pavement layer on the probability density distribution of the tangential contact force for the single-layered pavement

Extremum	Pavement layer	Initial	Pass 100	Pass 200	Pass 300
Negative	1	-0.6	-4.0	-9.8	-16.2
	2	-0.8	-1.4	-1.6	-1.8
	3	-1.4	-2.6	-2.6	-2.6
	4	-2.2	-4.4	-4.6	-4.0
Positive	1	0.6	3.2	7.8	13.0
	2	1.0	1.8	1.8	2.8
	3	1.6	2.2	2.4	2.0
	4	2.2	2.6	2.4	2.6

Table 7.3: Variation in the extremum of the tangential contact force with the pavement layer and wheel pass number for the single-layered pavement (the unit of the contact force: N)

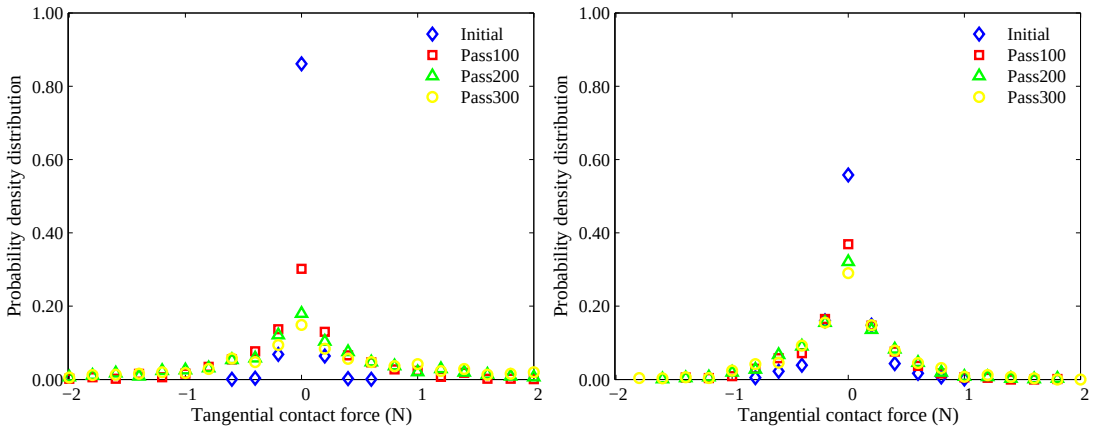

(a) Layer 1 *(b) Layer 2*

Figure 7.30: Effect of wheel pass number on the probability density distribution of the tangential contact force for the single-layered pavement

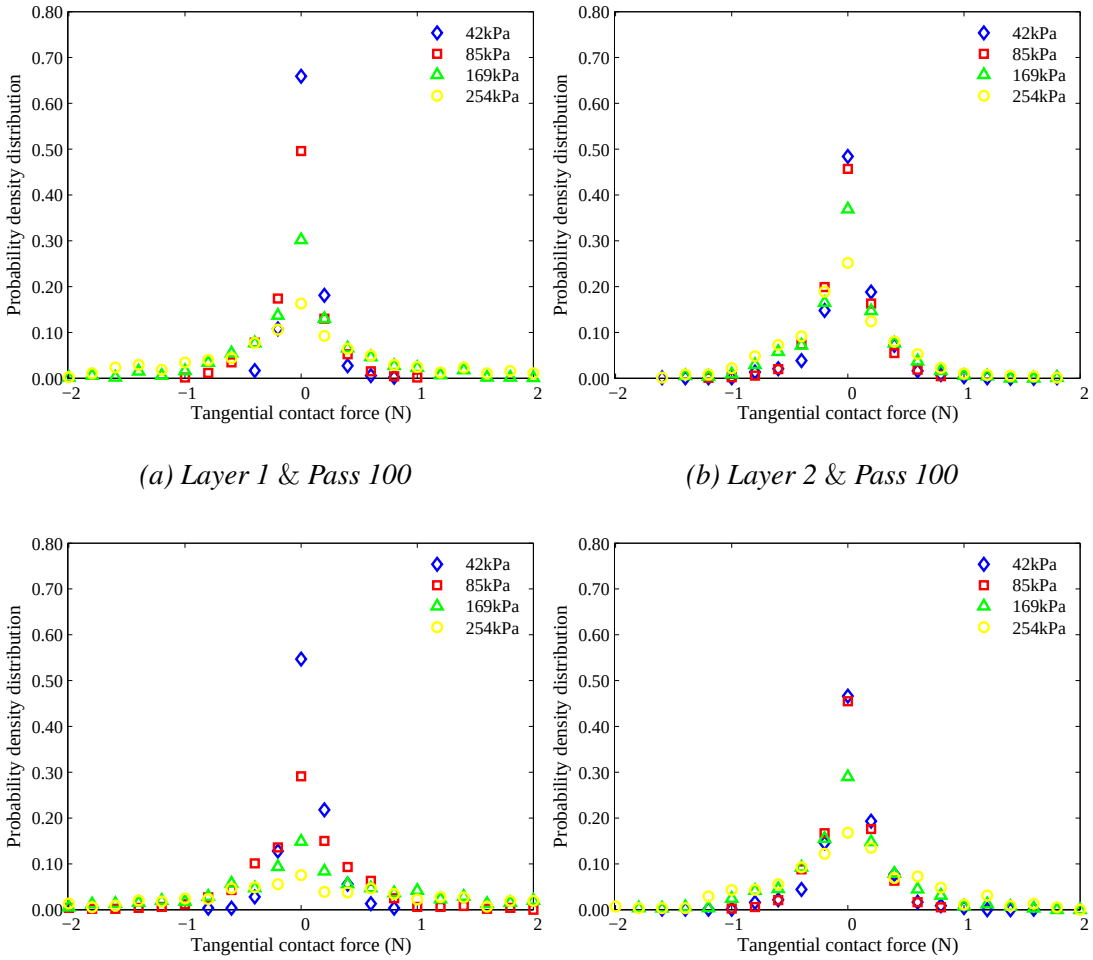

(a) Layer 1 & Pass 100

(b) Layer 2 & Pass 100

(c) Layer 1 & Pass 300

(d) Layer 2 & Pass 300

Figure 7.31: Effect of wheel pressure on the probability density distribution of the normal contact force for the single-layered pavement

Extremum	pavement layer	Wheel pressure (kPa)	Pass 100	Pass 300
Negative	1	42	-0.4	-0.8
		85	-1.0	-3.4
		169	-4.0	-16.2
		254	-10.8	-39.8
	2	42	-1.6	-1.6
		85	-1.2	-1.0
		169	-1.4	-1.8
		254	-1.6	-4.4
Positive	1	42	0.8	0.8
		85	1.0	3.2
		169	3.2	13.0
		254	7.6	31.4
	2	42	1.8	1.6
		85	0.8	0.8
		169	1.8	2.8
		254	1.8	4.2

Table 7.4: Variation in the extremum of the tangential contact force with the wheel pressure for the single-layered pavement (the unit of the contact force: N)

7.3.1.3 Normal bond force

In a parallel bond, a tangential force and a compressive or tensile normal force can be generated. For the normal contact force, the positive sign denotes a compressive normal force in the bond. Therefore, a tensile normal force is described by the minus sign. For the initial pavement sample, there is no force in the parallel bonds because the bonds are added to the interparticle contacts after the gravity acceleration is applied to the pavement particles. The effect of the pavement layer on the probability distribution of the normal bond force has been studied for wheel passes 100, 200 and 300 (see

Figure 7.32). The wheel pressure is 169kPa. The proportion of the contacts with small forces increases with the pavement depth, irrespective of the number of wheel passes. The probability distribution tends to be uniform near the pavement surface. Compared to the other three layers, the absolute extremum is quite large for the top layer, as shown in Table 7.5. This indicates that the effect of the wheel pressure on the normal bond force is mainly restricted to shallow depth in the pavement.

The distribution of the normal bond force is also affected by the number of wheel passes. Wheel passes 100, 200 and 300 have been studied for the top two layers. When the normal bond force ranges from -2 to 2N, in the top layer, there is a decrease in the probability density with an increase in the number of repeated loadings (see Figure 7.33a). With regard to the second layer, the proportion of the contacts with small forces reduces as the pavement experiences the wheel loading from pass 100 to 300 (see Figure 7.33b). For the normal bond forces, the development of the extrema with wheel passes is demonstrated in Table 7.5. In the top two layers, a gradual increase in the absolute extremum is observed as the pass number increases.

Wheel pressure is an important factor affecting the probability distribution. Wheel passes 100 and 300 are selected. Large wheel pressure tends to produce a low proportion of contacts with small forces, irrespective of the pass number or the pavement depth (see Figure 7.34). Large normal bond forces are easily generated by high wheel pressure. The extremum in absolute terms increases with the wheel pressure, for the top layer in particular, as shown in Table 7.6. For example, when the wheel pressure is low, namely 42kPa, after wheel pass 100, the negative extremum is -1.4N. When the pressure is 254kPa, the corresponding negative extremum is changed to -48.6N.

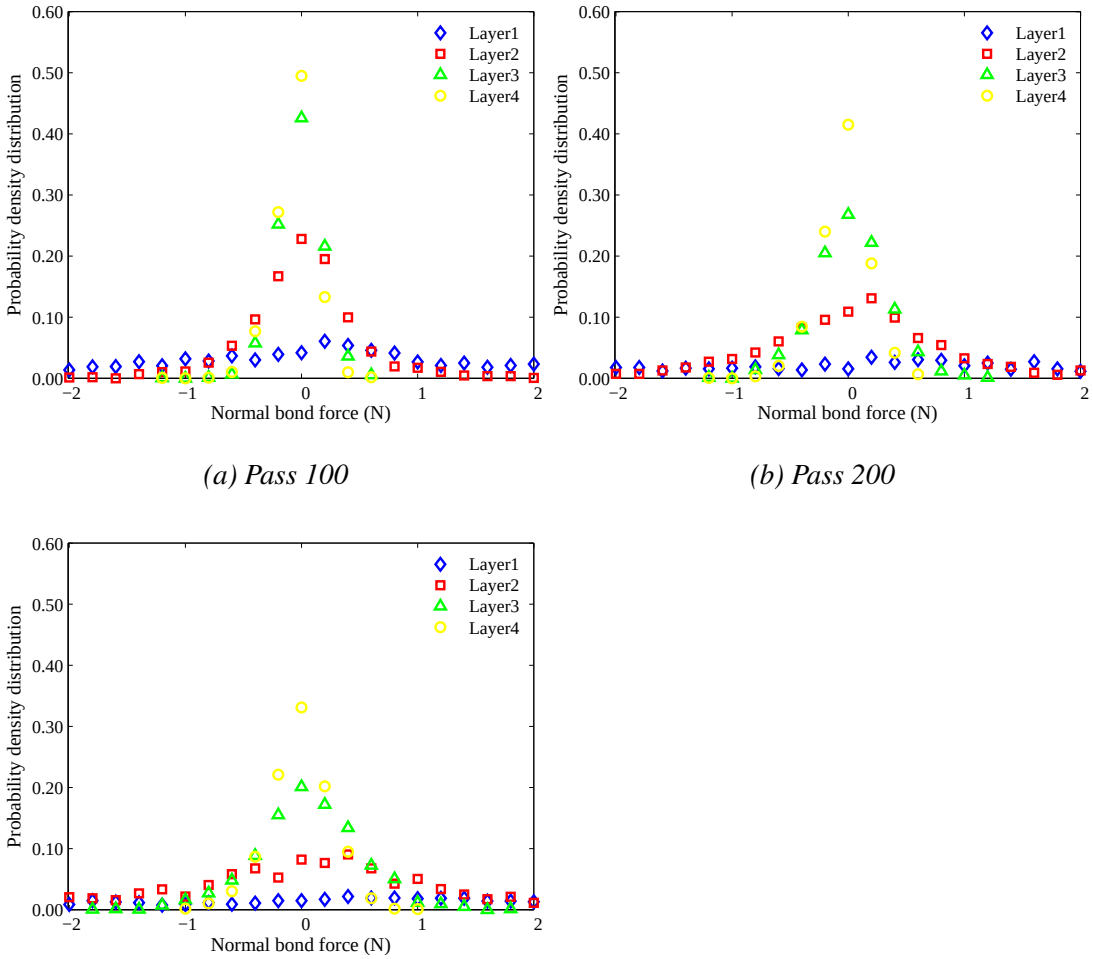

(a) Pass 100

(b) Pass 200

(c) Pass 300

Figure 7.32: Effect of pavement layer on the probability density distribution of the normal bond force for the single-layered pavement

Extremum	Pavement layer	Pass 100	Pass 200	Pass 300
Negative	1	-21.6	-43.4	-65.0
	2	-3.0	-6.6	-10.2
	3	-1.2	-1.2	-1.8
	4	-1.2	-1.2	-1.0
Positive	1	10.8	21.6	32.2
	2	2.0	3.8	5.6
	3	0.6	1.2	1.8
	4	0.6	0.6	1.0

Table 7.5: Variation in the extremum of the normal bond force with the pavement layer and wheel pass number for the single-layered pavement (the unit of the bond force: N)

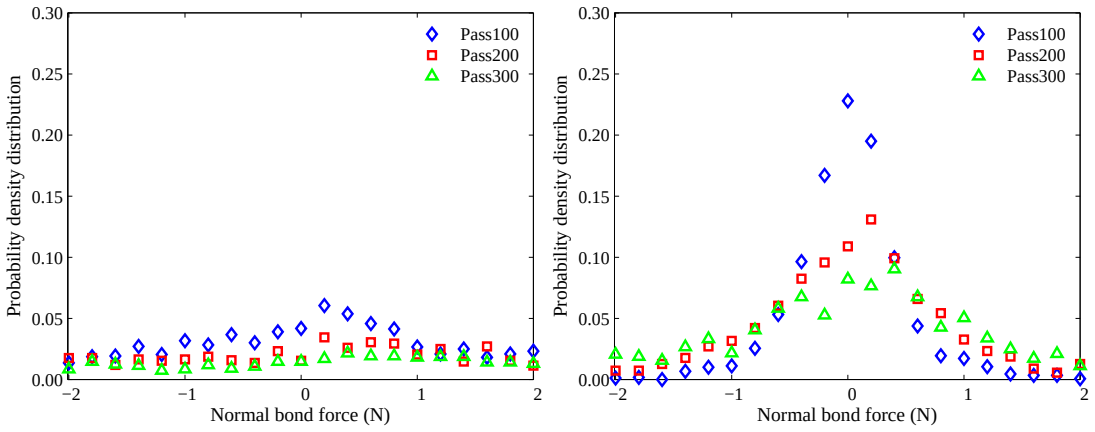

(a) Layer 1 *(b) Layer 2*

Figure 7.33: Effect of wheel pass number on the probability density distribution of the normal bond force for the single-layered pavement

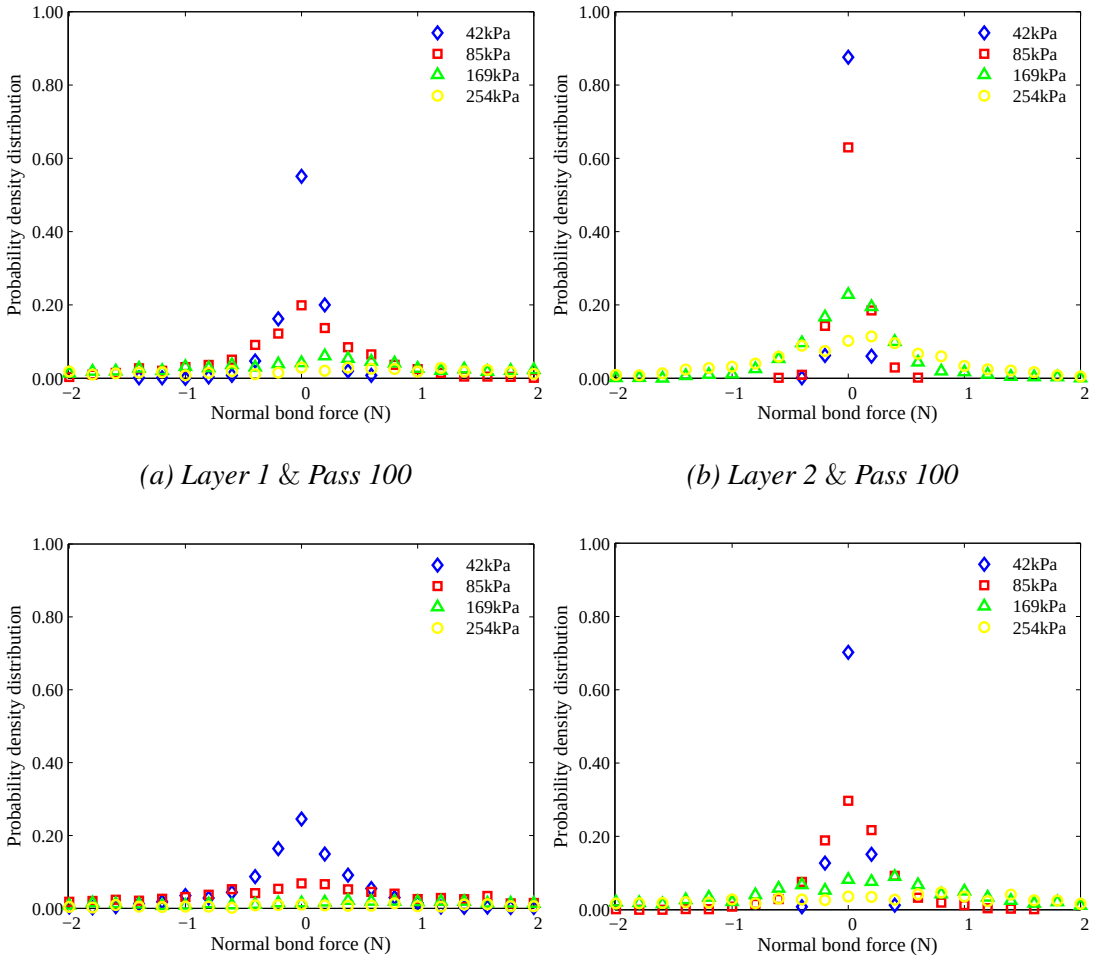

(a) Layer 1 & Pass 100

(b) Layer 2 & Pass 100

(c) Layer 1 & Pass 300

(d) Layer 2 & Pass 300

Figure 7.34: Effect of wheel pressure on the probability density distribution of the normal bond force for the single-layered pavement

Extremum	pavement layer	Wheel pressure (kPa)	Pass 100	Pass 300
Negative	1	42	-1.4	-4.0
		85	-5.4	-16.4
		169	-21.6	-65.0
		254	-48.6	-144.6
	2	42	-0.4	-0.4
		85	-0.6	-2.0
		169	-3.0	-10.2
		254	-7.4	-23.2
Positive	1	42	0.6	2.0
		85	2.8	8.2
		169	10.8	32.2
		254	23.6	70.4
	2	42	0.2	0.4
		85	0.6	1.6
		169	2.0	5.6
		254	4.4	12.8

Table 7.6: Variation in the extremum of the normal bond force with the wheel pressure for the single-layered pavement (the unit of the contact force: N)

7.3.1.4 Tangential bond force

The probability distribution of the tangential bond forces has been investigated in terms of the pavement layer, wheel pass number and wheel pressure. The effect of the pavement layer on the distribution is demonstrated in Figure 7.35. The top four layers are compared to one another for different wheel passes, i.e. 100, 200 and 300. Like the normal bond force, the most evident change in the distribution of the tangential bond force is chiefly confined to the peak area. Similarly, with the pavement depth, the proportion of the contacts with small forces gradually increases, regardless of the

wheel pass number. That is probably because the stress in the pavement induced by the external wheel pressure progressively decays with pavement depth. A larger stress in the pavement may bring about a more uniform distribution of the bond forces. The extrema of the tangential bond forces have been studied in terms of the pavement layer and wheel pass number, as shown in Table 7.7. Compared to the other three layers, the absolute extrema for the top layer are quite large. The large extrema are possibly produced by the high stress near the pavement surface.

The distribution of the tangential bond force is affected by wheel pass number as well. Within a range of tangential bond force from -2 to 2N, there is a decrease in the distribution for the top layer with repeated wheel loading, as shown in Figure 7.36a. It is similar to the variation in the distribution of the normal bond force. Nevertheless, in the second layer, the decline in the probability distribution with wheel pass number is mainly restricted to the small bond forces (see Figure 7.36b). That is possibly because of the accumulation of plastic shear strain during repeated wheel loading. The development of the extrema for the tangential bond forces is displayed in Table 7.7, where the absolute extrema increase in the top two layers, with wheel pass increasing from 100 to 300.

Another important factor affecting the distribution of the tangential bond force is the wheel pressure. There are four wheel pressures, i.e. 42, 85, 169 and 254kPa. Wheel passes 100 and 300 are taken into consideration. In the top two layers, the high wheel pressure significantly reduces the proportion of small-force contacts, as shown in Figure 7.37. With the increase of the wheel pressure, the tangential bond force tends to distribute uniformly, which is identical to the situation for the normal bond force. Table 7.8 shows the variation in the extrema of the tangential contact force with wheel pressure. Generally speaking, there exists an increase in the extrema in absolute terms as the wheel pressure rises from 42 to 254kPa, for the top layer in particular.

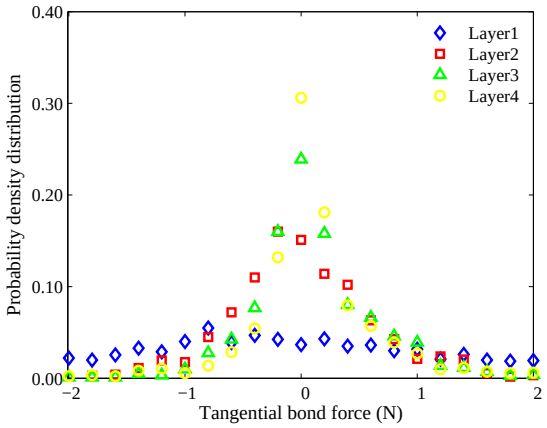

(a) Pass 100

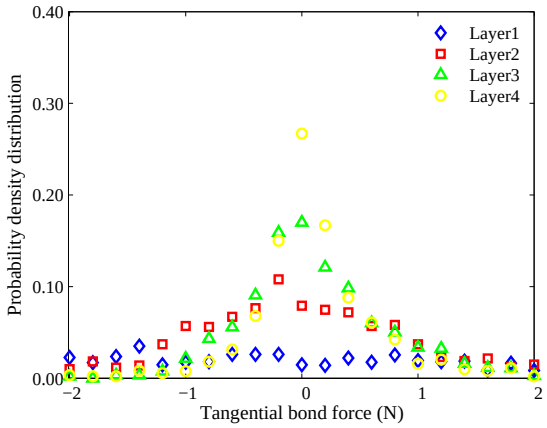

(b) Pass 200

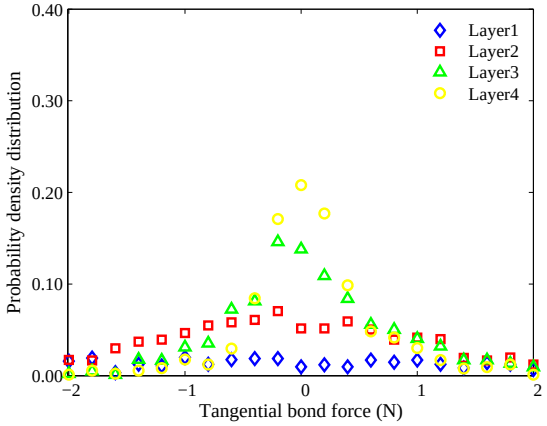

(c) Pass 300

Figure 7.35: Effect of pavement layer on the probability density distribution of the tangential bond force for the single-layered pavement

Extremum	Pavement layer	Pass 100	Pass 200	Pass 300
Negative	1	-16.8	-33.4	-49.8
	2	-1.8	-4.2	-6.6
	3	-2.2	-2.2	-2.4
	4	-2.2	-2.2	-2.2
Positive	1	18.2	37.4	55.6
	2	4.0	6.8	9.2
	3	2.4	3.0	3.8
	4	4.0	4.2	4.0

Table 7.7: Variation in the extremum of the tangential bond force with the pavement layer and wheel pass number for the single-layered pavement (the unit of the bond force: N)

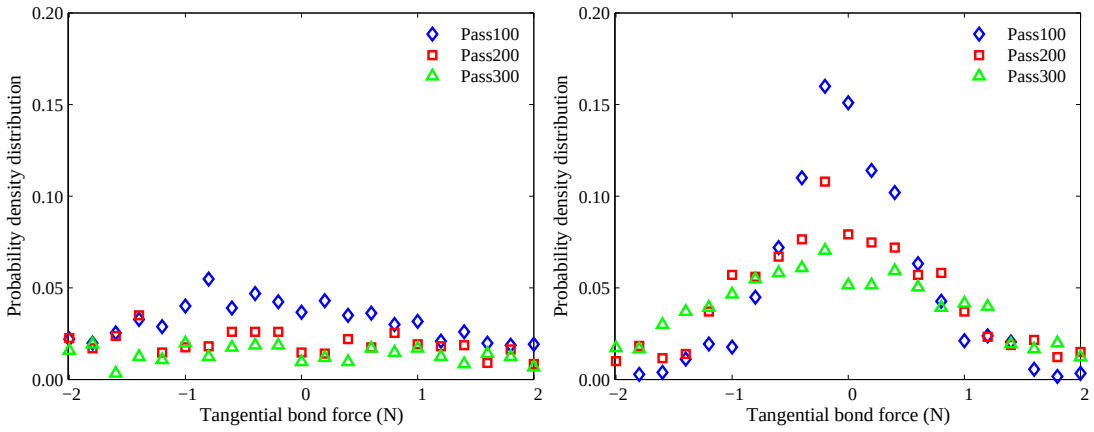

(a) Layer 1 *(b) Layer 2*

Figure 7.36: Effect of wheel pass number on the probability density distribution of the tangential bond force for the single-layered pavement

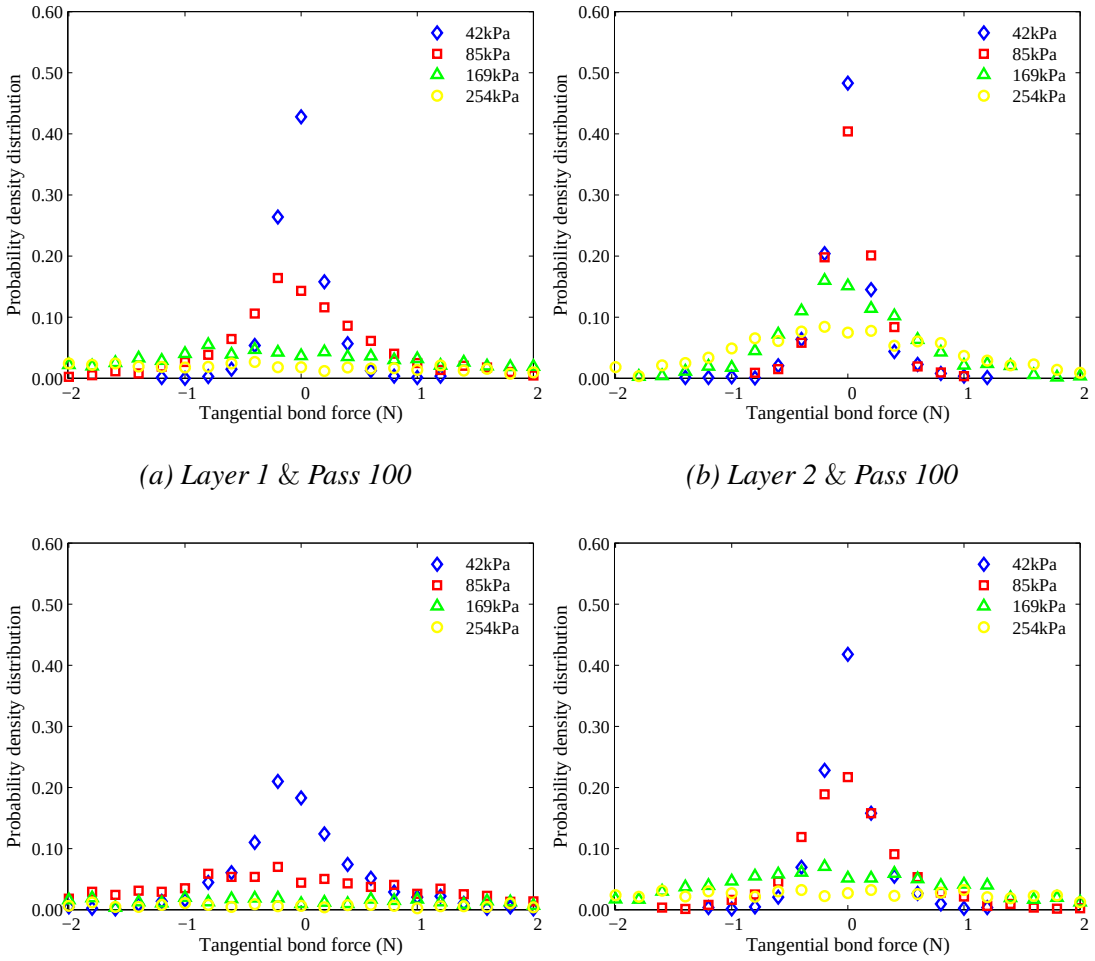

(a) Layer 1 & Pass 100

(b) Layer 2 & Pass 100

(c) Layer 1 & Pass 300

(d) Layer 2 & Pass 300

Figure 7.37: Effect of wheel pressure on the probability density distribution of the tangential bond force for the single-layered pavement

Extremum	pavement layer	Wheel pressure (kPa)	Pass 100	Pass 300
Negative	1	42	-1.2	-3.4
		85	-4.4	-12.8
		169	-16.8	-49.8
		254	-35.8	-108.4
	2	42	-1.4	-1.2
		85	-0.8	-1.6
		169	-1.8	-6.6
		254	-4.6	-13.8
Positive	1	42	1.2	3.6
		85	4.6	14.0
		169	18.2	55.6
		254	42.0	124.6
	2	42	1.2	1.2
		85	1.0	3.0
		169	4.0	9.2
		254	8.4	20.4

Table 7.8: Variation in the extremum of the tangential bond force with the wheel pressure for the single-layered pavement (the unit of the contact force: N)

7.3.1.5 Pavement particle displacement

The displacement vectors of the pavement particles have been studied after the wheel load is removed, as shown in Figures 7.38 and 7.39. In Figure 7.38, the gravity acceleration of the particles is 0.1m/s^2 and the wheel pressure is 169kPa. The wheel pass number is 100. The wheel particle moves with a constant translational velocity, namely 0.5m/s. The large particle displacements are close to the pavement surface, all the directions of which are approximately opposite to the translational direction of the wheel particle. In comparison, the particle displacements at depth can be disre-

garded. The maximum displacement is 1.02×10^{-6}m. Because of the parallel bonds at the interparticle contacts, the vertical displacements of the pavement particles are very small. Therefore, the relatively large particle displacements are in an almost horizontal direction. The plastic shear strain and horizontal residual stress are probably caused by these horizontal displacements.

There is an increase of the particle displacement as the wheel pass number increases from 100 to 300. For example, the maximum displacement rises to 3.07×10^{-6}m. Nevertheless, the distribution pattern for the displacement vectors is not changed (see Figure 7.39). On the other hand, the effect of the wheel pressure on the particle displacement has also been evaluated. Wheel pressures of 85 and 254kPa are added to the previous study. The wheel pass number is 100. It is found that there is hardly any variation in the distribution pattern of the displacement vectors, whereas the particle displacement increases with the increase of the wheel pressure. Take, for example, the maximum displacement. When the wheel pressure is 85kPa, it is 2.74×10^{-7}m. When a high wheel pressure of 254kPa is applied to the pavement, it increases to 2.29×10^{-6}m.

Figure 7.38: Total particle displacement after wheel pass 100 for gravity acceleration of 0.1m/s^2 and wheel pressure of 169kPa (maximum displacement $= 1.02\times10^{-6}m$)

Figure 7.39: Total particle displacement after wheel pass 300 for gravity acceleration of 0.1m/s^2 and wheel pressure of 169kPa (maximum displacement $= 3.07\times10^{-6}m$)

7.3.2 Double-layered pavement

In the double-layered pavement, the top layer is simulated asphalt concrete, in which the parallel bonds are added to the interparticle contacts. The microscopic properties include normal contact force, tangential contact force, normal bond force and tangential bond force. The bottom layer is comprised of unbound particles. The normal and tangential contact forces have been studied through microscopic analysis. In this subsection, the thickness of the simulated asphalt layer is 0.15m and the particle friction coefficient is 0.7. The interval of the force is selected to be identical to that for the single-layered pavement. Consequently, the force interval for the probability density distribution is 0.2N, which proves to be reasonable to study changes in the distribution. The factors affecting the probability distribution are considered, including pavement layer, number of wheel passes and wheel pressure. These distributions are all related to the condition after the wheel load has been removed.

7.3.2.1 Normal contact force

The self-weight stress and the stress in the pavement induced by the wheel pressure are a function of the the pavement depth. Therefore, the pavement layer may have an influence on the probability distribution of the normal contact force. The wheel pressure is selected as 10.0kPa. Figure 7.40 shows the probability distribution in terms of the pavement layer and the number of wheel passes. For the initial pavement sample, compared to the other layers, a very large proportion of the contacts have small forces in the top layer. Moreover, a slight decrease in this proportion is observed with the pavement layers from number 2 to 4. The extrema of the normal contact forces increase with the pavement depth, as shown in Table 7.9. Their values are 1.7, 3.7, 5.3 and 6.9N respectively.

On the other hand, after a number of repeated loadings, the second layer has the largest proportion of small-force contacts, while the smallest proportion is observed in the top layer. The extrema of the normal contact forces are significantly larger for the top

layer, in comparison with those for the other layers (see Table 7.9). That is probably due to the existence of the parallel bonds in the top layer. The internal structure of the top layer is more stable than that of the unbound layer. Therefore, the large contact forces are easily generated in the bonded layer. Also, it is worth mentioning that, for a certain number of the wheel passes (i.e. 100, 200 and 300), there is a gradual increase in the extrema of the normal forces with pavement depth, excluding the top layer. This may be caused by the gravity stress.

Another factor affecting the probability distribution is the wheel pass number. As in the study in Subsection 6.4.2, the development of the residual stress is mostly confined to the simulated asphalt layer. Therefore, the microscopic analysis concentrates on the top layer. The second layer is used as a comparison with the top layer. As shown in Figure 7.41a, there is a significant change in the probability distribution as the initial pavement sample undergoes a number of wheel loads. Nevertheless, the variation in the distribution with the further loading from pass 100 to 300 is hardly distinguishable. The normal contact force tends to be uniformly distributed, except for the initial sample. In the top layer, the extrema of the normal contact forces increase with repeated loading, as shown in Table 7.9. There is a significant increase in the extrema at the initial stage of the repeated loading. Afterwards, a gradual increase from 67.7 to 77.9N is observed.

In the second layer, the proportion of small-force contacts increases when the wheel pressure is applied to the initial pavement sample (see Figure 7.41b). Similar to the top layer, further loading has little influence on the distribution for the second layer. At the initial stage of the repeated loading, some small-force contacts are probably generated with the accumulation of permanent deformation in the unbound layer. Afterwards, the interparticle contacts become saturated although there is a further increase in the permanent deformation. In the unbound layer, there is no specific change in the extrema of the normal contact forces, as shown in Table 7.9.

The effect of the wheel pressure on the probability distribution is considered, as shown in Figure 7.42. The results for wheel pressures of 7.0 and 12.7kPa have been added.

Wheel passes 100 and 300 are selected. In the top layer, the wheel pressure has no obvious influence on the distribution within the range of the force from zero to 5.0N (see Figure 7.42a and 7.42c). The normal contact forces are almost uniformly distributed. The proportion of small-force contacts in the second layer progressively increases with the wheel pressure (see Figure 7.42b and 7.42d). That is probably because larger wheel pressure produces more new small-force contacts in the unbound layer. The variation in the extrema of the normal contact forces with the wheel pressure is displayed in Table 7.10. In the top layer, the extrema increase with the wheel pressure, whereas no regular pattern is observed for the unbound layer.

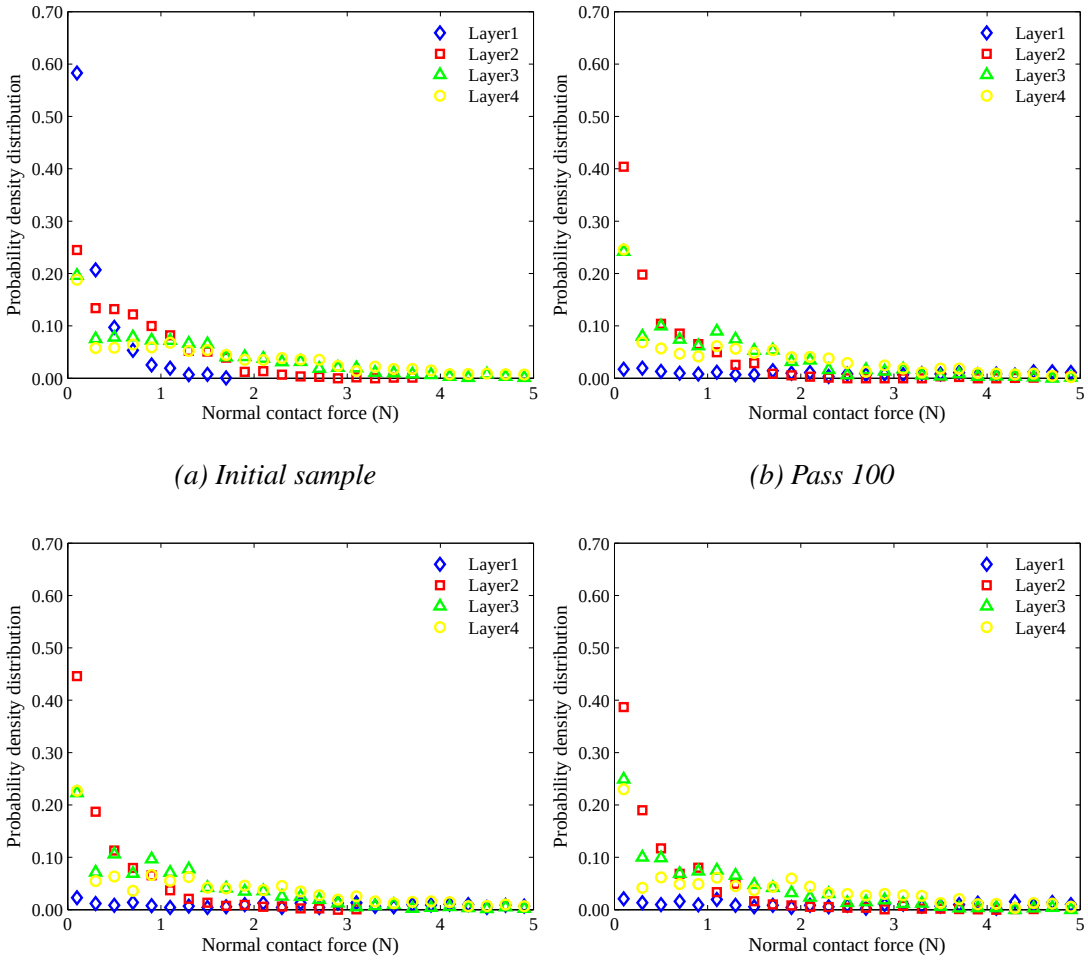

(a) Initial sample *(b) Pass 100*

(c) Pass 200 *(d) Pass 300*

Figure 7.40: Effect of pavement layer on the probability density distribution of the normal contact force for the double-layered pavement

Extremum	Pavement layer	Initial	Pass 100	Pass 200	Pass 300
Positive	1	1.7	67.7	73.7	77.9
	2	3.7	5.1	3.1	4.5
	3	5.3	6.7	5.3	6.1
	4	6.9	9.1	6.7	6.9

Table 7.9: Variation in the extremum of the normal contact force with the pavement layer and wheel pass number for the double-layered pavement (the unit of the contact force: N)

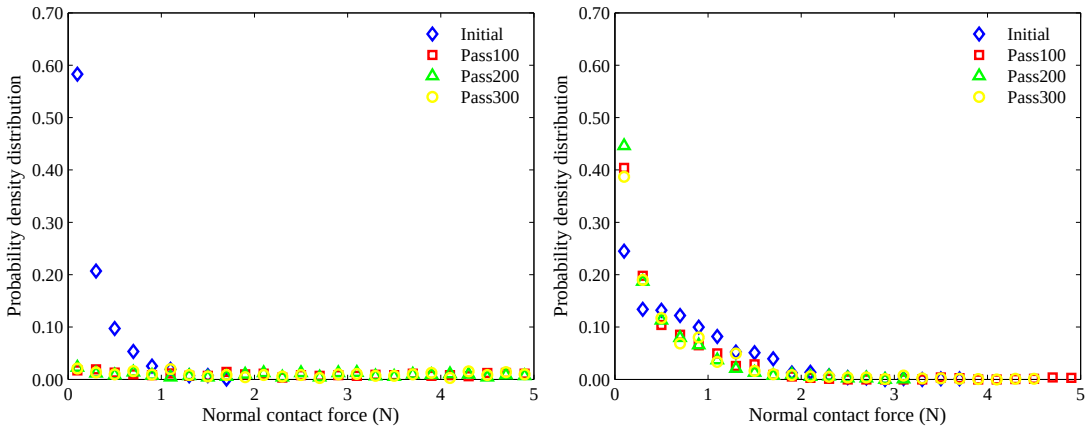

(a) Layer 1 *(b) Layer 2*

Figure 7.41: Effect of wheel pass number on the probability density distribution of the normal contact force for the double-layered pavement

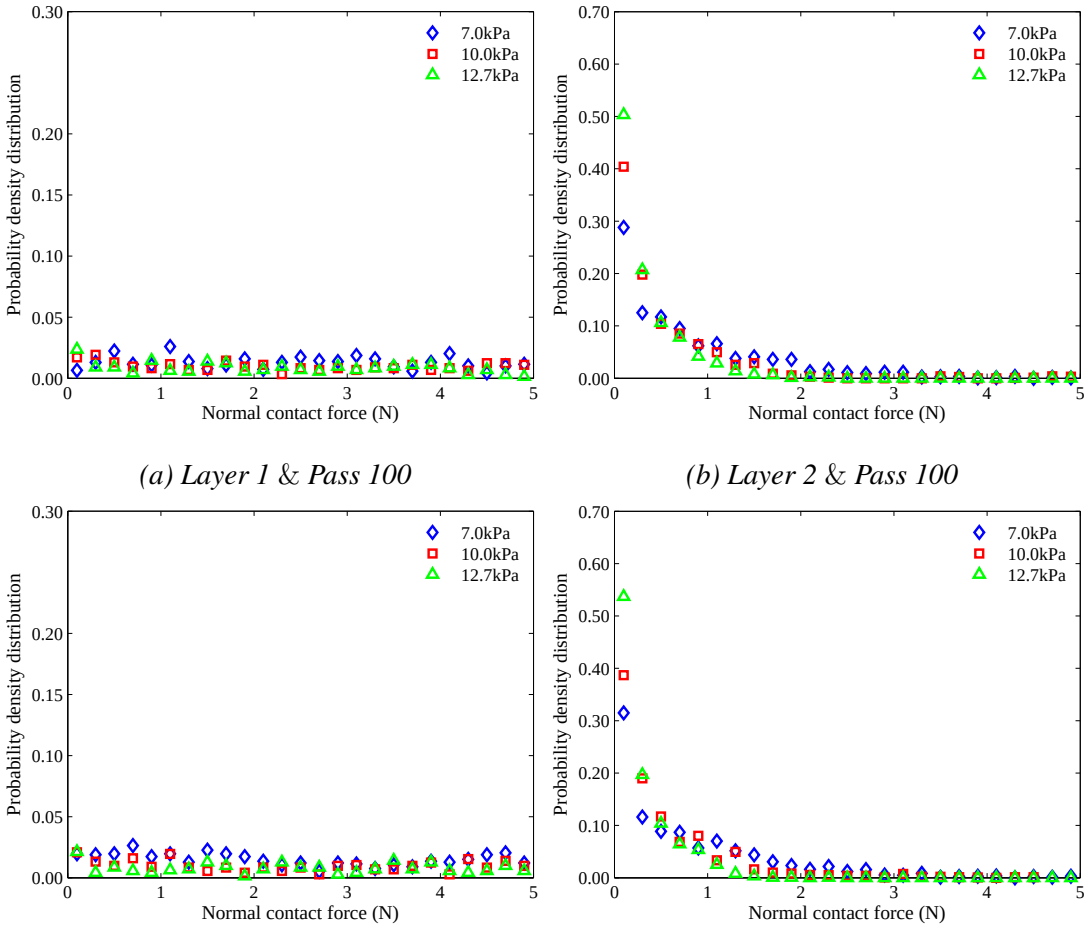

(a) Layer 1 & Pass 100

(b) Layer 2 & Pass 100

(c) Layer 1 & Pass 300

(d) Layer 2 & Pass 300

Figure 7.42: Effect of wheel pressure on the probability density distribution of the normal contact force for the double-layered pavement

Extremum	pavement layer	Wheel pressure (kPa)	Pass 100	Pass 300
Positive	1	7.0	56.1	71.7
		10.0	67.7	77.9
		12.7	73.7	80.7
	2	7.0	6.1	6.3
		10.0	5.1	4.5
		12.7	5.7	7.1

Table 7.10: Variation in the extremum of the normal contact force with the wheel pressure for the double-layered pavement (the unit of the contact force: N)

7.3.2.2 Tangential contact force

The probability distribution of the tangential contact force is studied in terms of the various pavement layers, as shown in Figure 7.43. In the initial pavement sample, the gravity stress is the dominant factor affecting the distribution. The proportion of the contacts with small forces decreases with the pavement depth (see Figure 7.43a). However, a gradual increase is observed for the absolute extrema of the tangential contact forces, as shown in Table 7.11. After the pavement experiences a number of repeated wheel loads (i.e. 10.0kPa), the top layer has the smallest proportion of small-force contacts (see Figure 7.43b, 7.43c and 7.43d). In the other three layers, the small-force proportion still decreases with the pavement depth. Therefore, in the unbound layer, the gravity stress is the chief factor for the force distribution, instead of the wheel pressure. However, in the top layer, the tangential force distribution is significantly changed by the external loads, which induce the residual stress. As shown in Table 7.11, compared to the other layers, the absolute extrema in the top layer are very large, probably related to the high residual stress (see Subsection 6.4.2). Generally speaking, the absolute extrema in the unbound layers increase with the pavement depth. That is mainly because of the self-weight stress, rather than the residual stress.

The wheel pass number is an important factor affecting the contact force distribution. Figure 7.44a shows that there is a dramatic decrease in the small-force proportion as the initial sample is subjected to repeated loading. A further wheel loading from pass 100 to 300 has a negligible effect on the distribution. In the unbound layer, there is an increase in the peak of the distribution, when a number of the repeated loads are applied to the initial pavement (see Figure 7.44b). That may be because some new contacts with small tangential forces are generated at the initial stage of the accumulation of the permanent pavement deformation. The force distribution is hardly affected by further wheel loading. In the top layer, the absolute extremum of the tangential contact force dramatically increases at the initial stage of wheel loading, followed by a progressive increase from wheel pass 100 to 300 (see Table 7.11). For the unbound materials, there is no obvious change in the absolute extrema with the wheel pass number.

The effect of wheel pressure on the force distribution is studied for wheel passes 100 and 300. Wheel pressures of 7.0 and 12.7kPa are added to the microscopic analysis. In the first layer, the change in the force distribution induced by the wheel pressure can be disregarded, at wheel pass 100 in particular, although there is a slight decrease in the peak of the distribution with increased wheel pressure at wheel pass 300 (see Figure 7.45). This indicates that the higher wheel pressure makes the tangential contact force slightly more uniformly distributed. On the other hand, the proportion of the small tangential forces increases with the wheel pressure for the second layer, irrespective of the wheel pass number. The larger particle displacements are probably induced by the higher wheel pressure. In such a way, more small-force contacts may be produced. The variation in the extrema of the tangential contact forces with wheel pressure is displayed in Table 7.12. In the simulated asphalt layer, the absolute extrema are larger for a higher wheel pressure. However, no unified pattern can be used to describe the mild change in the extrema for the unbound layer.

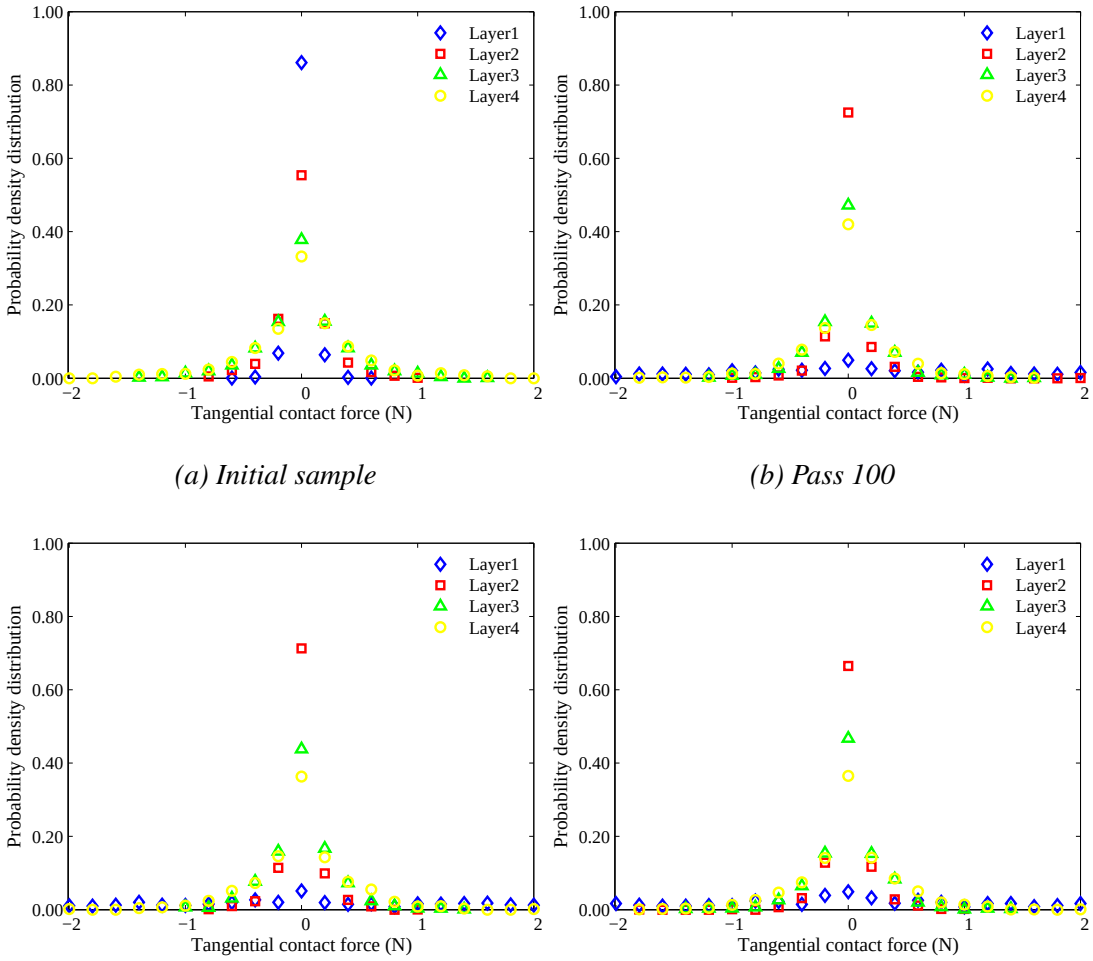

(a) Initial sample *(b) Pass 100*

(c) Pass 200 *(d) Pass 300*

Figure 7.43: Effect of pavement layer on the probability density distribution of the tangential contact force for the double-layered pavement

Extremum	Pavement layer	Initial	Pass 100	Pass 200	Pass 300
Negative	1	-0.6	-31.2	-33.8	-35.2
	2	-0.8	-1.0	-0.8	-1.8
	3	-1.4	-1.2	-1.0	-1.4
	4	-2.2	-1.8	-2.0	-1.8
Positive	1	0.6	27.8	30.4	32.4
	2	1.0	2.0	1.0	1.0
	3	1.6	1.6	1.4	1.4
	4	2.2	1.6	2.0	2.0

Table 7.11: Variation in the extremum of the tangential contact force with the pavement layer and wheel pass number for the double-layered pavement (the unit of the contact force: N)

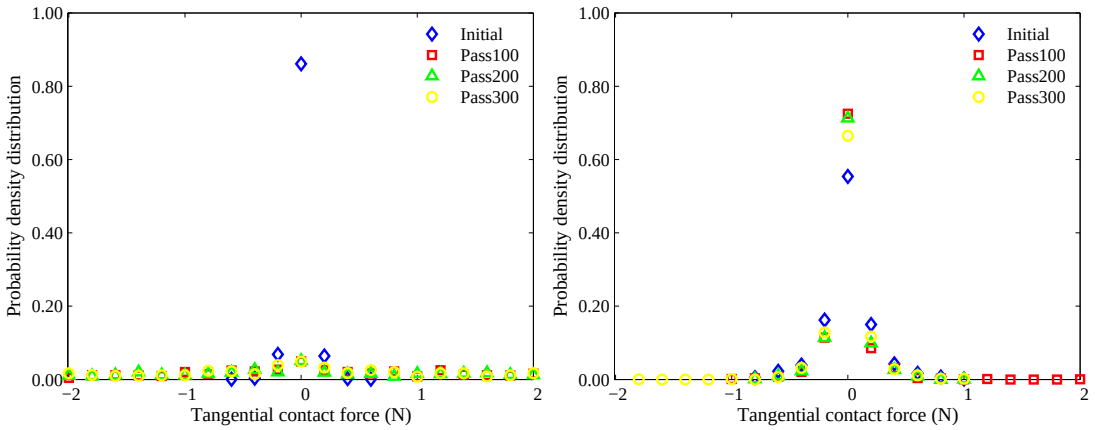

(a) Layer 1 *(b) Layer 2*

Figure 7.44: Effect of wheel pass number on the probability density distribution of the tangential contact force for the double-layered pavement

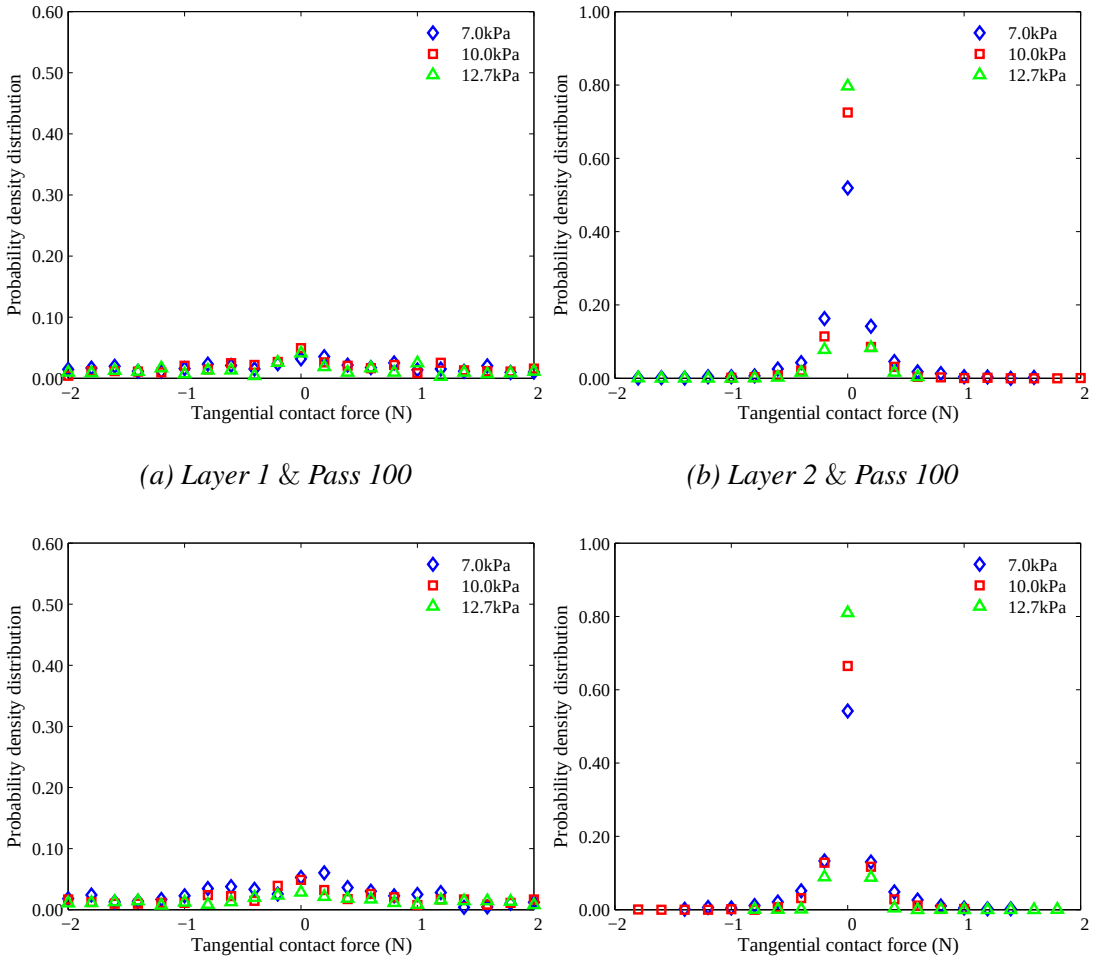

(a) Layer 1 & Pass 100

(b) Layer 2 & Pass 100

(c) Layer 1 & Pass 300

(d) Layer 2 & Pass 300

Figure 7.45: Effect of wheel pressure on the probability density distribution of the tangential contact force for the double-layered pavement

Extremum	pavement layer	Wheel pressure (kPa)	Pass 100	Pass 300
Negative	1	7.0	-26.0	-30.2
		10.0	-31.2	-35.2
		12.7	-39.6	-42.8
	2	7.0	-1.8	-1.4
		10.0	-1.0	-1.8
		12.7	-1.8	-0.8
Positive	1	7.0	19.2	25.0
		10.0	27.8	32.4
		12.7	33.4	40.6
	2	7.0	1.6	1.4
		10.0	2.0	1.0
		12.7	0.6	1.8

Table 7.12: Variation in the extremum of the tangential contact force with the wheel pressure for the double-layered pavement (the unit of the contact force: N)

7.3.2.3 Normal bond force

In the simulated asphalt layer, normal and tangential forces can be generated in the parallel bonds. The tensile or compressive normal bond force is denoted by the minus or plus sign in PFC^{2D}. The thickness of the pavement layer in the microscopic analysis is 0.15m, which is identical to that of the simulated asphalt layer. Therefore, only the top layer is used to study the probability distribution of the bond force. The wheel pass number is regarded as a factor affecting the probability distribution. The wheel pressure is selected as 10.0kPa, and the wheel pass numbers are 100, 200 and 300. Figure 7.46 shows that the number of wheel passes has a negligible effect on the distribution. The normal bond forces are almost uniformly distributed. However, a progressive increase in the absolute extrema is observed during the repeated wheel loading, as shown in Table 7.13.

In order to analyse the effect of wheel pressure on the probability distribution, wheel pressures of 7.0 and 12.7kPa are added to the previous study. Wheel passes 100 and 300 are chosen. As shown in Figure 7.47, there is no obvious change in the distribution with the increase in wheel pressure. On the other hand, the extrema of the normal bond forces are displayed in Table 7.14. Generally, the absolute extrema rise with increased wheel pressure. For example, at wheel pass 300, the negative extrema are -64.6, -75.2 and -98.4N as the corresponding wheel pressures are 7.0, 10.0 and 12.7kPa.

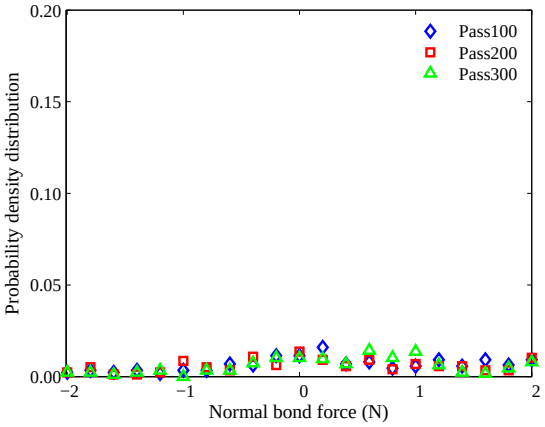

Figure 7.46: Effect of wheel pass number on the probability density distribution of the normal bond force for the double-layered pavement

Extremum	Pavement layer	Pass 100	Pass 200	Pass 300
Negative	1	-41.2	-46.4	-75.2
Positive	1	67.6	73.6	89.8

Table 7.13: Variation in the extremum of the normal bond force with the wheel pass number for the double-layered pavement (the unit of the bond force: N)

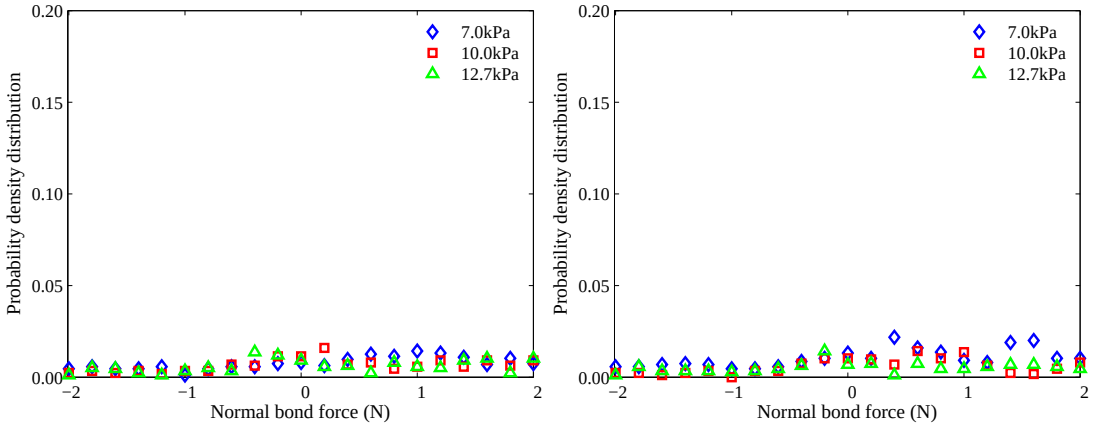

(a) Pass 100 *(b) Pass 300*

Figure 7.47: Effect of wheel pressure on the probability density distribution of the normal bond force for the double-layered pavement

Extremum	pavement layer	Wheel pressure (kPa)	Pass 100	Pass 300
Negative	1	7.0	-32.2	-64.6
		10.0	-43.2	-75.2
		12.7	-42.8	-98.4
Positive	1	7.0	54.6	70.2
		10.0	67.6	89.8
		12.7	86.0	100.4

Table 7.14: Variation in the extremum of the normal bond force with the wheel pressure for the double-layered pavement (the unit of the contact force: N)

7.3.2.4 Tangential bond force

The factors affecting the probability distribution of the tangential bond force have been taken into consideration, i.e. wheel pass number and wheel pressure. The wheel pressure is 10.0kPa for the analysis of the wheel pass number, while wheel passes 100 and 300 are selected for the wheel pressure investigation. Generally, the tangential bond forces are almost uniformly distributed, and are hardly affected by the wheel pass number (see Figure 7.48) and the wheel pressure (see Figure 7.49). This is similar to the situation for the normal bond force. The extrema of the bond forces are also studied. There is a gradual increase in the absolute extrema with the wheel pass number, as shown in Table 7.15. The effect of wheel pressure on the extrema is displayed in Table 7.16. Generally speaking, high wheel pressure induces large absolute extrema, regardless of the wheel pass number.

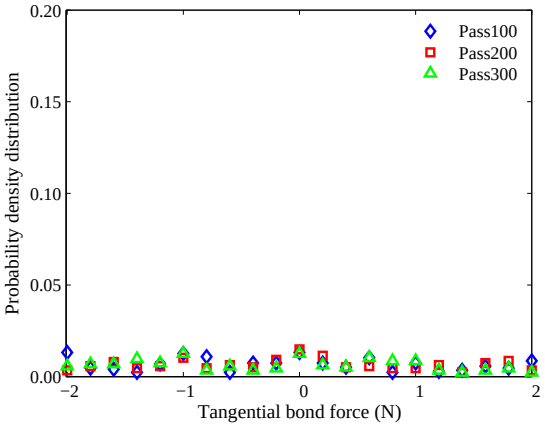

Figure 7.48: Effect of wheel pass number on the probability density distribution of the tangential bond force for the double-layered pavement

Extremum	Pavement layer	Pass 100	Pass 200	Pass 300
Negative	1	-60.8	-67.4	-75.4
Positive	1	65.8	71.8	76.6

Table 7.15: Variation in the extremum of the tangential bond force with the wheel pass number for the double-layered pavement (the unit of the bond force: N)

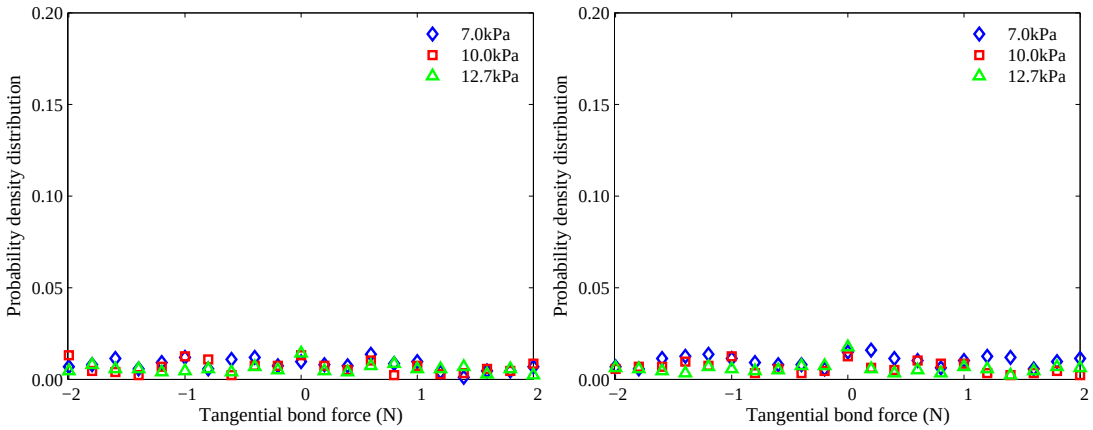

(a) Pass 100 *(b) Pass 300*

Figure 7.49: Effect of wheel pressure on the probability density distribution of the tangential bond force for the double-layered pavement

Extremum	pavement layer	Wheel pressure (kPa)	Pass 100	Pass 300
Negative	1	7.0	-54.0	-71.8
		10.0	-60.8	-69.4
		12.7	-70.4	-79.8
Positive	1	7.0	57.0	65.6
		10.0	65.8	76.6
		12.7	73.6	82.0

Table 7.16: Variation in the extremum of the tangential bond force with the wheel pressure for the double-layered pavement (the unit of the contact force: N)

7.3.2.5 Pavement particle displacement

For the double-layered pavement, the vectors of the particle displacements have been investigated after the wheel load is removed, as shown in Figures 7.50 and 7.51. In Figure 7.50, the wheel pressure is 10.0kPa and the wheel pass number is 100. In the simulated asphalt layer, large particle displacements are observed and all the displacement vectors are in an almost vertical direction. That is because there is little deformation in the simulated asphalt layer during repeated wheel loading, compared to the unbound layer. Consequently, the bonded layer can be approximately considered as a rigid body where all the particle displacement vectors are in the direction of the permanent pavement deformation. Besides, relatively large particle displacements are widely distributed in the pavement. Most of the directions for the displacement vectors deeper in the pavement are also downward. The maximum displacement is 2.91×10^{-2}m.

On the other hand, the distribution pattern for the displacement vectors is unchanged with further repeated loading (See Figure 7.51), whereas there is an increase in the particle displacement. For instance, the maximum displacement is 3.89×10^{-2}m at wheel pass 300. This is due to the fact that the permanent deformation increases with wheel pass number. Also, wheel pressure is considered to have an effect on

the particle displacement. Wheel pressures of 7.0 and 12.7kPa have been added to the previous study and the wheel pass number is selected as 100. It is found that the distribution pattern of the displacement vectors is approximately independent of the wheel pressure. Nevertheless, with the increase in wheel pressure, there is an augmentation in the particle displacement. For instance, the maximum displacements are 2.85×10^{-2} and 3.34×10^{-2}m for wheel pressures of 7.0 and 12.7kPa. That is because of the large permanent deformation induced by the high wheel pressure.

Figure 7.50: Total particle displacement after wheel pass 100 for gravity acceleration of 0.1m/s^2 and wheel pressure of 10.0kPa (maximum displacement $= 2.91 \times 10^{-2} m$)

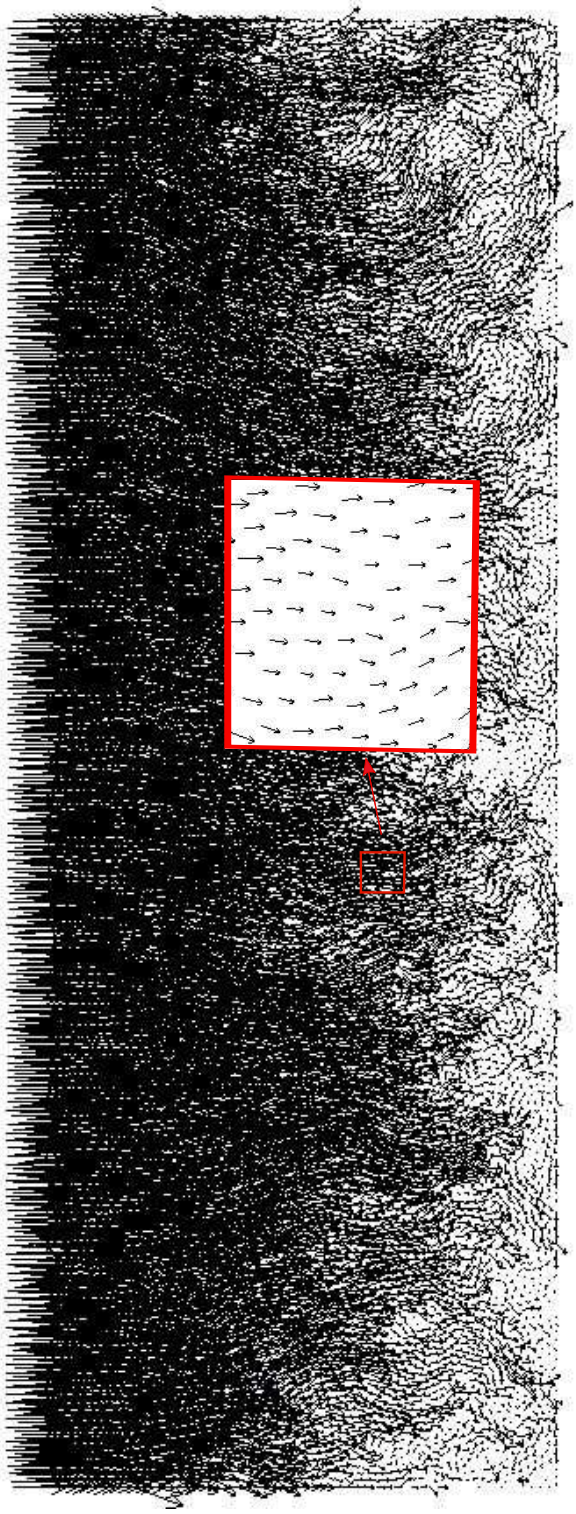

Figure 7.51: Total particle displacement after wheel pass 300 for gravity acceleration of $0.1m/s^2$ and wheel pressure of 10.0kPa (maximum displacement $= 3.89 \times 10^{-2} m$)

7.4 Summary

Since the elements of the unbound pavement at the same depth experience an identical stress path due to the periodic lateral boundary, after generation, the pavement is equally divided into several layers to carry out the microscopic analysis. The probability density distributions of the contact force and, in some cases, the bond force are employed in this analysis. Following the sensitivity study, for the unbonded pavement, the thickness of the pavement layer is selected as 0.10m and the interval of the contact force is set at 2N. The factors affecting the probability distribution are studied: pavement layer, number of wheel passes, wheel pressure, initial void ratio and interparticle friction. The top four layers of the unbonded pavement are considered.

For the distribution of the normal contact force a peak is generally observed at the small contact forces, followed by a rapid decrease stage and then the decrease rate gradually decays to nearly zero. The peak of the distribution decreases with pavement depth, particularly from the top to the second layer. However, an increased proportion of the large-force contacts exist as the pavement depth rises. Moreover, the effect of the wheel pass number on the probability distribution focuses on the small contact forces. In comparison with the initial pavement sample, there is a reduction in the peak, formed at the small forces, for a pavement subjected to a number of repeated loadings. Moreover, the wheel pressure has an influence on the peak of the probability distribution. However, there is no fixed pattern to describe it. In addition, for the dense sample, the proportion of the contacts with small contact forces is less than that for the loose sample, which applies to the top four layers of pavement. Finally, compared to the friction coefficient of 0.5, there is a reduction in the proportion of the small-force contacts for the large coefficient of 0.9. Nevertheless, when the coefficient of 0.7 is considered, no fixed pattern for the distribution can be found.

Generally speaking, for the tangential contact force, a peak of the distribution is observed at the small contact forces. There is a rapid drop from the two sides of the peak point, followed by a gradual decrease until the probability density approaches zero.

The probability distribution is significantly affected by the pavement depth, near the peak in particular, i.e. at the small tangential forces. The probability density near the peak decreases as the pavement depth increases, especially from the top to the second layer, irrespective of the wheel pass number. Furthermore, the variation in the distribution with the number of passes is generally restricted to the contacts for the small tangential forces. In general, there is a reduction in the peak when the initial sample experiences a number of repeated wheel loads. Moreover, in the top three layers, the distribution is insensitive to the wheel pressure, whereas a reduction in the peak is observed for the fourth layer when the pavement undergoes wheel pressures from 2.0 to 7.0kPa. Generally, two kinds of pavement response (i.e. shakedown and ratchetting) are observed when the unbonded pavement with high self-weight stress experiences different wheel pressures. However, there is no significant change in the probability density distribution of the contact force. In addition, there is a slight decrease in the peak of the distribution for the dense sample, excluding the top layer. The decrease is more evident for the fourth layer than the other two layers. Lastly, the peak of the distribution decreases with the increase in the interparticle friction coefficient from 0.5 to 0.9.

For the single- and double-layered pavements, the thickness of the layer for the microscopic analysis is 0.15m and the interval of the force for the probability density distribution is 0.2N. The normal contact force, tangential contact force, normal bond force and tangential bond force were studied. The factors affecting the probability distribution are considered, i.e. pavement layer, wheel pass number and wheel pressure. In the case of the single-layered pavement, there is a similar development pattern for both the normal and tangential contact forces as the pavement depth increases. At the initial stage, the proportion of the small-force contacts is largest for the top layer, compared to the other layers. After the pavement experiences the wheel pressure, this proportion for the top layer generally becomes the smallest. In comparison with the other layers, the extremum of the contact force in the top layer changes from the smallest to the largest, as the initial pavement undergoes wheel pressure. On the other hand, for both the normal and tangential bond forces, the proportion of the small-force con-

tacts increases with pavement depth, whereas the absolute extremum of the bond force in the top layer is significantly larger than those in the other layers. Moreover, for both the contact and bond forces, the proportion of the small-force contacts reduces but the absolute extrema of the forces in the top layer increase with the increase of the wheel pass number and the wheel pressure.

In the case of the double-layered pavement, the proportion of the small-force contacts for both the normal and tangential contact forces changes from the largest to the smallest for the top layer, compared to the other layers, as the initial pavement sample experiences a number of repeated wheel loads. At the initial stage, the absolute extrema of the contact forces are the smallest for the top layer, in comparison with the other layers. After repeated loading, the absolute extrema in the top layer generally change to be the largest. In addition, for both the normal and tangential contact forces, as the initial pavement undergoes repeated wheel loading, there is a significant decrease in the proportion of the small-force contacts for the top layer, whereas this proportion increases for the second layer. Additionally, for the top layer, the wheel pressure has a negligible effect on the distribution of both normal and tangential contact forces. Nevertheless, the proportion of the small-force contacts gradually increases in the second layer with the rise in the wheel pressure. On the other hand, for both the normal and tangential bond forces, the probability distribution is hardly affected by the wheel pass number and the wheel pressure. Lastly, in the top layer, the absolute extrema for both the contact and bond forces generally rise with the increase in the wheel pass number and the wheel pressure.

The sliding contact ratio for the unbonded pavement was analysed in terms of the pavement layer, wheel pass number, wheel pressure, and so on. The effect of the pavement layer on the sliding ratio depends on the wheel pressure. When the wheel pressure is relatively low, given a specific wheel pass, the ratio for the top layer is generally larger than for the other three layers. Nevertheless, the relationship between the ratios for the layers from the second to the fourth can hardly be described in terms of a specific pattern. On the other hand, subjected to a high wheel pressure, the pavement produces a decreased sliding ratio with pavement depth. In addition, there is no con-

tinuous decrease or increase in the ratio during repeated wheel loading. Instead, some fluctuations of the ratio are observed with trafficking. Moreover, high wheel pressure generally gives rise to a large sliding ratio for a given wheel pass number, in the top three layers. Also, the large ratio is generally caused by a low initial gravity stress and the low sample compaction in the top four layers. Finally, a specific pattern is hard to identify to summarise the effect of the friction coefficient on the contact slippage.

Pavement particle displacement was studied and the factors, such as wheel pass number and wheel pressure, are taken into consideration. For the unbonded pavement, the relatively large particle displacements are distributed from near the pavement surface to a wide range within the pavement, with an increase in the wheel pressure or a reduction in the initial gravity stress. The directions of the large displacement vectors are diverse for the high gravity stress field but become downward as the gravity stress decreases. In addition, the directions of the displacement vectors deep in the pavement are changed from being aligned with the wheel movement direction to being diverse with decrease in the gravity stress. Moreover, the particle displacement generally increases with increased wheel pass number and wheel pressure as well as reduction in the initial gravity stress.

In the case of single-layered pavements, the large particle displacements are close to the pavement surface and their directions are almost contrary to the wheel movement direction. In comparison, the particle displacements deep in the pavement can be disregarded. In addition, with the wheel pass number and the increase in wheel pressure, this distribution pattern for the displacement vectors is not changed, whereas the particle displacement generally increases. For the double-layered pavement, in the bonded layer, relatively large particle displacements can be found and their directions are close to a vertical direction. Furthermore, large particle displacements are widely distributed in the pavement. In addition, the directions for the displacement vectors deep in the pavement are mainly downward. Finally, although there is an increase in the magnitude of the particle displacement as the wheel pass number and the wheel pressure increase, the distribution pattern of the displacement vectors is unchanged.

Chapter 8

Conclusions and Recommendations for Future Research

8.1 Summary

This thesis has presented a series of 2D DEM biaxial test simulations on unbonded and bonded granular materials, which provides us with insight into the mechanical behaviour. The factors affecting the shear strength and dilatancy response are considered, namely particle stiffness, particle friction coefficient and so on. Guidance is provided for the selection of the particle properties for the pavement simulation.

Simulations of direct wheel load tests are carried out. Three kinds of pavement model are employed, i.e. unbound pavement, single- and double-layered bonded pavements. The vertical permanent surface deformation after a certain number of passes is recorded. Also, the variation in the deformation rate with load repetition is studied. Moreover, the horizontal residual stress is obtained using measurement circles. Finally, micro-analysis of the pavement simulation is conducted. Probability density distributions of contact and bond forces are considered. The sliding contact ratio after a number of wheel passes is analysed. The displacement vectors of pavement particles are found.

8.2 Conclusions

8.2.1 Biaxial test simulation

During the DEM compression tests on the unbonded and bonded granular materials, the typical stress-strain responses have four stages, namely a linear increase in strength, a peak strength stage, a gradual reduction and a relatively steady state. These are in qualitative agreement with the laboratory test results. Compared to disc particles, clump particles give behaviour closer to reality since the shape of clump particles is irregular, more similar to soil particle shape. Moreover, the sample volume generally undergoes a small contraction at the initial stage and then clearly begins to dilate. Nevertheless, for a loose unbonded sample, the shear strength gradually increases until a relatively stable state is reached, while the volume continues contracting and, finally, a stable global contraction is attained.

For the unbonded sample, the Young's modulus is significantly affected by the particle stiffness, which has an effect on peak shear strength but not ultimate strength. Moreover, the peak deviatoric stress increases with the increase of the interparticle friction. Furthermore, the particle shape and confining pressure affect not only peak strength but also ultimate strength. On the other hand, the volumetric dilation is enlarged by the increase in the particle stiffness and the interparticle friction coefficient. Compared to samples comprising discs, those comprising clumps exhibit a large volumetric dilation. In addition, the initial void ratio and confining pressure are the important factors to affect the volumetric strain.

For the bonded sample, by increasing the bond size, peak strength rises significantly and the dilatancy response is more and more evident. Generally speaking, the mechanical responses are insensitive to bond strength distributions such as the normal and Weibull distributions. Compared to the unbonded sample, there is a significant increase in Young's modulus and a clear decrease in Poisson's ratio for the bonded sample. However, these elastic parameters are hardly affected by the bond strength.

There is a linear increase in the primary yield stress for the bonded samples with the increase of the bond strength. In general, the friction angle decreases and the cohesion increases with the rise in bond strength. Increased particle friction generally yields an increased internal friction angle but has hardly any effect on the cohesion. The number of intact bonds for a specific axial strain increases with the reduction in the confining pressure and particle friction, as well as the increase in bond strength. A larger dilatancy is yielded by the bonded specimen than by the unbonded one, probably owing to the mix of clusters and debonded particles generated by bond breakage events. Large overall dilatancy tends to be caused by high bond strength and low confining pressure, associated with relatively mild bond breakage. In contrast, a smaller dilation results from reduced bond breakage in the particle friction study.

8.2.2 Permanent pavement deformation

Different load modes such as stationary, translational and rolling wheel loads, have a negligible effect on the contact pressure distribution under a wheel, which can be regarded as a Hertz distribution. For the unbonded pavement, periodic lateral boundaries prove to be feasible in DEM simulations. The simulated top surface of the pavement can be regarded as a circle and therefore the pavement response is identical in the same horizontal level after each load pass. The total pavement surface can be used to study the permanent deformation in pavements. The behaviour of the unbonded pavement matches laboratory test results pretty well in a qualitative way. However, for the bonded pavement, rigid lateral boundaries are necessary because of apparent force concentrations found at lateral boundaries if periodic lateral boundaries are used. Therefore the middle section of the pavement surface is used to study the permanent pavement deformation.

Generally, two kinds of pavement behaviour are successfully simulated for the unbonded pavement, namely pavement shakedown (no further accumulation of permanent deformation) and ratchetting (the continuous accumulation of permanent deformation). Compared to the particle radius expansion method, the sample generated with

the gravity expansion method exhibits a smaller surface deformation. However, the difference in rutting can be disregarded for relatively large wheel pressures. Rutting is also affected by the motion mode (i.e. translation and rolling) with the restriction of low wheel pressure, although the steady deformation rate remains unchanged. A relatively large permanent deformation and steady deformation rate are observed for pavements with low gravity stress. Two different responses to the varied contact pressures, i.e. pavement shakedown and ratchetting, are observed for the pavements with high gravity stress. However, the constant deformation rate is nonzero when the gravity acceleration is low, even if the contact pressure is very small. The slight decrease in the initial void ratio and the increase in the friction coefficient will cause a reduction in the permanent deformation.

For the single-layered bonded pavement, there is no obvious accumulation of vertical deformation because of parallel bonds at interparticle contacts. In the case of a double-layered pavement, a considerable permanent pavement deformation is involved, which is probably attributable to compaction of the granular base. There is no sign of the occurrence of pavement shakedown, since the deformation rate remains nonzero after pass 300. A larger permanent pavement deformation is observed with a decrease in the upper layer thickness and particle friction coefficient, as well as an increase in wheel pressure.

For the unbonded pavement, the vertical residual stresses are nearly zero and the horizontal residual stresses are independent of the wheel pass number. Generally, the horizontal residual stress is hardly affected by the wheel pressure for a pavement with low gravity stress, whereas larger horizontal residual stress is caused with a higher wheel pressure in a large gravity stress field. Pavement shakedown is observed when the horizontal residual stress can prevent the development of plastic strain in pavements. Otherwise, pavement ratchetting will take place. In addition, the horizontal residual stress is obviously influenced by the initial gravity stress. Large gravity stress corresponds to a relatively large horizontal residual stress. In the case of the single-layered bonded pavement, with the pavement depth, the horizontal residual stress increases rapidly to a peak value close to the pavement surface. A larger horizontal residual stress tends to

result from an increase of the wheel pass number and the wheel pressure. In contrast, the residual stress in the vertical direction can be disregarded. In the double-layered pavement, the horizontal residual stresses are not continuous at the interface between the different pavement layers. They increase to a peak from the pavement surface, and then a gradual decrease follows through the depth of the upper bonded layer. They are negligible in the granular base. It is noted that the peak of the horizontal residual stress increases with an increase of the wheel pass number and the wheel pressure, as well as a decrease in the upper layer thickness.

8.2.3 Micro-analysis of the pavement simulation

In the case of an unbonded pavement, for the probability density distribution of the normal contact force, a peak is generally observed at the small contact forces, then a stage of rapid decrease follows, and afterwards the probability density gradually decays to zero. For the tangential contact force, a peak of the probability distribution appears at the small contact forces, followed by a rapid drop from the two sides of the peak point. Later, a gradual decrease is observed until the probability density approaches zero. The peaks of the probability distributions for both the normal and tangential contact forces decrease with pavement depth, particularly from the top to the second layer. The other factors, such as wheel pass number, wheel pressure, etc., mainly affect the probability distribution of the small contact forces. It is found that for unbonded pavements with high self-weight stress, although two kinds of pavement response (i.e. shakedown and ratchetting) are observed based on different wheel pressures, there exits no significant change in the probability density distribution of the contact force.

For single- and double-layered bonded pavements, the probability distributions of the normal and tangential contact forces, as well as the normal and tangential bond forces, were studied. After the initial pavement sample undergoes a number of repeated wheel loads, the proportion of the small-force contacts for both the normal and tangential contact forces changes from the largest to the smallest for the top layer, in comparison with the other layers. In contrast, the absolute extrema of the contact forces for the

top layer change from the smallest to the largest. In the case of the single-layered pavement, the proportion of the small-force contacts for both the normal and tangential bond forces increases with the pavement depth. The absolute extremum of the bond force in the top layer is evidently larger than those in the other three layers. For both the contact and bond forces, the proportion of the small-force contacts reduces with the rise in the wheel pass number and the wheel pressure. Nevertheless, the reverse applies to the absolute extrema of the forces in the top layer.

In the case of the double-layered pavement, for both the normal and tangential contact forces, as the initial pavement is subjected to repeated wheel loads, an evident decrease in the proportion of the small-force contacts is observed in the top layer, although this proportion increases for the second layer. For the top layer, the effect of the wheel pressure on the distribution of the contact forces can be disregarded, whereas the proportion of the small-force contacts gradually increases in the second layer with the increase in wheel pressure. The probability distribution for both the normal and tangential bond forces is independent of the wheel pass number and the wheel pressure. In the top layer, the absolute extrema for both the contact and bond forces generally increase with an increase of the wheel pass number and the wheel pressure.

For the unbonded pavement, the effect of the pavement layer on the sliding contact ratio depends on the wheel pressure. In general, given a specific wheel pass number, the sliding ratio for the top layer is larger than that for the other three layers. Subjected to a relatively high wheel pressure, the pavement produces a decreased sliding ratio with pavement depth. In addition, no continuous decrease or increase in the ratio is observed during repeated wheel loading. Moreover, a large sliding ratio for a given wheel pass number is generally caused by the high wheel pressure in the top three layers as well as the low initial gravity stress and low sample compaction in the top four layers.

In the case of the unbonded pavement, the distribution of relatively large displacements depends on the wheel pressure and the initial gravity stress. The directions of the large displacement vectors are diverse for the high self-weight stress but become downward

when the self-weight stress decreases. For the pavement with high self-weight stress, all the particles deep in the pavement move in nearly the direction of the external wheel load, whereas the directions of displacement vectors deep in the pavement are diverse for the pavement with low self-weight stress. In general, the particle displacement increases with a rise in the wheel pass number and the wheel pressure, as well as a reduction in the initial gravity stress. For the single-layered bonded pavement, relatively obvious particle displacements, with direction almost contrary to the movement direction of the wheel, are found near the pavement surface. In the case of the double-layered pavement, the relatively large particle displacements are widely distributed in the pavement. In the bonded layer, the directions for the large displacement vectors are in an almost vertical direction. For both the single- and double-layered pavements, with the increase of the wheel pass number and the wheel pressure, there is little change in the distribution of the displacement vectors, although the particle displacement generally increases.

8.3 Suggestions for future research

Future research could be conducted on the following aspects:

1. For the double-layered pavement, further repeated wheel loading should be applied to the pavement to study the accumulation of permanent pavement deformation. If the rate of the plastic deformation finally approaches zero, pavement shakedown can be considered to be taking place.

2. In the present study, the granular particles are considered to be discs. In reality, the shapes of granular particles are usually irregular and diverse. The particle shape may have an influence on permanent pavement deformation, since the interparticle interlocking effect is probably strong for irregular particles. After the removal of the wheel load, it is possible that the residual stress would become noticeable in the pavement.

3. Particle breakage is an important factor affecting rutting. A fracture criterion to model the crushing of a particle needs to be determined. The crushing particle is replaced by a number of small particles. Pioneering numerical simulation for the degradation of a granular base under a flexible pavement was undertaken by Vallejo et al. (2006). Particle fracture could be applied to model permanent deformation in pavements.

4. In the bonded pavement, parallel bonds are used to simulate the asphalt layer. This model simply represents the interparticle cementation in the asphalt layer. However, the behaviour of an asphalt mixture is time dependent, which can be reproduced by Burger's model or the modified model in DEM simulation (e.g. Collop et al., 2004; Dondi et al., 2005; Cai et al., 2013). Consequently, these models could be employed to more correctly represent the permanent deformation in flexible pavements.

5. To reveal the real behaviour of a pavement under repeated wheel loading, an extension of the DEM pavement model from 2D to 3D is required. In the pavement design, the plain strain condition is conservative. In addition, the transverse deformation in 3D has a significant effect on the permanent pavement deformation. Moreover, the interparticle interlocking effect may be evident in 3D, which probably affects the residual stress and the probability density distribution of both the contact and bond forces.

Appendix A

Mechanical behaviour for DEM biaxial test simulation

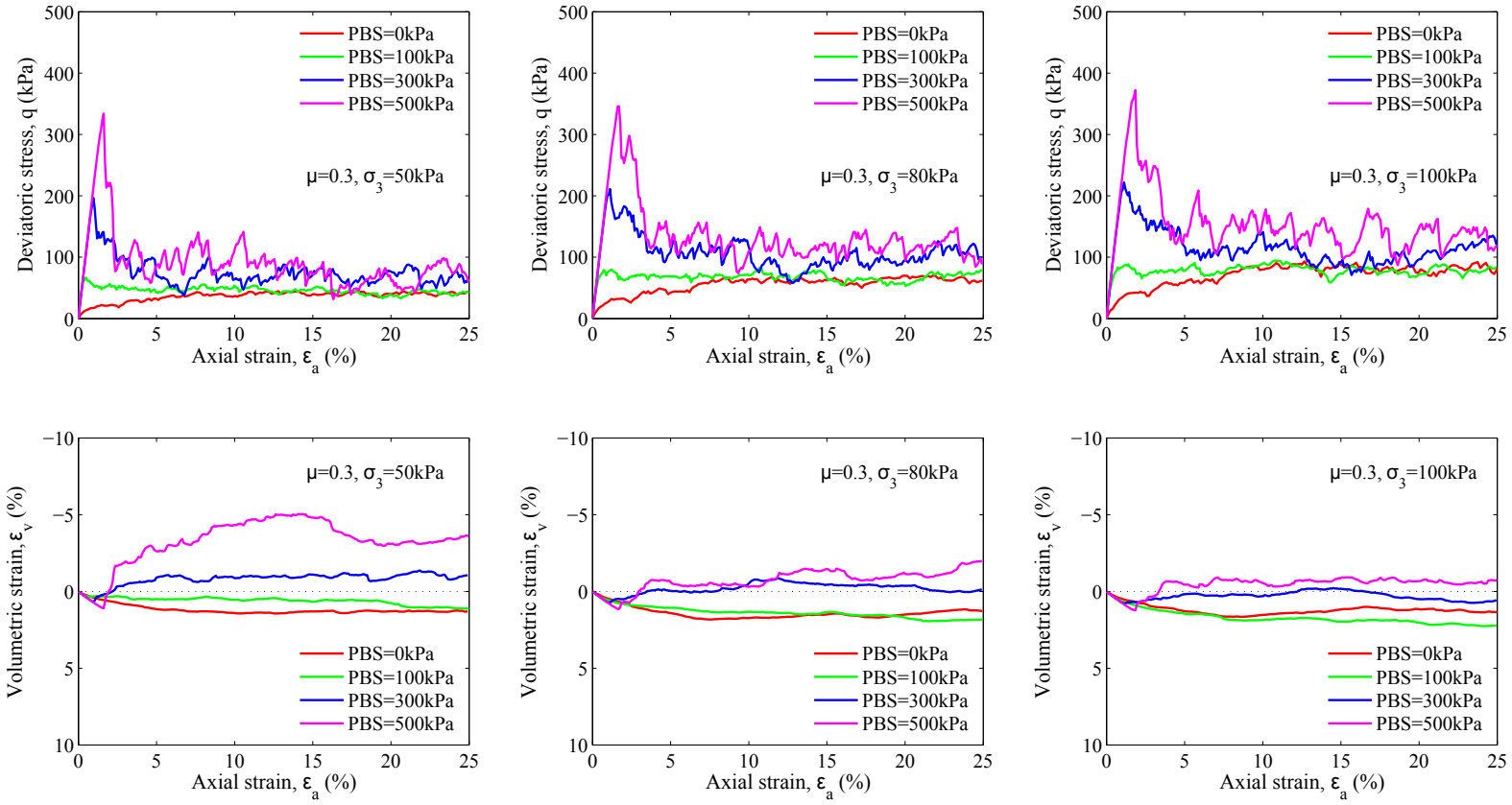

(a) μ=0.3

Figure A.1: Biaxial behaviour of loose sample associated with various bond strengths and particle friction coefficients, sheared across a range of confining pressures

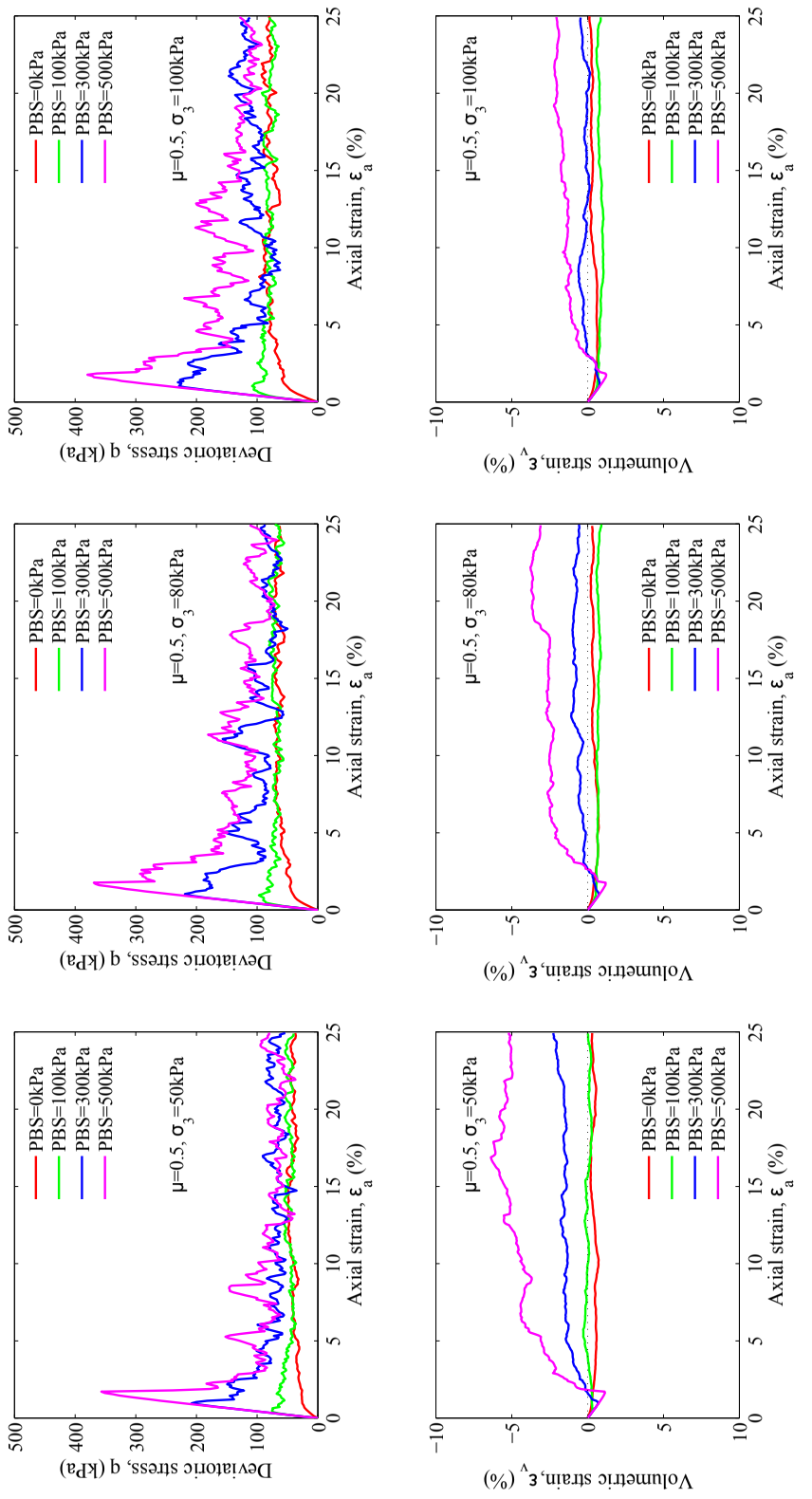

(b) μ=0.5

Figure A.1: Biaxial behaviour of loose sample associated with various bond strengths and particle friction coefficients, sheared across a range of confining pressures

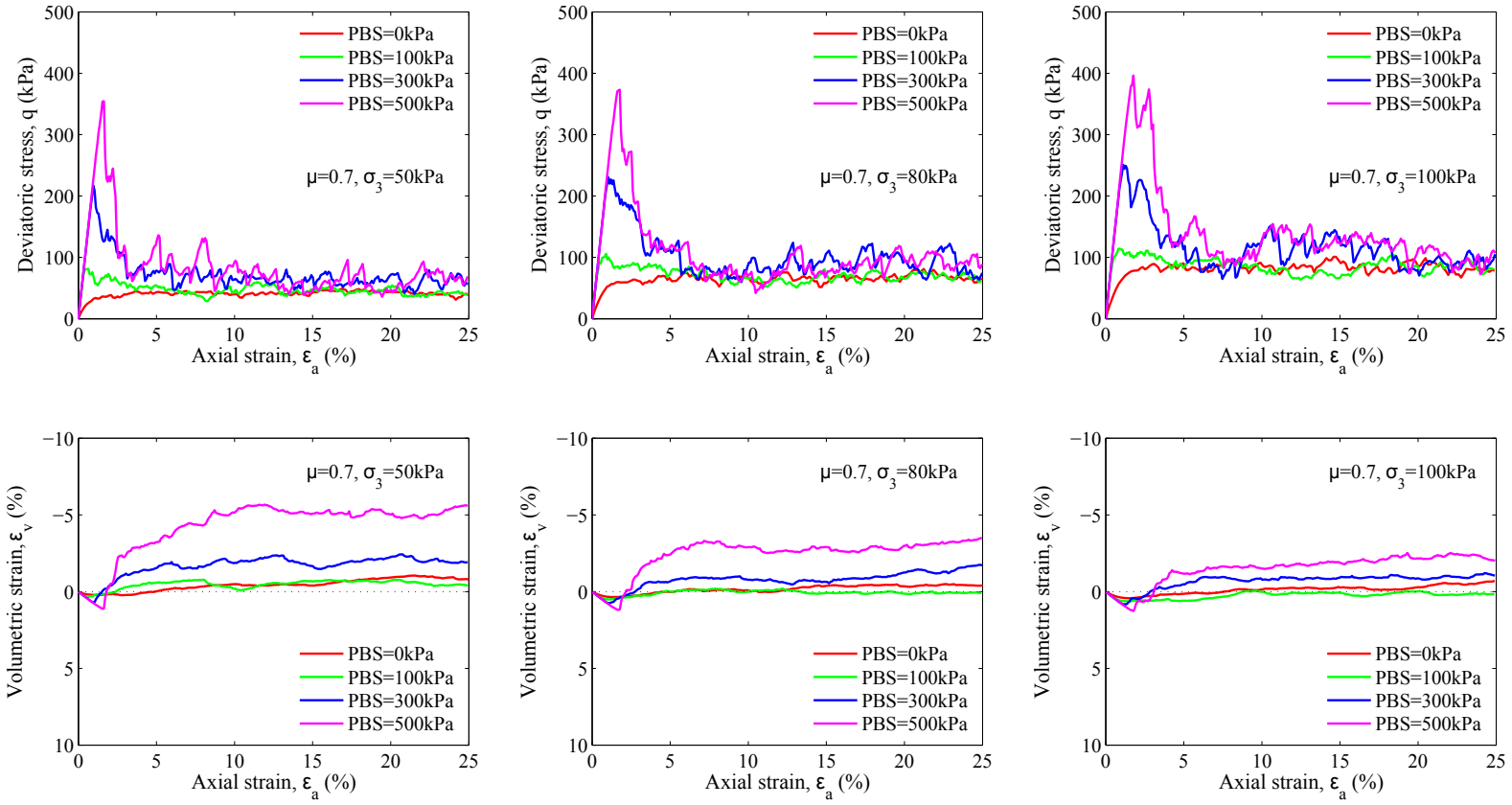

(c) μ=0.7

Figure A.1: Biaxial behaviour of loose sample associated with various bond strengths and particle friction coefficients, sheared across a range of confining pressures

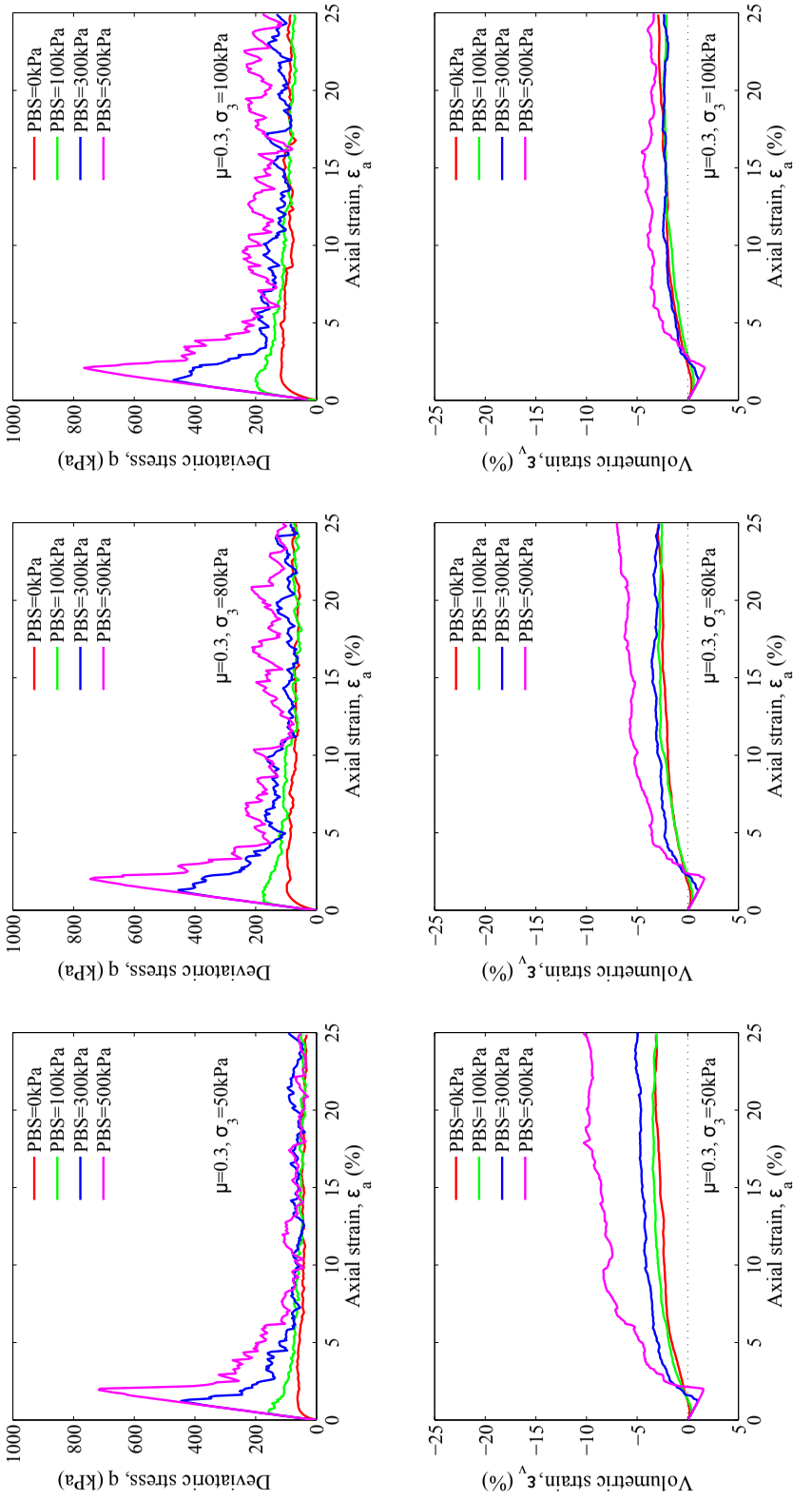

(a) μ=0.3

Figure A.2: Biaxial behaviour of dense sample associated with various bond strengths and particle friction coefficients, sheared across a range of confining pressures

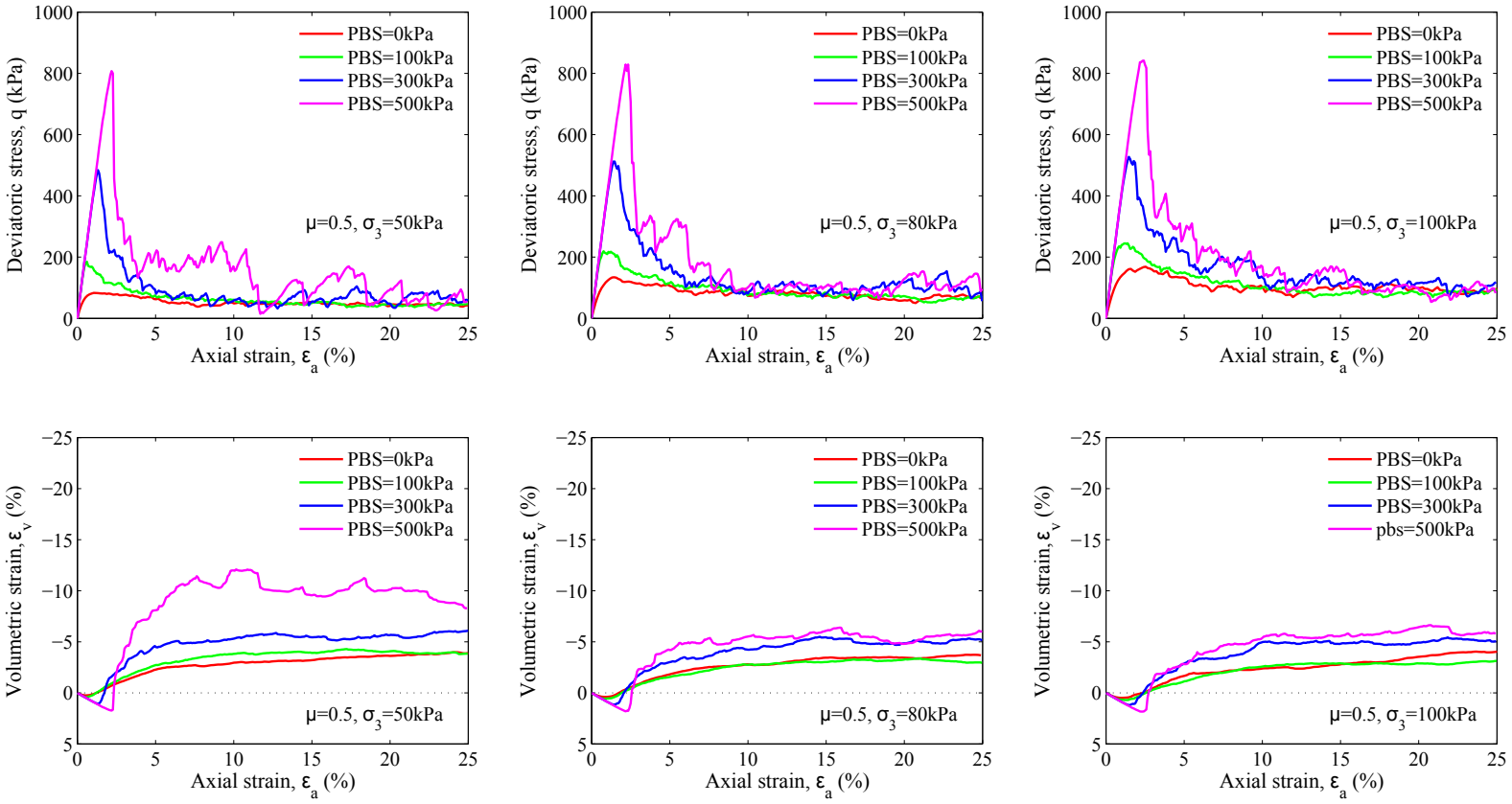

(b) μ=0.5

Figure A.2: Biaxial behaviour of dense sample associated with various bond strengths and particle friction coefficients, sheared across a range of confining pressures

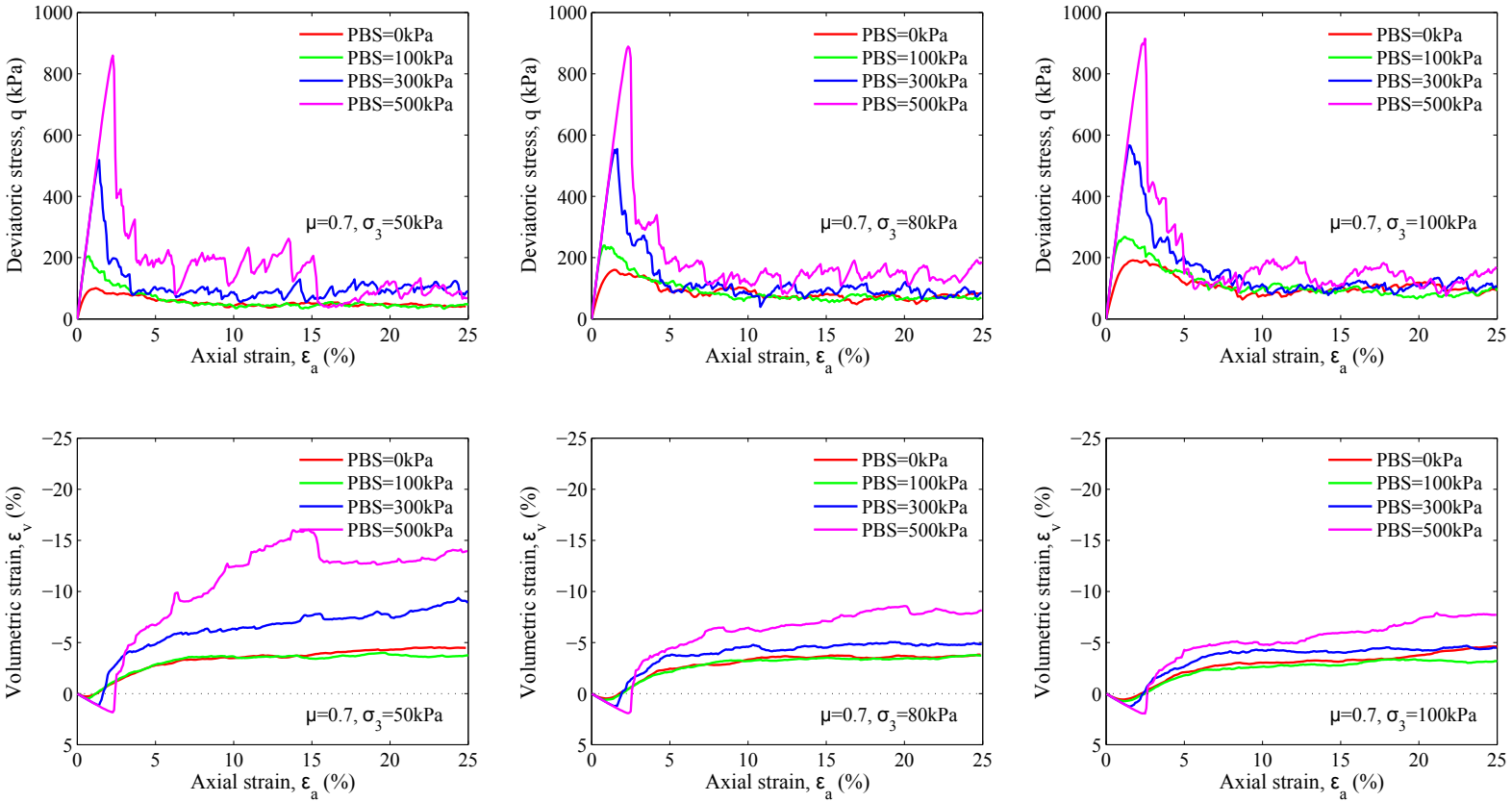

(c) μ=0.7

Figure A.2: Biaxial behaviour of dense sample associated with various bond strengths and particle friction coefficients, sheared across a range of confining pressures

Reference

AASHTO (1993). *AASHTO Guide for Design of Pavement Structures*. American Association of State Highway and Transportation Officials, Washington, D.C.

Abdulla, A. A. and Kiousis, P. D. (1997). Behavior of cemented sands-i. testing. *International Journal for Numerical and Analytical Methods in Geomechanics*, 21(8):533–547.

Ai, J., Langston, P. A., and Yu, H. S. (2014). Discrete element modelling of material non-coaxiality in simple shear flows. *International Journal for Numerical and Analytical Methods in Geomechanics*, 38(6):615–635.

Airey, D. W. (1993). Triaxial testing of naturally cemented carbonate soil. *Journal of Geotechnical Engineering*, 119(9):1379–1398.

Alshibli, K. A. and Sture, S. (2000). Shear band formation in plane strain experiments of sand. *Journal of Geotechnical and Geoenvironmental Engineering*, 126(6):495–503.

Asghari, E., Toll, D. G., and Haeri, S. M. (2003). Triaxial behaviour of a cemented gravely sand, tehran alluvium. *Geotechnical & Geological Engineering*, 21(1):1–28.

Bagi, K. (1997). Analysis of micro-variables through entropy principle. In R. P. Behringer, J. T. J., editor, *Powders & Grains 97*, pages 251–254.

Barber, E. S. (1946). Application of triaxial compression test results to the calculation of flexible pavement thickness. In *Proceedings, Highway Research Board*, volume 26, pages 26–39.

Bathurst, R. J. (1985). *A Study of Stress and Anisotropy in Idealised Granular Assemblies*. PhD thesis, Queen's University, Kingston, Canada.

Blair, D. L., Mueggenburg, N. W., Marshall, A. H., Jaeger, H. M., and Nagel, S. R. (2001). Force distributions in three-dimensional granular assemblies: Effects of packing order and interparticle friction. *Physical Review E*, 63(4):041304.

Bonse, R. P. and Kuhn, S. H. (1959). Dynamic forces exerted by moving vehicles on a road surface. *Highway Research Board Bulletin*, (233):9–23.

Boulbibane, M. and Collins, I. F. (2000). The calculation of shakedown loads for contact problems. *Key Engineering Materials*, 177:763–774.

Boulbibane, M., Collins, I. F., Weichert, D., and Raad, L. (2000). Shakedown analysis of anisotropic asphalt concrete pavements with clay subgrade. *Canadian geotechnical journal*, 37(4):882–889.

Brown, S. F. and Chan, F. W. K. (1996). Reduced rutting in unbound granular pavement layers through improved grading design. *Proceedings of the ICE-Transport*, 117(1):40–49.

Brown, S. F., Juspi, S., and Yu, H. S. (2008). Experimental observations and theoretical predictions of shakedown in soils under wheel loading. In *Advances in Transportation Geotechnics: Proceedings of the 1st International Conference on Transportation Geotechnics, Nottingham, UK*, pages 25–27.

Brown, S. F. and Selig, E. T. (1991). The design of pavement and rail track foundations. *Cyclic Loading of Soils: From Theory to Design*, pages 249–305.

Cai, W., McDowell, G. R., and Airey, G. (2013). Discrete element modelling of uniaxial constant strain rate tests on asphalt mixtures. *Granular Matter*, 15(2):163–174.

Camusso, M. and Barla, M. (2009). Microparameters calibration for loose and cemented soil when using particle methods. *International Journal of Geomechanics*, 9(5):217–229.

Chang, C. S. (1988). *Micromechanical Modelling of Constitutive Equation for Granular Material*. Micromechanics of Granular Materials, Satake and Jenkins (Eds.), Elsevier Science Publishers, Amsterdam, Netherlands.

Chang, K. N. G. and Meegoda, J. N. (1997). Micromechanical simulation of hot mix asphalt. *Journal of Engineering Mechanics*, 123(5):495–503.

Chen, L. H., Tang, S. T., and Zhang, H. T. (2010). Excel method in triaxial test data processing. *Journal of Beijing Jiaotong University*, 34(1):54–57.

Cheng, Y. P., Nakata, Y., and Bolton, M. D. (2003). Discrete element simulation of crushable soil. *Géotechnique*, 53(7):633–641.

Cheung, G. and O'Sullivan, C. (2008). Effective simulation of flexible lateral boundaries in two-and three-dimensional DEM simulations. *Particuology*, 6(6):483–500.

Clough, G. W., Iwabuchi, J., Rad, N. S., and Kuppusamy, T. (1989). Influence of cementation on liquefaction of sands. *Journal of Geotechnical Engineering*, 115(8):1102–1117.

Collins, I. F. and Boulbibane, M. (2000). Geomechanical analysis of unbound pavements based on shakedown theory. *Journal of Geotechnical and Geoenvironmental Engineering*, 126(1):50–59.

Collins, I. F. and Cliffe, P. F. (1987). Shakedown in frictional materials under moving surface loads. *International journal for numerical and analytical methods in geomechanics*, 11(4):409–420.

Collins, I. F., Wang, A. P., and Saunders, L. R. (1993). Shakedown in layered pavements under moving surface loads. *International journal for numerical and analytical methods in geomechanics*, 17(3):165–174.

Collop, A. C., McDowell, G. R., and Lee, Y. (2004). Use of the distinct element method to model the deformation behavior of an idealized asphalt mixture. *International Journal of Pavement Engineering*, 5(1):1–7.

Coppersmith, S. N., Liu, C. H., Majumdar, S., Narayan, O., and Witten, T. A. (1996). Model for force fluctuations in bead packs. *Physical Review E*, 53(5):4673–4685.

Croney, D. (1977). *The Design and Performance of Road Pavements*. Transport and Road Research Laboratory, London.

Cui, L. (2006). *Developing A Virtual Test Environment for Granular Materials Using Discrete Element Modelling*. PhD thesis, University College Dublin, Ireland.

Cundall, P. A. (1971). A computer model for simulating progressive large scale movements in blocky rock systems. In *Proc. Symp. Int. Soc. Rock Mech.*, volume 2, pages 132–150, Nancy.

Cundall, P. A. (1974). Rational design of tunnel supports: A computer model for rock mass behavior using interactive graphics for the input and output of geometrical data. Technical report, Report for the Missouri River Division, U.S. Army Corps of Engineers, University of Minnesota.

Cundall, P. A. (1988). Computer simulations of dense sphere assemblies. *Micromechanics of Granular Materials*, 4:113–123.

Cundall, P. A. and Hart, R. D. (1992). Numerical modelling of discontinua. *Engineering Computations*, 9(2):101–113.

Cundall, P. A. and Strack, O. D. L. (1979a). A discrete numerical model for granular assemblies. *Géotechnique*, 29(1):47–65.

Cundall, P. A. and Strack, O. D. L. (1979b). The distinct element method as a tool for research in granular media. Technical report, Part II. Report to National Science Foundation, Department of Civil and Mineral Engineering, University of Minnesota, Minneapolis, Minnesota.

Dantu, P. (1957). A contribution to the mechanical and geometrical study of non-cohesive masses. In *Proceedings of the 4th International Conference on Soil Mechanics and Foundation Engineering*, volume 1, pages 144–157.

Darter, M. I., Becker, J. M., Snyder, M. B., and Smith, R. E. (1985). Portland cement concrete pavement evaluation system (copes). *NCHRP Report 277, Transportation Research Board.*

Dawson, A. and Kolisoja, P. (2004). Roadex II, northern periphery. Technical report, Permanent Deformation, Report on Task 2.1.

De Beer, M., Fisher, C., and Jooste, F. J. (1997). Determination of pneumatic tyre/pavement interface contact stresses under moving loads and some effects on pavements with thin asphalt surfacing layers. In *Proceedings of the 8th International Conference on Asphalt Pavements*, volume 1, pages 10–14.

De Bono, J. P. (2013). *Discrete Element Modeling of Cemented Sand and Particle Crushing at High Pressures*. PhD thesis, University of Nottingham, the United Kingdom.

De Josselin de Jong, G. and Verruijt, A. (1969). Etude photo-elastique d'un empilement de disques. In *Cahires du group Francais de Rheologie, Janvier 1969*, volume II, pages 73–86.

Deresiewicz, H. (1958). Mechanics of granular matter. *Advances in Applied Mechanics*, 5:233–306.

Dondi, G., Bragaglia, M., and Vignali, V. (2005). Bituminous mixtures simulation with distinct particle elements method. In *III International SIIV Congress, Bari*, pages 22–24.

Dondi, G., Bragaglia, M., and Vignali, V. (2007). Flexible pavement simulation with distinct particle element method. In *Proceedings of the 4th International SIIV Congress, Palermo, Italy*.

Drescher, A. (1976). An experimental investigation of flow rules for granular materials using optically sensitive glass particles. *Géotechnique*, 26(4):591–601.

Dupas, J.-M. and Pecker, A. (1979). Static and dynamic properties of sand-cement. *Journal of the Geotechnical Engineering Division*, 105(3):419–436.

Fatigue cracking (2015). Road science. www.roadscience.net/services/distress-guide.

Fernando, E. G., Luhr, D. R., and Saxena, H. N. (1987). Analysis of axle loads and axle types for the evaluation of load limits on flexible pavements. *Transportation Research Record*, (1136):7–14.

Garca-Rojo, R. and Herrmann, H. J. (2005). Shakedown of unbound granular material. *Granular Matter*, 7(2-3):109–118.

Geng, Y. (2010). *Discrete Element Modelling of Cavity Expansion in Granular Materials*. PhD thesis, University of Nottingham, the United Kingdom.

Ginsberg, J. H. and Genin, J. (1984). *Dynamics*. New York: John Wiley & Sons.

Hall, K. T., Conner, J. M., Darter, M. I., and Carpenter, S. H. (1989). Rehabilitation of concrete pavements. Technical report, Concrete pavement evaluation and rehabilitation system, Report No. FHWA-RD-88-073, Federal Highway Administration.

Harireche, O. and McDowell, G. R. (2003). Discrete element modelling of cyclic loading of crushable aggreates. *Granular Matter*, 5(3):147–151.

Himeno, K., Kamijima, T., Ikeda, T., and Abe, T. (1997). Distribution of tire contact pressure of vehicles and its influence on pavement distress, seattle, washington. In *Eighth International Conference on Asphalt Pavements*.

Huang, J. T. and Airey, D. W. (1998). Properties of artificially cemented carbonate sand. *Journal of Geotechnical and Geoenvironmental Engineering*, 124(6):492–499.

Huang, Y. H. (1993). *Pavement analysis and design*. Prentice hall.

Hveem, F. N. and Sherman, G. B. (1962). California method for the structural design of flexible pavements. In *International Conference on the Structural Design of Asphalt Pavements, Ann Arbor, Michigan*, pages 851–866.

Ismail, M. A., Joer, H. A., Randolph, M. F., and Meritt, A. (2002). Cementation of porous materials using calcite. *Géotechnique*, 52(5):313–324.

Itasca (2004). *Particle Flow Code in Two Dimensions*. Software Manual, Itasca Consulting Group, Inc., Minnesota.

Iwashita, K. and Oda, M. (1998). Rolling resistance at contacts in simulation of shear band development by DEM. *Journal of Engineering Mechanics*, 124(3):285–292.

Jiang, M. J., Yan, H. B., Zhu, H. H., and Utili, S. (2011). Modeling shear behavior and strain localization in cemented sands by two-dimensional distinct element method analyses. *Computers and Geotechnics*, 38(1):14–29.

Johnson, K. L. (1962). A shakedown limit in rolling contact. In *Proceedings of the Fourth US National Congress of Applied Mechanics, Berkeley, California*, pages 971–975.

Johnson, K. L. (1986). Plastic flow, residual stress and shakedown in rolling contact. In *Proceedings of the Second International Symposium on Contact Mechanics and Wear of Rail/Wheel Systems*, pages 83–97.

Johnson, K. L. and Jefferis, J. A. (1963). Plastic flow and residual stresses in rolling and sliding contact. In *Proceeding of the Institution of Mechanical Engineers: Fatigue in Rolling Contact*, volume 177, pages 54–65.

Juran, I. and Riccobono, O. (1991). Reinforcing soft soils with artificially cemented compacted-sand columns. *Journal of Geotechnical Engineering*, 117(7):1042–1060.

Juspi, S. (2007). *Experimental validation of the shakedown concept for pavement analysis and design*. PhD thesis, University of Nottingham, the United Kingdom.

Kenis, W. J. (1977). Predictive design procedures-a design method for flexible pavements using the vesys structural subsystem. In *Proceedings of 4th International Conference on Structural Design of Asphalt Pavements, Ann Arbor, Michigan*, volume I, pages 101–130.

Kerkhoven, R. and Dormon, G. M. (1953). *Some considerations on the California bearing ratio method for the design of flexible pavements*. Shell Petroleum Company.

Klomp, A. J. G. and Niesman, T. W. (1967). Observed and calculated strains at various depths in asphalt pavements. In *2nd International Conference Structural Design of Asphalt Pavements, Ann Arbor, Michigan*, pages 671–688.

Koiter, W. T. (1960). *General theorems for elastic-plastic solids*. In: SNEDDON, I. N. A. H., R. (ed.) Progress in solid mechanics.

Korkiala-Tanttu, L. (2009). *Calculation method for permanent deformation of unbound pavement materials*. VTT.

Krabbenhøft, K., Lyamin, A. V., and Sloan, S. W. (2007). Shakedown of a cohesive-frictional half-space subjected to rolling and sliding contact. *International journal of solids and structures*, 44(11):3998–4008.

Kruyt, N. P. (2003). Contact forces in anisotropic frictional granular materials. *International journal of solids and structures*, 40:3537–3556.

Kuwano, R. and Jardine, R. J. (2007). A triaxial investigation of kinematic yielding in sand. *Géotechnique*, 57(7):563–579.

Ladd, R. S. (1978). Preparing test specimens using under-compaction. *Geotechnical Testing Journal*, 1(1):16–23.

Lagioia, R. and Nova, R. (1995). An experimental and theoretical study of the behaviour of a calcarenite in triaxial compression. *Géotechnique*, 45(4):633–648.

Lekarp, F., Isacsson, U., and Dawson, A. (2000). State of the art. I: Resilient response of unbound aggregates. *Journal of Transportation Engineering*, 126(1):66–75.

Li, D. Q. and Selig, E. T. (1996). Cumulative plastic deformation for fine-grained subgrade soils. *Journal of Geotechnical Engineering*, 122(12):1006–1013.

Li, H. X. and Yu, H. S. (2006). A nonlinear programming approach to kinematic shakedown analysis of frictional materials. *International journal of solids and structures*, 43(21):6594–6614.

Li, X. (2006). *Micro-scale Investigation on the Quasi-static Behaviour of Granular Material*. PhD thesis, The Hong Kong University of Science and Technology, Hong Kong, China.

Li, X. and Yu, H. S. (2011). Applicability of stress-force-fabric relationship for non-proportional loading. *Computers & Structures*, 89(11):1094–1102.

Li, X., Yu, H. S., and Li, X. S. (2013). A virtual experiment technique on the elementary behaviour of granular materials with discrete element method. *International Journal for Numerical and Analytical Methods in Geomechanics*, 37(1):75–96.

Li, X. S., Chan, C. K., and Shen, C. K. (1988). An automated triaxial testing system. *Advanced Triaxial Testing of Soil and Rock*, pages 95–106.

Lin, X. S. and Ng, T. T. (1997). A three-dimensional discrete element model using arrays of ellipsoids. *Géotechnique*, 47(2):319–329.

Liu, C. H., Nagel, S. R., Schecter, D. A., Coppersmith, S. N., Majumdar, S., Narayan, O., and Witten, T. A. (1995). Force fluctuations in bead packs. *Science*, 269(5223):513–515.

Lobo-Guerrero, S., Vallejo, L. E., and Vesga, L. F. (2006). Visualization of crushing evolution in granular materials under compression using DEM. *International Journal of Geomechanics*, 6(3):195–200.

Løvoll, G., Måløy, K. J., and Flekkøy, E. G. (1999). Force measurements on static granular materials. *Physical Review E*, 60(5):5872–5878.

Luding, S., David, C. T., Garcia-Rojo, R., and Herrmann, H. J. (2007). Frictional powders: Ratcheting under periodic strain in 3d. In *Partec 2007*, Nuremberg, Germany.

Lytton, R. L., Uzan, J., Fernando, E. G., Roque, R., Hiltunen, D., and Stoffels, S. M. (1993). *Development and validation of performance prediction models and specifications for asphalt binders and paving mixes*. Strategic Highway Research Program A-357 Rep., National Research Council, Washington, D.C.

Makse, H. A., Johnson, D. L., and Schwartz, L. M. (2000). Packing of compressible granular materials. *Physical review letters*, 84(18):4160–4163.

Marri, A. (2010). *The Mechanical Behaviour of Cemented Granular Materials at High Pressures*. PhD thesis, University of Nottingham, the United Kingdom.

Marwick, A. H. D. and Starks, H. J. H. (1941). Stresses between tyre and road. *Journal of Civil Engineers*, 6:309–325.

Maynar, M. J. and Rodrguez, L. E. (2005). Discrete numerical model for analysis of earth pressure balance tunnel excavation. *Journal of Geotechnical and Geoenvironmental Engineering*, 131(10):1234–1242.

McDowell, G. R. and Harireche, O. (2002). Discrete element modelling of yielding and normal compression of sand. *Géotechnique*, 52(4):299–304.

McGuire, W. and Gallagher, R. H. (1979). *Matrix Structural Analysis*. New York: Jonhn Wiley & Sons.

Melan, E. (1938). Der spannungsgudstand eines henky-mises schen kontinuums bei verlandicher belastung. *Sitzungberichte der Ak Wissenschaften Wie (Ser. 2A)*, 147:73.

Merwin, J. E. and Johnson, K. L. (1963). An analysis of plastic deformation in rolling contact. *Proceedings of the Institution of Mechanical Engineers*, 177(1):676–690.

Miller, J. S. and Bellinger, W. Y. (2003). Distress identification manual for the long-term pavement performance program. Technical report, In Fourth (Ed.) Virginia, Federal Highway Administration.

Mindlin, R. D. (1949). Compliance of elastic bodies in contact. *Journal of Applied Mechanics*, 16:259–268.

Mohamed, A. and Gutierrez, M. (2010). Comprehensive study of the effects of rolling resistance on the stress-strain and strain localization behavior of granular materials. *Granular Matter*, 12(5):527–541.

Monismith, C. L. (1973). Highway research board, special report 140, 1. Technical report.

Monismith, C. L. and Brown, S. F. (1999). Developments in the structural design and rehabilitation of asphalt pavements over three quarters of a century. *Journal of the Association of Asphalt Paving Technologist 68A*, pages 128–251.

Monismith, C. L., Inkabi, K., Freeme, C. R., and McLean, D. B. (1977). A subsystem to predict rutting in asphalt concrete pavement structures. In *Proceedings of 4th International Conference on Structural Design of Asphalt Pavements*, volume I, pages 529–539, University of Michigan, Ann Arbor, Michigan.

Monismith, C. L., Ogawa, N., and Freeme, C. R. (1975). Permanent deformation characteristics of subsoil due to repeated loading. *Transportation Research Record: Journal of the Transportation Research Board*, 537:1–17.

Mueth, D. M., Jaeger, H. M., and Nagel, S. R. (1998). Force distribution in a granular medium. *Physical Review E*, 57(3):3164–3169.

NCHRP (1999). Development of the 2002 guide for the design of new and rehabilitated pavement structures. Technical report, National Cooperative Highway Research Program (NCHRP) Research Project Rep., Transportation Research Board, Washington, D.C.

Ng, T. T. (1994). Numerical simulations of granular soil using elliptical particles. *Computers and Geotechnics*, 16(2):153–169.

Ng, T. T. and Dobry, R. (1994). Numerical simulations of monotonic and cyclic loading of granular soil. *Journal of Geotechnical Engineering*, 120(2):388–403.

Norman, P. J., Snowdon, R. A., and Jacobs, J. C. (1973). Pavement deflection measurements and their application to structural maintenance and overlay design. Technical report, Transport and Road Research Laboratory Report LR 571.

Oda, M., Nemat-Nasser, S., and Mehrabadi, M. (1982). A statistical study of fabric in a random assembly of spherical granules. *International Journal for Numerical and Analytical Methods in Geomechanics*, 6(1):77–94.

Pena, A. A., Lizcano, A., Alonso-Marroquin, F., and Herrmann, H. J. (2008). Biaxial test simulations using a packing of polygonal particles. *International Journal for Numerical and Analytical Methods in Geomechanics*, 32(2):143–160.

Ponter, A. R. S., Hearle, A. D., and Johnson, K. L. (1985). Application of the kinematical shakedown theorem to rolling and sliding point contacts. *Journal of the Mechanics and Physics of Solids*, 33(4):339–362.

Potyondy, D. O. and Cundall, P. A. (2004). A bonded-particle model for rock. *International Journal of Rock Mechanics and Mining Sciences*, 41(8):1329–1364.

Qiao, Y., Dawson, A., Huvstig, A., and Korkiala-Tanttu, L. (2014). Calculating rutting of some thin flexible pavements from repeated load triaxial test data. *International Journal of Pavement Engineering*, pages 1–10.

Quang, M. T. (2014). Rutting phenomenon, an analysis of incidents in the east-west highway project-causes and remedies. www.dnqnep.com.

Radjai, F., Jean, M., Moreau, J.-J., and Roux, S. (1996). Force distributions in dense two-dimensional granular systems. *Physical review letters*, 77(2):274–277.

Radovsky, B. S. and Murashina, N. V. (1996). Shakedown of subgrade soil under repeated loading. *Transportation Research Record: Journal of the Transportation Research Board*, 1547(1):82–88.

Ravindra, P. S. and Small, J. C. (2008). Shakedown analysis of road pavements. In *the 12th International Conference of International Association for Computer Methods and Advances in Geomechanics (IACMAG), Goa, India*.

Rothenburg, L. (1980). *Micromechanics of idealised granular materials*. PhD thesis, Carleton University, Ottawa, Ontario, Canada.

Rothenburg, L. and Bathurst, R. J. (1989). Analytical study of induced anisotropy in idealized granular materials. *Géotechnique*, 39(4):601–614.

Rowe, P. (1962). The stress-dilatancy relation for static equilibrium of an assembly of particles in contact. *Proceedings of the Royal Society of London. Series A, Mathematical and Physical Sciences*, 269(1339):500–527.

Saal, R. N. J. and Pell, P. S. (1960). Kolloid-zeitschrift mi. *Heft*, 1:61–71.

Schnaid, F., Prietto, P. D. M., and Consoli, N. C. (2001). Characterization of cemented sand in triaxial compression. *Journal of Geotechnical and Geoenvironmental Engineering*, 127(10):857–868.

Sharp, R. W. and Booker, J. R. (1984). Shakedown of pavements under moving surface loads. *Journal of Transportation Engineering*, 110(1):1–14.

Shiau, S.-H. (2001). *Numerical methods for shakedown analysis of pavements under moving surface loads*. PhD thesis, University of Newcastle.

Shiau, S. H. and Yu, H. S. (2000). Load and displacement prediction for shakedown analysis of layered pavements. *Transportation Research Record: Journal of the Transportation Research Board*, 1730(1):117–124.

Sitharam, G. T. (1991). *Numerical Simulation of Hydraulic Fracturing in Granular Media*. PhD thesis, University of Waterloo, Waterloo, Ontario, Canada.

Sitharam, T. G. (1999). Micromechanical modeling of granular materials: Effect of confining pressure on mechanical behavior. *Mechanics of Materials*, 31(10):653–665.

Sitharam, T. G. (2003). Discrete element modelling of cyclic behaviour of granular materials. *Geotechnical and Geological Engineering*, 21(4):297–329.

Strack, O. D. L. and Cundall, P. A. (1984). Fundamental studies of fabric in granular materials. Technical report, Interim Report to NSFCEE-8310729, Dept. of Civil and Mineral Engineering, Univ. of Minnesota.

Theyse, H. L. (1997). Mechanistic-empirical modelling of the permanent deformation of unbound pavement layers. In *8th International Conference on Asphalt Pavements, Federal Highway Administration, Washington DC*, volume 19.

Theyse, H. L., De Beer, M., and Rust, F. C. (1996). Overview of south african mechanistic pavement design method. *Transportation Research Record: Journal of the Transportation Research Board*, 1539(1):6–17.

Thom, N. (2008). *Principles of pavement engineering*. Thomas Telford Publishing.

Thomas, P. A. and Bray, J. D. (1999). Capturing nonspherical shape of granular media with disk clusters. *Journal of Geotechnical and Geoenvironmental Engineering*, 125(3):169–178.

Thornton, C. (1979). The conditions for failure of a face-centered cubic array of uniform rigid spheres. *Géotechnique*, 29(4):441–459.

Thornton, C. (1997). Force transmission in granular media. *Kona Powder and Particle Journal*, 15:81–90.

Thornton, C. (2000). Numerical simulations of deviatoric shear deformation of granular media. *Géotechnique*, 50(1):43–53.

Thornton, C. and Antony, S. J. (1998). Quasi-static deformation of particulate media. *Philosophical Transactions-Royal Society of London Series A Mathematical Physical & Engineering Sciences*, pages 2763–2782.

Ting, J. M., Meachum, L., and Rowell, J. D. (1995). Effect of particle shape on the strength and deformation mechanisms of ellipse-shaped granular assemblages. *Engineering Computations*, 12(2):99–108.

Tsoungui, O., Vallet, D., and Charmet, J.-C. (1999). Numerical model of crushing of grains inside two-dimensional granular materials. *Powder Technology*, 105(1):190–198.

Tsunekawa, H. and Iwashita, K. (2001). Numerical simulation of triaxial test using two and three dimensional DEM. In Kishino, Y., editor, *Powders & Grains 01*, pages 177–182.

Utili, S. and Nova, R. (2008). DEM analysis of bonded granular geomaterials. *International Journal for Numerical and Analytical Methods in Geomechanics*, 32(17):1997–2031.

Uzan, J. (2004). Permanent deformation in flexible pavements. *Journal of Transportation Engineering*, 130(1):6–13.

Vallejo, L. E., Lobo-Guerrero, S., and Hammer, K. (2006). Degradation of a granular base under a flexible pavement: Dem simulation. *International Journal of Geomechanics*, 6(6):435–439.

Wakabayashi, T. (1950). Photo-elastic method for determination of stress in powdered mass. *Journal of the Physical Society of Japan*, 5(5):383–385.

Wang, J. (2011). *Shakedown analysis and design of flexible road pavements under moving surface loads*. PhD thesis, University of Nottingham, the United Kingdom.

Wang, Y. H. and Leung, S. C. (2008a). Characterization of cemented sand by experimental and numerical investigations. *Journal of Geotechnical and Geoenvironmental Engineering*, 134(7):992–1004.

Wang, Y. H. and Leung, S. C. (2008b). A particulate-scale investigation of cemented sand behavior. *Canadian Geotechnical Journal*, 45(1):29–44.

Werkmeister, S., Dawson, A. R., and Wellner, F. (2004). Pavement design model for unbound granular materials. *Journal of Transportation Engineering*, 130(5):665–674.

Yamamuro, J. A. and Lade, P. V. (1996). Drained sand behavior in axisymmetric tests at high pressures. *Journal of Geotechnical Engineering*, 122(2):109–119.

Yoder, E. J. (1959). *Principles of pavement design*. John Wiley & Sons.

Yoder, E. J. and Witczak, M. W. (1975). *Principles of pavement design*. John Wiley & Sons.

Yoon, J. (2007). Application of experimental design and optimization to PFC model calibration in uniaxial compression simulation. *International Journal of Rock Mechanics and Mining Sciences*, 44(6):871–889.

Yu, H. S. (2005). Three-dimensional analytical solutions for shakedown of cohesive-frictional materials under moving surface loads. *Proceedings of the Royal Society A: Mathematical, Physical and Engineering Science*, 461(2059):1951–1964.

Yu, H. S. and Hossain, M. Z. (1998). Lower bound shakedown analysis of layered pavements using discontinuous stress fields. *Computer Methods in Applied Mechanics and Engineering*, 167(3):209–222.

Zhou, J. (2011). *Multi-scale Investigation on the Effect of the Specimen Preparation on Sand Behaviour*. PhD thesis, China University of Mining and Technology, Xuzhou, Jiangsu, China.

Zhou, J., Su, Y., and Chi, Y. (2006). Simulation of soil properties by particle flow code. *Chinese Journal of Geotechnical Engineering*, 28(3):390–396.